Investigating the sorption phenomena of free fatty acids using the Quartz Crystal Microbalance

By Kebonyetsala Aobakwe Laurel Seanneng

A thesis submitted to Imperial College London for the degree of Doctor of Philosophy

Department of Chemical Engineering, Imperial College London

South Kensington Campus, London, SW7 2AZ, United Kingdom

December 2025

Declaration of Originality

I hereby declare that this thesis is a result of my own work and that any information or ideas from other people's work has been appropriately referenced.

Kebonyetsala Seanneng, 2025

Copyright Declaration

The copyright of this thesis rests with the author. Unless otherwise indicated, its contents are licensed under a Creative Commons Attribution-Non-Commercial-No Derivatives 4.0 International Licence (CC BY-NC-ND). Under this licence, you may copy and redistribute the material in any medium or format on the condition that; you credit the author, do not use it for commercial purposes and do not distribute modified versions of the work. When reusing or sharing this work, ensure you make the licence terms clear to others by naming the licence and linking to the licence text. Please seek permission from the copyright holder for uses of this work that are not included in this licence or permitted under UK Copyright Law.

Abstract

Fatbergs have become an increasing problem with the increase in demand and use of products that contain fats oil and grease (FOG) formed when FOG and sanitary products lump together forming huge masses in sewers thus creating problems such as sewer overflows. This poses a danger as sewage making its way into water streams contaminates water. To address the problem, the adsorption of fatty acids identified in sewer systems i.e. palmitic acid , oleic acid and linoleic acid by He et al. (2013) onto polystyrene, aluminium oxide, and silicon dioxide was investigated using Quartz crystal microbalance with dissipation (QCMD). The emphasise of the study was to minimize the impact of the FOG deposits by prevention hence the study focuses exclusively of adsorption of free fatty acids (FFA).

Pseudo first order and pseudo second order models revealed that experimental results were a good fit for the PSO model with $R^2 > 0.93$ thereby suggesting that the fatty acids chemically adsorbed to the sensors and formed a monolayer. Chemical adsorption was confirmed by Xray photoelectron spectroscopy (XPS). Competitive adsorption studies revealed that palmitic acid introduced rigidity to the adlayer and the extent of this dependent on its position in the sequence. Linoleic acid adsorbed in an extended state while oleic acid adsorbed parallel to the quartz sensors (Lundgren et al., 2006). This effect was affected by the position of linoleic acid and oleic acid in the sequence thus resulting in different conformational changes within the adlayers. The effect of pH determined that adsorption of the FFA was highest around the pKa values of 9.85, 9.24 and 8.6 respectively with palmitic acid forming the thickest layer. Calculation of the thermodynamic parameters revealed that the adsorption of the fatty acids onto a gold sensor was an endothermic process with a great degree of spontaneity.

Dedication

This thesis is dedicated to my family, whose unwavering love and support have been my foundation. To my husband, Mr. Clint N. O. Okeyo, my mother, Mrs. Otsilegape Seanneng, my sister, Phenyo N. C. Seanneng, and my grandmother, Ntesang Keitebetse, I express my deepest gratitude for your care and encouragement which have been my constant source of strength.

To my daughter Komie Botshelo Thelma Okeyo whom I love. I express my deepest gratitude for your presence in my life. Thank you for the motivation to keep going.

Acknowledgements

I would like to extend my gratitude to the Department of Tertiary Education Financing Botswana for sponsoring my PhD. I also extend my thanks to my dear friend, Mbabi Tema, for her support throughout this journey. I also extend my gratitude to Dr Gwilherm Kerherve , Ms Patricia Carry, Mr Andrew C. Macey, Dr Umang V. Shah and Dr James I. Campbell for their assistance during this PhD and offering me training on various analytical techniques some of which are used in this thesis. Finally, I am grateful to my supervisor, Prof. Jerry Heng, for his invaluable guidance and support during my PhD.

Table of contents

Declaration of Originality i

Copyright Declaration ii

Abstract iii

Dedication iv

Acknowledgements v

List of Figures x

List of Tables xix

Nomenclature xxi

Abbreviations xxiii

Chapter 1 Introduction 1

1.1 Literature Review 4

1.1.1 Fatberg Formation 4

1.1.2 Silica 6

1.1.3 Quartz Crystal Microbalance with Dissipation 14

1.1.4 Adsorption kinetics on QCM-D 19

1.1.5 Adsorption 21

1.2 Chemistry of fats and oils 31

1.3 Conclusions 33

Chapter 2 Investigating adsorption of palmitic acid using Quartz crystal Microbalance with Dissipation 35

2.1 Abstract 35

2.2 Introduction 35

2.2.1 Review of Literature 37

2.3 Materials and methods 39

2.3.2 Adsorption of palmitic acid using QCM-D 39

2.3.3 Characterization by XPS 40

2.3.4 Statistical Analysis 42

2.4 Results and Discussion 43

2.4.1 QCM-D 43

2.4.2 Xray photoelectron Spectroscopy of Palmitic acid adsorption 61

2.5 Conclusions 74

Chapter 3 Investigating adsorption Kinetics of Oleic and Linoleic acid using Quartz crystal Microbalance with Dissipation 76

3.1 Abstract 76

3.2 Introduction 76

3.2.1 Materials and Methods 77

3.2.2 Results and Discussion 81

3.3 Conclusion 116

Chapter 4 Investigation of Palmitic acid, Oleic Acid and Linoleic adsorption using QCMD: effect of sequencing..... 117

4.1 Abstract 117

4.2 Introduction..... 117

4.2.1 Materials and Methods 118

4.2.2 Results and Discussion 121

4.3 Conclusions..... 155

Chapter 5 Effect of pH, Temperature and Inserts on adsorption using QCM 156

5.1 Abstract 156

5.2 Introduction..... 156

5.2.1 Materials and methods 158

5.2.2 Results and Discussion 162

5.2.3 Conclusion 181

Chapter 7 Main conclusion..... 183

Chapter 6 Further Work 185

6.1 Spin Coating..... 186

6.2 Proof of concept 187

6.2.1 Experimental Methods 188

6.2.2 QCM-D..... 190

6.2.3 Results and Discussion 191

Chapter 7 References 198

Chapter 8 Appendices 220

8.1 Appendix for Chapter 3 220

8.1.1 Oleic Acid 220

8.1.2 Aluminium Oxide 223

8.1.3 Linoleic Acid 225

8.1.4 Silicon Dioxide 226

8.1.5 Aluminium Oxide 227

8.2 Appendix for Chapter 4 228

8.2.1 Raw data for Sequencing Experiments 228

8.2.2 Effect of sequencing : Mass Adsorbed 236

8.3 Appendix for Chapter 5 244

8.3.1 Palmitic Acid 244

8.3.2 Oleic Acid 245

8.3.3 Linoleic Acid 246

Copyright Permission Table 249

List of Figures

Figure 1.1 Oliobox collection box at a supermarket in Belgium to recycle frying cooking oil. (Seanneng, 2025) photo taken outside a local supermarket. 2

Figure 1.2 Mechanism by which Fatbergs are formed. Reprinted with permission from (He et al., 2013) 5

Figure 1.3 shows the sequential addition method for synthesis of silica. Reprinted from (Rao et al., 2005) 7

Figure 1.4 The variation of particle size with change in ammonia/ethanol ratio. Reproduced from (Zulfiqar et al., 2016) 9

Figure 1.5 The results of small x-ray scattering for mesoporous ordered silica synthesised at different temperatures. Reproduced from (Li et al., 2016) 10

Figure 1.6 Scanning Electron Microscopy images of mesoporous silica synthesized at different temperatures. Reproduced from (Li et al., 2016) 11

Figure 1.7 shows effect of increasing concentration of ammonia on the particle size. Reprinted from (Rao et al., 2005). 12

Figure 1.8 Methods used to synthesise silica nanoparticles; Reproduced from (Liberman et al., 2014). 13

Figure 1.9 shows frequency and dissipation shifts when a mass is applied onto a quartz sensor. Adapted from (Biolin Scientific, 2020). 14

Figure 1.10 shows different shapes of quartz sensors. Reproduced from (Anderson et al., 2007). 15

Figure 1.11 shows the average frequency response for circular and rectangular quartz sensors. Reproduced from (Anderson et al., 2007). 16

Figure 1.12 shows proposed mechanisms by which adsorption occurred for the fatty acids under test. Adapted from (Lundgren et al., 2007). 21

Figure 1.13 Shows a depiction of the adsorption process. Reproduced from (Butt et al., 2003) 22

Figure 1.14 Shows different types of isotherms. Reproduced from (Butt et al., 2003) 23

Figure 1.15 shows the binding isotherm for polymer Ethyl adenine-9-acetate. Reproduced from (Umpleby II et al., 2001) 24

Figure 1.16 Shows the Langmuir adsorption model. Reprinted from (Butt et al., 2003). 25

Figure 1.17 shows the results adsorption of lauric acid (●) , stearic acid (∆), palmitic acid (♦), myristic acid (◊) and capric acid (○) **q** (m/g) is the amount of adsorbate adsorbed (mg/g) of adsorbent and $\mathbf{x_e}$ (mg) is the adsorbate in solution at equilibrium. Reproduced from (Bayrak, 2006). 26

Figure 1.18 Shows BET multilayer adsorption. Reprinted from (Wang & Guo, 2020) 27

Figure 2.1 Shows the structure of Palmitic acid. 37

Figure 2.2 QCMD experimental set up made up of the Qsense explorer, batch module and user interface. 40

Figure 2.3 The third overtone QCMD response when palmitic acid ss was added onto different substrate sensors (a) Aluminium Oxide , (b) Polystyrene and (c) Silicon Dioxide at a concentration of 150mg/ml. The plots show ∆F (blue line) and ∆D (red line) before addition of ethanol (1) during addition of ethanol (2) and after the addition of palmitic acid (3). 43

Figure 2.4 Adsorption isotherms for all the different surfaces with increasing concentration of palmitic acid. The experiments were repeated twice. The mean frequency change is plotted against changing concentration. The error bars represent the standard deviation. 46

Figure 2.5 Mass adsorbed with time calculated using Sauerbrey equation at the third overtone. 47

Figure 2.6 Adsorbed mass obtained from DFind SmartFit. 50

Figure 2.7 Frequency and dissipation shift at the 3rd overtone for palmitic acid adsorption.. 51

Figure 2.8 PSO models for palmitic acid adsorption on different surfaces. 53

Figure 2.9 shows plot of the areal mass density at equilibrium versus concentration for the PSO adsorption kinetics of Palmitic acid onto Polystyrene, Aluminium oxide, and Silicon Dioxide. 55

Figure 2.10 Linearized plot for modelling pseudo-first-order kinetics for adsorption of Palmitic acid onto Aluminium Oxide at different concentrations. 57

Figure 2.11 Linearized plot for modelling pseudo-first-order kinetics using experimental data for adsorption of Palmitic acid onto Silicon Dioxide at different concentrations. 57

Figure 2.12 Linearized plot for modelling pseudo-first-order kinetics from experimental data for the adsorption of Palmitic acid onto Polystyrene at different concentrations. 58

Figure 2.13 Areal mass density at equilibrium with increasing concentration for the PFO adsorption kinetics of Palmitic acid onto Polystyrene, Aluminium oxide, and Silicon Dioxide. 60

Figure 2.14 XPS surveys for silica surface. (a) shows a survey for a new silica surface (b) shows a survey for the same sensor after use for palmitic acid adsorption studies. 61

Figure 2.15 XPS survey spectra for rinsed silicon dioxide sensors following QCMD experiments with 125mg/ml of palmitic acid ss. (A) rinsed with deionised water (B) rinsed with ethanol. 62

Figure 2.16 Full XPS Spectrum for unused QSX 303 SiO_2 from Qsense (a) O1s (b) C1s and (c) Si2p 64

Figure 2.17 XPS Spectra following palmitic acid adsorption onto SiO_2 sensor (a) C1s (b) O1s (c) Si2p 65

Figure 2.18 Results of aluminium oxide substrate sensor after 125mg/ml palmitic acid has been adsorbed. 67

Figure 2.19 XPS Spectra of polystyrene (a) Survey (b) O1s (c) C1s 69

Figure 2.20 shows 125mg/ml palmitic acid ss on polystyrene. 71

Figure 2.21 Atomic % of C1s on different substrate sensors 73

Figure 2.22 Atomic % of O1s on different substrate sensors. 73

Figure 3.1 structure of oleic acid and linoleic acid 77

Figure 3.2 shows adsorption isotherm of oleic acid adsorbing onto different substrate sensors. 81

Figure 3.3 shows adsorption isotherm of linoleic acid adsorbing onto different substrate sensors. 83

Figure 3.4 Pseudo-second-order adsorption kinetics of linoleic acid onto Aluminium Oxide at different initial concentrations. 84

Figure 3.5 Pseudo-second-order adsorption kinetics of linoleic acid onto Silicon Dioxide at different initial concentrations. 85

Figure 3.6 Pseudo-second-order kinetics of Linoleic acid on Polystyrene at various initial concentrations..... 85

Figure 3.7 Plot of the adsorption capacity versus time for the effect of concentration on the adsorption kinetics of Linoleic acid onto Aluminum Oxide. 86

Figure 3.8 Plot of the adsorption capacity versus time for effect of concentration on the adsorption kinetics of linoleic acid onto Silicon dioxide. 87

Figure 3.9 Plot of the adsorption capacity versus time for effect of concentration on the adsorption kinetics of linoleic acid onto Polystyrene. 88

Figure 3.10 Pseudo second order rate constant of linoleic acid adsorption at different concentrations..... 89

Figure 3.11 shows plot of the areal mass density at equilibrium versus concentration for the adsorption kinetics of linoleic acid onto Polystyrene, Aluminium oxide, and Silicon Dioxide. 90

Figure 3.12 Adsorption kinetics (PSO) of Oleic acid on Aluminium Oxide at different concentrations from experimental data..... 91

Figure 3.13 Adsorption capacity versus time for effect of concentration on the adsorption kinetics of Oleic acid onto Aluminium oxide (A) Experimental (B) Theoretical. 93

Figure 3.14 Adsorption kinetics (PSO) of Oleic acid on Silicon Dioxide. 95

Figure 3.15 Adsorption capacity versus time for effect of concentration on the adsorption kinetics of Oleic acid onto Silicon dioxide oxide (A) Experimental (B) Theoretical. 96

Figure 3.16 Adsorption kinetics (PSO) of Oleic acid on Polystyrene..... 97

Figure 3.17 shows plot of the adsorption capacity versus time for effect of concentration on the adsorption kinetics of Oleic acid onto Polystyrene (A) Experimental (B) Theoretical. 98

Figure 3.18 Plot of the areal mass density at equilibrium versus concentration for the adsorption kinetics of Oleic acid onto Polystyrene, Aluminium oxide, and Silicon Dioxide. .. 99

Figure 3.19 Pseudo second order rate constant (Oleic acid) at different concentrations on the three substrate sensors. 100

Figure 3.20 Shapes of oleic acid adsorbed onto (a) polystyrene (b) Silicon dioxide (c) Aluminium Oxide shown of the measurement window of the K-Alpha XPS Machine and operated using the Avantage software. 101

Figure 3.21 Survey spectra of 25mg/ml and 125mg/ml oleic acid adsorbed on polystyrene. 104

Figure 3.22 Deconvolution of Si2p, C1s and O1s scans of 25mg/ml oleic acid on polystyrene. 105

Figure 3.23 Deconvolution of Si2p, C1s and O1s scans of 125mg/ml oleic acid on polystyrene. 106

Figure 3.24 Silicon dioxide substrates and survey scan for adsorption of 125mg/ml oleic acid on SiO2. 107

Figure 3.25 Deconvolution of O1s , C1s and Si2p scans or adsorption of 125mg/ml oleic acid on SiO2. 108

Figure 3.26 Deconvolution of O1s , C1s and Si2p scans and of aluminium oxide substrate sensor at 125mg/ml oleic acid adsorption. 109

Figure 3.27 Deconvolution of peaks on polystyrene substrate. (A) analysis window of silicon substrates with linoleic acid adsorption (B) Survey scan with 75mg/ml linoleic acid adsorbed (C) C1s scan (D) O1s scan (E) Si2p scan. 111

Figure 3.28 shows deconvolution of peaks on silicon dioxide substrate. (A) analysis window of silicon substrates with linoleic acid adsorption (B) Survey scan with 75mg/ml linoleic acid adsorbed (C) C1s scan (D) O1s scan (E) Si2p scan. 112

Figure 3.29 deconvolution of peaks on aluminium oxide substrate. (A) analysis window of silicon substrates with linoleic acid adsorption (B) Survey scan with 75mg/ml linoleic acid adsorbed (C) C1s scan (D) O1s scan (E) Si2p scan. 113

Figure 3.30 C1s region of linoleic acid adsorbed onto different materials. 114

Figure 3.31 static contact angle measurement on an unused Hydrophobic polystyrene sensor 115

Figure 3.32 static contact angle measurement on used Hydrophobic polystyrene sensor . 115

Figure 4.1 Oleic acid Linoleic acid and Palmitic acid injection sequence on a Polystyrene substrate sensor. 120

Figure 4.2 Shows ∆F for sequential addition tests of FFA on Polystyrene sensor substrate. 122

Figure 4.3 shows total mass adsorbed on Polystyrene sensor substrate at the end of each experiment 123

Figure 4.4 shows the total change in frequency of sequential addition of FFA onto Silicon Dioxide 124

Figure 4.5 shows the total mass adsorbed due to sequential addition of FFA onto Silicon Dioxide. 125

Figure 4.6 Shows sequencing of Linoleic acid Palmitic acid and Oleic acid QCMD experimental results. 127

Figure 4.7 shows ∆F for sequential addition of FFA onto Aluminium Oxide. 128

Figure 4.8 Total mass adsorbed due to sequential addition of FFA onto Aluminium Oxide. 129

Figure 4.9 shows Changes in dissipation energy for LPO. 130

Figure 4.10 shows frequency and dissipation over different harmonics for sequence LPO. 131

Figure 4.11 Dissipation vs Frequency plots for sequence LPO and OPL on aluminium oxide. 133

Figure 4.12 Viscosity changes of the sequences LPO and OPL as calculated by Voight. . 135

Figure 4.13(A) and (B) show the Voigt thickness of the adlayer for sequence LPO and OPL 137

Figure 4.14 Total thickness of FFA adsorbed calculated as the average shift of the last period i.e. fatty acid added. 138

Figure 4.15 shows Sauerbrey mass for LPO and OPL. 139

Figure 4.16 Images taken by the Raman microscope during analysis of Silicon dioxide sensor flowing sequencing experiment OLP (A) before analysis (B) shows degradation of the sample after analysis. 140

Figure 4.17 Raman microscope image of sequence POL on Silicon dioxide surface 140

Figure 4.18 Raman spectra for adsorbed sequences on silicon dioxide sensor. 141

Figure 4.19 Raman Spectra of Palmitic Acid with those of the sequencing tests. 143

Figure 4.20 Raman shift sequencing plots on Aluminium oxide sensor substrates. 143

Figure 4.21 shows the Raman microscope image sequence POL. 144

Figure 4.22 shows the Raman microscope image sequence LPO. 144

Figure 4.23 shows the Raman microscope image sequence OPL. 145

Figure 4.24 shows the Raman spectra between 1400 and 1500cm^{-1} in sequence LOP. ... 146

Figure 4.25 shows the number of peaks fitted for LOP. 148

Figure 4.26 shows Intensity of Raman peaks for sequence LOP. 148

Figure 4.27 shows the number of peaks fitted for LPO. 150

Figure 4.28 shows the number of peaks fitted for OLP. 151

Figure 4.29 shows the number of peaks fitted for OPL. 152

Figure 4.30 shows the number of peaks fitted for POL. 153

Figure 4.31 shows FTIR spectrum from sequencing tests on polystyrene substrate sensor. 154

Figure 5.1 shows the QCMD setup for temperature experiments. 160

Figure 5.2 shows copper and tinned copper inserts used as secondary surface. 161

Figure 5.3 Shows the effect of pH on the thickness of the fatty acid layer adsorbed onto Gold. 163

Figure 5.4 Effect of pH on Dissipation for adsorption onto gold substrate sensors. 165

Figure 5.5 shows frequency and dissipation plots for Palmitic acid (pH 8.6), Oleic acid (pH 9.85) and Linoleic acid (pH 9.24). The plots show different overtones and (A) Baseline (B) buffer added (C) Fatty acid ss added 167

Figure 5.6 Rate of palmitic acid adsorbed at different pH. 168

Figure 5.7 Rate of adsorption of Oleic acid on Gold at different pH. 169

Figure 5.8 Rate of adsorption of Linoleic acid on Gold at different pH. 170

Figure 5.9 Rate of adsorption of Palmitic acid on Gold at different pH values 170

Figure 5.10 Oleic acid on aluminium oxide (A) and silicon dioxide (B)..... 171

Figure 5.11 Effect of pH 3.75 on FFA..... 171

Figure 5.12 Effect of temperature on adsorption of 50mg/ml ss of fatty acid onto gold sensor at 15ºC (A) Palmitic Acid (B) Oleic Acid (C) Linoleic Acid..... 173

Figure 5.13 Shows influence of temperature on ∆F (Hz) of FFA..... 174

Figure 5.14 Effect of temperature on ∆Dissipation (ppm) of FFA..... 174

Figure 5.15 Endothermic reaction as calculated by Van´t Hoffs equation FFA adsorption on Gold. 176

Figure 5.16 Effect of inserts on palmitic acid adsorption [A] Frequency (Hz), [B] Dissipation (ppm). 178

Figure 5.17 Effect of inserts on adsorption of oleic acid. 179

Figure 5.18 Effect of inserts on adsorption of linoleic acid. [A] Frequency (Hz), [B] Dissipation (ppm). 180

Figure 6.1 Spin coating of particles with different functional groups on quartz sensors. 187

Figure 6.2 Procedure for synthesis of silica nanoparticles using the Stober method. 190

Figure 6.3 shows the Scanning Electron Microscopy image of silica made at 0.81M of ammonium-hydroxide(28%) 192

Figure 6.4 A histogram of the particle size distribution of silica made at 0.81M of ammonium-hydroxide(28%)..... 193

Figure 6.5 Scanning Electron Microscopy image of silica made at 1.66M of ammonium-hydroxide(28%)..... 194

Figure 6.6 A histogram of the particle size distribution of silica made at 1.66M of ammonium-hydroxide(28%)..... 195

Figure 6.7 shows the QCM output for adsorption of Octadecane 197

Figure 6.8 shows the adsorption behaviour of Octadecane when melted then cooled and the process repeated. 197

List of Tables

Table 1.1 shows different types of adsorbents. Reproduced from (Dąbrowski, 2001) 22

Table 1.2 shows other techniques that can support the study of the kinetics of adsorption. 28

Table 1.3 shows examples of common fatty acids. Reproduced from (Wittcoff et al., 2012) 31

Table 2.1 Acoustic Ratio for palmitic acid adsorption at concentration of 150mg/ml 45

Table 2.2 Standard deviation of ΔF presented as error bars in Figure 2.4. 46

Table 2.3 Mass and thickness of Palmitic acid onto Silicon dioxide calculated using Dfind SmartFit model and based on the 3rd to 7th overtone. 49

Table 2.4 Mass and thickness of Palmitic acid on Aluminium Oxide based on the 3rd to 7th overtone. 49

Table 2.5 Equilibrium rate constant for Al_2O_3 54

Table 2.6 Equilibrium rate constant for Silicon dioxide 54

Table 2.7 Equilibrium rate constant for Polystyrene 55

Table 2.8 Equilibrium rate constant and R^2 59

Table 2.9 XPS Binding energy assignment of C1s 68

Table 2.10 XPS Binding energy assignment for polystyrene following palmitic acid adsorption 72

Table 3.1 R^2 values for different plots of t/q_t vs time for pseudo second order equation for Linoleic Acid. 84

Table 3.2 shows R^2 values for the different plots of t/q_t vs time for the pseudo second order equation for Oleic Acid. 100

Table 4.1 Shows proportions used to make Oleic Acid stock solutions. 118

Table 4.2 Shows proportions used to make Linoleic Acid stock solutions. 118

Table 4.3 Shows proportions used to make Palmitic Acid stock solutions. 119

Table 4.4 shows configuration settings for LPO on D-find. 131

Table 4.5 K values calculated from the slope of ∆D /∆F at the 3rd overtone. 134

Table 4.6 Total Viscosity of Adsorbed layer calculated using the average viscosity of shift of the last fatty acid added. 135

Table 4.7 Total thickness of adsorbed layer calculated by Sauerbrey equation at the 3rd overtone. 139

Table 4.8 Show deconvolution of bands between 2600 cm^{-1} and 3100 cm^{-1} for LOP. 149

Table 4.9 Show deconvolution of bands between 2600 cm^{-1} and 3100 cm^{-1} for LPO. 150

Table 4.10 Show deconvolution of bands between 2600 cm^{-1} and 3100 cm^{-1} for OLP 151

Table 4.11 Show deconvolution of bands between 2600 cm^{-1} and 3100 cm^{-1} for OPL. 152

Table 4.12 Show deconvolution of bands between 2600 cm^{-1} and 3100 cm^{-1} for POL. 153

Table 5.1 Shows the pH ranges tested for the FFA. 159

Table 5.2 shows contact angle measurements after adsorption of FFA using QCM at pH 3.75 171

Table 5.3 Thermodynamic parameters for FFA on Gold. 175

Table 6.1Shows the material and Equipment list needed for Experiments 189

Table 6.2 shows the amounts of each regent used in the experiment 190

Table 6.3 shows the statistical output from Minitab of the SEM images 195

Nomenclature

A_q	Area of the sensor
Z_{load}	Load on the sensor
Z_q	Impedence on the sensor
f_0	Fundamental resonance frequency
k_1, k_2	Rate constants
q_e	Amount of adsorbate adsorbed at equilibrium
q_t	Amount of adsorbate adsorbed at time t
τ_0	Decay time
∆D	Dissipation Change
∆F	Frequency Change
∆G	Change in the Gibbs free energy
∆H	Enthalpy Change
∆m	Adsorbed mass,
∆S°	Change in Entropy
a and *m*	Constants
A	Electrode area.
B	Concentration of the bound guest
C	Mass sensitivity constant
F	Concentration of free guest
FOG	Fats oils and grease
G	Gibbs free energy

n	Overtone /harmonic number
QCM	Quartz crystal microbalance
QCM-D	Quartz crystal microbalance with dissipation
R^2	Correlation Coefficient
T	Temperature
t	time
$\Delta\tilde{f}$	Complex frequency shift sensor
$\Delta\Gamma$	Energy loss due to dampening
D	The dissipation factor
f	Resonance frequency
m	Mass of sample
ρ	Density of the sensor
υ	Shear wave velocity in the quartz sensor
ω	Angular frequency

Abbreviations

AFM	Atomic Force Microscopy
ATR	Attenuated Total Reflectance
FFA	Free fatty acids
FOG	Fats oils and grease
FTIR	Fourier transform infrared spectroscopy
FWHM	Full width half maximum
IPA	Isopropyl alcohol
L	Linoleic Acid
O	Oleic Acid
P, PA	Palmitic Acid
PFO	Pseudo first order
PSO	Pseudo second order
QCM	Quartz crystal microbalance
QCM-D	Quartz crystal microbalance with dissipation
SEM	Scanning electron microscopy
ss	Stock solutions
XPS	Xray photoelectron spectroscopy

Chapter 1 Introduction

The blockage of sewers by fats oil and grease (FOG) together with other sanitary products like wet wipes, cotton pads etc has resulted in the formation of what is termed FATBERGS. These ‘fatbergs’ are formed when FOG and sanitary products lump up together forming a huge mass in sewers and thus creating a problem. The issue remains unknown or forgotten as these products are usually thrown down sinks and toilets. Since things out of sight are usually forgotten the scale of the problem only becomes evident when these fatbergs have caused blockages resulting in overflow of sewers either in homes or businesses. At the community level, overflow from sewers results in sewage making its way into water streams and thus contaminating water as it brings bacteria, disease causing pathogens and contaminated solids (Wallace et al., 2017). This is when maintenance teams are usually required to physically remove these fatbergs to unblock the sewer systems and get the system running smoothly again until the next blockage is discovered.

The problem of FOG in sewer systems dates to the 1940’s (Wallace et al., 2017). However not much has been done to address the problem. Governments and companies have come up with strategies to either prevent the formation of fatbergs. Failing which, reduction of the impact of the FOG is done by encouraging proper disposal (Figure 1.1), re-cycling the FOG to make biodiesel or to investing in alternative recovery methods such as bioaglumeration. This was usually done by community education encouraging people not to pour oils and grease down their drains but rather to dispose them in refuse bins (Wallace et al., 2017). However, since a large contributor to the Fatberg crisis is restaurants, the FOG is usually washed down drains when cleaning utensils. The amount of fats and oils used cannot be reduced as they are part of the 5 main food groups that are needed to keep people healthy (Wittcoff et al., 2012). According to Wallace et al. (2017), ‘FOG consumption per capita was 50kg/annum in developed countries as compared to 20kg/annum in developing countries.’ As such this problem is mainly a crisis in the developed countries. An example would be the FATBERG found in Whitechapel in London which was 250 meters long and weighing 130 tonnes (BBC News, 2017).



Figure 1.1 Oliobox collection box at a supermarket in Belgium to recycle frying cooking oil. (Seanneng, 2025) photo taken outside a local supermarket.

Existing work on the management of FOG deposits it mainly focused on used cooking, waste from oil and grease in food service outlets as well understanding how FOG deposits build up in sewers. However ,the limitations of this are that experiments are done under controlled laboratory conditions which do not replicate real sewer conditions. They are unable to account for the impact of microbial activity on FOG deposits in sewers, effect of temperature , flow rates, time ,pH etc. While the study by He et al. (2013) attempted to give materials that prevent release of calcium ions into wastewater, no tests have been performed to verify this.

The aim of this research as a response to finding a sustainable way of prevention of fatbergs was to investigate the adsorption of fatty acids found in FOG deposits onto surfaces. The focus was however on understanding the kinetics of adsorption of the fatty acids onto the

substrate materials. An attempt was also made to coat the QCM sensors with silica particles due to the ease of its synthesis and a well-documented study around its synthesis and functionalisation. The Quartz crystal microbalance with dissipation (QCM-D) was identified as one of the tools that could be used to study the kinetics of adsorption of a material along with other analytical and characterization techniques such as contact angles measurements, SEM, XPS etc. The terms QCM and QCMD are used interchangeably in this work.

The work in this thesis explored the adsorption of FFA identified in literature using QCMD. The effect of concentration, temperature, pH on the adsorptions of oleic acid, linoleic acid and palmitic acid were investigated to study the kinetics. Pseudo first order and second order kinetic models were applied to investigate whether chemisorption or physisorption where the driving force behind these adsorptions. Competitive adsorption of the fatty acids was also investigated as well as the effect of introducing a secondary surface by using inserts on adsorption.

Thus far, silica particles have been synthesised using the Stober method. The particles produced have then been characterized using SEM. These are unfunctionalized silica particles. Functionalization of the silica nanoparticles is beyond the scope of the research. Attempts to modify the quarts sensors by spin coating unfunctionalized silica were unsuccessful as such further work is required as this could potentially prolong the lifespan of the quartz sensors and give control to tailor the surface properties such as the surface's reusability hence the recovery of the adsorbed fatty acids.

To prove the validity of QCM-D being a viable method to understanding adsorption kinetics, a gold-plated quartz crystal was used to test if an alkane, octadecane can be adsorbed and desorbed from the crystal before being extended to free fatty acid adsorption. This method was chosen as it has already proven successful in a study of wettability of oil and adsorption kinetics for recovery of oil in the petroleum engineering sector as discussed by (Erzuah et al., 2018). Erzuah et al. (2018) was able to demonstrate that oil recovery was possible by testing using a gold-plated quartz sensor and kaolinite and testing its adsorption tendencies with different quantities of formation water, brine, and stock tank oil and n-decane to mimic an actual reservoir for crude oil recovery.

Competitive adsorption of the free fatty acids (FFA) was investigated by studying the impact of sequential addition of the FFA into the system. The effect of increasing concentration from 25mg/ml to 150mg/ml on different substrate sensors was also investigated as well as the effect of pH and temperature on adsorption. One of the characterization methods of choice for many researchers using QCMD is atomic force microscopy (AFM) particularly determining surface

topography coverage and heterogeneity (Adamczyk et al., 2020; Westwood et al., 2012; Reimhult et al., 2008). AFM is usually chosen as it is non-destructive to the quartz sensors. However, in this work X-ray photoelectron spectroscopy (XPS) and Raman microscopy were used to study effect of substrate surface chemistry on the sensors. Both techniques were found to be non-destructive under conditions discussed later in this work. They also provide an image of the sensors hence it is possible to determine the surface coverage. This was however outside the scope of this work as the focus was on studying the surface chemistry of the sensors.

1.1 Literature Review

1.1.1 Fatberg Formation

Metallic salts of fatty acids have been identified to be a contributing factor to the formation of FOG deposits in sewer systems. Calcium has been identified to be the dominant metal as it can be found in concrete which is used to line the sewer systems (He et al., 2013; Iasmin et al., 2016). Calcium leaching from concrete was investigated and it was found that leaching of calcium is high at low pH values, and this greatly contributed to concrete corrosion. In fact, the presence of oil from wastewater provides free fatty acids resulting in an interface saponification reaction where calcium salts of fatty acids are formed thus resulting in the formation of FOG deposits along the sewer as shown in Figure 1.2. Palmitic, oleic, and linoleic acid are the three major free fatty acids that were found present in FOG deposits (He et al., 2013). Oil acts as a grease interceptor thus facilitating transport of hydrolysed free fatty acids to the interfaces and this is also encouraged by their hydrophobicity. FOG deposits tend to form along the pipeline cross-section above the water level (He et al., 2013). Palmitic acid has been identified as the most prominent free fatty acid in FOG solids (Iasmin et al., 2016). Given the rising problem with FOG deposits, high costs are associated with their removal highlighting the environmental, health and financial impact of the FOG deposits (Stein & Miller, 2019).

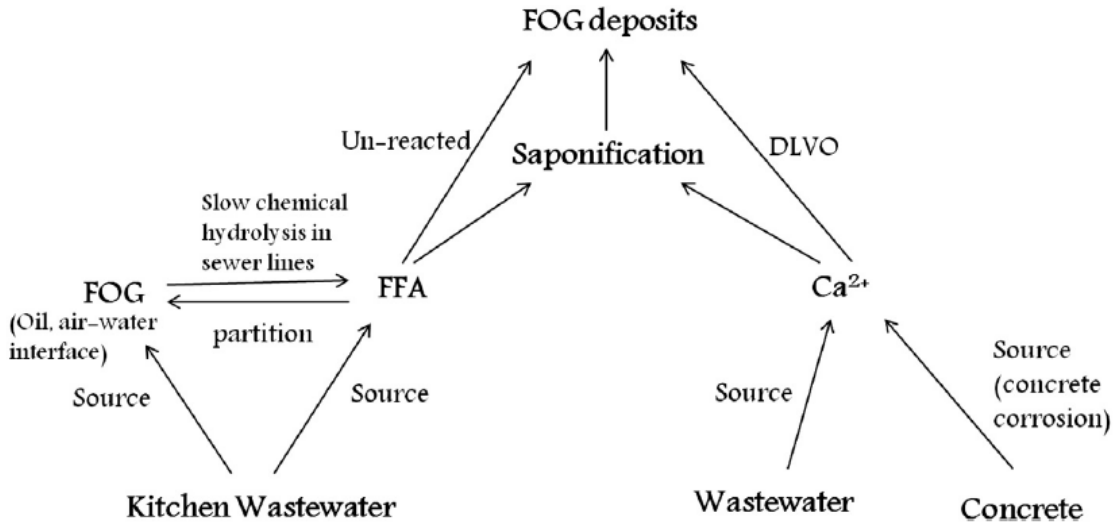


Figure 1.2 Mechanism by which Fatbergs are formed. Reprinted from (He et al., 2013)

1.1.2 Silica

Silica has been used in this work to investigate adsorption kinetics of palmitic acid, oleic acid and linoleic acid using QCMD. The sensors used are made of quartz (a form of silica) with different materials coated onto them. The sensors are the centre of the QCM technique. Hence it was important to investigate silica synthesis in the amorphous form and to determine if both forms amorphous and crystalline form (in the form of the quartz sensors) can be used in the QCM technique.

Silica occurs naturally in mineral such as quartz, flint and even in plants such as barley and rice. The conditions under which silica forms greatly affect the phase in which it will exist e.g. whether it will exist in crystalline form or amorphous form (Vansant et al., 1995). Factors that influence this are temperature, hydration level, and the pressure during its formation. Most silica occurs in crystalline form in nature and as a result the active surface able to take part in chemical reaction is limited to the outside surface due to its densely packed nature (Vansant et al., 1995).

Silica is highly used in many industries such as in the pharmaceutical and catalysis industries to name a few. Its widespread use is mainly too due to its preparation and the fact that the particle size and shape can easily be controlled to give the desired output (Rao et al., 2005). Further the synthesis of silica nanoparticles is widely documented.

1.1.2.1 Characterisation of nanoparticle

The design or synthesis of silica nanoparticle is very important. Properties such as the particle size, shape, pore size, and surface area will in turn affect the particles' performance (Vansant et al., 1995). It has been already established that the desire is to design an amorphous silica to increase its overall surface area. The preparation as already mentioned is most important.

1.1.2.2 Sols and gels

The preparation of the sol-gel form of silica results in $Si(OH)_4$ condensing and thereby forming a siloxane network (Vansant et al., 1995). However, this happens in a two-step process involving hydrolysis into silanol groups followed by condensation thereby forming the siloxane network (Rao et al., 2005). These processes occur simultaneously during a reaction. The reaction path is as shown in Figures 1.2 and 1.3. Over time, a turbid suspension will be observed. As a result of the reactions, the sol will have progressed to become a gel. This is accompanied by an increase in the viscosity of the reaction medium (Vansant et al., 1995). The result of this will be formation of a hydrogel. As mentioned before, reaction conditions

such as temperature, pH, the solvents used in the reaction and the alkoxide determine the properties of the formed particles (Zulfiqar et al., 2016). A xerogel is formed upon further drying of the particles. The liquid that occupied the pore of the particles is expelled by the capillary forces because of the drying process. As a result, the conditions under which drying or aging occurs determine characteristics such as the porosity and the total surface area of the particles (Vansant et al., 1995).

Hydrolysis

$$S_i - (OR)_4 + H20 \rightleftharpoons S_i - (OH)_4 + 4R - OH$$

Equation1.1

Condensation

$$2S_i - (OH)_4 \rightarrow 2(S_i - O - S_i) + 4H_2O$$

Equation1.2

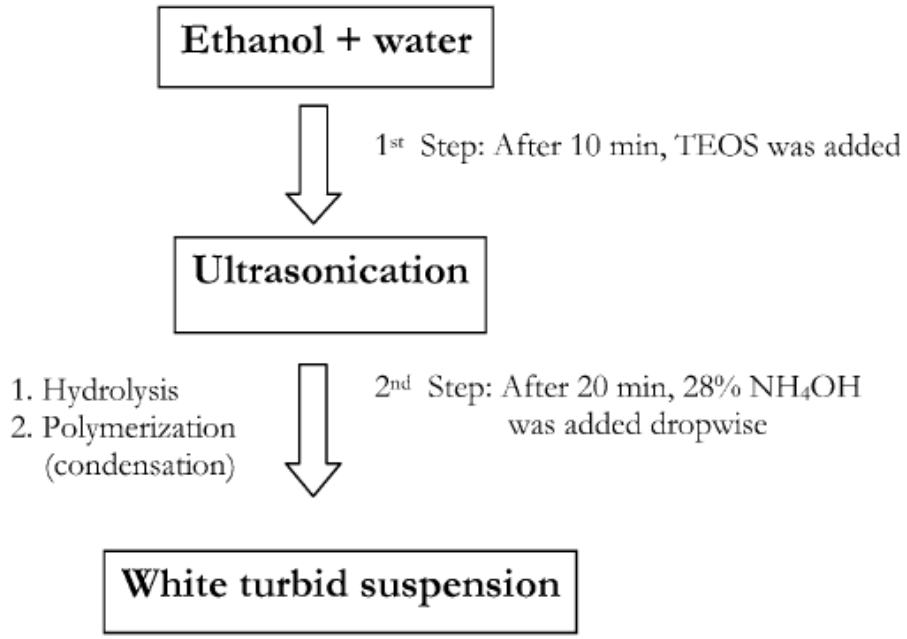


Figure 1.3 shows the sequential addition method for synthesis of silica. Reprinted from (Rao et al., 2005)

1.1.2.3 Mechanism of particle formation

Particles can be formed via the sol-precipitation method. Particles nucleate in the supersaturated solution. As a result of the growth of the particles, stable primary particles are

formed (Ibrahim et al., 2010). The period in which particles form in the supersaturated solution is called the induction time. As such with time, more primary particles will be formed which will then be used for growth of the primary particles already formed resulting in increase of their stability. These can be observed or seen as the turbid suspension referred to in Figure 1.3.The formation of these particles can also be observed by an increase in viscosity of the reaction mixture. This is how mono-disperse particles are formed.

Another way the particles are formed is via aggregation. This occurs when the consumption of primary particles for growth resulting in stable particles is exceeded. When this happens, particles will then be spontaneously formed via aggregation. However, for such a suspension, a multi-modal particle size distribution will be observed (Chen et al., 1997).

1.1.2.4 Factors that affect the characteristics of silica

1.1.2.4.1 Effect of pH

Tetraethyl orthosilicate (TEOS) is usually used as a precursor in the synthesis of silica in either an acid or basic medium. This will be dependent on the properties of the desired particle as the pH plays a major role on the aggregation of particles formed hence affecting the size (Zulfiqar et al., 2016). Another precursor that can be used in the synthesis of silica is sodium silicate solution. The factors affecting choice of the precursor include but are not limited to, the cost, the uniformity of particles produced, concentration of particles as well as the agglomeration tendencies of particles. Usually, a precursor used in an acidic medium result in particles with high agglomeration while a basic medium results in less agglomeration (Zulfiqar et al., 2016). From the various studies conducted, it can be found that the pH has a direct impact on the agglomeration but also on the overall particle size.

The initial pH of the TEOS-water phase directly affects the particle size. To fine tune the pH of the system, the concentration of the base catalyst would need to be altered. In a study comparing the use of n-butylamine and lysine catalysed systems, it was found that increasing the pH resulted in a decrease in the particle size. Zulfiqar et al. (2016) also came to the same conclusion. In their case, the pH was varied mainly by changing the ratio of ethanol to ammonia as shown in Figure 1.4. The key difference between the n-butylamine and lysine reactions is that lysine acts as a buffer. The hydrolysis rate of the n-butylamine catalysed reactions is higher at high pH e.g. 11 as compared to a lower pH e.g. 9. However, at these low pH values, the hydrolysis is faster for the lysine system as compared to the n-butylamine system (Wang et al., 2011). This can give a conclusion that for specific species of catalyst at specific pH values, generally the reaction rate increases with an increase in pH. It should be noted that in the lysine system, no alcohols were used. As a result, silicate species are

released slowly into the water phase and as such are immediately used up. There is also less contact between the water and TEOS surface. Hence the hydrolysis of TEOS is slow while the condensation rate is quick. This is what provides the buffering for the reaction (Wang et al., 2011).

1.1.2.4.2 Size distribution

The Stober method has been used widely in the synthesis of colloidal silica. This method is a single-phase technique that involves a reaction between TEOS, ethanol and a catalyst which can either be a base or an acid. Examples of some catalysts that have been used include sodium hydroxide, lysine etc. Figure 1.3 shows a sequential method that can be used to make silica. However, this method has a limit to the tuning of the particle size below 30nm (Wang et al., 2011). To control the particle size distribution, Wang et al. (2011) designed a two-phase experiment that would ensure that as the particles were synthesised, the pH was relatively constant throughout the experiment. In this experiment, a base catalyst lysine was used which acted as a buffer in the reaction resulting in only a slight in pH decrease (9.8 - 9.2). However, upon investigation of other unbuffered reactions, it was established that uniform sized particles can also be achieved (Wang et al., 2011). Figure 1.4 shows another study on the effect of the particle size distribution. It was found that though increasing ammonia may decrease the particle size, it also resulted in a decrease in the particle size distribution (Zulfiqar et al., 2016). The inverse effect was observed for ethanol which resulted in an increase in particle size and particle size distribution when the ratio of ethanol to ammonia was increased.

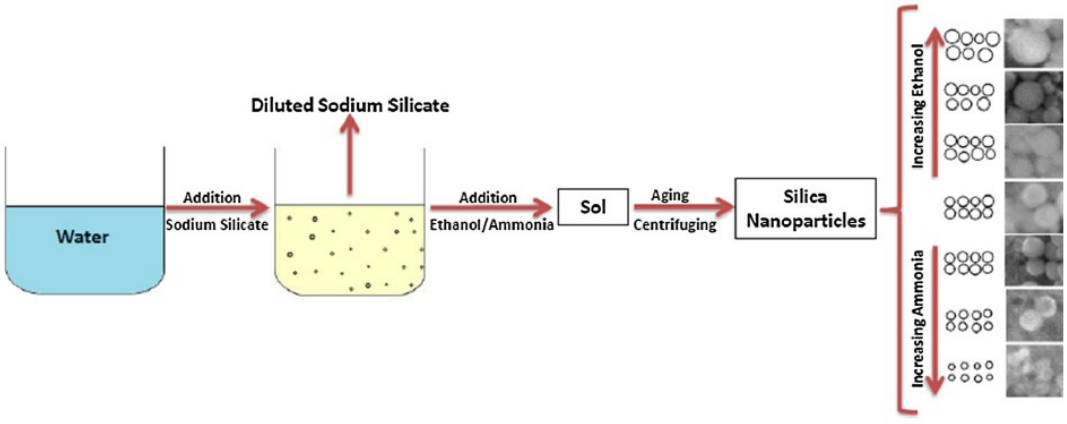


Figure 1.4 The variation of particle size with change in ammonia/ethanol ratio. Reproduced from (Zulfiqar et al., 2016)

Silica nanoparticles were synthesized using the Stober method in this work and the effect of pH on the particle size distribution was studied.

1.1.2.4.3 Temperature

Temperature plays a major role in many reactions. It influences the rate at which silica is formed and the structure of the pores hence affecting the pore size distribution and inevitably the size and shape of the formed silica (Li et al., 2016). Figure 1.6 and Figure 1.5 demonstrate the effect of temperature on the structure of the pores of silica. From these two figures it can be deduced that at temperatures lower than 130°C, the pore structure is well ordered. This is also observed at 150°C, and the structure is further distorted beyond this temperature. Figure 1.5 shows 3 main peaks (100, 110 and 200). The strength of these peaks is shown at temperatures below 130°C and again at 150°C. These peaks are weak at 130°C and at 180°C, the 100 peak is very weak while the other two peaks cannot be seen, meaning that their structure is not ordered. In Figure 1.6 the pores at these two temperatures appear cracked while the others are smooth (Li et al., 2016).

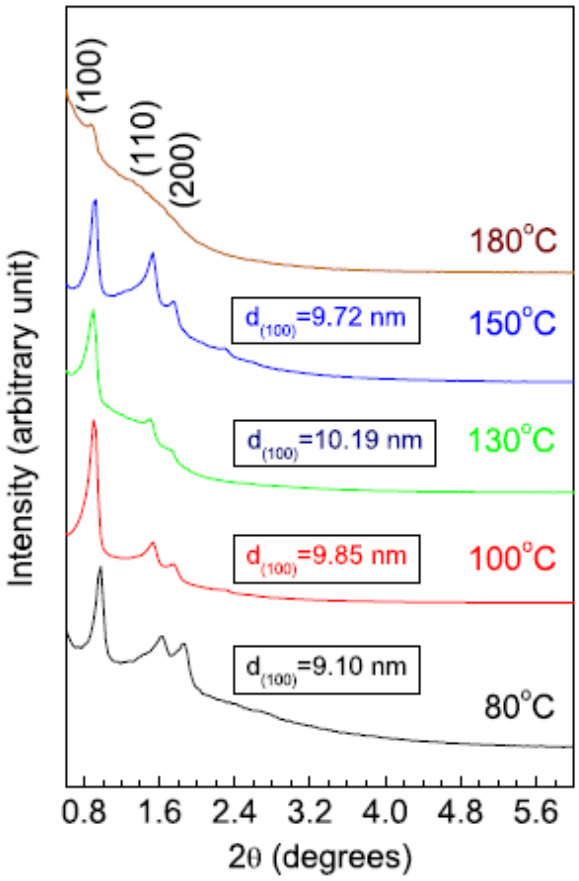


Figure 1.5 The results of small x-ray scattering for mesoporous ordered silica synthesised at different temperatures. Reproduced from (Li et al., 2016)

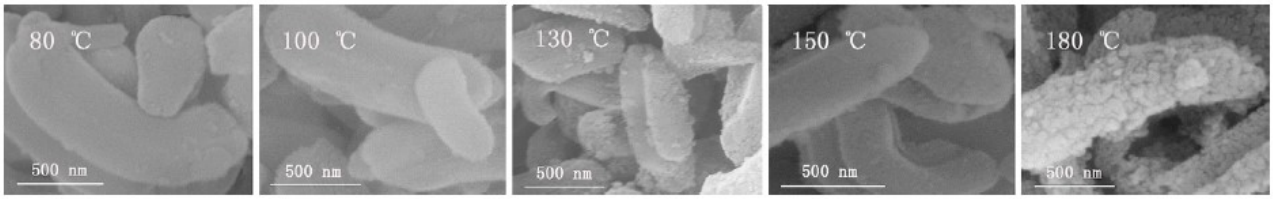


Figure 1.6 Scanning Electron Microscopy images of mesoporous silica synthesized at different temperatures. Reproduced from (Li et al., 2016)

In a different study by Rao et al. (2005) on the synthesis of spherical silica nanoparticles, the effect of temperature was also investigated. It was found that increase in temperature resulted in an increase in particle size. However, the reverse was also observed in the study. The determining difference was the concentration of ethanol used. It was found that between 4-6M, an increase in particle size was observed while above 14M a decrease in particle size was seen. Electrostatic repulsive forces from silanol groups are responsible for insuring stability of the particle. However, they dissolve in ammonia and when temperature increase, ammonia evaporates thereby resulting in increase in the amount of water present hence the size of particle increases (Rao et al., 2005). A balance needs to thus be found which will not result in collapse of the silica pore and results in a stable structure (pore stability and structure) (Li et al., 2016).

1.1.2.4.4 Concentration

Concentration of various regents can be varied to control the morphology of the synthesised silica particles. Various studies have been made on how changing concentration of regents such as ammonia, ethanol or even the water content can affect the silica particles. Zeng et al. (2015) studied how varying the concentration of ammonia affected silica particles formed via the Stober method. In this study it was found that increasing the concentration of ammonia resulted in an increase in the particle size. In another study conducted by Rao et al. (2005) the reverse was the case with a decrease in particle size with increasing ammonia concentration as shown in Figure 1.7. These results are supported by the work done by Zulfiqar et al. (2016) as shown in Figure 1.4. In the same study by Rao et al. (2005) it was found that increasing the water content resulted in smaller particle sizes being formed. Ethanol influences the monodispersity of particles being formed. If ethanol is low in concentration, more aggregation could be seen resulting from a decrease in pH (Rao et al., 2005). Figure 1.4 also shows that increasing ethanol concentration also results in large particles being formed.

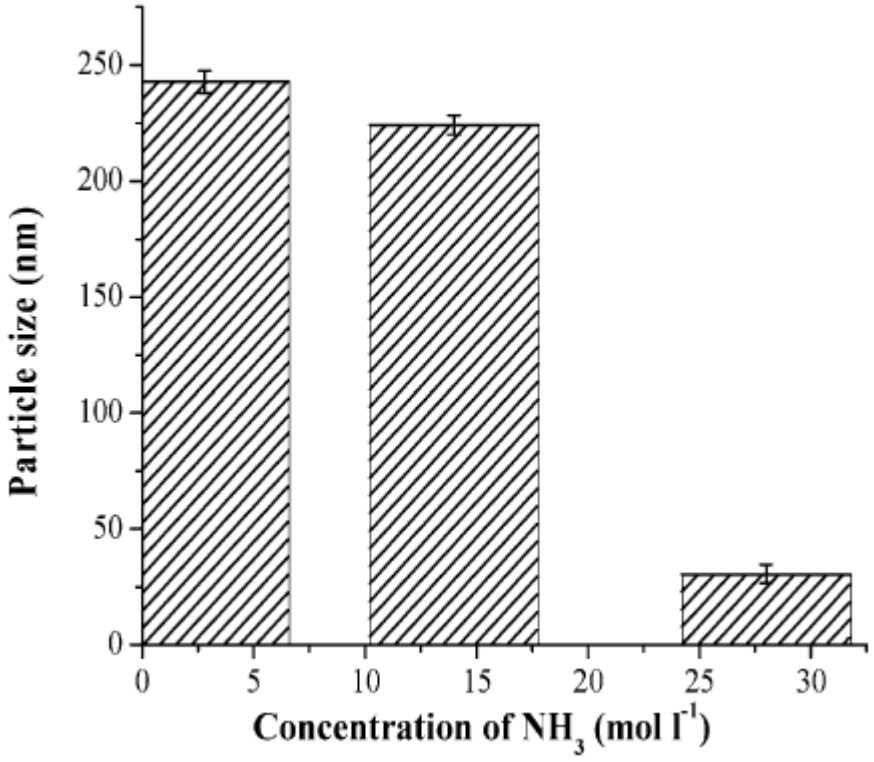


Figure 1.7 shows effect of increasing concentration of ammonia on the particle size. Reprinted from (Rao et al., 2005).

Methods that can be used for synthesis of silica nanoparticles are as shown in Figure 1.8.

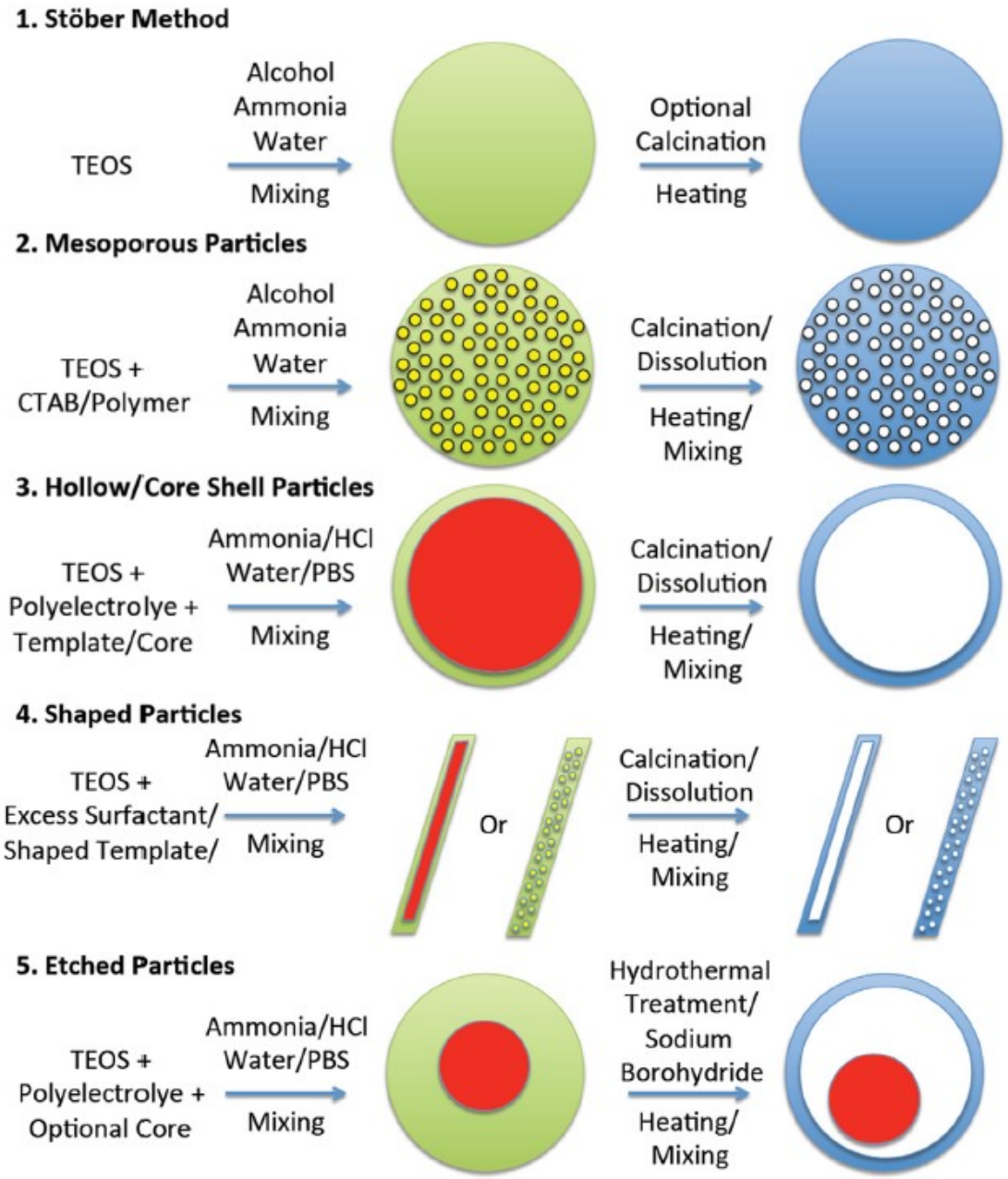


Figure 1.8 Methods used to synthesise silica nanoparticles; Reproduced from (Liberman et al., 2014).

1.1.3 Quartz Crystal Microbalance with Dissipation

The quartz crystal microbalance (QCM) is a surface phenomenon technique which can be used to study the interactions occurring on the surface of the quartz crystal and study the thin film material on the surface (Biolin Scientific, 2020). It can be used to study if a material can adsorb onto the surface of the quartz crystal. The change in mass is always accompanied by a shift in the frequency and energy dissipation as shown in Figure 1.9. The energy dissipation can sometimes be used to tell more information about the type of material that is on the surface i.e. it gives information about the structural and viscoelastic changes of the material (Anderson et al., 2007). This change in dissipation gives information about surface free energy changes due to film formation during adsorption, degradation of a material or desorption. As such, the QCM-D can be used to measure changes in the bulk density of a solution (Irwin et al., 2005).

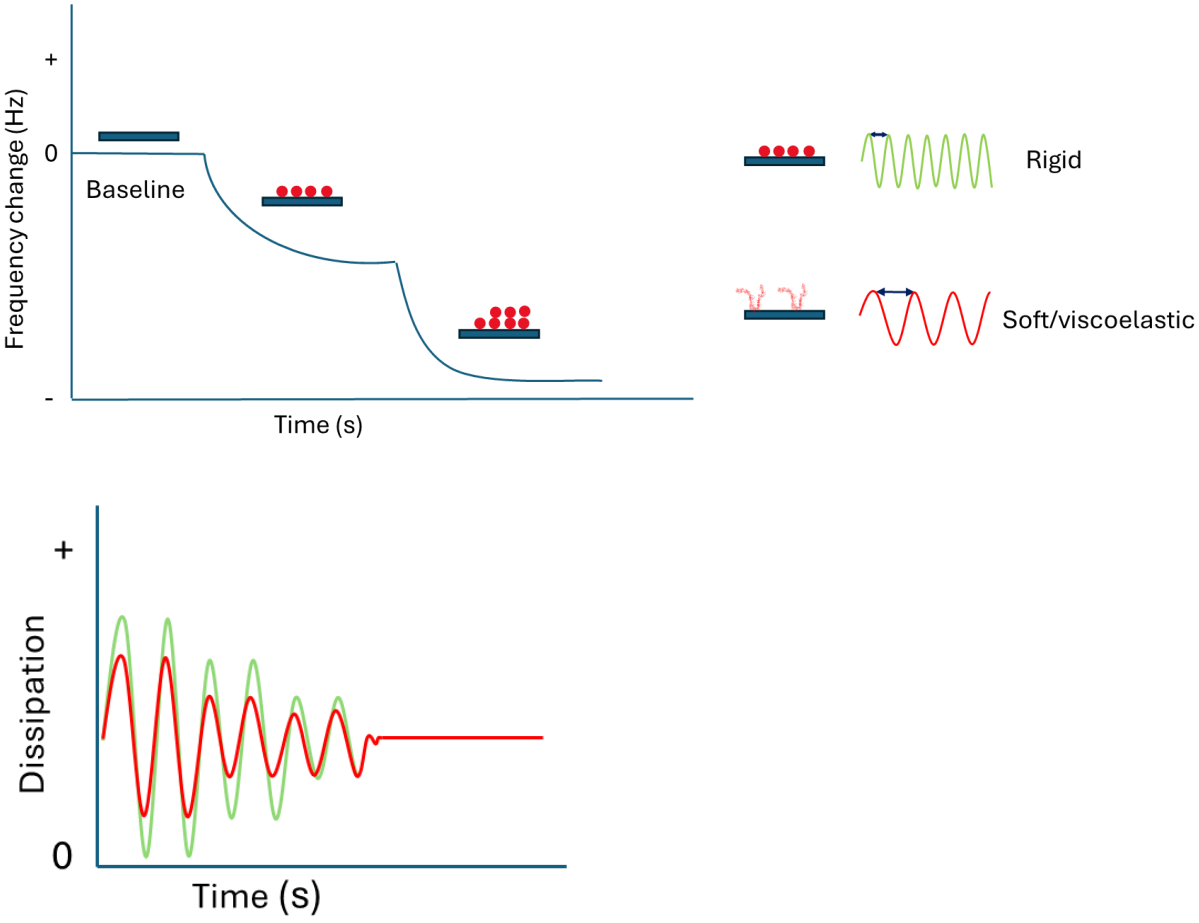


Figure 1.9 shows frequency and dissipation shifts when a mass is applied onto a quartz sensor. Adapted from (Biolin Scientific, 2020).

1.1.3.1 Quartz sensor

The quartz sensor (crystal) is thin and located in-between a pair of electrodes. The quartz crystal has a piezoelectric effect as such will oscillate on application of AC voltage across the electrodes (Biolin Scientific, 2020). The most common material for this sensor is gold as shown in Figure 1.10, however the sensor can be made from any material e.g. silver, aluminium, copper etc.

Figure 1.10 also shows different shapes and sizes for the sensor. The shape size and geometry of the flow cell in which the sensor is used greatly affect the performance of the sensor (Anderson et al., 2007). Anderson et al. (2007) conducted a study on the performance of the quartz crystals shown in Figure 1.10. They found that in an air medium, the crystals were very sensitive as compared to when operating in a liquid. This was observed by a large reduction in the energy lost (dissipation). The study showed that the smaller crystals had a higher sensitivity and overall, the rectangular sensor was the most sensitive as it has a higher response to any change as shown in Figure 1.11.

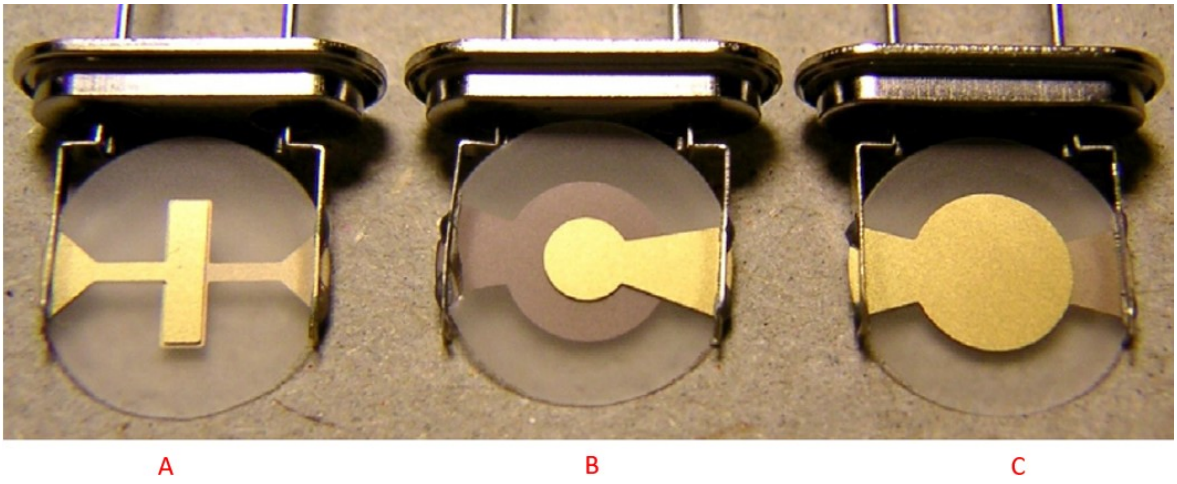


Figure 1.10 shows different shapes of quartz sensors. Reproduced from (Anderson et al., 2007).

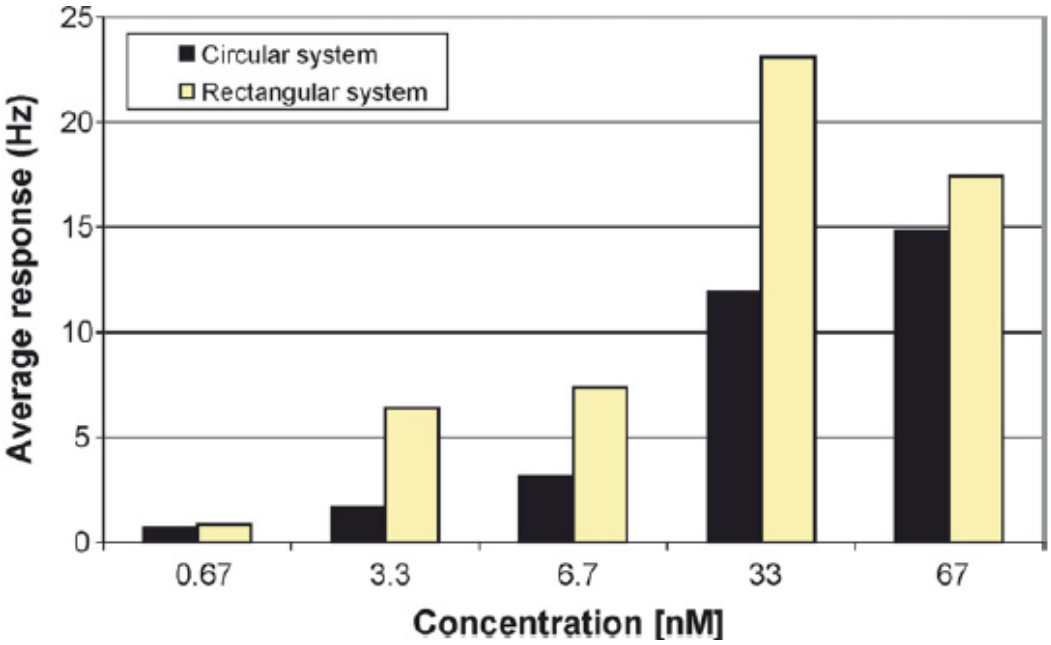


Figure 1.11 shows the average frequency response for circular and rectangular quartz sensors. Reproduced from (Anderson et al., 2007).

According to Biolin Scientific, 2020 the sensors are most sensitive at the centre of the crystal. This is because a higher amplitude is always detected at the centre of the crystal. In addition to this, the Qsense software that is used to record the changes in oscillatory behaviour the crystal always assumes that when measurements are taken, the surface of the crystal has been homogeneously coated (Biolin Scientific, 2020).

1.1.3.2 Measurement Models

Many authors have used and reviewed different analysis methods to interpret data measured using the QCM-D. Some of the methods include but are not limited to ; the Sauerbrey model, the Maxwell model, Kelvin-Voigt model, Hydrodynamic model, and the Mason model. The Sauerbrey model is used for thin evenly distributed and rigid layers on the sensor surface (Lundgren et al., 2006). However, depending on the system, this is not always the case. To account for this, other models such as the Mason model, Maxwell model etc can be used alongside other complimentary techniques such as AFM (atomic force microscopy), ellipsometry, SEM (scanning electron microscopy) and XPS (X-ray photoelectron spectroscopy) to confirm the surface morphology and surface coverage. The complimentary characterization techniques can be used regardless of whether the film adsorbed follows Sauerbrey or any other Visco-elastic model.

1.1.3.2.1 Sauerbrey Model

If the adsorbed film follows Sauerbrey, the mass adsorbed can be determined by:

$$\Delta f = -\frac{2f^2\Delta m}{\sqrt{\rho \upsilon A}} \; or \; \Delta m = -\frac{\rho_q t_q \Delta f}{f_0 n} = -\frac{\rho_q \mu_q \Delta f}{2{f_0}^2 n} = -\frac{C\Delta f}{n}$$

Equation1.3

Where: f is the resonance frequency, m is mass of sample, ρ is the density of the sensor, υ shear wave velocity in the quartz sensor, A is the electrode area. ∆m is the adsorbed mass, C is the mass sensitivity constant is $17.7\, ng\, cm^{-2}Hz^{-2}$ when the fundamental resonance frequency, $f_0 = 5H_Z$ and n =1, where n is the harmonic number (1,3,5,7) (Cho et al., 2010). The drawback of the Sauerbrey model is that it does not consider the effect of the surrounding fluid as well as multilayer adsorption since Sauerbrey only hold for thin films (Lapidot et al., 2016). Therefore, it is not applicable for systems exploring adsorption of lipids, proteins, polymers, or any others that may have a viscous or elastic nature.

1.1.3.2.2 Mason Model

The Mason model is used for addressing viscoelastic effects involving crystalline point contact loads which result in non-uniformity of deposits (Lapidot et al., 2016). It addresses any changes in the frequency as a complex number thus having a real part which represents energy stored and the imaginary part for any energy lost (Lapidot et al., 2016). The Maison model uses a complex function to better understand the frequency and dissipation data at multiple overtones. The model accounts for nucleation and the growth of the crystal clusters but it also considers the entrapped fluid in between the growing crystals. The complex frequency shift (energy stored and energy lost) is determined by:

$$\frac{\Delta\tilde{f}}{f_f} = \frac{\Delta f + i\Delta\Gamma}{f_f} = \frac{i}{\pi A_q Z_q} Z_{load}$$

Equation1.4

Where $\Delta\tilde{f}$ is the complex frequency shift made of Δf the real part (stored energy with the sensor) and the imaginary part (energy loss due to dampening) is represented by $\Delta\Gamma$. A_q is the area of the sensor, Z_q the impedence on the sensor, Z_{load} the load on the sensor (Lapidot et al., 2016). While the Mason model does well for systems that consider constant nucleation and crystal growth it cannot be used for systems where the driving mechanism is not

crystallization but is adsorption. This of course is determined by the nature of the material that is being measured.

1.1.3.2.3 Kelvin-Voigt Model and Maxwell-Wiechert Model

The Voigt and Maxwell models are commonly used to model materials that exhibit viscoelastic behaviour. The Voigt Model is commonly used to represent a spring, and dashpot is parallel while the Maxwell model represents the spring and dashpot in series (Chindam et al., 2013). The Maxwell model is usually applied to solutions that are liquid like while the Voigt model is usually applied to model films that do not change shape/deform or flow upon application of a stress (Voinova et al., 1999; Lapidot et al., 2016). The Voigt model assumes that the viscoelastic film deposited on the quartz sensor is of uniform thickness, homogenous ,covers the whole sensor surface and is operating in a Newtonian liquid under no-slip boundary conditions (Voinova et al., 1999; Paul et al., 2008; Qsense DFind, 2024). The equations for viscoelastic modelling have been described elsewhere in literature (Voinova et al., 1999; Johannsmann, 2015). Another important parameter which helps in deciding which model to apply is the acoustic ratio.

The acoustic ratio which is given by:

$$= -\frac{\Delta D_n}{\frac{\Delta f_n}{n}}$$

Equation 1.5

The acoustic ratio is a purely material property and is important as it helps to determine whether changes observed in the frequency and dissipation when applying a viscoelastic model are due to adsorption or are the results of the effect of the bulk fluid. ΔD_n is the dissipation change at nth overtone and Δf_n is the frequency shit at the nth overtone. The acoustic ratio is 0.4 for a purely viscous fluid in a 5MHz quartz sensor for all overtones (Reviakine et al., 2011; Gopalakrishna et al., 2021; Fredrik Pettersson, 2022). However, for acoustic ratio $\Delta D_n/(-\Delta f_n/n) \ll 4 \times 10^{-7}$ Hz^{-1} the Sauerbery equation can be recovered and used for determining the areal mass (Reviakine et al., 2011). This may be because even though the adsorbed film is soft, it could be considered rigid in comparison to the bulk fluid (Johannsmann, 2015). Cho et al. (2010) suggested that viscoelastic modelling can be used if the dissipation change is large i.e. if $|\Delta D_n/\Delta f_n| > 1 \times 10^{-8}$ Hz^{-1}.

Measurements of frequency shifts are taken at four separate fundamental frequencies as these are the ones that cause the quartz crystal to oscillate. These four overtones are the

fundamental overtone n=1 at 5MHz, n=3 at 15MHz, n=5 at 25MHz and n=7 at 35MHz. The corresponding dissipation factors are as such good for taking measurements (D1,D3,D5 and D7) (Irwin et al., 2005).To take measurements of frequency and dissipation, the piezoelectric quartz sensor is switched off, the voltage over the resonator then oscillates as an exponentially damped sinusoidal wave. This is the main principle by which these measurements are made. When taking measurements, stability of the measurement taken is far more important in comparison to the initial offset that will be observed (Rodahl & Kasemo, 1966).

1.1.4 Adsorption kinetics on QCM-D

Adsorption kinetics are studied by observing the changes in frequency and dissipation as mentioned above. If a material is adsorbed and is rigid and evenly distributed, then the change in frequency would be equivalent to the mass adsorbed hence following the Sauerbery model. The energy dissipated is thus negligible. However, the dissipation energy is observed in cases where the viscoelastic materials have adsorbed onto the sensor surface. This then introduces an important factor called the dissipation factor/energy which is used to give information about the material (Liu & Ki, 2009).

The dissipation factor is:

$$D = \frac{1}{\pi f_0 \tau_0} = \frac{2}{\omega \tau_0} \; or \; D = \frac{E_{dissipation}}{2\pi E_{stored}}$$

Equation1.6

Where:

f_0= resonance frequency, τ_0= decay time, ω= angular frequency and D = the dissipation factor.

To understand the viscoelastic properties of the adlayer, a theoretical model needs to be developed. Two models as mentioned above can be used. Either the Kelvin-Voight (the storage and loss moduli affect the frequency of oscillation) or the Maxwell model (Liu & Ki, 2009). These two models would first need to be individually tested and the one representing the results from the QCM-D for that specific material chosen. Hence an understanding of characteristics of any material used is important (Regmi et al., 2014). The Maxwell model is represented by a spring and dashpot connected in series was used to determine the molecular weight of ionic liquids with varying concentrations. The Maxwell model agreed with results obtained from the QCM-D technique (Regmi et al., 2014). The Kelvin-Voigt model has been used to show how changes in solution concentration affected the mechanics and catalytic activity of the adsorbed layer on the sensor (McArdle et al., 2015).

The chemical composition of the adsorbed layer is usually studied by using a spectroscopic technique. Some of the techniques that have been used are FRAP (fluorescence recovery after photo bleaching). This technique was used to study the kinetics of binding or diffusion of planar supported lipid bilayer molecules on the surface (Weng et al., 2006). Another technique that can be used is X-ray photo electron spectroscopy which has been used to study how a cationic polymer and anionic surfactant affected the adsorbed layer in a study to on how adsorption and viscoelasticity were affected by polyelectrolyte-surfactant on the hydrophilic surface. The quartz sensor in this case was coated with amphoteric alumina and the charge on the hydrophilic surface controlled by changing the pH (Dhopatkar et al., 2015). The study of adsorption kinetics can be studied by optimising the process. Examples including changing pH, temperature, or the surface on the material. The QCM-D hence assesses changes in hydrated sample mass thus giving information on adsorption, desorption, and binding of adsorbate onto the adsorbent. It can further give information about surface and structural changes of molecules such as crosslinking, collapsing of a membrane as well as degradation or corrosion at the surface of the sensors (Biolin Scientific, 2018).

The QCM technique has also been used in a study of unsaturated fatty acid (oleic acid, linoleic acid, and linolenic acid) adsorption onto a steel surface (Lundgren et al., 2007). The study found that the chain length, the structure (whether it is linear or branched) of the fatty acids as well as whether a chemisorption or physisorption was occurring, affected the amount of the fatty acids being adsorbed. Figure 1.12 showed that oleic acid was adsorbed however it reached a plateau and no more could be adsorbed even if the concentration was increased. Linoleic acid and linolenic acid on the other hand never reached a plateau. This suggests more of the adsorption of the fatty acids could occur. However, since the number of binding sites on the steel surface is limited, it was suggested that multilayer adsorption of the fatty acids occurred (Lundgren et al., 2007). For oleic acid only monolayer adsorption occurred as shown in Figure 1.12. Since oleic acid is a linear fatty acid, it was also suggested that is adsorbed parallel to the surface hence a physisorption occurring as compared to the other fatty acids where a chemisorption is suggested to have taken place (Lundgren et al., 2007).

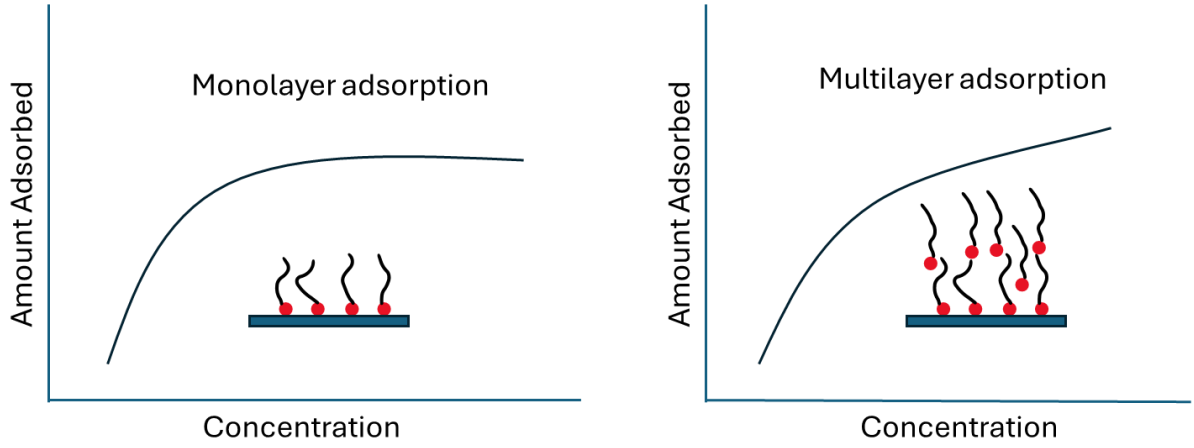


Figure 1.12 shows proposed mechanisms by which adsorption occurred for the fatty acids under test. Adapted from (Lundgren et al., 2007).

1.1.5 Adsorption

Attractive forces existing between the adsorbate (substance being adsorbed) and the adsorbent surface result in a process called adsorption just as shown in Figure 1.13. The attractive forces that can exist between the adsorbent surface and the adsorbate are van der Waals' forces, electrostatic forces as well as chemical bonding. These forces are highly dependent on the types of the materials that are interacting. As a result of these interactions, adsorption can be classified as either a physical adsorption (physisorption) or chemical adsorption. The main difference between the two is that physisorption is because of weak forces (van der Waals' or electrostatic forces of attraction) and in chemisorption (covalent bonding, metallic or ionic bonding), the attractive forces result in chemical bonding (Ramaswamy et al., 2013; Saleh, 2021). Hence physisorption is reversible (bonds can be broken). Chemisorption on the other hand is surface specific. It has been described in literature as irreversible or dissociative (Saleh, 2021). An example is in the formation of rust where the surface is changed due to the redox reaction involving the reaction of iron, oxygen and water to for iron oxide (Britannica, 2025). However, this is not always the case as chemisorption can be reversed with sufficient energy input to overcome the energy barrier of the specific reaction e.g. pressure-swing manipulation has been used to prove the reversible chemisorption of carbon monoxide on nickel (o) complexes (Yamauchi et al., 2022).

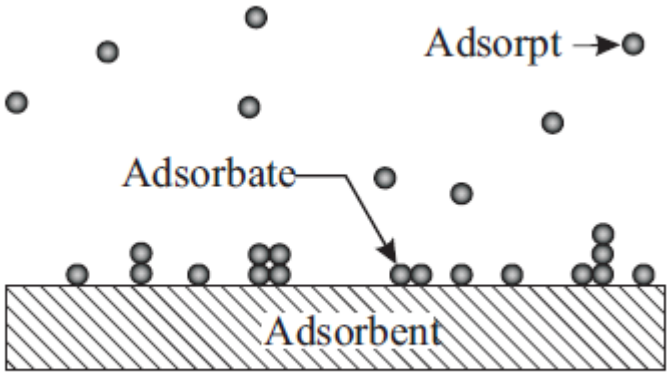


Figure 1.13 Shows a depiction of the adsorption process. Reproduced from (Butt et al., 2003)

1.1.5.1 Adsorbents

Table 1.1 shows different types of commercial adsorbents. Some of the factors to be considered when choosing an adsorbent for a process are the cost of adsorbent, its ability to regenerate, its adsorption capacity, the kinetics and selectivity (Ramaswamy et al., 2013). Silica was chosen for this work as it is quite easy to vary its characteristics by simply varying the pH, temperature, and concentration. The main factors supporting the desirability of silica in use in this work are as discussed in section 1.1.2.4.

Table 1.1 shows different types of adsorbents. Reproduced from (Dąbrowski, 2001)

Carbon adsorbents	Mineral adsorbents	Other adsorbents
Active carbons	Silica gels	Synthetic polymers
Activated carbon fibres	Activated alumina	Composite adsorbents:
Carbon molecular sieves	Oxides of metals	(complex mineral carbons,
Mesocarbon microbeads	Hydroxides of metals	X-elutrilithe; X = Zn, Ca)
Fullerenes	Zeolites	
Heterofullerenes	Clay minerals	Mixed sorbents
Carbonaceous nanomaterials	Pillared clays	Metal organic frameworks
	Porous clay	(MOF)
	hetero-structures	
	(PCHs)	
	Inorganic nanomaterials	

1.1.5.2 Adsorption Isotherms

An adsorption isotherm is a graphical representation of the quantity of adsorbate adsorbed as a function of pressure at a constant temperature (Toppr, 2020). There are three main adsorption isotherms which are Freundlich, Langmuir and BET theory (XAmplified, 2009). The basic principle of an isotherm is as shown:

$$Adsorbent + Adsorbate \underset{Desorption}{\overset{Adsorption}{\rightleftharpoons}} Adsorption$$

Equation1.7

(XAmplified, 2009)

Figure 1.14 shows a broader list of some of the isotherms that have been observed in various literature studies. However, the discussion will focus on the three main isotherms which are listed above.

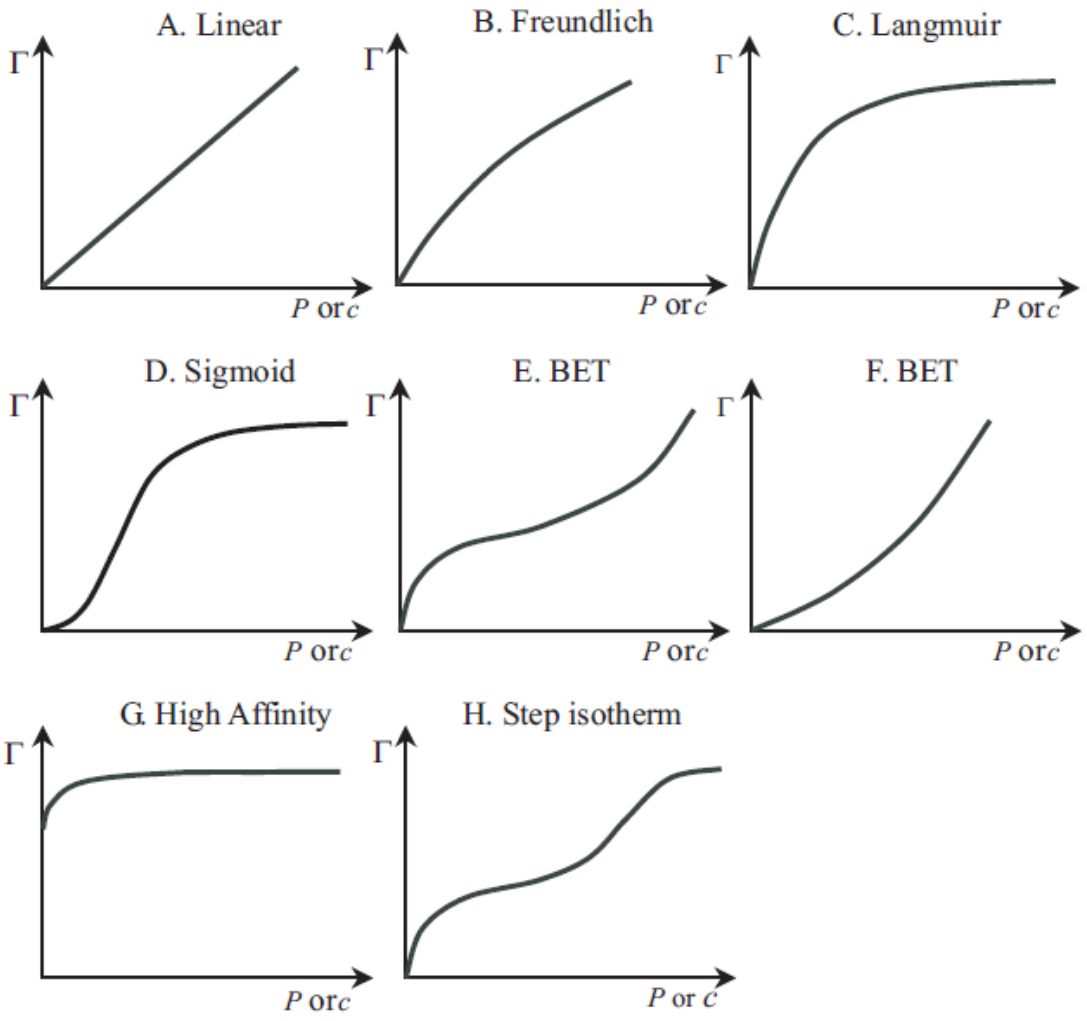


Figure 1.14 Shows different types of isotherms. Reproduced from (Butt et al., 2003)

1.1.5.2.1 Freundlich Adsorption Isotherm

The Freundlich adsorption isotherm gives a relation of the amount of gas adsorbed as a function of pressure at a constant temperature. It tries to relate the number of atoms adsorbed from a gaseous phase onto a solid surface. The amount of gas adsorbed is also dependent on the surface geometry, presence of binding sites as well as the interactions that the adsorbed gaseous atoms have with each other (Appel, 1973). The Freundlich isotherm assumes that the adsorbent surface is heterogeneous (e.g. activated carbon, silica etc) thus having different binding energies for the binding sites (Appel, 1973; Umpleby II et al., 2001). The equation below describes the isotherm:

$$B = aF^m$$

Equation1.8

(Umpleby II et al., 2001)

Where:

The constants are ***a*** and ***m***, concentration of the bound guest is ***B,*** and the concentration of free guest is represented by ***F***.

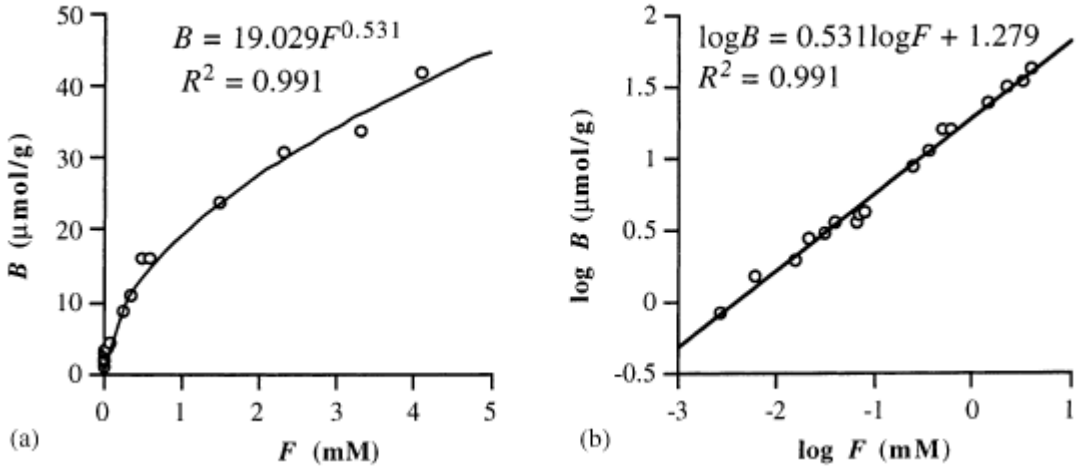


Figure 1.15 shows the binding isotherm for polymer Ethyl adenine-9-acetate. Reproduced from (Umpleby II et al., 2001)

Figure 1.15 shows the data/ binding isotherms in a study of non-covalently bonded molecular imprinted polymers in this case of ethyl-9-acetate. The data shows a good fit of data. However, a disadvantage of this method is that data usually shows a good fit at concentrations below

the saturation point and therefore fails to represent data at low concentrations (Umpleby II et al., 2001).

1.1.5.2.2 Langmuir Adsorption Isotherm

Figure 1.16 shows the Langmuir adsorption model. It assumes that the area of the adsorbent has a restricted number of binding sites. It also assumes a homogeneous surface of adsorption with identical binding sites and that there are no interactions between the adsorbed atoms (Liu, 2006; Appel, 1973).

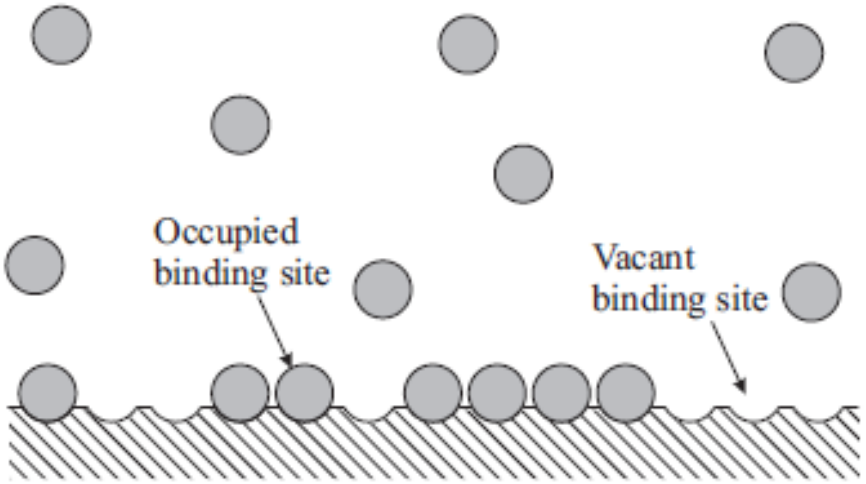


Figure 1.16 Shows the Langmuir adsorption model. Reprinted from (Butt et al, 2003).

$$Q = Q_{max}\frac{K[A]}{1 + K[A]}$$

Equation1.9

(Liu, 2006)

The equation above the Langmuir equation. Where ***Q*** is the adsorption capacity, ***Qmax*** the maximum adsorption capacity, ***K*** is the equilibrium constant and [***A***] is the molar concentration of adsorbate (Liu, 2006). The adsorption free energy is represented as:

$$\Delta G^{\circ}_{ads} = -RTlnK_A$$

Equation1.10

(Bayrak, 2006)

$\Delta G°_{ads}$ is the adadsorption free energy.

R is the universal gas constant

T is the temperature in Kelvin

The Langmuir equation was used to measure the adsorption of saturated fatty acids on montmorillonite (clay mineral) as shown in Figure 1.17. It was found that the Langmuir isotherm was a good representation of the equilibrium adsorption data collected. The monolayer formation/ coverage, the absence of interactions between adsorbed atoms and the adsorption site equivalence are the three main parameters that are the basis of the validity of the Langmuir equation (Bayrak, 2006). The Langmuir isotherm also proved that physisorption occurred and that montmorillonite can be used for adsorption of the fatty acids shown in Figure 1.17.

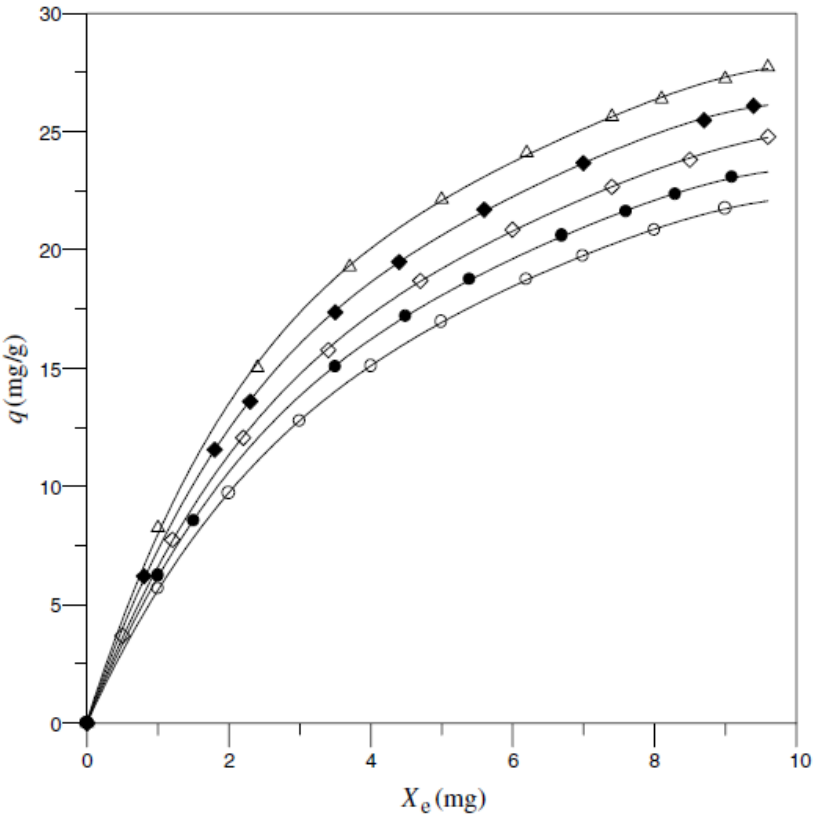


*Figure 1.17 shows the results adsorption of lauric acid (●) , stearic acid (Δ), palmitic acid (♦), myristic acid (◊) and capric acid (○) **q** (m/g) is the amount of adsorbate adsorbed (mg/g) of adsorbent and x_e (mg) is the adsorbate in solution at equilibrium. Reproduced from (Bayrak, 2006).*

1.1.5.2.3 BET Adsorption Isotherm

BET (Brunauer, Emmett, and Teller, 1938) adsorption is well suited for multilayer adsorption of gas onto a solid surface as shown in Figure 1.18 unlike with the Langmuir adsorption which focuses on just monolayer adsorption (Hunter , 2001). The model is suitable for systems involving physisorption where the main forces of attraction are van der Waal's forces of attraction (Saevels et al., 2004). The are no forces of attraction between the adsorbed layers and the Langmuir adsorption equation can be applied to each individual adsorbed layer.

The BET equation is as shown below:

$$\frac{x}{q(1-x)} = \frac{1}{qm^c} + \left(\frac{c-1}{qm^c}\right)x$$

Equation1.11

(Rangabhashiyam et al., 2014)

Where ***x*** = BET adsorption constant, ***q*** =adsorbate per unit adsorbent (mg/g), ***c*** = constant and $\boldsymbol{qm^c}$ = adsorption capacity of monolayer (Rangabhashiyam et al., 2014).

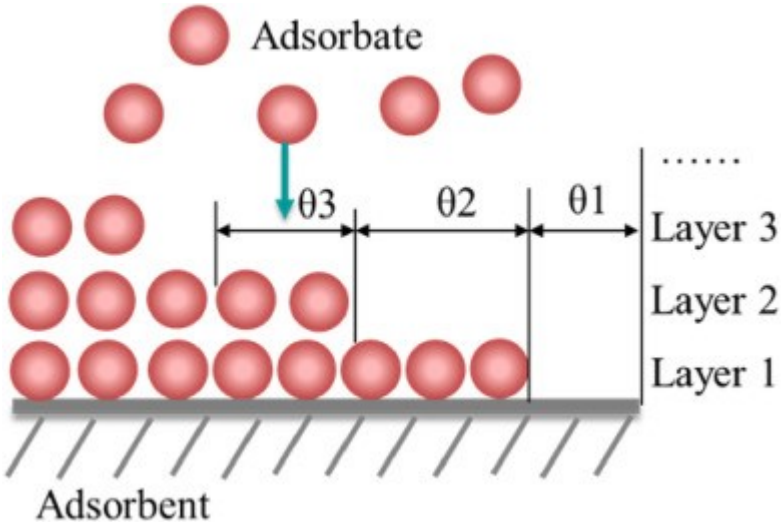


Figure 1.18 Shows BET multilayer adsorption. Reprinted from (Wang & Guo, 2020)

1.1.5.3 Alternative Techniques

To be able to fully identify the kinetic of adsorption at the surface interface, it is imperative that a microscopic technique is used in conjunction with the QCM-D. While QCM-D gives indication of the adsorbed material e.g. viscoelastic properties, and the adsorption capacity of the quartz crystal, it does not give enough information on interactions happening between the adsorbent

and the adsorbate. Hence the spectroscopic and analytical techniques and are important in nanoscale characterization. Below are a few techniques that can be used.

Table 1.2 shows other techniques that can support the study of the kinetics of adsorption.

Technique	Description
Atomic Force Microscopy	AFM belongs to a group of instruments called scanning probe microscopes (SPM) (Johnson et al., 2009). The SPM uses a sharp probe to scan the area of interest. In the case of AFM, the result of force measurements between the stylus probe and the surface results in a high-resolution three-dimensional image topography (Mai, 2020; Westwood et al., 2012). E.g. the method has been used to give information of surface roughness in a study about adsorption of unsaturated fatty acids onto steel surfaces (Lundgren et al., 2007).
Scanning Electron Microscopy	Like AFM, SEM scans the surface of interest however instead of using a probe it uses electron beams to interact with the surface. Thus, gives a two-dimensional image which gives information about the topography and composition of the sample under test (Nanoscience Instruments , 2020). The advantage of the SEM is the resolution power as well as that it gives a chemical analysis of the sample. The downside of it is that is limited to solid samples (Mathias, 2020).
Fourier Transform Infrared Spectroscopy	It is a technique used to identify chemical properties of materials (organic and inorganic). Infrared radiation that is adsorbed by samples causes the molecules to vibrate, these vibration signals result in production of a spectra image representing individual chemical species/groups (RTI Laboratories, 2015).

X-ray Photoelectron Spectroscopy	XPS is used for compositional analysis of materials. Like SEM it uses photo electrons to scan samples to give information. XPS has three resolution levels, the first being the energy resolution which refers to the equipment's ability to differentiate chemical states and bonding for elements by measuring at the full width of the half maximum intensity (FWHM) of the Ag $3d_{5/2}$ peak (Thermo Fisher Scientific, 2008) (Kratos Analytical Ltd, 2025). The second is the lateral spatial resolution which is dependent of the spot size of the area that is analysed. This is also equipment specific e.g. it is about 7.5μm for Physical Electronics, Inc XPS instruments Physical Electronics Inc (2020) and 10 μm for Thermo Scientific Nexsa Surface Analysis System (Thermo Fisher Scientific Inc, 2006). Another source stated that the lateral resolution is between 5-50 μm (Drummond et al., 1996). The last is the depth resolution in which ion sputtering is used on the sample to expose new layers at various depths. This can result in the surface roughening and atomic mixing Hofmann et al. (2017) which can compromise the resolution depending on the desired outcome (it is important to consider the charge compensation steady state at the different layers). The depth of analysis is thus affected by the material being analysed as well as the etch rate of the ion gun (CasaXPS, 2008).
Inverse Gas Chromatography	IGC is used to determine surface properties/measurements of solid materials. The measurements that can be determined by this technique include surface energies, solubility parameters e.g. cohesion and adhesion, diffusion kinetics, polar/ acid /basic nature of material, phase transition temperatures etc (Surface Measurement Systems Ltd, 2015).

Contact Angle Goniometer	This instrument is used to determine the wettability of solid materials i.e. if the material is hydrophilic or hydrophobic. Contact angle below 30° is said to be hydrophilic and super hydrophilic if the angle is below 10°. A material with a contact angle greater than 90° is referred to as hydrophobic and superhydrophobic if the measured contact angle is above 150° (Arkles, 2006).

1.2 Chemistry of fats and oils

Triglycerides are esters of glycerol which can either contain saturated or unsaturated fatty acids. Hence the fatty acids which are liquid at room temperature are called oils while those that are solids are called fats. The chain length of the fatty acid hence the molecular weight greatly affects the melting point of the fats or oils. The presence of a double bond as well as the structural conformation (cis or trans) of the fatty acids will also affect the ability of the fats or oils to melt as shown in Table 1.3 (Wittcoff et al., 2012).

Table 1.3 shows examples of common fatty acids. Reproduced from (Wittcoff et al., 2012)

Formula	Trivial Name	Melting Point (°C)	Double-Bond Position and Stereochemistry	Source
n-$C_{13}H_{23}COOH$	Lauric acid	44.2		Coconut oil, palm kernel oil
n-$C_{13}H_{27}COOH$	Myristic acid	53.9		Coconut oil, palm kernel oil
n-$C_{15}H_{31}COOH$	Palmitic acid	63.1		Most vegetable oils and animal fats
n-$C_{17}H_{35}COOH$	Stearic acid	69.6		Most vegetable oils and animal fats
n-$C_{17}H_{33}COOH$	Oleic acid [a]	16.0	cis-9	Most vegetable oils and animal fats (olives, nuts, beans, tall oil)

n-$C_{17}H_{31}COOH$	Linoleic acid [a]	-9.5	cis-9, cis-12	Tall oil, most vegetable oils (safflower, sunflower, soy)
n-$C_{17}H_{29}COOH$	α-Linoleic acid [a]	-11.3	cis-9, cis-12, cis-15	Linseed oil
n-$C_{17}H_{29}COOH$	γ-Linoleic acid		cis-6, cis-9, cis-12	Evening primrose oil
n-$C_{17}H_{29}COOH$	α-Eleostearic acid	48.5	cis-9, trans-11, trans-13	Tung oil
n-$C_{17}H_{29}COOH$	β- Eleostearic acid	71.5	trans-9, trans-11, trans-13	Tung oil
n-$C_{17}H_{32}(OH)COOH$	Ricinoleic acid [a]	5.0	cis-9	Castor oil
n-$C_{19}H_{29}COOH$	Eicosapentaenoic acid		cis-5, cis-8, cis-11, cis-14, cis-17	Fish oil
n-$C_{19}H_{29}COOH$	Arachidonic acid	-49.5	cis-5, cis-8, cis-11, cis-14	Animal fats and organs
n-$C_{21}H_{41}COOH$	Erucic acid	33.5	cis-13	Rapeseed (canola oil)
n-$C_{21}H_{31}COOH$	Docosahexaenoic acid	22.6	cis-4, cis-7, cis-10, cis-13, cis-16, cis-19	Fish oil

[a] *Oleic acid : $CH_3(CH_2)_7CH=CH(CH_2)_7COOH$; Linoleic acid: $CH_3(CH_2)_4CH=CHCH_2CH=CH(CH_2)_7COOH$; Linolenic acid:*

$CH_3CH_2CH{=}CHCH_2CH{=}CHCH_2CH{=}CH(CH_2)_7COOH$; *Ricinoleic acid:* $CH_3(CH_2)_4CH_2CH(OH)CH_2CH{=}CH(CH_2)_7COOH$.

The longer the chain length and the presence of a double bond (unsaturated) in a fatty acid result in an increase in the melting point. Other important factors affecting the behaviour of a fatty acid include the position of the double bond and the amount of the trans-form of an unsaturated fatty acid present (Crowther, 2008). Fatty acids undergo a process called esterification where a glycerol molecule reacts with the fatty acid in the presence of an acid catalyst to form the ester (Clark , 2015). The main difference between saturated and unsaturated fatty acid is that unsaturated fatty acids have a double bond. This allows for carbon atoms to be bonded to other groups of atoms which allows the molecule to bend, hence unsaturated fatty acid chains are not tightly packed together making them a liquid at room temperature. On the other hand, saturated fatty acid chains have carbon atoms bonded to just hydrogen atoms. They are straight chains causing them to be tightly packed together hence the characteristic solid nature of such fatty acids at room temperature (Soult et al., 2019).

Fatty acids play a key role in this work. The aim was to investigate how palmitic acid, linoleic acid and oleic acid adsorb onto different surfaces under different conditions (concentration, pH, temperature) using QCM. Palmitic acid has been proven to be the most prevalent of the fatty acids in the FOG deposits as it reacted faster with calcium ions in sewers to form soap while oleic acid contributed to harder FOG deposits (He et al., 2013; Del Mundo & Sutheerawattananonda, 2017). The systems in this work do not contain calcium ions however the hypothesis is that palmitic acid would adsorb more onto all surfaces. This is because previous work by Calvo et al. (2008) found that palmitic acid had a low solubility is pure solvents such as ethanol. With this information, it would mean palmitic acid has higher tendency to form aggregates due to the low solubility in ethanol thereby influencing the amount sensed by the QCMD.

1.3 Conclusions

This chapter highlights the problem that brought about the need for the purpose of this thesis. An understanding of the adsorption behaviour of FFA is essential in being able to design systems that aid in the recovery of the fatty acids from FOG deposits in wastewater. Silica and its synthesis and characterization were explored with the aim of being able to use the synthesised particles to coat quartz sensors (as shown in chapter 6) . This would allow for flexibility in tailoring the adsorbent surface to different needs. However, this was beyond the scope of this work. The focus of this work as highlighted in this work by the proof of concept (section 6.1), is the use of the QCM technique to study adsorption of fatty acids. The literature

review also highlighted that the QCM technique can be used to study adsorption of fatty acids. This method compared to other techniques is quick and requires very little sample. Hence the waste produced from this work would have very little impact to the environment. To the best of my knowledge, not much work has been done using QCM to study adsorption of fatty acids particularly oleic acid, linoleic acid and palmitic acid using QCM. The next chapters would thus explore factors such as concentration, pH, temperature, and effect of sequential addition of the FFA on adsorption using QCM. All the experiments were conducted in batch mode hence this work does not consider the impact of flow rates on adsorption using QCM.

Chapter 2 Investigating adsorption of palmitic acid using Quartz crystal Microbalance with Dissipation

2.1 Abstract

The quartz crystal microbalance with dissipation was used to investigate the adsorption of palmitic acid onto polystyrene, aluminium oxide, and silicon dioxide. Application of pseudo first order (PFO) and pseudo second order (PSO) models revealed that experimental results were a good fit for the PSO model thereby suggesting palmitic acid chemically adsorbed to the sensors thereby forming a monolayer. Chemical adsorption of palmitic acid was confirmed by Xray photoelectron spectroscopy (XPS) were the -COOH group on C1s was found on the surface of all sensors following the QCMD experiments indicating that the fatty acids had been adsorbed. This supports the results obtained from the QCMD experiments. This shows that all the materials studied are suitable adsorbents for palmitic fatty acid. The QCMD technique has been previously used to study adsorption of unsaturated fatty acids from alkane solutions onto steel surfaces with results indicating only slight amounts of the fatty acids (oleic acid, linoleic acid and linolenic acid) adsorbed from the alkane solutions (Lundgren et al., 2007). This work extended the work by (Lundgren et al., 2007) by exploring the adsorption of a saturated fatty acid.

2.2 Introduction

Palmitic acid is a saturated fatty acid that can be found in many things like meats, dairy products, palm oil, cocoa butter, olive oil as well as in the human body (Carta et al., 2017). Breast milk as an example contains about 20-30% palmitic acid while most traditional formula milk for infants have less than 20% palmitic acid (from vegetable fats) (Carta et al., 2017). However, the palmitic acid residues in formula milk tend to be excreted as calcium salts by infants affecting the stool making it harder. This in turn affects an infant's ability to digest and absorb nutrients (Wittcoff et al., 2013). This is due to the position of palmitic acid in the glycerol chain (palmitic acid is located at the end of the chain). Palmitic acid is located at the centre of the glycerol chain in breast milk while the end chains are occupied by oleic acid and linoleic acid residues (Carta et al., 2017). This demonstrates that human start interacting with fatty acids from early on in life. These fatty acids have also been found in many consumer products such as vegetable oils, body creams, cleansers etc.

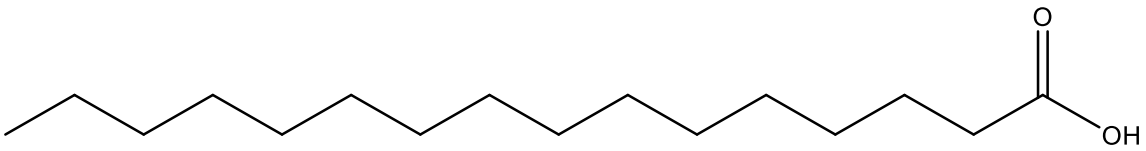
Due to their prevalence in everyday life, palmitic acid, oleic acid and linoleic acid have been found to contribute to the formation of large masses of fat that have resulted in the blockage

of sewer systems. Apart from these free fatty acids, other contributing factors to this include oil, grease, nappies, hair etc as they tend to be thrown down toilets or in the case of oil and grease washed down sinks in lots of kitchens around the world (He et al., 2013).This seemingly simple and convenient method of disposing sanitary products and grease/ oils has resulted in huge blockages of sewer systems. He et al. (2013) has already explored the role of FFA including palmitic acid on the saponification reaction at the interface (FFAs ,water, concrete and air) and proved that this resulted in the formation of the FOG deposits. Their study focused on the role of calcium leaching under different pH conditions to extend the understanding on the mechanisms involved in FOG formation. Palmitic acid (shown in Figure 2.1) has also been used in the form of sodium palmitate as a surfactant to produce soap, cosmetics etc in the saponification of palm oil (Punvichai & Pioch, 2019). Lundgren et al. (2007) has already explored the adsorption of unsaturated fatty acids from alkane solution onto steel surfaces using QCMD with applications in tribology as fatty acids have applications in fuels and oils as friction modifiers. This demonstrates that the role of FFA is vast. Previous studies explored the mechanisms and kinetics for FOG formation in wastewater (He et al., 2013; Iasmin et al., 2016; Williams et al., 2012).

Saponification has extensively been explored as the main driving force for FOG formation in wastewater (He et al., 2013; Iasmin et al., 2016). The need for different materials in sewers to minimize calcium leaching has been suggested in previous studies but much exploration still remains (He et al., 2013; Kusum et al., 2025). As FFA are present in wastewater and contribute to FOG formations, their interactions i.e. of un-reacted FFA with different surfaces needs exploration. FOG deposits have been confirmed to not adhere to granite, porcelain ceramic and polyvinyl chloride (Kusum et al., 2025).To address this gap, this chapter explored the interactions of palmitic acid at the interface with different surfaces using the QCMD. The aim of this chapter was to investigate the adsorption kinetics of palmitic acid onto silicon dioxide, polystyrene and aluminium oxide by application of pseudo first order and pseudo second order models to experimental results obtained through QCMD. This helped extend the knowledge on the adsorption of palmitic acid. Characterization of the adsorbents was done through X-ray photoelectron spectroscopy. This was of great importance as it could help in minimizing the role of palmitic acid in the formation of FOG through understanding which material(s) could be well suited for its removal from wastewater.

To the best of my knowledge, the exploration of the adsorption kinetics of palmitic acid on a sensor electrode coated with different materials (aluminium oxide, silicon dioxide and polystyrene) has yet to be explored. Sewer like conditions were not accounted for in this study as the interest was on the adsorption of palmitic acid onto quartz sensors under laboratory

conditions. Consideration of sewer like conditions such as presence of concrete or calcium ions using QCMD was beyond the scope of this work and remains for future exploration.



Palmitic Acid

Figure 2.1 Shows the structure of Palmitic acid.

2.2.1 Review of Literature

2.2.1.1 Quartz Crystal Microbalance with Dissipation

The quartz crystal microbalance with dissipation is a surface phenomenon that uses changes is resonance frequency due to an applied stress on a sensor surface to determine the interactions of the adlayer onto the sensor surface (Biolin Scientific, 2020). During an adsorption event, molecules adsorbed from the aqueous solution onto the sensor result in a negative shift in frequency which is accompanied by a positive shift in the dissipation energy. This is particularly important as this can give information about the adlayer morphology or give information on conformation changes of the layer. The dissipation energy gives information about the material properties i.e., whether the material is a thin rigid film, or the material is viscoelastic (Anderson et al., 2007). Such shifts in frequency and dissipation make it possible to also trace material degradation or desorption from the surface (Irwin et al., 2005). The QCMD technique has been used in many studies involving crystallisation and adsorption. A model for understanding crystallisation on the surface of the sensor has been previously developed by studying crystallisation of calcium sulfate on the surface of a sensor (Lapidot et al., 2016). Kinetic studies involving different systems can be also studied using QCMD. For example, water adsorption in Nafion thin films Krtil et al. (2001), adsorption and equilibrium characteristics of organic vapours and liquids in Matrimid Stanford et al. (2016) and conformation studies of adsorbed dodecylamine onto zinc sulfide (Kou & Xu, 2016).

The quartz crystal microbalance with dissipation is a technique that is used in a wide variety of adsorption studies. The key is in the A-T cut piezoelectric sensor. To determine the interaction between any material and the sensor surface, the quartz sensor allows for frequency (ΔF) and dissipation (ΔD) shifts to be traced. As a general principle, the shift in frequency shows whether an adsorption or desorption event is taking place. A negative shift indicates an adsorption event as stated above while a positive shift indicates that a layer is being desorbed from the surface. This information allows for the approximation of the mass of

the adlayer to be calculated. It should be noted that this calculated mass is the hydrated or wet mass of the adlayer (Edvardsson, 2018). This phenomenon happens because the solvent will either be surrounding the adsorbed film or entrapped within the film (Edvardsson, 2018). Thus, the sensed mass (∆m) of the QCMD is always that of the film and the solvent. An understanding of the adsorbed film is required to calculate the sensed/adsorbed mass. For thin rigid films with no deformation or slip with low dissipation of less than $1x10^{-6}$, the Sauerbrey model can be used (Kou & Xu, 2016). In addition to this the adlayer must also be evenly distributed on the sensor. Apart from the low dissipation energy, another indication that the adlayer follows Sauerbrey model is that no spread between the harmonics of the frequency shifts will be observed.

2.2.1.2 Kinetics models of adsorption

Different models have been used in the past to model the adsorption of different materials onto different surfaces. Some of the kinetic models that have been used to model adsorption have been pseudo- first order (PFO), pseudo-second order (PSO), Elovich model, mixed surface reaction and diffusion and Bangham just to name a few (Revellame et al., 2020). The PFO and PSO tend to be used the most with much preference to the PSO as most data fits tend to favour this model. This chapter explored experimental data fits of both the PFO and PSO models.

The pseudo first order model is usually presented as follows:

$$\frac{dq_t}{dt} = k_1[q_e - q_t]$$

Equation2.1

When integrating for the boundary conditions q_t= 0 at t=0 and $q_t = q_t$ at t=t. The equation is re-written as:

$$q_t = q_e\left(1 - e^{-k_1 t}\right)$$

Equation2.2

Where q_t is the amount of adsorbate adsorbed at time t and q_e is the amount of adsorbate adsorbed at equilibrium. k_1 is the rate constant and t is time.

The integrated and linearized form as given by Revellame et al. (2020) is:

$$\ln[q_e - q_t] = -k_1 t + lnq_e$$

Equation2.3

The pseudo-second order rate expression is:

$$q_t = \frac{{q_e}^2 k_2 t}{1 + q_e k_2 t}$$

Equation2.4

The linearized form upon integrating is (Revellame et al., 2020):

$$\frac{t}{q_t} = \left(\frac{1}{q_e}\right) t + \frac{1}{k_2 {q_e}^2}$$

Equation2.5

2.3 Materials and methods

2.3.1.1 Materials

The interactions between palmitic acid (≥99% purchased from Merk) and the adsorbent sensors were studied using the Biolin scientific Qsense explorer (shown in Figure 2.2) from Biolin Scientific. The sensors (silicon dioxide (QSX 303), polystyrene (QSX 305), and aluminium oxide (QSX 309) also from Biolin Scientific were used unmodified. The sensors consisted of a 5MHz quartz crystal coated with the three materials mentioned. Ethanol (≥99%) was used for making the stock solutions. De-ionised water was provided by ELGA water treatment system PURELAB Chorus 1.

2.3.1.1.1 Preparation of Stock solutions

Palmitic acid was dissolved in ethanol to make concentration within the range of 25mg/ml to 150mg/ml. The upper limit was chosen as the point when no more palmitic acid dissolved in ethanol at room temperature (25°C). The solubility of palmitic acid in ethanol has already been described elsewhere and was beyond scope of this work (Calvo et al., 2008).

2.3.2 Adsorption of palmitic acid using QCM-D

The Qsoft 401 software was used to capture experimental data i.e. changes in frequency and dissipation while the Dfind software (from Biolin Scientific) was used for analysis of the data. The experiments consisted of three steps. The first step was the establishment of a stable baseline (around 0Hz) on a bare surface (nanoScience Instruments, 2024). This ensured that any differences of an adlayer due to adsorption or desorption could be clearly determined from a reference point (Biolin Scientific, 2023). A clean 5MHz sensor operated at room temperature

is expected to have a frequency and dissipation drift of <0.5Hz/h and 0.2×10^{-8}/h in air while water these are <1.5Hz/h and $<2\times10^{-8}$/h (Biolin Scientific, 2023; Easley et al., 2022). This was measured at the 3rd, 5th and 7th harmonic. Once the baseline had been established, the second step was the addition of ethanol solvent. The signal was allowed to stabilize within this layer after which the last step of addition of palmitic acid stock solutions followed. The QCMD measured changes in frequency and dissipation with time. Once the final step frequency had stabilized, the experiment was terminated. All experiments were conducted at room temperature and pressure. Before use, all sensors were washed with absolute ethanol in an ultrasonic bath for 30minutes. This was followed by drying with nitrogen gas.

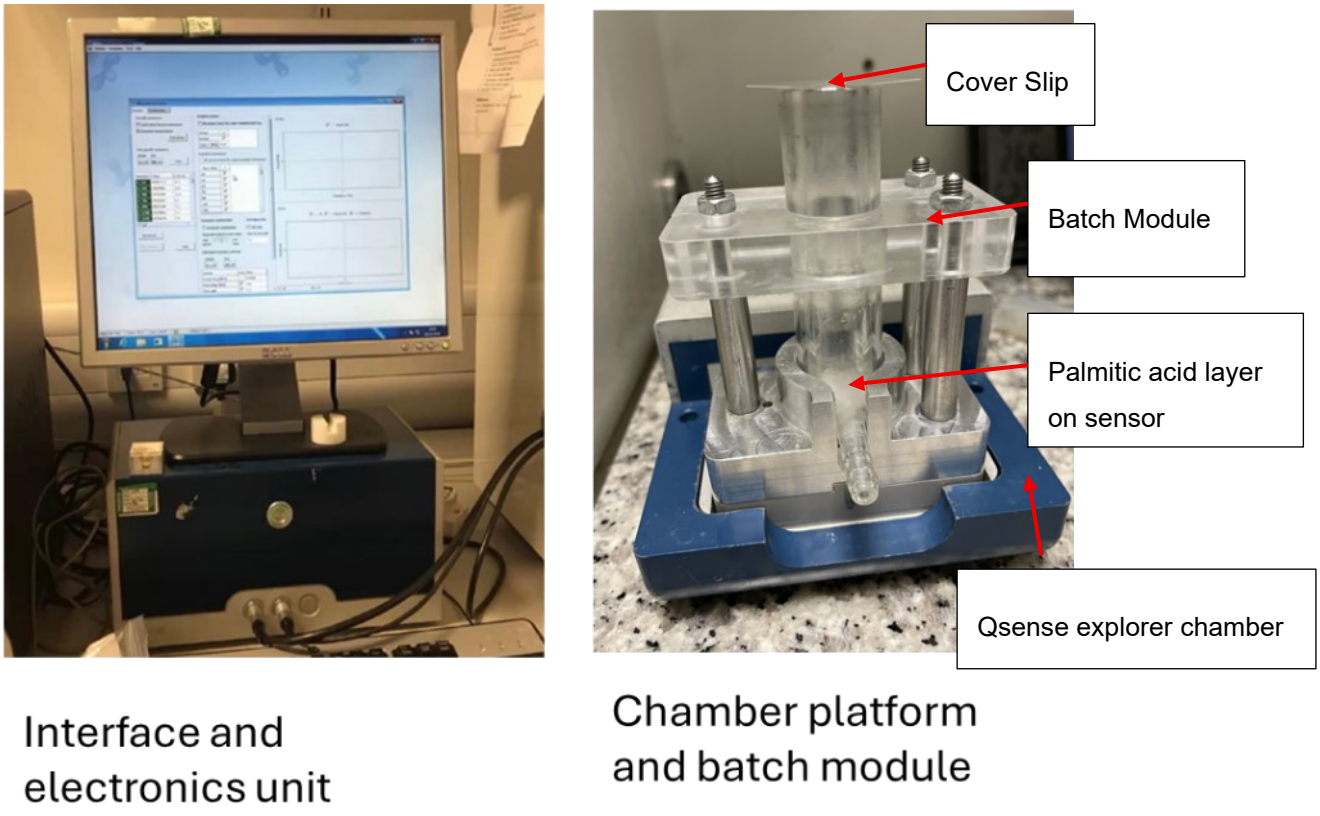


Figure 2.2 QCMD experimental set up made up of the Qsense explorer, batch module and user interface.

2.3.3 Characterization by XPS

Xray photoelectron spectroscopy has sometimes been referred to as ESCA (electron spectroscopy chemical analysis) (HEIDE, 2012; Kumar et al., 2023). XPS is a surface sensitive technique that can detect atoms on the outermost 10nm of a surface (Li et al., 2023). The surface is made up of different elements. An experiment starts with an X-ray source firing X-rays (photons) at a sample where electrons that adsorbed the energy are ejected from the core of an atom. These electrons emitted have a kinetic energy which is detected by a detector

in the XPS machine. This kinetic energy is a function of the binding energy which is very specific to different elements and their environment. This is how XPS helps identify elements on the surface. Once an electron is emitted, a de-excitation process occurs which results in emission of electrons. Electrons emitted from this process result in the formation of Auger peaks which are important in identifying the elements on the surface (HEIDE, 2012). $E_{binding}$ represents the energy of electrons that are attracted to the nucleus of an atom, E_{hv} is the energy of X-ray photons for the specific equipment being used, ϕ is the work function of the equipment which is the minimum amount of energy needed for electrons to be ejected from the surface. The $E_{kinetic}$ is the measured kinetic energy of the ejected electrons as they follow a specific path. This allows for differentiating different atoms as they are ejected with different kinetic energies (Good & Facey, 2018).

$$E_{binding} = E_{hv} - (E_{kinetic} + \phi)$$

(Good & Facey, 2018)

It was important to understand what functional groups were on the sensor surface before and after the QCMD experiments. Once sensors were received from the manufacturer, they were tested to obtain a survey spectrum of the elements on the surface. The Thermo Scientific K-Alpha+ X-ray Photoelectron Spectrometer was used to take these measurements. Post the QCMD experiments, the first step involved preparation of the sensors by allowing them to dry in glass petri dishes. Once this was done, the sensor samples were mounted onto a standard sample holder which consisted of a stainless-steel top and a main part of the holder which was made of copper. The sensors were then secured onto the central part of the stainless-steel plate using clips (the clips were positioned such that they were flat and were not in the way of the X-ray/flood gun). Lastly, the optimum height of the sample holder was determined to ensure it could be transferred safely into the spectrometer.

Avantage software from ThermoFisher Scientific was used for surface analysis. The software came already integrated with the K-Alpha XPS equipment. This made it possible to collect process and analyse the data all within one system. In the sample window of the software user interface, the load lock was closed, and the pumping down initiated which took on average about 45minutes. The sample holder was then transferred into the analysis chamber once the pressure in the load lock had reached $5 \times 10^{-7}\ mbar$. The pressure in the analysis window was below $8 \times 10^{-8}\ mbar$ before the experiment could begin. The experiment started with running an initial survey scan followed by the finals scans which included core levels auger lines and valence bands. The X-ray spot size used was the largest at 400μm. The smallest that could be used was 30μm. Pass energy was typically about 20eV. The type of source gun

was the Al K- Alpha. Depending on the peak intensity, the number of scans for each element of interest were determined to obtain a good spectrum/ peak. The main elements of interest were carbon oxygen and silicon. The chemical states were identified to determine if the acidic group of palmitic acid could be identified to determine if adsorption had taken place.

2.3.4 Statistical Analysis

All experiments were repeated twice and the results for ΔF vs Concentration reported as the means ± standard deviations. The results were processed with a two-way analysis of variance (ANOVA) with OriginPro 2026. A probability of $P < 0.05$ was considered significantly different (Yang et al., 2024). In addition to this, a correlation coefficient R^2 analysis was performed to assess how well the model (PFO and PSO) fit experimental data. For $R^2 \approx 0$, there was no correlation, R^2 closer to +1 or -1 showed that there was a strong relationship between the model and the experimental data (Ahmed et al., 2025).

2.4 Results and Discussion

2.4.1 QCM-D

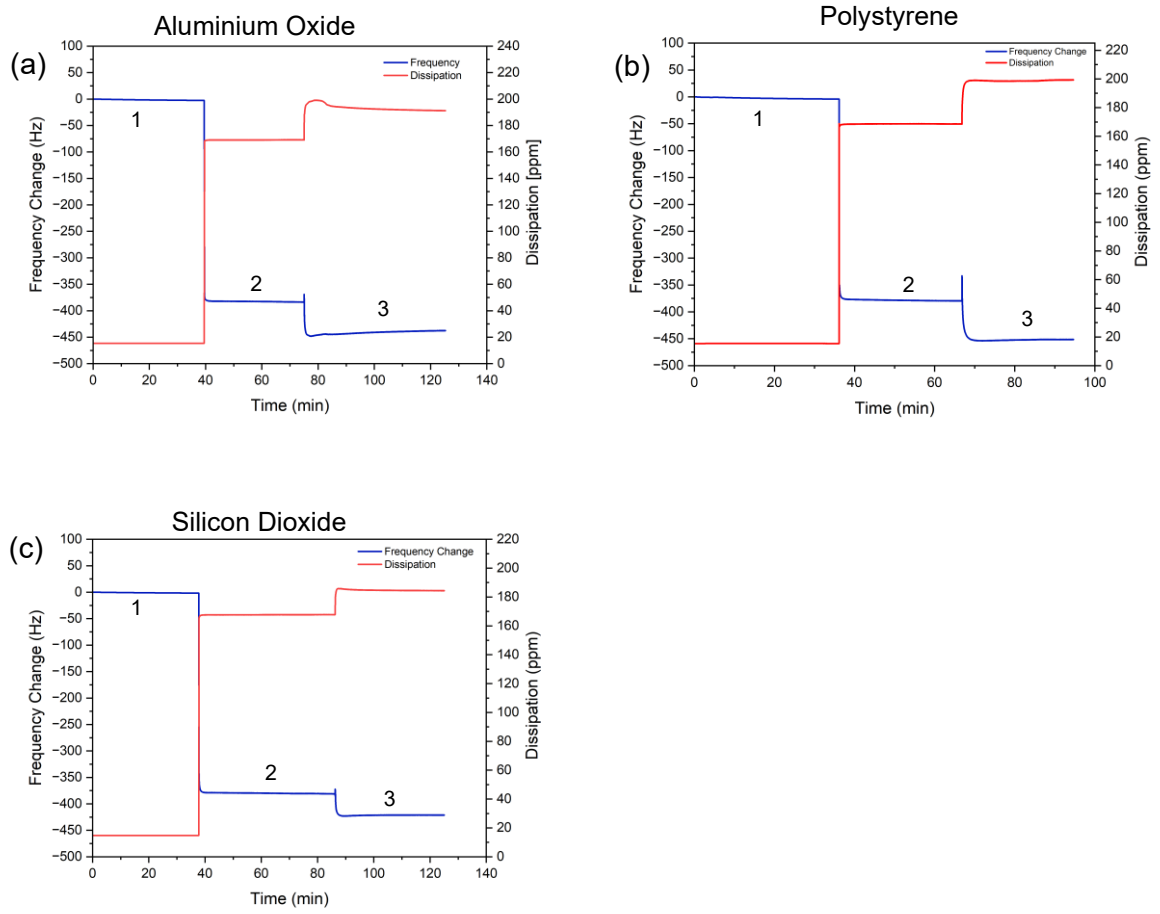


Figure 2.3 The third overtone QCMD response when palmitic acid ss was added onto different substrate sensors (a) Aluminium Oxide, (b) Polystyrene and (c) Silicon Dioxide at a concentration of 150mg/ml. The plots show ΔF (blue line) and ΔD (red line) before addition of ethanol (1) during addition of ethanol (2) and after the addition of palmitic acid (3).

A stable baseline was established with the frequency at 0hz as shown in step 1 of Figure 2.3. The addition of ethanol to the substrate sensors in step 2 was accompanied by a negative shift frequency and simultaneously a positive shift in the dissipation. ΔF was about 380Hz and ΔD 170ppm for the addition of ethanol for all surfaces. The addition of palmitic acid in step 3 was accompanied by different shift pattern for both ΔF and ΔD. A change of about 40.45Hz was observed between step 2 and 3 for silica with the frequency remaining stable once this layer was added. A much larger ΔF of 72.09Hz was recorded for the polystyrene for the same step with both frequency and dissipation remaining stable thereafter. The maximum ΔF recorder for the aluminium oxide sensor was 64.31Hz which continued to reduce until ΔF for

this step was 54.34Hz by the end of the experiment. ∆D for aluminium oxide increased to 183.51ppm and then reduced steadily to 176.0ppm.

Early studies on the adsorption of ethanol onto aluminium oxide reported that ethanol had adsorbed physically onto aluminium oxide and then transitioned to be dissociatively chemisorbed upon heating from 77K to room temperature (Shklyarevskii et al., 1976). This was later confirmed in another study where spectra analysis showed presence of aluminium ethoxide (Evans & Weinberg, 1979). The experiments were conducted in a vacuum with vapourised ethanol and different exposure levels from 0.01 Torr-sec to above 100 Torr-sec. These conditions may have facilitated the adsorption of ethanol onto aluminium oxide. Generally, aluminium oxide is very stable and does not react with ethanol unless at high temperatures and in the presence of a catalyst. In this study, experiments were conducted at room temperature and pressure. The experiments were also short hence there was not enough time to be able to determine if ethanol could form any physical bonds with the aluminium oxide sensor surface. Despite this, a negative shift was observed owing to the sensitivity of the QCMD. The surface free energy is an important parameter in understanding adsorption behaviour. While the QCMD does not directly measure the surface energy, the surface energy could be derived through contact angle measurements. This could help determine the relationship between frequency change due to adsorption and the surface free energy. However, determination of the surface energy through contact angle measurements was not explored here as the focus was rather on the adsorption kinetics of palmitic acid.

Once the alumina-ethanol layer was stabilized, palmitic acid stock solutions were added. Palmitic acid formed hydrogen bonds with ethanol. This was formed between the hydrogen from the carbonyl group and oxygen of hydroxyl group of ethanol. Calvo et al. (2008) reported in their work that ethanol tends to associate with itself rather than palmitic acid. This suggests that the solubility of palmitic acid in ethanol reduced as the concentration increased. This occurrence was observed as a white aggregate on the sensor surfaces. However, this contradicts the work by Beula & Sai (2013) where they suggested that reactions of organic acids such as palmitic acid with alcohols could take days in the absence of an acid catalyst. Frequency and dissipation measurements happened quickly when palmitic acid was added.

Dissolved palmitic acid in ethanol also formed covalent bonds with aluminium oxide. The COOH end of palmitic acid then attacks the Al-O thereby forming a covalent bond (Karaman et al., 2001). On polystyrene, van der Waals forces between the surface and palmitic acid resulted in the frequency change. Palmitic acid is saturated and hence the fatty acid chains are packed closely together (Kanicky & Shah, 2002). This resulted in ethanol being expelled

between the chains resulting in the positive shift in frequency observed in step 3 for adsorption onto aluminium oxide.

Table 2.1 Acoustic Ratio for palmitic acid adsorption at concentration of 150mg/ml

Surface	Ethanol	Palmitic Acid
Silicon Dioxide	-0.403	-0.404
Polystyrene	-0.403	-0.408
Aluminium oxide	-0.403	-0.404

The acoustic ratio given by Equation 1.6 was calculated using Qsense Dfind software using the third harmonic. The acoustic ratio is given by $\Delta D_n/(-\Delta F_n)$ where n is the overtone number (Fredrik Pettersson, 2022; Reviakine et al., 2011; Gopalakrishna et al., 2021). The importance of the acoustic ratio is that it assists in determining if the frequency changes observed were due to adsorption or due to viscous loading. The acoustic ratio is a purely material property relating to the ability of the molecules at the interface to dissipate acoustic energy (BioNavis, 2024).For a purely viscous liquid, the acoustic ratio is -0.4. Table 2.1 shows the acoustic ratios for palmitic acid and ethanol. The acoustic ratios are very close to that of a purely viscous fluid. However, even though the acoustic ratio is close, Reviakine et al. (2011) suggested that if the acoustic ratio is $\ll 4 \times 10^{-7}$ Hz^{-1} then the Saubery approximation can be used for mass estimation. Again Fredrik Pettersson (2022) acknowledged that while the acoustic ratio is good at giving quantitative clues as to whether the changes in frequency and dissipation are due to influences by the bulk shift or not, an acoustic ratio of -0.4 does not always rule out the presence of an adsorption event. Owing to this, I have used XPS to analyse the surfaces to gain more clarity.

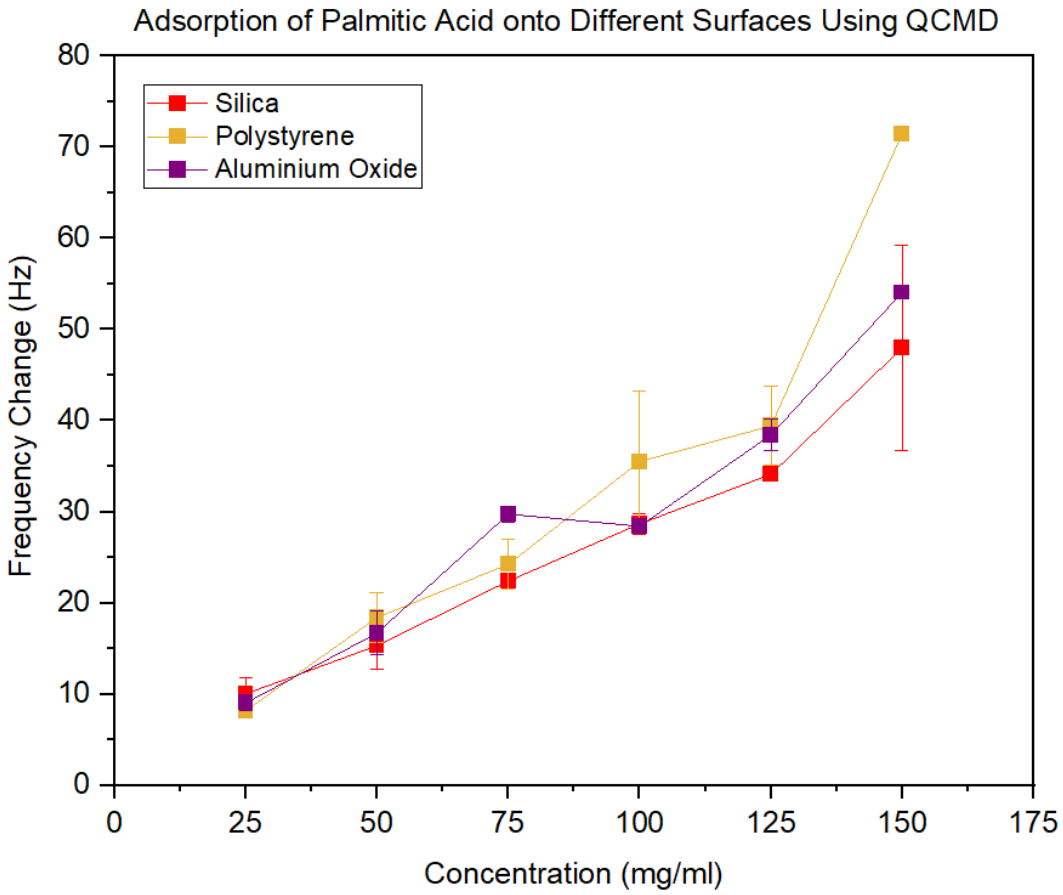


Figure 2.4 Adsorption isotherms for all the different surfaces with increasing concentration of palmitic acid. The experiments were repeated twice. The mean frequency change is plotted against changing concentration. The error bars represent the standard deviation (Seanneng, 2023).

Table 2.2 Standard deviation of ΔF presented as error bars in Figure 2.4.

Concentration	Silicon Dioxide (Standard deviation)	Aluminium Oxide (Standard deviation)	Polystyrene (Standard deviation)
25	1.72958	0.86055	0.34295
50	2.55266	2.39709	2.7365
75	0.80257	0.87328	2.74428
125	1.11016	0.53033	7.78525
150	0.18173	1.68574	4.3084

Figure 2.4 shows an isotherm of frequency change with concentration. Each experiment had two repeats with frequency changes determined directly on the QSoft401 software. The general trend shows that increasing the concentration of palmitic acid resulted in increased

frequency change for all surfaces i.e. there is a positive correlation between the frequency change and concentration for all surfaces with correlation coefficients of 0.971 for aluminium oxide, 0.985 for silicon dioxide and 0.947 for polystyrene.

Based on the frequency change alone, the results suggests that as the concentration of palmitic acid increased, dispersive forces became more prevalent especially because ethanol tends to self-associate (Calvo et al., 2008). This resulted in palmitic acid forming aggregates thus resulting in increased frequency changes particularly at high concentrations.

2.4.1.1 Mass adsorbed

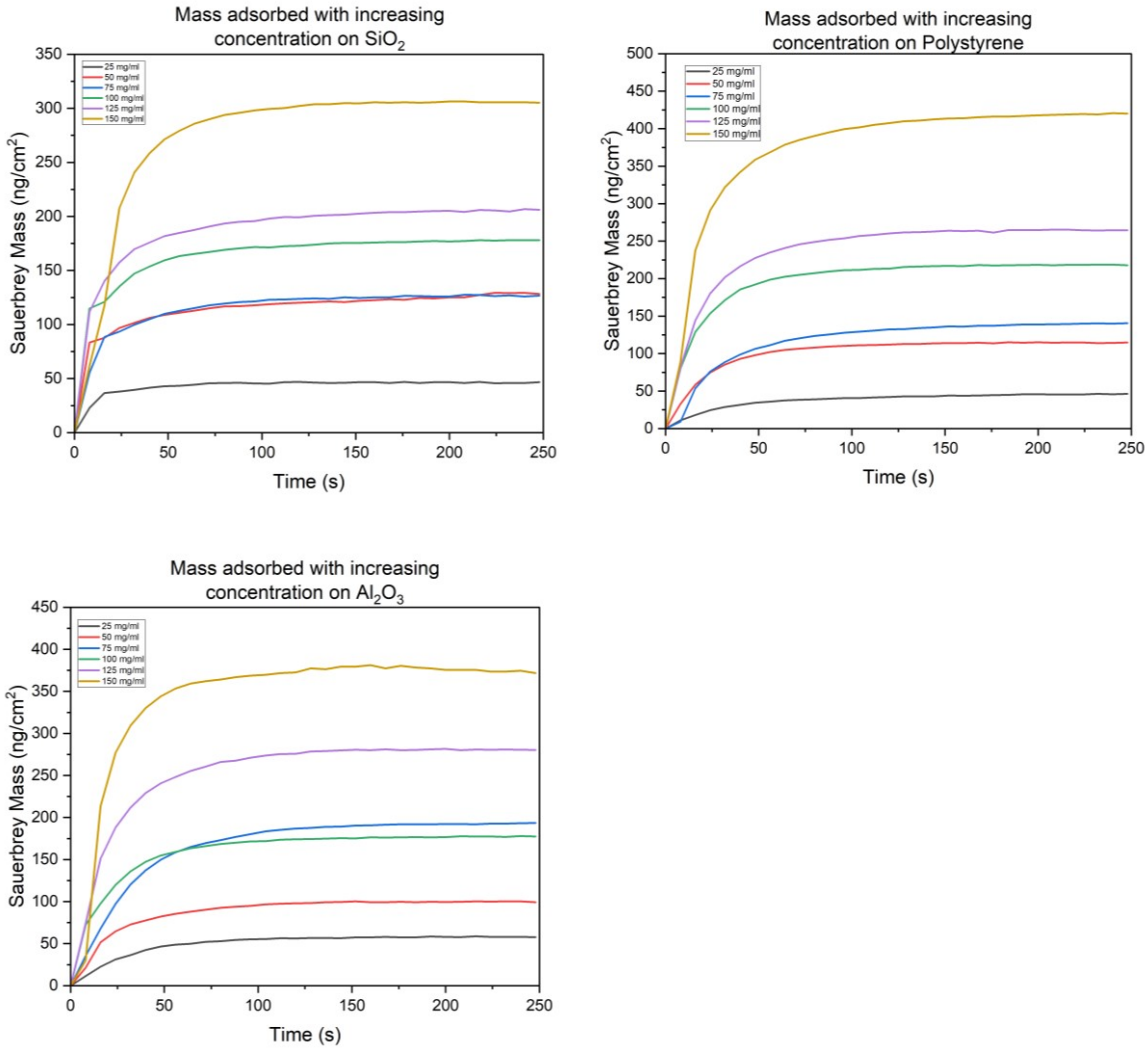


Figure 2.5 Mass adsorbed with time calculated using Sauerbrey equation at the third overtone.

A key feature of the quartz crystal microbalance with dissipation is in the ability for the piezoelectric sensor to detect changes in the stress applied on the sensor surface which in some cases may be due to adsorption. When deciding on which model best fits the raw data, there were two main parameters that where considered. The first was whether or not the

experimental data showed a spread across all harmonics (this was the case for my results) as this is very characteristic of viscoelastic materials. The second was if $\Delta D > 0$ which was also the case. Various sources in literature suggest that if both conditions are met then viscoelastic modelling should be used (Malin Edvardsson, 2023; Easley et al., 2022; Reviakine et al., 2011). After assessing the acoustic ratio, it was determined that the data could not be modelled by Sauerbrey since the acoustic ratio was >> 4×10^{-7} Hz^{-1}. The experimental results also showed that $\Delta D > 1 \times 10^{-6}$. This also reinforces that viscoelastic modelling must be used as $\Delta D > 1 \times 10^{-6}$ is characteristic for non-rigid films that can dissipate acoustic energy (Paul et al., 2008; Setiowati et al., 2021). It is important to note is that Sauerbrey model is not recommended for viscoelastic modelling as it gives an underestimation of the mass adsorbed (Paul et al., 2008).

Despite this, the Sauerbrey equation through its simplicity in equating changes in the resonance frequency to the mass adsorbed is still useful for mass estimation (Paul et al., 2008). Figure 2.5 shows the Sauerbrey mass adsorbed at different concentrations of FFA for the three materials used. The results showed that increasing concentration resulted in increased sensed mass. The graphs suggest that adsorption is quick with equilibrium being reached quickly. The quick saturation suggests that palmitic acid has a high affinity to the sensors. The mass calculated by Sauerbrey are significantly smaller than that determined by Voight as ΔF was determine manually from Qsoft 401 as the difference between the frequency of the last period (palmitic acid ss) and the second period (ethanol).

Earlier Figure 2.3 showed large changes for both frequency and dissipation. Lundgren et al. (2006) explored introducing a correction factor to the Sauerbrey equation to account for changes due to the bulk effects of the adsorbed material. However, this method had its limitations which included that it only worked for polymers where adsorption was irreversible with respect to dilution and that low molecular weight systems could easily desorb from the surface during rinsing (Tiberg, 1996; Lundgren et al., 2006). The use of a correction factor was not explored here but rather Dfind software was used to calculate the Voight mass using Smartfit.

Table 2.3 Mass and thickness of Palmitic acid onto Silicon dioxide calculated using Dfind SmartFit model and based on the 3rd to 7th overtone.

Concentration (mg/ml)	Voight mass (ng/cm^2)	Voight thickness (nm)
25	21978.134 ± 2.174	256.749 ± 0.021
50	114323.024 ± 23.956	1340.246 ± 0.281
100	115311.699 ± 24.755	1351.837 ± 0.290
125	107069.023 ± 69.218	1255.205 ± 0.811
150	127779.252 ± 48.120	1497.998 ± 0.564

Table 2.4 Mass and thickness of Palmitic acid on Aluminium Oxide based on the 3rd to 7th overtone.

Concentration (mg/ml)	Voight mass (ng/cm^2)	Voight thickness (nm)
25	99772.522 ± 26.233	1169.666 ± 0.308
50	99513.474 ± 36.793	1166.629 ± 0.431
100	184178.242 ±15.688	2159.182 ± 0.184
125	189106.74 ± 34.491	2216.961 ± 0.404
150	111026.781 ± 40.912	1301.604 ± 0.480

When modelling experimental data, the DFind software uses a traffic light system where green represents that the data fits the model well , amber is for medium fit and red shows that the model does not fit the data. Table 2.3 and Table 2.4 data showed that the results were a good fit as determined on the DFind. However, it is important to note on application on the Voight model, ΔF used was from a combination of the accumulated frequency shift caused by ethanol and the palmitic acid ss. As such naturally the mass calculated shown in the tables is an overestimation of the singular effect of palmitic. Most studies using this model operate using a flow cell which means there is no accumulation of e.g. ethanol molecules at the sensor surface in this case as this will be followed by another period which in this case would introduce palmitic acid to the system. In such a case ΔF calculated in each period is a result of the singular interaction of the components in that period. The method usually includes a rinsing stage done in situ to remove any loosely bound adsorbate. The drawback of this method is that large volumes of materials are used. The use of a flow cell also means that the effect of

flow rate on adsorption can be studied which was not possible when using a batch module. Different authors in literature employed the use of a flow cell for deposition of adsorbate onto the quartz sensors (Easley et al., 2022). Easley et al. (2022) identified that this method is particularly preferred in studies involving sequential addition of charged polymers. In another study, Hu et al. (2020) used a flow cell with a set flowrate of 100 µL/min to study the adsorption of methylene blue dye molecularly imprinted polymers coated sensor. They also used DFind smart for mass estimations like what was done in this work.

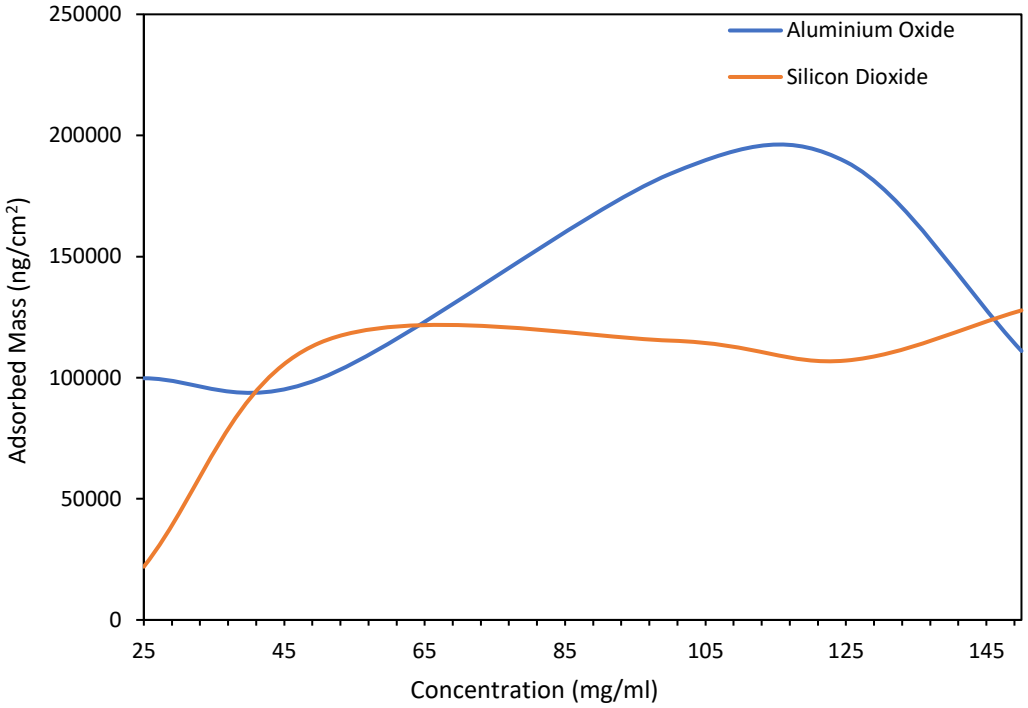


Figure 2.6 Adsorbed mass obtained from DFind SmartFit.

The results for Voight mass suggest that increasing the concentration results in increased sensed mass up to 125mg/ml and then reduces at 150mg/ml for palmitic acid on aluminium oxide. The amount adsorbed onto silicon dioxide plateaued at 50mg/ml and then increased again at 150mg/ml (Figure 2.6).The plateau starting at 50mg/ml for silicon dioxide suggests that the number of binding sites on the sensor were saturated, beyond 125mg/ml the amount of palmitic acid adsorbed began to increase (Alsharif, 2025). The isotherm for silicon dioxide follows the Langmuir isotherm. Alsharif (2025) reviewed the shapes of the Langmuir isotherm and from the results , the Silicon dioxide isotherm follows the LS shape. The isotherm for aluminium oxide follows the S shape Langmuir isotherm up 125mg/ml beyond this the mass of palmitic acid adsorbed starts to reduce. This is shown by the mass loss after 125mg/ml for aluminium oxide. This might be because the quartz resonator senses hydrated mass (Malin

Edvardsson, 2025).The rearrangement/expulsion of the solvent trapped between the fatty acid molecules in the monolayer as shown in Figure 2.7 (A) shows the point at which the solvent in between palmitic acid molecules is expelled from the adsorbed layer causing the dissipation to reduce by 5.5 ppm thus making it more rigid/ less soft in relation to the bulk fluid. Figure 2.7 (B) the frequency increased by 4Hz (positive shift) suggesting mass lost from the monolayer. Malin Edvardsson (2025) and Lind & Cárdenas (2016) reported that the formation of lipid bilayers via vesicle fusion. Their adsorption fusion and spreading resulted in a profile like that shown in Figure 2.7 (A) and (B). They attributed this 'mass loss' to expulsion of water from the vesicle. Earlier it was discussed that ethanol tends to self-associate. This resulted in palmitic acid chains packing close together via van der Waals forces of attraction. The results here show that silicon dioxide is a better adsorbent at concentrations above 125mg/ml. However, below this concentration aluminium oxide is a better adsorbent. This is crucial in removing palmitic acid from e.g. wastewater (and for use in biodiesel production) as it can help in the selection of suitable adsorbents. Adsorption of palmitic acid onto Polystyrene data was not presented here as the data did not fit the Voight model. As such the Sauerbrey approximation was used for mass estimation for adsorption of palmitic acid onto polystyrene.

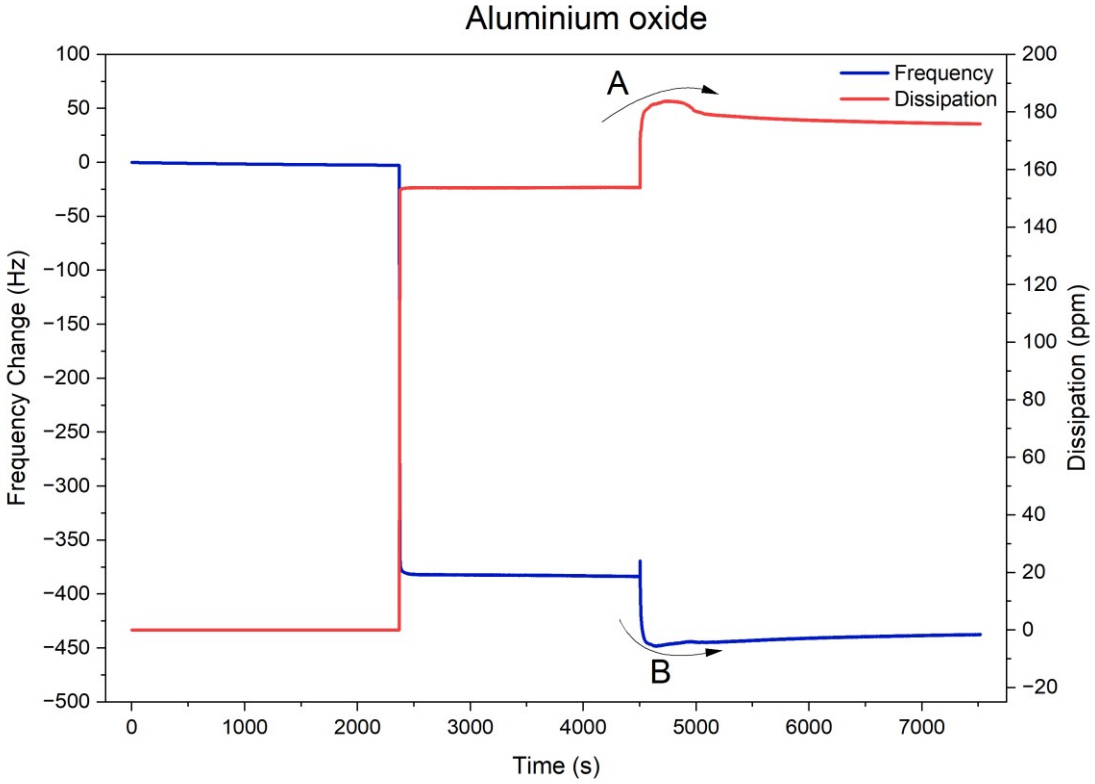


Figure 2.7 Frequency and dissipation shift at the 3rd overtone for palmitic acid adsorption.

2.4.1.2 Kinetic data

Suitable kinetic models were needed to be able to determine the mechanism of adsorption e.g., chemisorption or mass transfer onto the surface of the sensor etc. Many models exist which can be categorised as adsorption reaction models (Pseudo-first-order rate equation**,** Pseudo-second-order rate equation, Elovich's equation and Second-order rate equation) and adsorption diffusion models (Liquid film diffusion model, Intraparticle diffusion model and Double-exponential model (DEM)) (Ebelegi et al., 2020; QIU et al., 2009). In this work, only PSO and PFO where applied. The assumption of the PSO equation is that chemisorption is the rate limiting step (QIU et al., 2009). The PFO model was used with the assumption that the adsorption rate is dependent on the number of unoccupied binding sites and follows the Langmuir equation (Largitte & Pasquier, 2016).

The diffusion models where not explored as they are generally used to describe to film diffusion or interparticle diffusion with the drawback that for such systems the adsorption can be rapid thus not suitable for kinetic study (QIU et al., 2009). For these models, diffusion is assumed at the rate limiting step (Largitte & Pasquier, 2016). Lastly the Elovich's equation was not suitable as it is usually applied for kinetics involving chemical reactions on heterogenous surfaces which was not the case in this work as all sensor surfaces are assumed to be homogenous (QIU et al., 2009).

PFO, PSO and intraparticle diffusion kinetic model equations have been used to explain the kinetics of adsorption for hemicellulose onto nanofibril cellulose following the use of QCMD for estimation of mass adsorbed (Yao et al., 2021). However, they determined that their results were best represented the by intraparticle diffusion kinetic model. Hu et al. (2020) in their work where a magnetic imprinted polymer was coated onto a quartz sensor to study the adsorption of methylene blue dye. They were able to determine that the PSO equations best described their results based on $R^2 > 0.99$. These two studies demonstrate that there is relevance for the application of PFO and PSO equations to effectively describe experimental results obtained from QCMD. The successful application of these models is dependent on using correct mass estimations. Improper application of both Sauerbrey and Voigt equations can result in wrong interpretation of the kinetic equations. PSO and PFO models were used after determining the areal mass density.

2.4.1.2.1 Pseudo Second Order

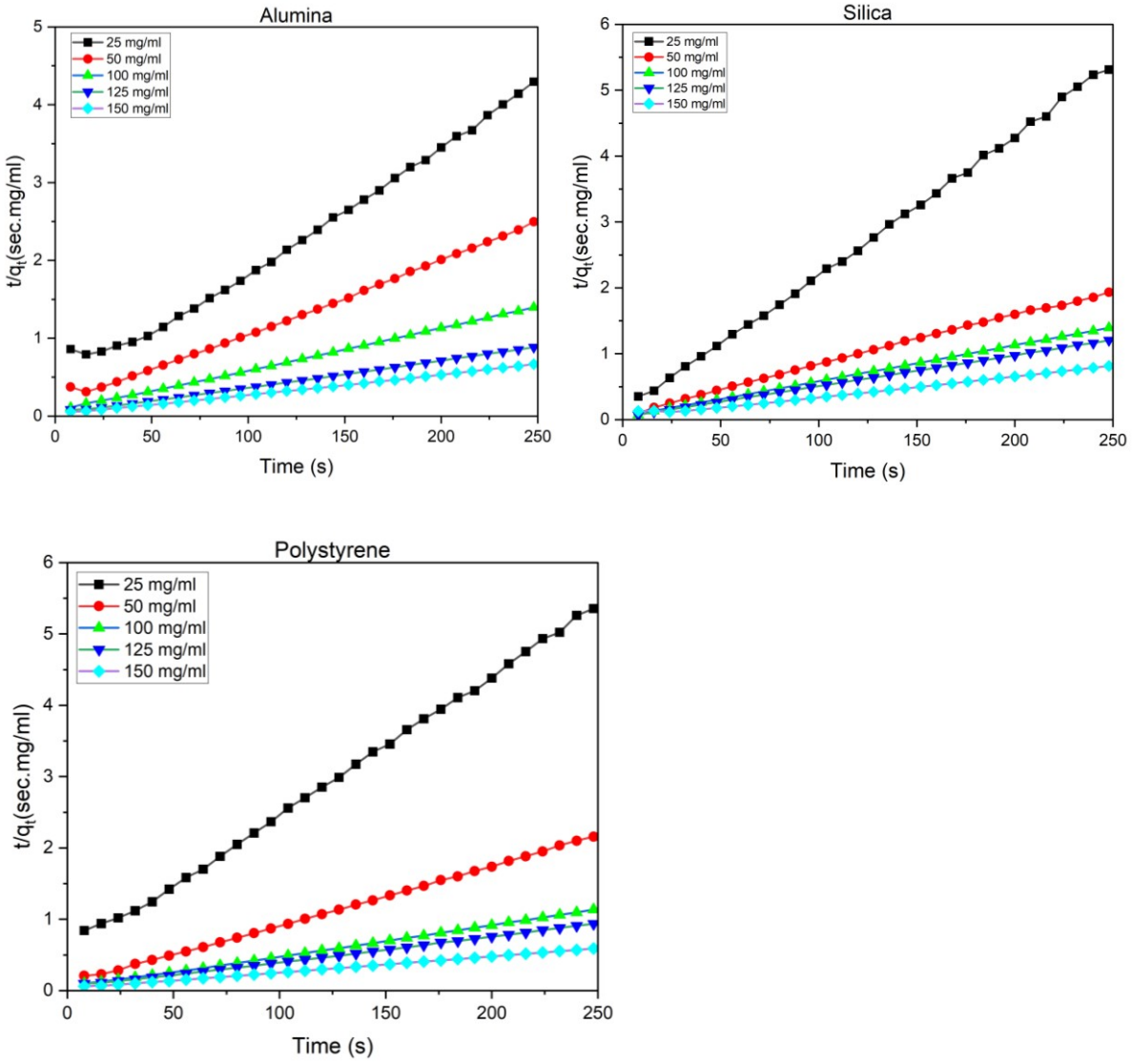


Figure 2.8 PSO models for palmitic acid adsorption on different surfaces.

The interaction of palmitic acid at different concentrations was studied further using PFO and PSO equations. Figure 2.8 shows the linearized PSO rate equation kinetics. The slopes for all concentrations on the different surfaces show a linear correlation. This facilitated the estimation of the amount of palmitic acid adsorbed at equilibrium (q_e) and the PSO equilibrium rate constant k_2 from the slope and the y-intercept (Revellame et al., 2020). These values are present in Table 2.5 to Table 2.7 alongside the correlation coefficient R^2. The values of R^2 for the PSO equation were greater than 0.99 suggesting that there was chemisorption played a crucial role in the adsorption of palmitic acid onto all sensors (Ho & Mckay, 1999). Talebi et al. (2020) in their study of adsorption of acetic and butyric acids from fermented landfill leachate where able to determine that the controlling mechanism was chemisorption by

obtaining a value of R^2 greater than 0.9. In another study (Phetrungnapha et al., 2023) where FFA where adsorbed from cooking oil using casava peels proved that both PSO and PFO models were a good fit for their results, however concluded that PSO was a better fit at the amount of FFA adsorbed at equilibrium was close those obtained from their experiment. While the application of PFO and PSO equations to data obtained from QCMD data has been done before, the application of these models to palmitic acid adsorption using QCMD presented here for the first time is very valuable in assisting to choose adsorbents that could potentially be used to adsorb fatty acids from wastewater.

Table 2.5 Equilibrium rate constant for Al_2O_3.

Aluminium Oxide					
Concentration (mg/ml)	25	50	100	125	150
$q_{e\ (mg/ml)}$	65.36	107.53	185.19	294.12	384.62
$k_{2(mg.sec)}$ $(\times 10^{-4})$	6.38	6.00	5.34	4.62	4.15
R^2	0.9918	0.9972	0.9995	0.9992	0.999

Table 2.6 Equilibrium rate constant for Silicon dioxide

Silicon Dioxide					
Concentration (mg/ml)	25	50	100	125	150
$q_{e\ (mg/ml)}$	47.39	133.33	181.82	212.77	333.33
$k_{2\ (mg.sec)}$	4.68×10^{-3}	7.00×10^{-4}	7.80×10^{-4}	5.74×10^{-4}	2.14×10^{-4}
R^2	0.9992	0.9988	0.9999	1	0.9941

Table 2.7 Equilibrium rate constant for Polystyrene

Polystyrene					
Concentration (mg/ml)	25	50	100	125	150
$q_{e\ (mg/ml)}$	51.55	120.48	227.27	277.78	454.55
$k_{2\ (mg.sec)}$ $(\times 10^{-4})$	7.15	7.78	4.61	3.12	1.62
R^2	0.9989	0.9993	0.9995	0.999	0.9987

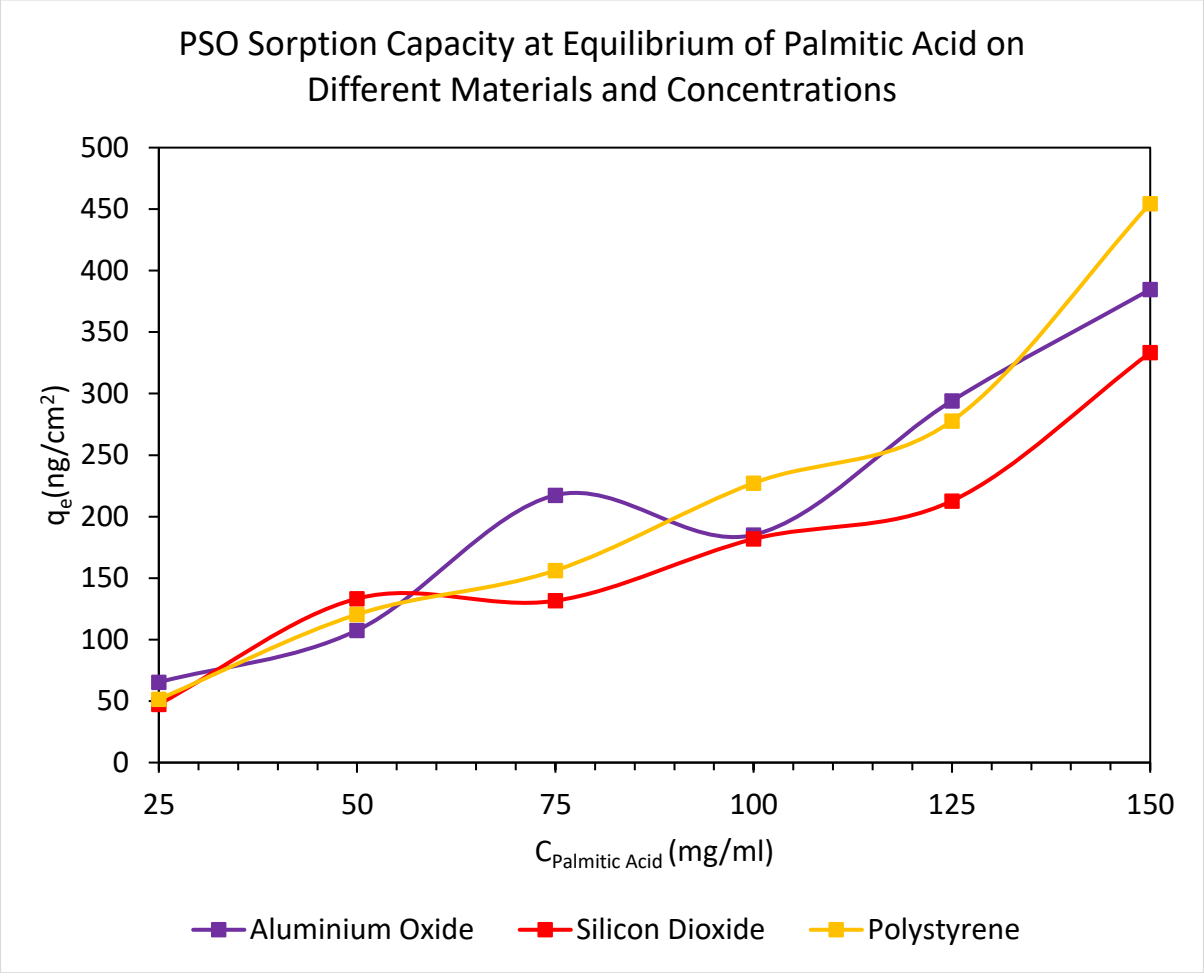


Figure 2.9 shows plot of the areal mass density at equilibrium versus concentration for the PSO adsorption kinetics of Palmitic acid onto Polystyrene, Aluminium oxide, and Silicon Dioxide.

Figure 2.9 shows the amount of palmitic acid adsorbed at equilibrium for all sensors. The results show q_e increased with concentration for all the substrate sensors. The results suggest that at 150mg/ml, polystyrene was a better adsorbent. Based on the adsorption capacity at equilibrium the surfaces performance at low concentrations is similar (below 50mg/ml) however at concentrations increase polystyrene outperforms the other substrate sensors. The R^2 values of PSO suggest that this is a good model fit. Statistical analysis showed that $P < 0.05$ for the mean of q_e at different concentrations, therefore there was no significant difference in the amount adsorbed at equilibrium at different concentrations.

2.4.1.2.2 Pseudo First Order

Figure 2.10 to Figure 2.12 present linearized plots for PFO equation. The same process was followed in determining q_e and k_1 as in the PSO model where k_1 the rate constant was found by plotting $\ln[q_e-q_t]$ vs time (sec) and plotting the line of best fit and finding the trend line. k_1 and q_e were calculated by $k_1 = -m$ where m is the slope of the equation of the line and $q_e = \exp(c)$ where c is the intercept (Revellame et al., 2020). The value of R^2 was determined to be < 0.9 (Table 2.8). The values of R^2 suggested that the PFO model was not a good fit for the data. Chu et al. (2025) and Revellame et al. (2020) suggested that the PFO model is only correctly applied when used in its linearized form (Equation2.3) which was the case in this work. Ho & Mckay (1999) suggested that PFO is only valid at the onset of adsorption which the PSO being more applicable over a wide range. Revellame et al. (2020) and Nascimento et al. (2023) on analysing the linearized equation reported that the limitation of the PFO was purely mathematical as when $q_e=q_t$ the left-hand side of Equation2.3 becomes undefined. Therefore, is a limitation of the PFO model not being applicable at any time which the PSO does not have. One in fitting PFO identified in literature was the use of different time intervals when determining q_e (Nascimento et al., 2023). This was not the case in this work. The advantage of the QCMD in adsorption studies is that it measures frequency and dissipation changes with time which were used to calculate the mass. This made it easier to have predetermined time interval when applying both PSO and PFO models.

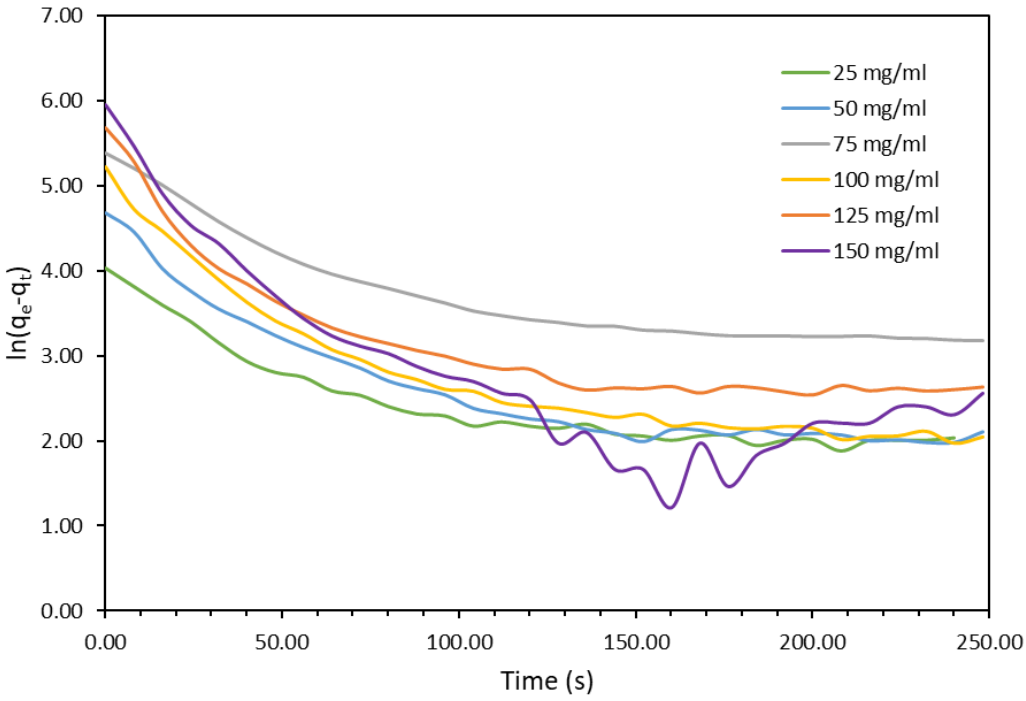


Figure 2.10 Linearized plot for modelling pseudo-first-order kinetics for adsorption of Palmitic acid onto Aluminium Oxide at different concentrations.

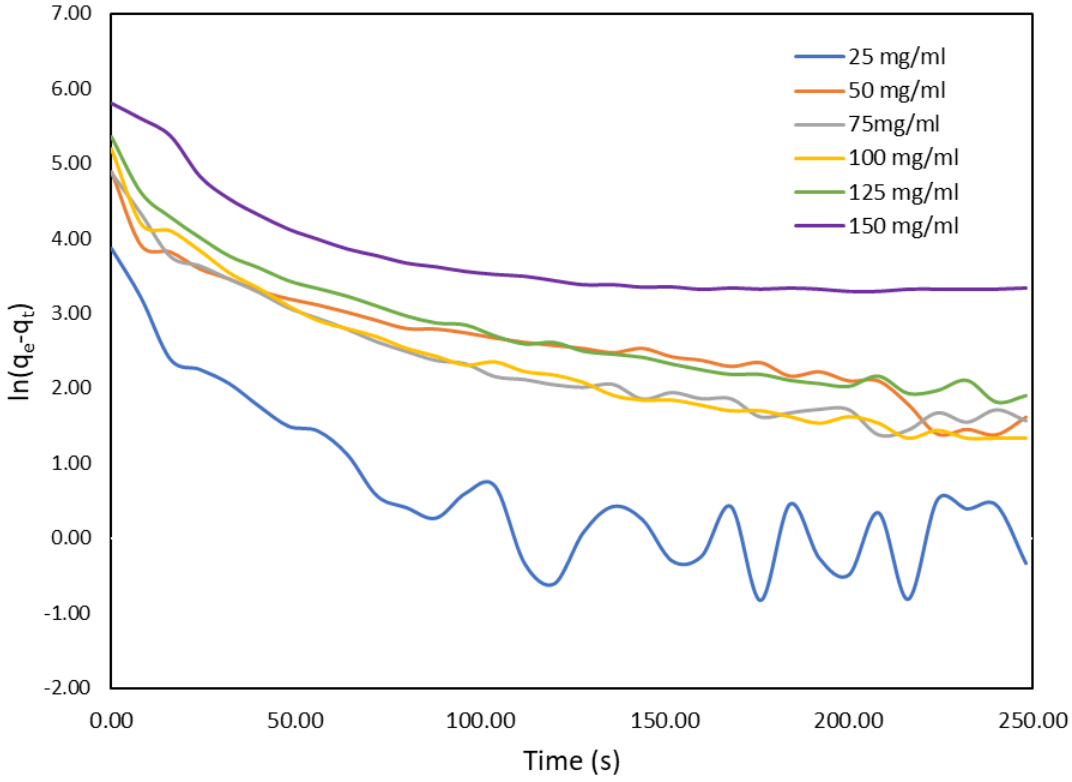


Figure 2.11 Linearized plot for modelling pseudo-first-order kinetics using experimental data for adsorption of Palmitic acid onto Silicon Dioxide at different concentrations.

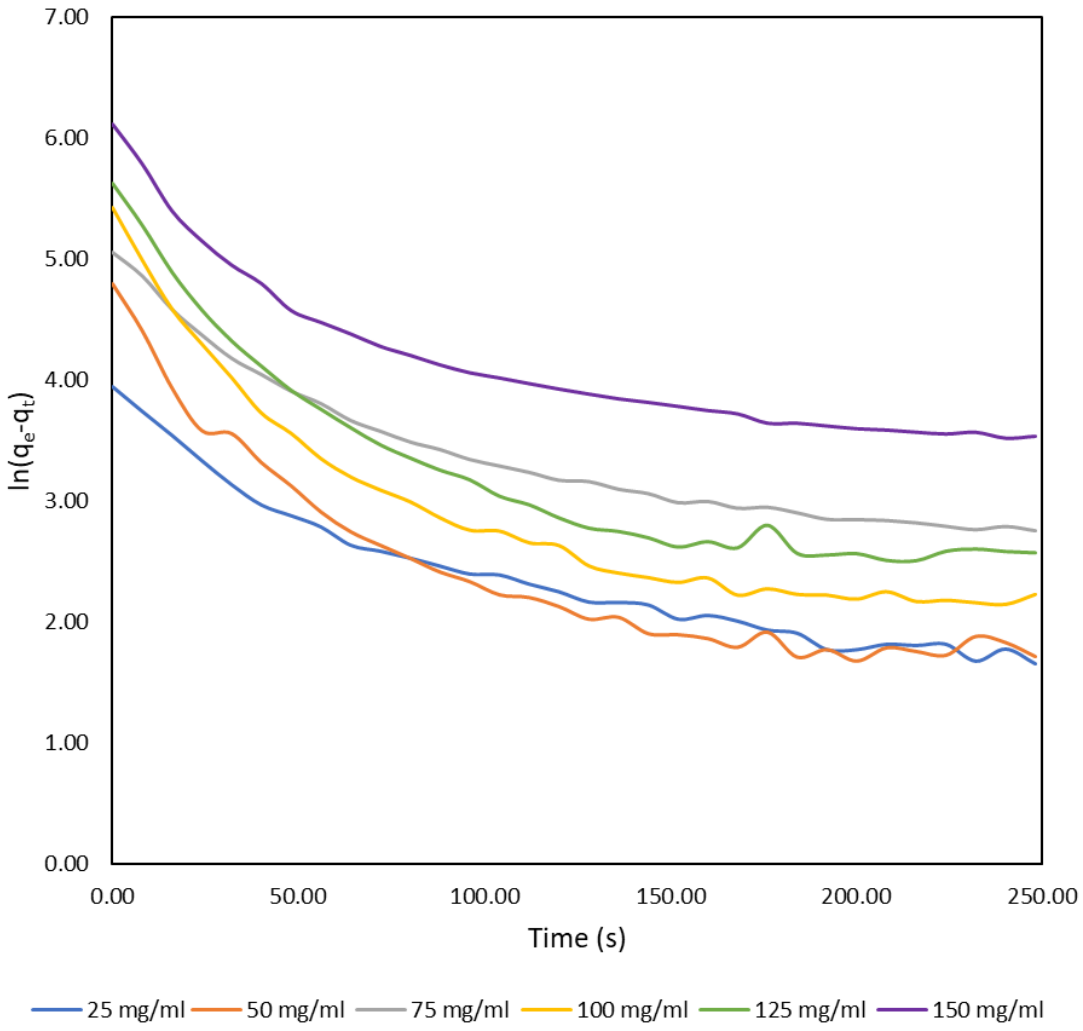


Figure 2.12 Linearized plot for modelling pseudo-first-order kinetics from experimental data for the adsorption of Palmitic acid onto Polystyrene at different concentrations.

Table 2.8 Equilibrium rate constant and R^2

Sensor	Concentration (mg/ml)	k_1	R^2
Aluminium Oxide	25	7.60E-03	0.7592
	50	9.00E-03	0.7742
	75	7.70E-03	0.7889
	100	1.04E-02	0.7870
	125	9.20E-03	0.6862
	150	1.24E-02	0.6397
Silicon Dioxide	25	1.16E-02	0.5919
	50	9.80E-03	0.8958
	75	1.07E-02	0.8238
	100	1.21E-02	0.8644
	125	1.07E-02	0.8507
	150	7.70E-03	0.6560
Polystyrene	25	7.80E-03	0.8896
	50	1.00E-02	0.7858
	75	7.90E-03	0.8501
	100	1.06E-02	0.7831
	125	1.03E-02	0.7835
	150	8.20E-03	0.7986

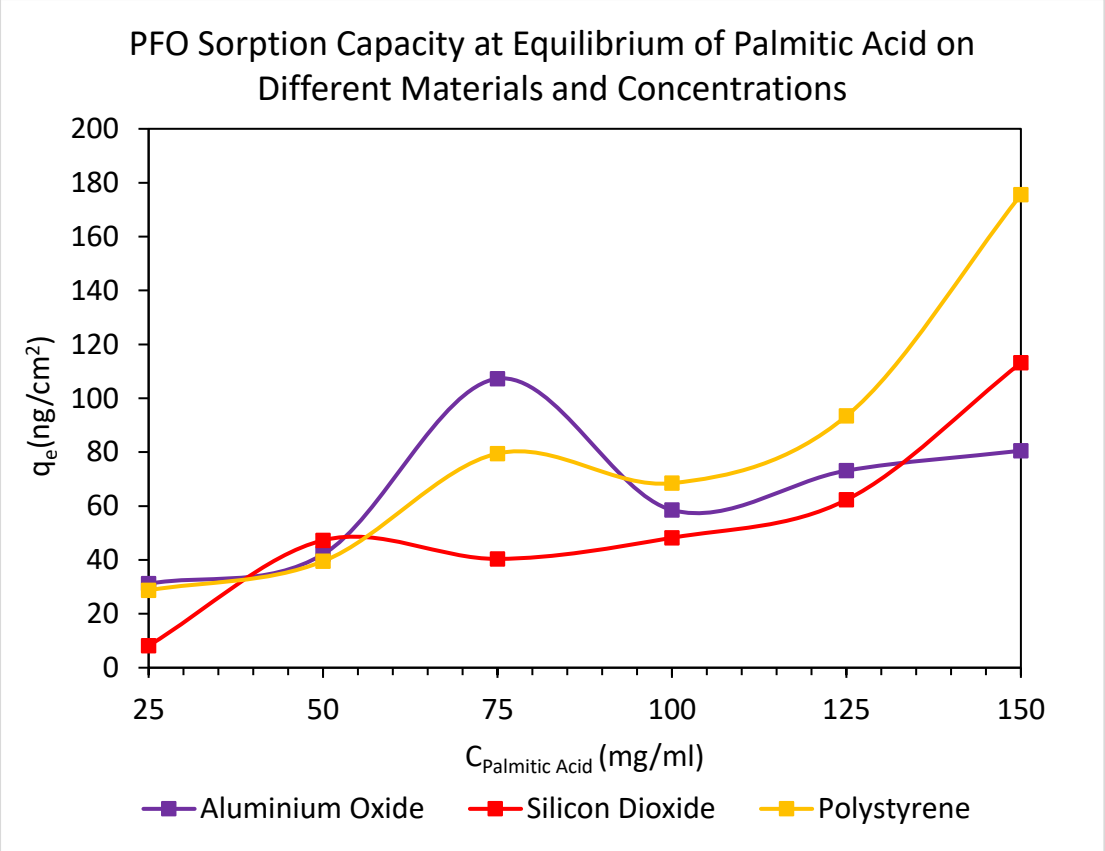


Figure 2.13 Areal mass density at equilibrium with increasing concentration for the PFO adsorption kinetics of Palmitic acid onto Polystyrene, Aluminium oxide, and Silicon Dioxide.

Figure 2.13 is a plot of the areal mass density at equilibrium as determined by the PFO model equation. However, as the R^2 was less than 0.9, the estimation of the mass of palmitic acid at equilibrium by this fit was unreliable. Figure 2.9 for q_e as determined from application of PSO model was much closer to the mass adsorbed experimentally. Despite the PFO model being a better fit for the experimental data, comparison of the amount adsorbed at equilibrium by the two-way Anova using the Turkey and Bonferroni method both yielded the same results that there was no significant difference in the means of the amount of palmitic acid adsorbed at equilibrium at different concentrations for the three surfaces.

2.4.2 Xray photoelectron Spectroscopy of Palmitic acid adsorption

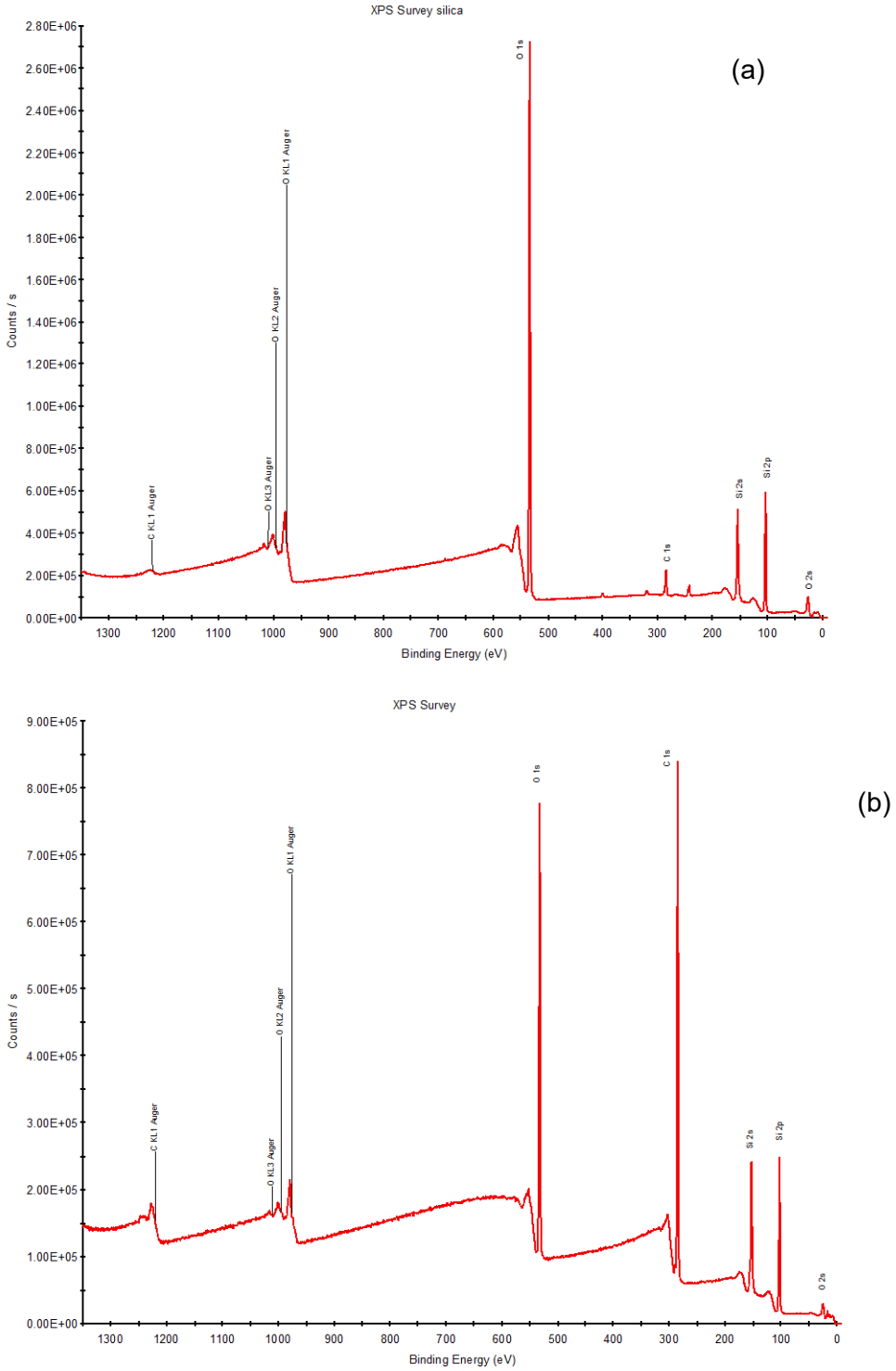


Figure 2.14 XPS surveys for silica surface. (a) shows a survey for a new silica surface (b) shows a survey for the same sensor after use for palmitic acid adsorption studies.

XPS allows for the surface composition and chemical states on the surface to be determined (Watts & Wolstenholme, 2003). This makes it possible to determine the elements on a surface and their chemical states/ environments of a sample by first performing a survey scan followed by an elemental scan. This secondary analysis makes it important to understand the peak shape and peak intensity as it will give further details on the type of bonds between elements, and the concentration of the functional groups present on the surface. Three types of surfaces were examined in this work: silicon dioxide, aluminium oxide, and polystyrene. A survey scan was performed for three surfaces.

Figure 2.14 (a) is a survey spectrum of a silicon dioxide sensor before and (b) after adsorption of palmitic acid ss using QCMD. The first apparent difference between the two survey spectrums of the silicon dioxide sensors was the change in peaks intensities at 284.62eV and 532.53eV corresponding to C1s and O1s respectively. The used silicon dioxide sensor exhibited higher peak intensities for the C1s peak and a reduced peak intensity for O1s after 50mg/ml palmitic acid ss interacted with the surface. This increased intensity of the C1s peak suggests that palmitic acid had adsorbed onto the surface. The silicon peaks Si2p also showed a slight decrease in peak intensity although the difference was not as large as the C1s and O1s peaks. This will be explained further in section 2.4.2.1. Survey spectra peak intensities have been compared in literature to determine the evolution C1s and O1s peaks (Yang et al., 2014; Fraxedas et al., 2021). Jensen et al. (2013) reported low quantities nitrogen and fluorine in addition to low amounts of C1s with the SiO2 predominantly made up of oxygen and silicon. Comparison of the survey spectrum of Jensen et al. (2013) with the those shown in Figure 2.14 revealed that the was no presence of contaminants i.e. nitrogen and fluorine.

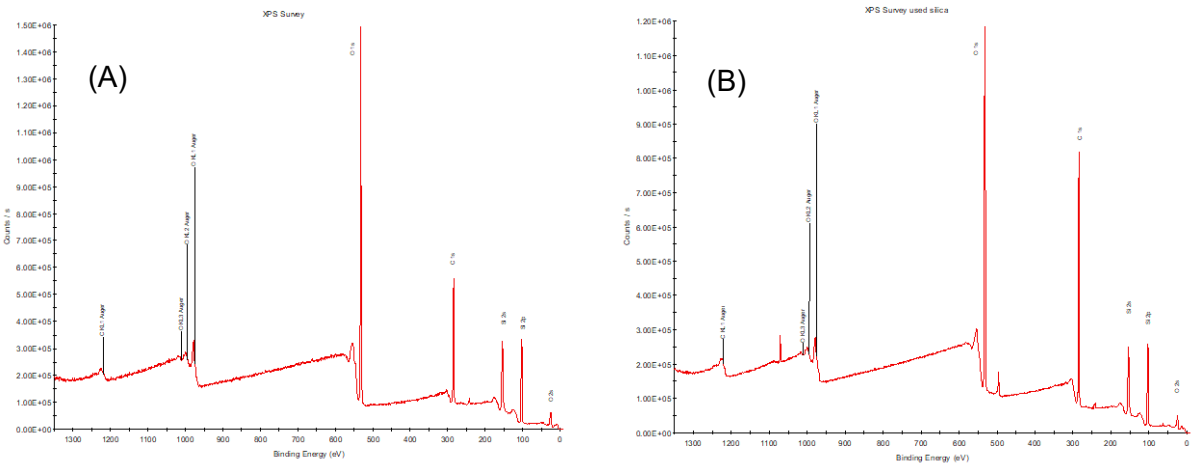


Figure 2.15 XPS survey spectra for rinsed silicon dioxide sensors following QCMD experiments with 125mg/ml of palmitic acid ss. (A) rinsed with deionised water (B) rinsed with ethanol.

Figure 2.15 presents the results of effect of rinsing the sensor substrate surfaces with two different solvents. QCMD experiments were performed in batch mode. Experiments using a flow cell were able to perform the rinsing step in situ (Easley et al., 2022). Rinsing of loosely bound palmitic acid molecules was done at the end of each experiment. The survey spectra for Figure 2.15 (A) and (B), C1s showed higher intensities when ethanol was used for rinsing as opposed to deionised water. The O1s intensity is also slightly reduced in the case of the sensor rinsed with ethanol. Results for the thickness of the measured layer (Table 2.3 and Table 2.4) showed thicknesses above the 10nm limit that applies for XPS measurements (Thermo Fisher Scientific, 2008; Jablonski & Zemek, 2009). This would have meant the sensors would not have been measured by XPS thus the rinsing step was necessary. The thickness of the adsorbed film after rising was not determined as this was outside the scope of this work. Jablonski (2019) reported overlay thickness of in literature was in the range of 0.3 nm to 7.1nm while Gunter & Niemantsverdriet (1995) reported much lower thickness of between 0.8nm (flat) and 1.6nm (water roughened side) for SiO_2 depending on the orientation of the sensor.

2.4.2.1 XPS spectra of Silicon dioxide

Following the survey scan, elemental scans were done to understand the chemical states of the elements by using the peak fitting technique. Smart fit analysis on the Avantage software was used to account for any background corrections. The smart background follows the Shirley background correction. However, it has an additional constraint in that it ensures that the background used is not larger than the peak area as such ensures all calculations are within the peak region which was suitable for samples used.

2.4.2.1.1 New Silica sensor

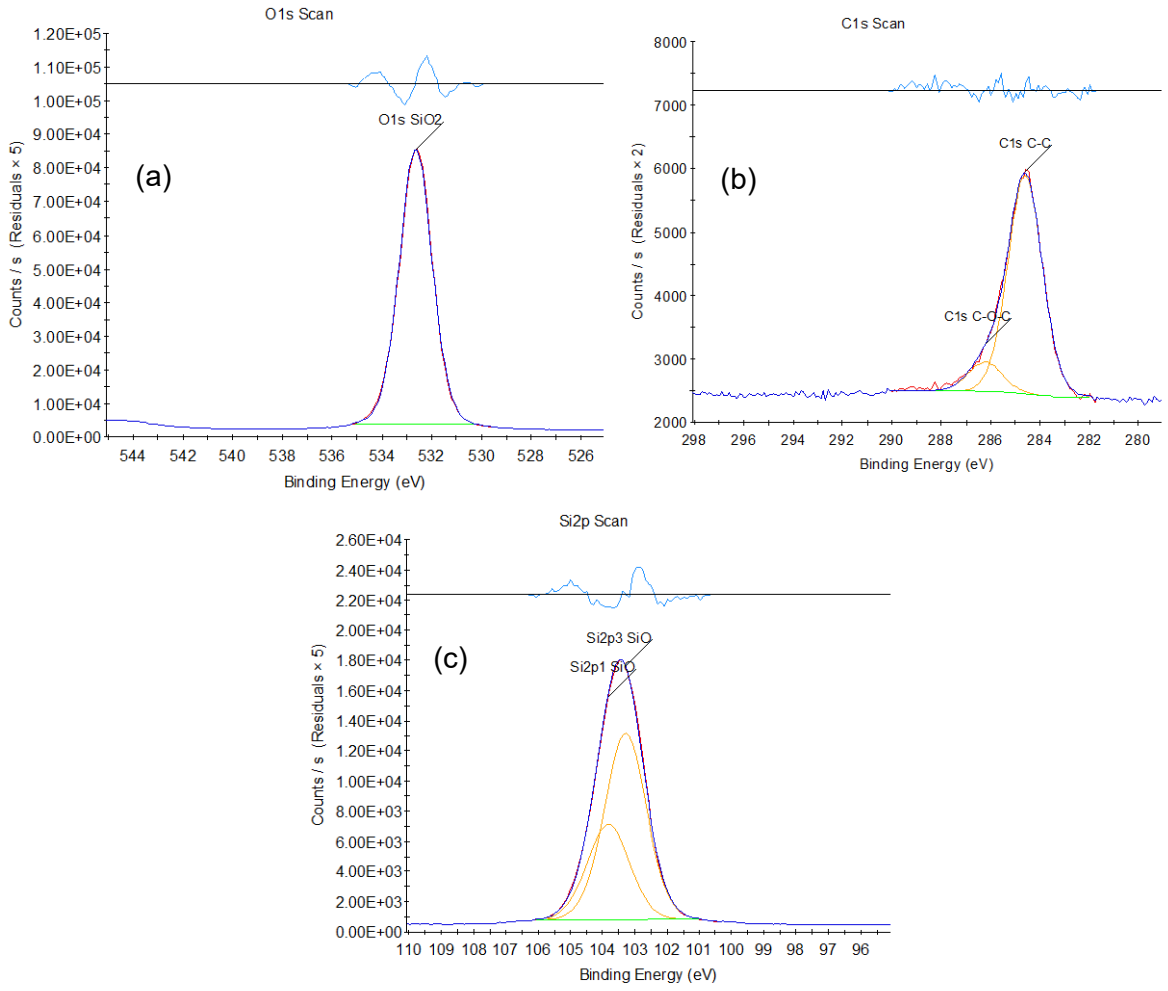


Figure 2.16 Full XPS Spectrum for unused QSX 303 SiO_2 from Qsense (a) O1s (b) C1s and (c) Si2p

Figure 2.16 presents three regions O1s, C1s and Si2p. Following peak fitting on Avantage software, two peaks were found for the Si2p spectra at 103.29 and 103.82 eV. These correspond to SiO (SiO_2) and SiO (SiO_2) respectively. While the O1s spectra had one peak at 532.63 eV which was assigned SiO_2 as shown in Figure 2.16 (a). The C1s spectra also had two peaks at 284.60 and 286.22 eV corresponding to C-C and C-O-C. The presence of the C1s spectra showed the presence of naturally occurring silanols on the silicon dioxide sensor which might have been introduced when rinsing the sensor with DI water before QCMD experiments.

2.4.2.1.2 XPS spectra for Palmitic acid adsorption on SiO2

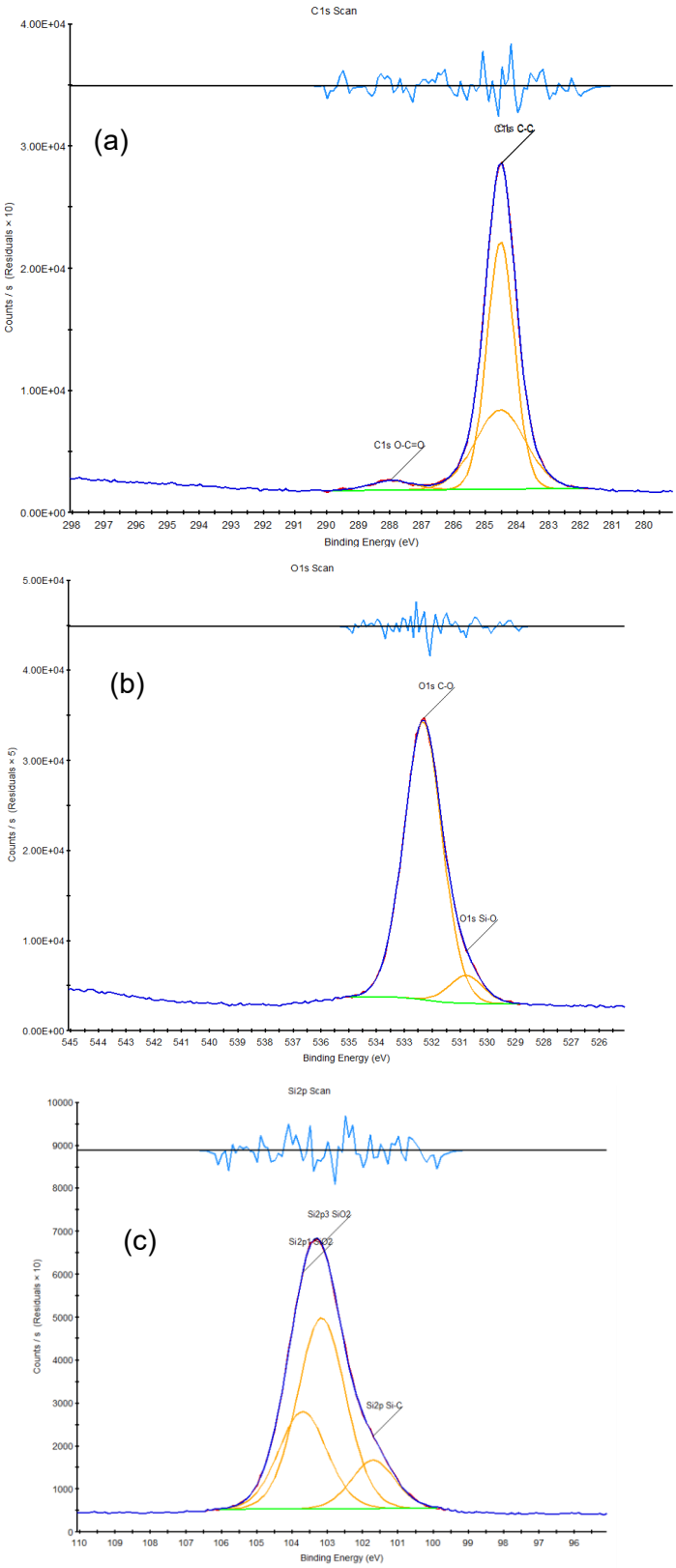


Figure 2.17 XPS Spectra following palmitic acid adsorption onto SiO_2 sensor (a) C1s (b) O1s (c) Si2p

Elemental scans after palmitic acid experiments are as shown in Figure 2.17. Si2p has three peaks which suggest palmitic acid adsorbed onto SiO_2. The most pronounced difference was the appearance of a third peak observed for the Si2p spectra with the Si peak bound to a carbon atom at 101.69eV. The O1s spectra also had two peaks showing that a siloxane bond formed (530.78eV) from a condensation reaction with the one oxygen atom lost. The other peak shows that the oxygen atom was bonded to the carbon atom of the palmitic acid at 532.33eV. The appearance of the acid group COOH at 288eV for the C1s spectra suggest the chemisorption of palmitic acid onto the surface. Earlier in Table 2.1 the acoustic ratios alone suggested that ΔF was caused purely by viscous effects of the bulk. However, the results from XPS verifying the presence of the acid group confirm that the acoustic ratio alone was not enough to conclude that ΔF was not because of adsorption measured using QCMD on SiO_2. This supports work by Fredrik Pettersson (2022) where they reported that an acoustic ratio of 0.4 does not always mean there is no adsorption. SiO_2 is thus a good adsorbent for palmitic acid. Further studies involving evaluation of the thickness of the adsorbed layer using XPS could be beneficial in extending knowledge on a possible adsorbent for FFA in wastewater. Again, complex systems involving impurities in wastewater using QCMD for SiO_2 sensors remains for further exploration.

2.4.2.2 XPS Spectra of Aluminium oxide after adsorption of palmitic acid.

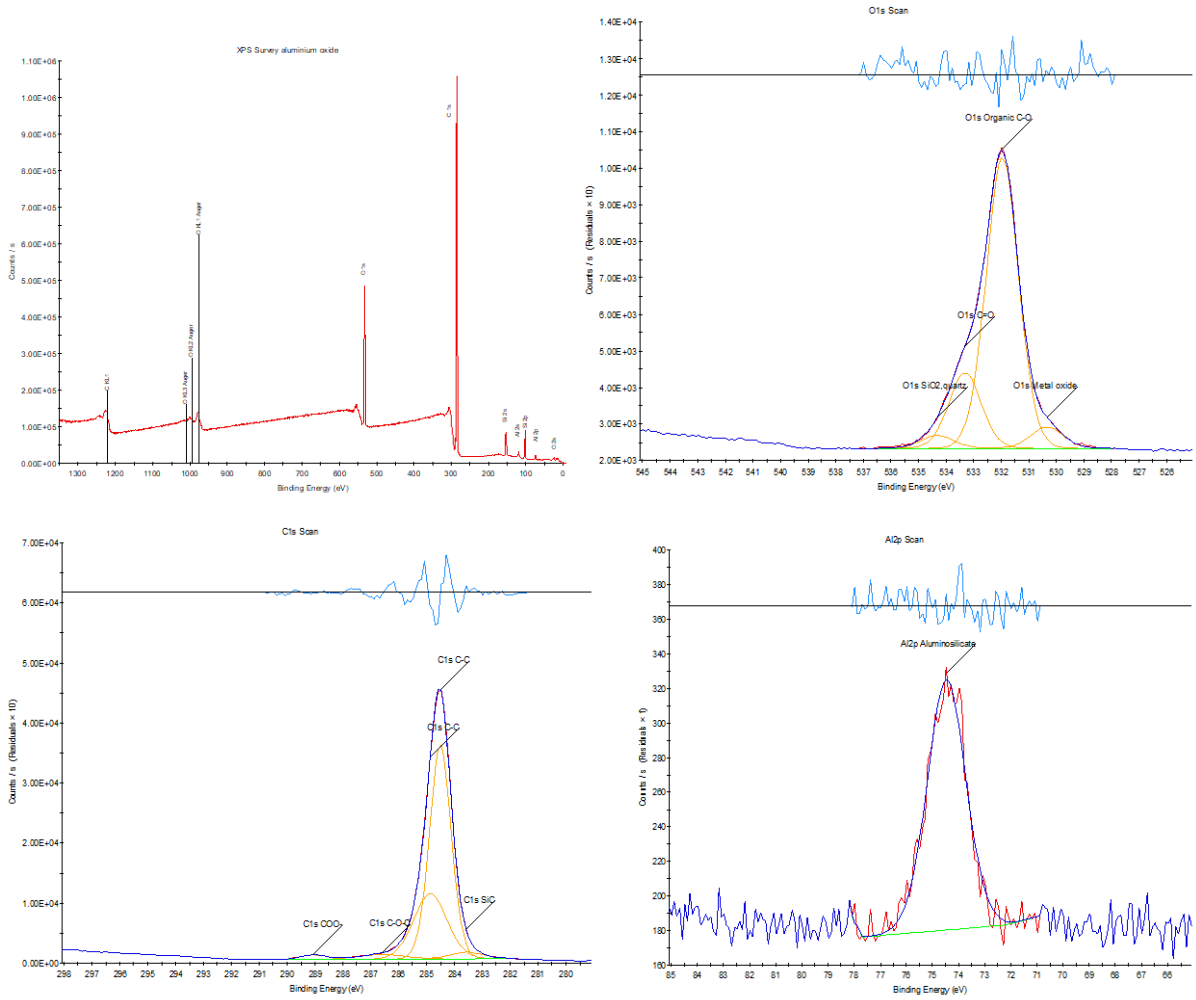


Figure 2.18 Results of aluminium oxide substrate sensor after 125mg/ml palmitic acid has been adsorbed.

Figure 2.18 shows the characterization of aluminium oxide following the adsorption of palmitic acid. The results present four spectra i.e. a survey scan of aluminium oxide, O1s , C1s and Al 2p. The Al2p spectra revealed one peak at 74.46eV which was assigned aluminium silicate. This was not surprising as the QCMD sensors are made of a quartz crystal coated with different materials (Biolin Scientific, 2019). In this case was coated with aluminium oxide. Following monitoring of the O1s region, a slight change in shape of the region accompanied by four peaks were observed at 530.33eV ,531.96eV,533.31eV and 534.31eV (FWHM =1.44eV for all). These were assigned Al-O-Al, C-O, C=O and SiO_2 respectively. (Bournel et al., 1996) reported that the assignment of the O1s peak at 531.90eV corresponded to oxygens in aluminium oxide when studying adsorption of acrylic acid on aluminium. Much more recently, Wang et al. (2024) investigated the assignment of O1s between 531eV and 532eV and reported that a common mistake made in literature was associating this peak with oxygen

vacancies which is not possible as an XPS signal is only generated in the presence of electrons. They suggested that this peak generally arises from adsorbed oxygen species such as hydroxyls onto an oxide surface. Lim et al. (2007) previously studied adsorption of steric acid onto aluminium oxide and assigned the 533.31eV region carboxylate oxygen (Al-O-C). Bournel et al. (1996) assigned it the same but at 533.80eV. Similar results were observed in this work assigning the same region C=O thus confirming the adsorption of palmitic acid onto aluminium oxide. The C1s region had five peaks. Their assignment is in Table 2.9. At 289.07eV, the carboxyl was observed. Similar results were observed by Bournel et al. (1996) at 290.60eV and Lim et al. (2007) at 290eV. The C1s region also supports the that palmitic acid adsorbed onto aluminium oxide during the QCMD experiments.

Table 2.9 XPS Binding energy assignment of C1s

C1s Binding energy (eV)	Assignment
283.58	SiC
284.50	C-C
284.86	C-C
286.61	C-O-C
289.07	COO-

2.4.2.3 XPS spectra of Polystyrene

2.4.2.3.1 NEW/unused surface

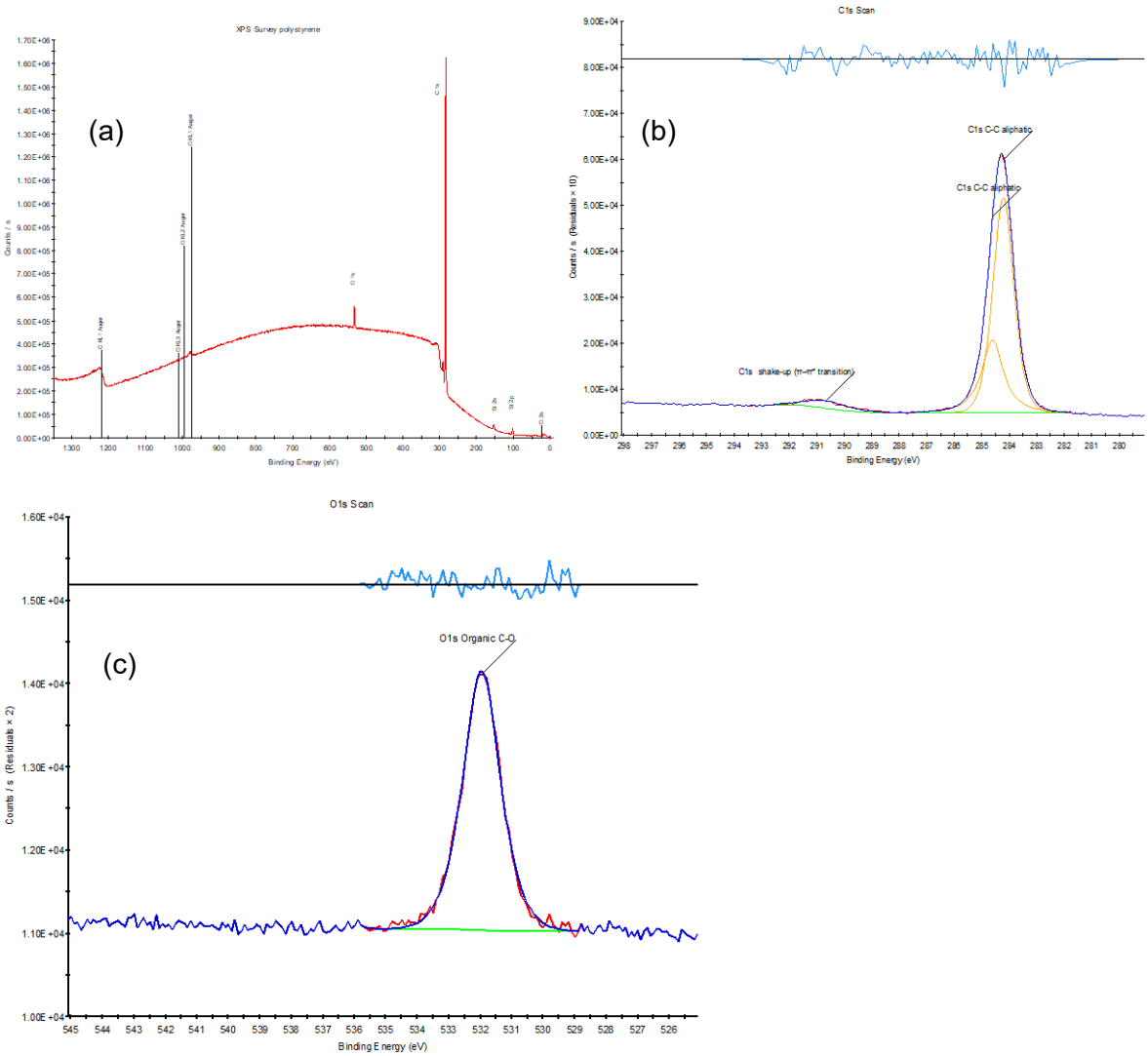


Figure 2.19 XPS Spectra of polystyrene (a) Survey (b) O1s (c) C1s

XPS analysis was performed on a polystyrene sensor as shown in Figure 2.19. Polystyrene is a polymer of styrene and has a benzene ring. By nature, is hydrophobic. A survey scan on the polystyrene coated sensor showed that there was a lot of background noise. However, even with this the key peaks of C1s and O1s were identified and the focus was on these two regions. A scan of the C1s showed that two aliphatic carbon was detected in the range 282.21eV to 286.61eV. The results closely mirror the work by Girardeaux & Pireaux (1996) on their analysis of polystyrene. The slight differences in the binding energy are attributed to the fact that they had used a Shirley background correction whereas the smart background correction was used

in this work. The shake-up satellite (π-π*) at 291.18eV is characteristic of polystyrene because of the aromatic group found in polystyrene (Adam Bushell, Paul Mack,East Grinstead, 2019).

2.4.2.3.2 Used surface.

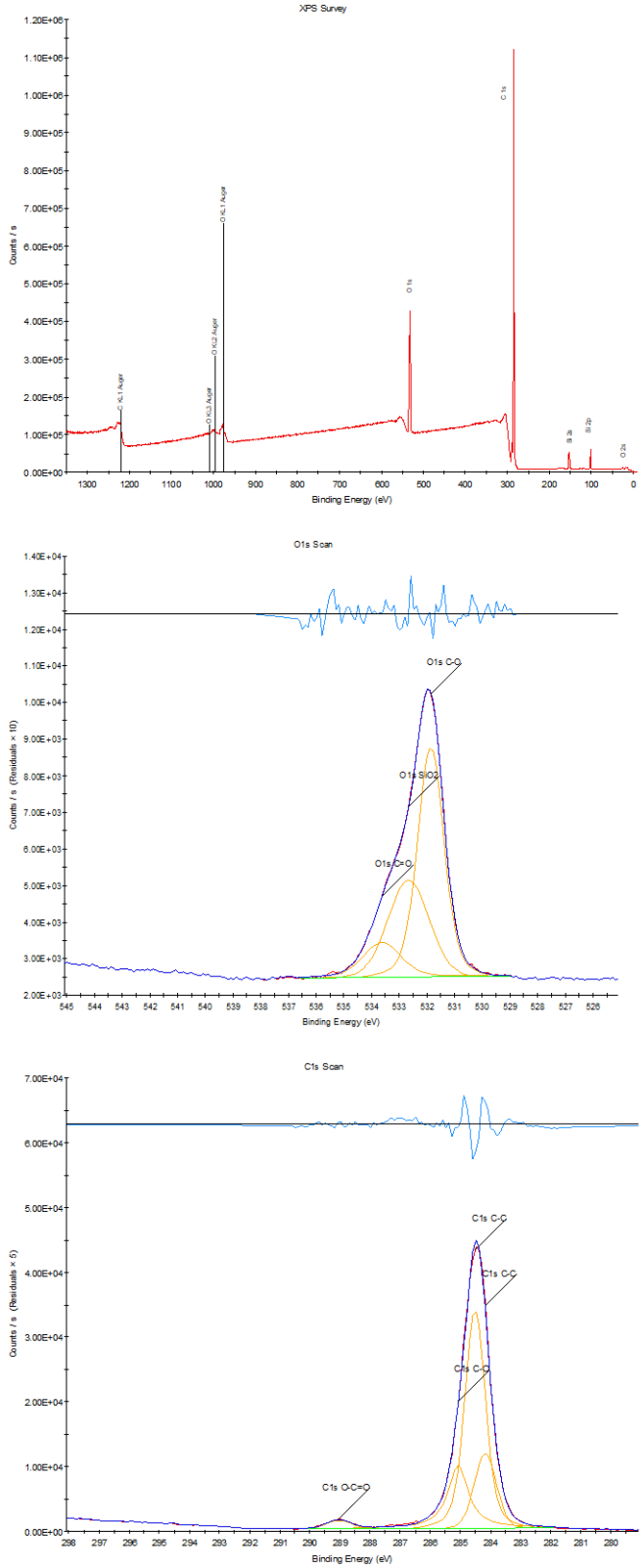


Figure 2.20 shows 125mg/ml palmitic acid ss on polystyrene.

Figure 2.20 shows the difference in the XPS spectra once palmitic acid has adsorbed onto the surface. The most obvious difference observed was the reduction in background noise between 250eV and 1300eV of the survey spectra. On of the challenges of measuring polystyrene via XPS was because of the background noise. Sputtering of the sample to get a better shift only resulted in destruction of the polystyrene surface. However, following palmitic acids adsorption studies with QCMD a more defined survey spectra was observed. Four peaks were observed in the C1s region assigned in Table 2.10. The inelastically scattered electron from the C1s in Figure 2.19 which resulted in the shake up satellite peak at 290.66eV was replaced by the O-C=O carboxyl group at 289eV. There was also the appearance of C-O peak at 285.07eV. Three peaks were observed in the O1s region. Palmitic acid adsorption resulted in the appearance of C-O at 531.85eV and C=O at 533.61eV. Many studies involving polystyrene are limited to its role in microplastics in wastewater (Zheng et al., 2025; Li et al., 2025). The results observed here suggest that polystyrene has the potential to be used as an adsorbate for palmitic acid. Protein (albumin) adsorption studies onto polystyrene have already been done by Browne et al. (2004) where they found that unoxidized polystyrene adsorbed more protein than oxidized polystyrene. This demonstrates the potential of polystyrene as an adsorbent of palmitic acid. Applications of polystyrene in wastewater conditions for palmitic acid adsorption is still an area that needs further research. This work reported here for the first time the adsorption of palmitic acid onto a polystyrene coated quartz sensor.

Table 2.10 XPS Binding energy assignment for polystyrene following palmitic acid adsorption

Binding energy (eV)		Assignment	FWHM (eV)
C1s	284.17	C-Si	0.87
	284.51	C-C	0.81
	285.07	C-O	0.8
	289.03	O-C=O	0.97
O1s	531.85	C-O	1.13
	532.66	SiO_2	1.75
	533.61	C=O	1.61

2.4.2.4 Atomic Percentage

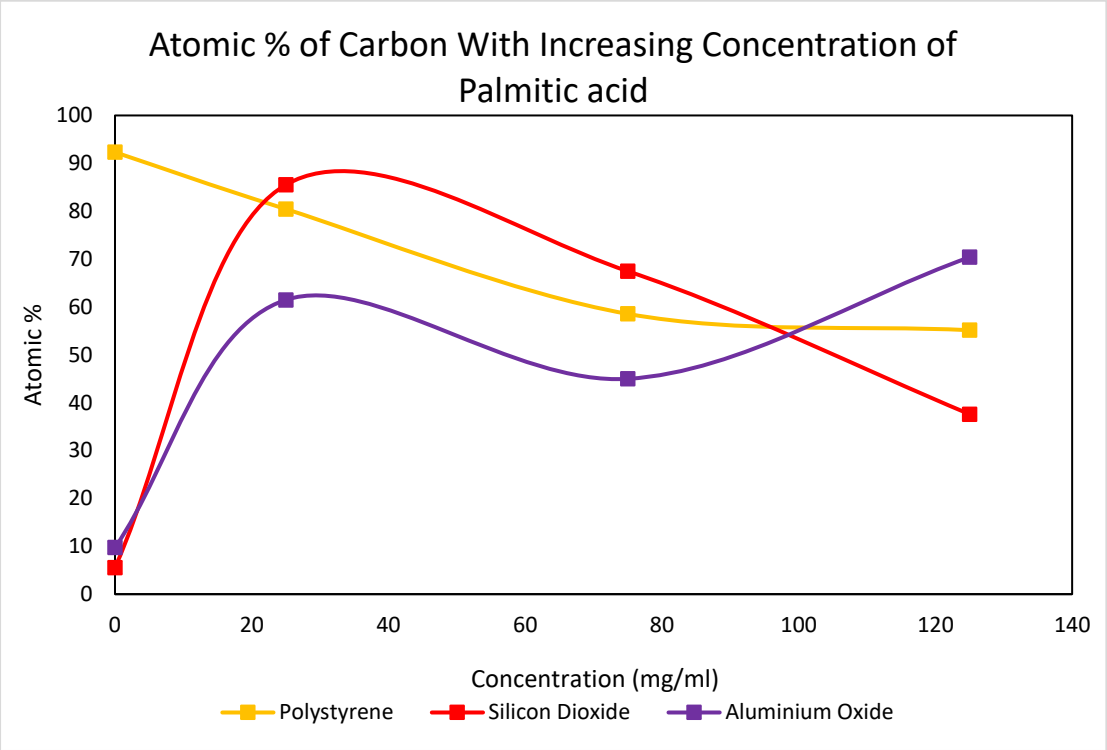


Figure 2.21 Atomic % of C1s on different substrate sensors

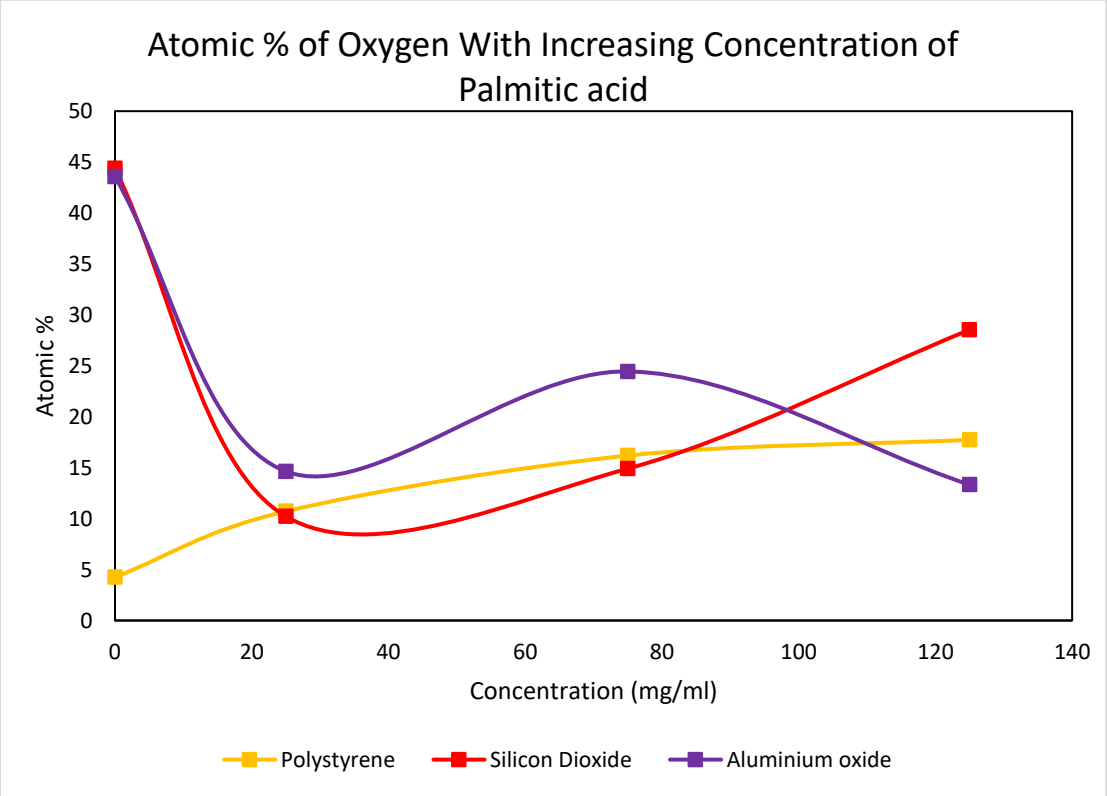


Figure 2.22 Atomic % of O1s on different substrate sensors.

Figure 2.21 and Figure 2.22 show the changes in atomic % of C1s and O1s. The results show that the concentration/ atomic percentage of C1s on polystyrene substrate decreases with increasing concentration of palmitic acid adsorbed while the atomic percentage of O1s increases. The results for aluminium oxide and silicon dioxide fluctuate. For silicon dioxide C1s starts off with an increase and then a steady decrease in atomic % with increasing concentration. The reverse is observed for O1s. The increase in O1s atomic percentage suggests that more palmitic acid is adsorbed as the acid group concentration increases. The trend of the atomic % of C1s and O1s on polystyrene also show to what extent the surface was modified by addition of the palmitic acid. The atomic % on aluminium oxide supports the results from the adsorption isotherm from QCMD in Figure 2.4. At 75mg/ml a high frequency shift was observed suggesting more palmitic acid adsorbed on aluminium oxide. This corresponded with the decrease in atomic % of C1s and an increase in O1s %. At 125mg/ml O1s atomic % decrease while that of C1s increases. Although palmitic acid concentration increased less was adsorbed onto the substrate particularly less than on polystyrene. Silicon dioxide shows at 125mg/ml the highest atomic % for O1s despite having lowest frequency change than the other substrates at the same concentration. This suggest that the Si-O groups on the silicon dioxide were also measured during analysis by XPS hence why the higher oxygen atomic percentage.

2.5 Conclusions

The results from QCMD confirmed the adsorption of palmitic acid while XPS confirmed surface modification before and after the experiments thereby confirming the adsorption of palmitic acid to the surface through identification of the -COOH at 289eV. Krishna & Philip (2022) in their review on XPS suggested that XPS can be used for surface analysis which includes obtaining information on chemical composition (which has been done in this chapter), confirming surface functionalization, presence of adsorbates and in some case determining the thickness of the layer. The application of the PFO and PSO models revealed chemisorption played a crucial role in the adsorption of palmitic acid at room temperature. The equilibrium rate constants for PSO and PFO kinetic models showed that the rate of adsorption was fastest with increasing concentrations for all three surfaces. Both the Sauerbrey and Voight models were applied for mass estimation. The Voight model perfectly described the results from silicon dioxide and aluminium oxide while the experimental results on polystyrene were not a good fit. It remains unclear why palmitic acid adsorption onto polystyrene could not fit the Voight model and therefore is an area for exploration for future research. The adsorption of palmitic acid at different concentrations appeared to follow the Langmuir isotherm for Silicon dioxide and Aluminium oxide thereby suggesting palmitic acid formed a monolayer on the sensor

surface. The chemical adsorption of palmitic acid on the sensors was followed by aggregation which was observed during the experiment. Bere et al. (2025) reported aggregation following the adsorption of undecafluorohexanoic acid on amidine-functionalized polystyrene. However, this phenomenon was observed also on silicon dioxide and aluminium oxide.

Chapter 3 Investigating adsorption Kinetics of Oleic and Linoleic acid using Quartz crystal Microbalance with Dissipation

3.1 Abstract

The PSO equations were used to model experimental results of oleic acid and linoleic acid onto silicon dioxide, aluminium oxide and polystyrene. The correlation coefficient R^2 >0.997 for all surface involved in the adsorption of linoleic acid suggested that chemisorption was the rate limiting step. R^2 > 0.93 for the adsorption of oleic acid also confirmed chemisorption as the rate limiting step. This excluded the adsorption of oleic acid at 25mg/ml where the correlation coefficient was low. The rate constants were able to valuable information about the adsorption of both fatty acids. Characterization of the surfaces revealed the presence of adsorbed fatty acid. The contact angle measurements of polystyrene were 77.7^o ± 2^o after adsorption of the fatty acids. The kinetics data from this work is important in helping to predict the behaviour of the fatty acids that were under study as it could help advance the development of suitable adsorbents for various application including the removal of FFA from wastewater.

3.2 Introduction

Chapter 2 explored the adsorption of saturated fatty acid palmitic acid using QCM which is usually found as part of the constituents in fats and oils in food (Orsavova et al., 2015). However, alongside palmitic acid, unsaturated fatty acids such as oleic and linoleic acid have also been confirmed to form part of the FOG deposits and sewage sludge in wastewater in various studies by (Wang et al., 2008; Grosser et al., 2017; Long et al., 2012). One of the primary contributions to FOG deposits in wastewater is naturally from food waste as determined by Neves et al. (2009) and Zhang et al. (2014). A study by Williams et al. (2012) reported that there was more FOG consumption in developed countries (50 kg/annum) as compared to developing countries (less than 20kg/annum) with this having both an impact on health and the environment. While Lundgren et al. (2006) did explore adsorption of oleic acid and linoleic acid from alkane solutions using QCMD, the investigation was limited to just stainless steel. This work to extends this study by investigating their adsorption on three new surfaces i.e. silicon dioxide , polystyrene and aluminium oxide for potential applications in wastewater. While their study involved adsorption from 2,2,4,4,6,8,8-heptamethylnonane, ethanol was used in this work to keep the solvent used the same as for investigations done in the previous chapter.

The purpose of this work was to extend the investigation done in the previous chapter to unsaturated fatty acids. However, this was restricted to oleic acid and linoleic acid. Better understanding of the interaction of the unsaturated fatty acids with different materials may help in controlling the formation of FOG deposits and their recovery thereby reducing their contribution to FOG in wastewater. Increased knowledge of this may also influence behavioural change particularly in food waste and waste cooking oil disposal.

Oleic acid is a straight chain fatty acid with one cis double bond whereas linoleic acid has two cis double bonds as shown in Figure 3.1. The Prescence of two double bonds in linoleic acid means it is not as straight as oleic acid hence tends to have bends (Kanicky & Shah, 2002). Apart from the obvious difference of degree of unsaturation, the adsorption of these fatty acids was also investigated at different concentrations. The results were then modelled using pseudo second order equations to determine adsorption capacity at equilibrium of the fatty acids onto the substrate sensors. X-ray photoelectron spectroscopy was used to confirm the adsorption of the fatty acids onto the substrates. Information of atomic percentages and fit of the atoms of interest e.g. C1s can be found in the appendix 8.1. To the best of my knowledge, the adsorption of oleic and linoleic acid from ethanol using QCMD with the application of PSO and PFO models is reported here for the first time.

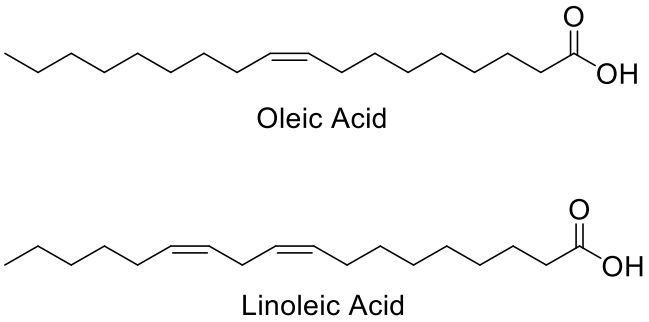


Figure 3.1 structure of oleic acid and linoleic acid

3.2.1 Materials and Methods

3.2.1.1 Characterization of unsaturated fatty acids

See section 2.3 for detailed methodology on QCM and XPS. All fatty acids were dissolved in absolute ethanol (99%) to make the stock solution of different concentrations. All QCM experiments were repeated twice under the same conditions. Figure 3.4 shows the substrates under analysis using Xray photoelectron spectroscopy captured during some of the measurements. The stock solutions were made using oleic acid ≥99% (GC) CAS: 112-80-1 and linoleic acid ≥99% CAS:60-33-3. Both fatty acids where from Merck Chemicals Limited,

Millipore (UK) Limited. A 10ml ±1 volumetric cylinder was used for measuring out the volume of ethanol. The mass of the fatty acids was measured using an analytical balance. The Ramé-hart 590 goniometer/tensiometer was used to conduct static water contact angle measurements to study the wettability of polystyrene following adsorption by fatty acids. The experiment was conducted at room temperature. The method used was as previously reported by Chen et al. (2021) with a slight difference. Two hundred measurements were taken in 20 seconds. Surface chemistry was determined using the K-Alpha XPS spectrometer as previously reported in section 2.4.2

3.2.1.2 Pseudo second order kinetics

To model experimental data, the pseudo second order equation was applied. The form of the pseudo second order equation written in *Equation 3.1* by Ho & Mckay (1999) is well known. However upon integrating and application of the boundary conditions (t=0 to t=t and q_t=0 to q_t=q_t, Ho & Mckay (1999); Revellame et al. (2020) the non-linear form results in Equation 3.2 which is rearranged to the linear form in Equation 3.3 (Revellame et al., 2020; Canzano et al., 2012; Azizian, 2004).

$$\frac{dq_t}{dt} = k_2[q_e - q_t]^2$$

Equation3.1

$$q_t = \frac{{q_e}^2 k_2 t}{1 + q_e k_2 t}$$

Equation3.2

$$\frac{t}{q_t} = \left(\frac{1}{q_e}\right) t + \frac{1}{k_2 {q_e}^2}$$

Equation3.3

The linear equation shows q_t (ng/cm^2) which is the areal mass density adsorbed at time t , q_e (ng/cm^2) areal mass density at equilibrium , t (seconds) is time and k_2 is the pseudo second order rate constant. The slope of t/q_t was used to calculate q_e and k_2 from the line of best fit (Huang et al., 2018; Kumar, 2006). Given a straight-line equation y=mx+ c, q_e was determined by m^{-1} and the rate constant k_2 by $\frac{m^2}{c}$ (Revellame et al., 2020; Robati, 2013).

3.2.1.3 Mass estimation of adsorbed fatty acids

The Voight model was used to estimate the mass adsorbed as ∆D>0 and there was there was a spread across all harmonics (Easley et al., 2022). These two conditions justified the use of the Voight model. This was discussed earlier in section 2.4.1.1 when discussing mass changes for palmitic acid adsorption. Three overtones were used to model the data at the 3rd,5th and 7th overtone to improve accuracy (Schönwälder et al., 2014).

Voight mass is given by :

$$\Delta m = \rho_f \times h_f$$

Equation 3.4

Where $\Delta m\ is\ change\ in\ mass$,$\rho_f\ is\ density\ of\ film$, $h_f\ is\ film\ thickness$

(Setiowati et al., 2021)

$$\frac{\Delta f}{n} = -\frac{1}{2\pi\rho_o h_o}\left\{\frac{\eta_3}{\delta_3} + h_f\rho_f\omega - 2hf\left(\frac{\eta_3}{\delta_3}\right)^2\frac{\eta_f\omega^2}{{\mu_f}^2 + \omega^2{\eta_f}^2}\right\}$$

Equation 3.5

$$\Delta D = \frac{1}{\pi f\rho_o h_o}\left\{\frac{\eta_3}{\delta_3} + 2hf\left(\frac{\eta_3}{\delta_3}\right)^2\frac{\eta_f\omega}{{\mu_f}^2 + \omega^2{\eta_f}^2}\right\}$$

Equation 3.6

Where $\frac{\Delta f}{n}$ was the normalised frequency change at a specific overtone n, ρ_o and h_o were the density and thickness of the quartz sensor. The viscosity of the bulk liquid was given by η_3 while η_f and μ_f were the viscosity and shear elasticity of the film. The viscous penetration of the bulk liquid was given by $\delta_3 = \sqrt{\frac{2\eta_3}{\rho_3\omega}}$ where ω was the angular frequency of the oscillation. Lastly ∆D was the dissipation change and Δf the frequency change of a 4.95 MHz quartz sensor.

(Setiowati et al., 2021 ; Voinova et al., 1999)

3.2.1.4 Statistical Analysis

Normality testing was done using the Kolmogrov-Smirnov on OriginPro 2026 for all k_2 values for linoleic acid. Hypothesis testing was performed using two sample t-tests were a probability of $P < 0.05$ meant the null hypothesis was rejected. The null hypothesis was that there was no difference between the k_2 values. A probability of $P < 0.05$ was considered significantly different (Yang et al., 2024). In addition to this, a correlation coefficient R^2 analysis was performed to assess how well the model (PSO) fit experimental data. For $R^2 \approx 0$, there was no correlation, R^2 closer to +1 or -1 showed that there was a strong relationship between the model and the experimental data (Ahmed et al., 2025).

3.2.2 Results and Discussion

Frequency changes were investigated to determine the impact of increasing concentration of unsaturated FFA onto different substrate sensors. Oleic and linoleic acid are investigated in this chapter. Oleic acid has a cis double bond at position 9 along the carbon chain while linoleic acid has two cis double bonds at positions 9 and 12 along the carbon chain (Kanicky & Shah, 2002). Both fatty acids have the same chain length (C_{18}). Apart from the increase in concentration, another factor that was determined was whether the degree of unsaturation of the fatty acids at the same concentration affected adsorption.

3.2.2.1 QCM-D

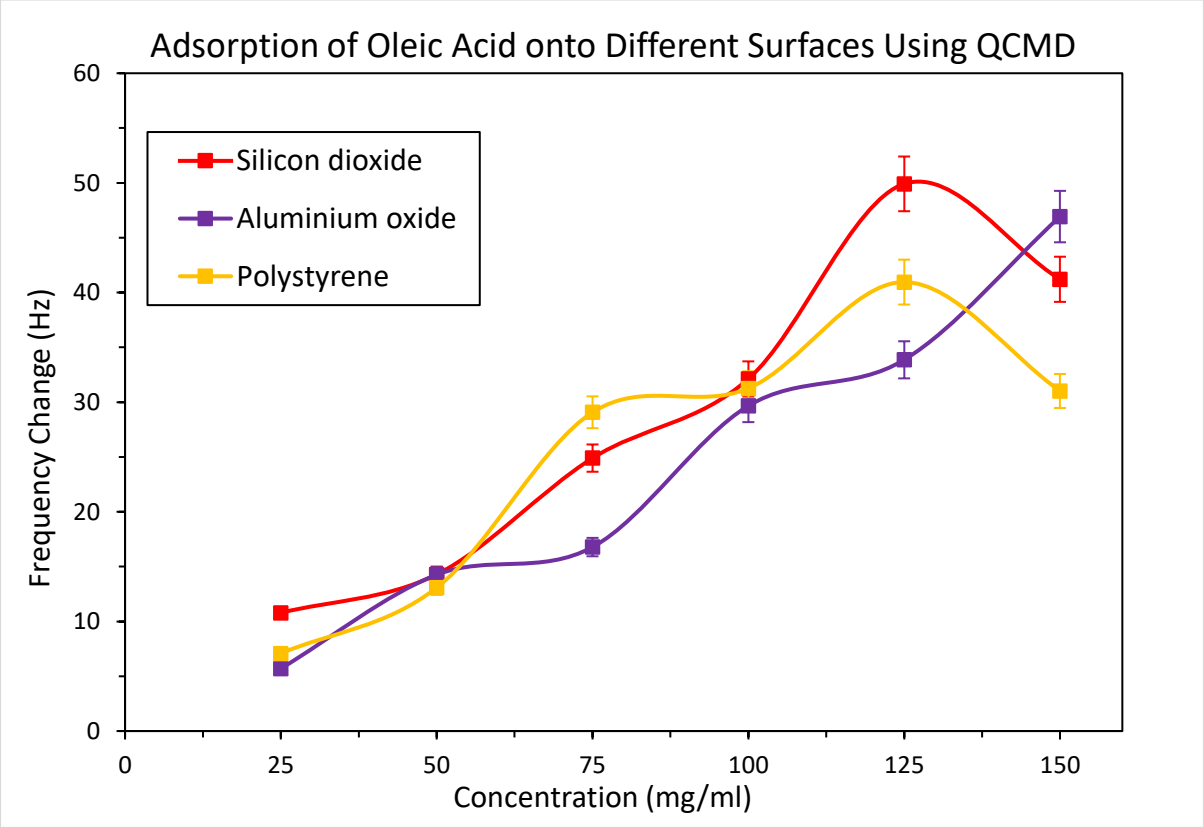


Figure 3.2 shows adsorption isotherm of oleic acid adsorbing onto different substrate sensors.

Adsorption isotherms in Figure 3.2 and Figure 3.3 show that increasing concentration of fatty acids results in increasing change in frequency. The results suggest that as the number of fatty acid particles available at the interface between the substrate sensor and the bulk solution increases, hence increased interaction with the substrate, the amount adsorbed also increases. This is registered by the overall change in frequency recorded by the resonator.

Looking at each individual substrate material, at the lowest concentration (25mg/ml), in the case of oleic acid as shown in Figure 3.2, silicon dioxide is the most favourable substrate sensor followed by polystyrene and lastly aluminium oxide. The same results were observed at 100mg/ml and 125mg/ml. The results also suggest that for aluminium oxide substrate sensor , there is a linear relationship between the amount adsorbed onto the sensor and the concentration of oleic acid and linoleic within the tested range of 25mg/ml to 150mg/ml (Figure 3.3). The results suggest the same is true for silicon dioxide and polystyrene substrate sensors up until 125mg/ml. Beyond this concentration the frequency reduces with increased concentration (also shown in Figure 3.3 for linoleic acid). The reduction in frequency change of silicon dioxide and polystyrene show that beyond 125mg/ml, the substrate sensor is saturated from adsorption of either oleic or linoleic fatty acid. The reduced frequency change suggests that diffusion effects influence the reduction in frequency change as more of the fatty acid diffuses back into the bulk solution from the interface. Another factor might be because the quartz resonator senses hydrated mass, the rearrangement of the solvent trapped in between the fatty acid molecules and the fatty acid molecules adsorbed results in less solvent trapped in the adsorbed layer thus reducing the overall stress on the sensor thus the reduction in frequency change. Figure 3.3 also highlights that on average, linoleic acid adsorbed more onto the different substrate sensors than oleic acid, suggesting that more fatty acids are adsorbed with increasing unsaturation. Mass estimation using Equation 3.4 was used as qt for the PSO model.

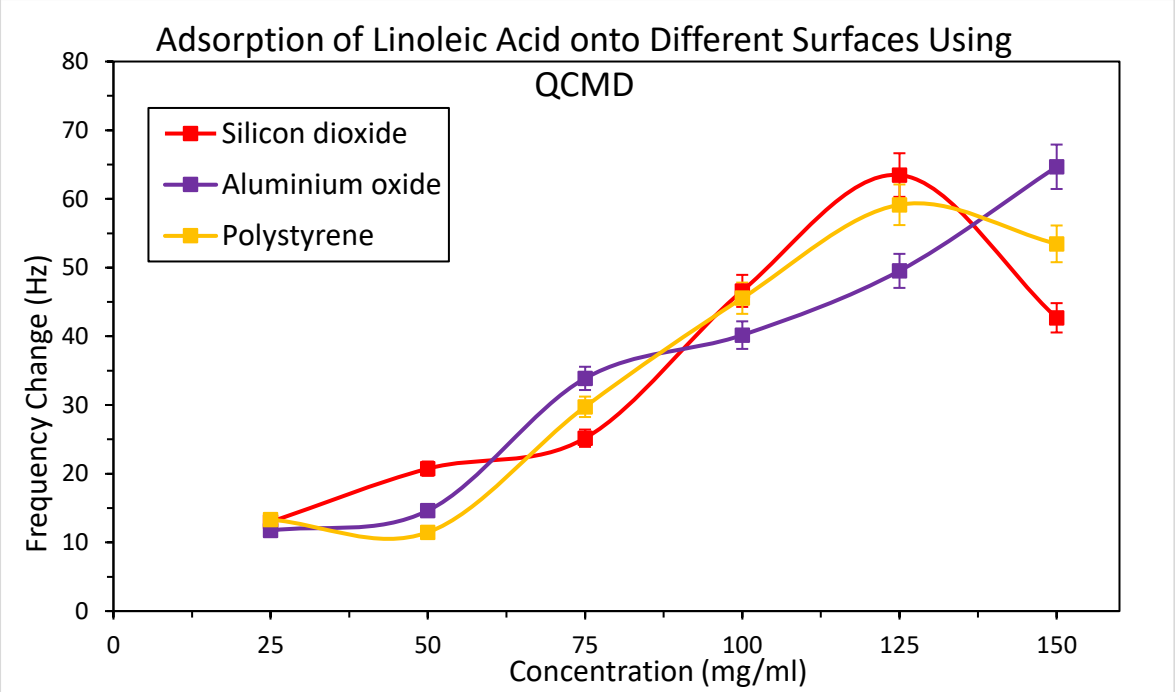


Figure 3.3 shows adsorption isotherm of linoleic acid adsorbing onto different substrate sensors.

3.2.2.1.1 Kinetics of Linoleic Acid Adsorption

Adsorbate and solvent density have been assumed to be similar thus Sauerbrey equation was used to determine q_t (Setiowati et al., 2021). The linear version of the pseudo second order equation was used to plot t/q_t on the Y-axis against time on the X-axis. Nonlinear regression modelling was applied directly to experimental data to estimate the values q_e, k_2 and R^2 (Huang et al., 2018). Nonlinear regression modelling has been highly recommended for adsorption data (Zhang, 2019). Six different concentrations were plotted for each material as shown in Figure 3.4 for Aluminium oxide , Figure 3.5 for Silicon Dioxide and lastly Figure 3.6 for Polystyrene. Table 3.1 presents the values of R^2. The correlation coefficient, R^2 was > 0.97 at all concentrations indicating that the pseudo second order equation was a good fit for experimental data obtained through QCMD experiments for contact times of 250 seconds. This meant that the PSO model was suitable for predicting the kinetics of linoleic acid on the tested materials. Ho & Mckay (1999) reported that a correlation coefficient > 0.996 for PSO equations suggested that the rate limiting might be chemical adsorption. For linoleic acid this meant that electrons were transferred or shared between the carboxylic acid group -COOH and polystyrene or Si-O-Si for silicon dioxide. Ionic bonding would dominate between the carboxylic acid group and Al-O of aluminium oxide.

Table 3.1 R^2 values for different plots of t/q_t vs time for pseudo second order equation for Linoleic Acid.

Adsorbent	Concentration (mg/ml)	25	50	75	100	125	150
Al_2O_3	R^2	0.9977	0.9747	0.9951	0.9974	0.9942	0.9975
SiO_2	R^2	0.9965	0.9975	0.9976	0.9979	0.9986	0.9999
Polystyrene	R^2	0.9980	0.9867	0.9774	0.9961	0.9981	0.9964

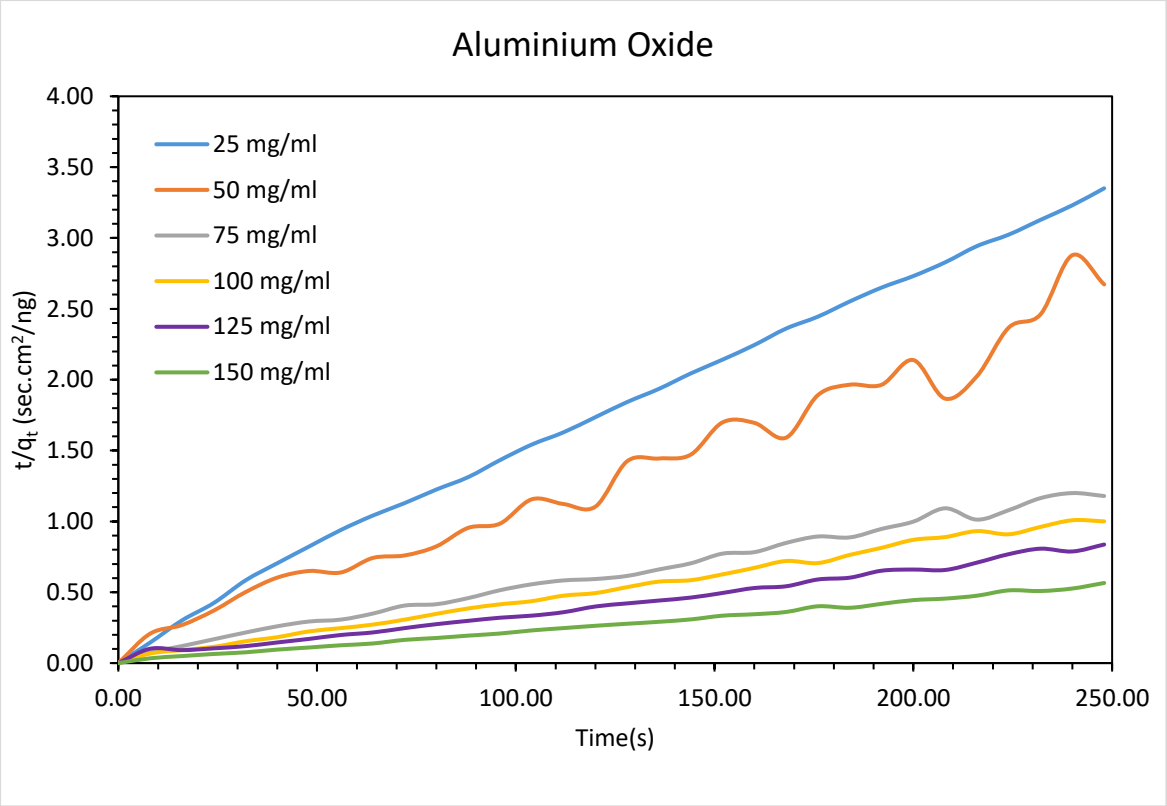


Figure 3.4 Pseudo-second-order adsorption kinetics of linoleic acid onto Aluminium Oxide at different initial concentrations.

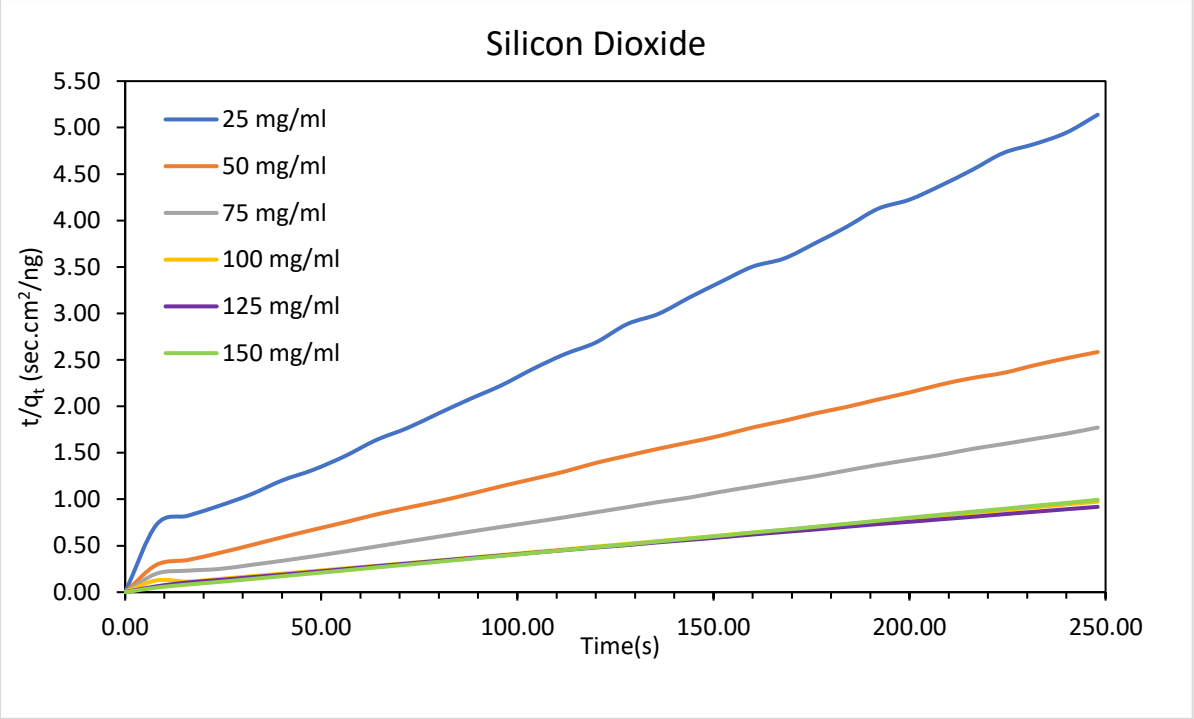


Figure 3.5 Pseudo-second-order adsorption kinetics of linoleic acid onto Silicon Dioxide at different initial concentrations.

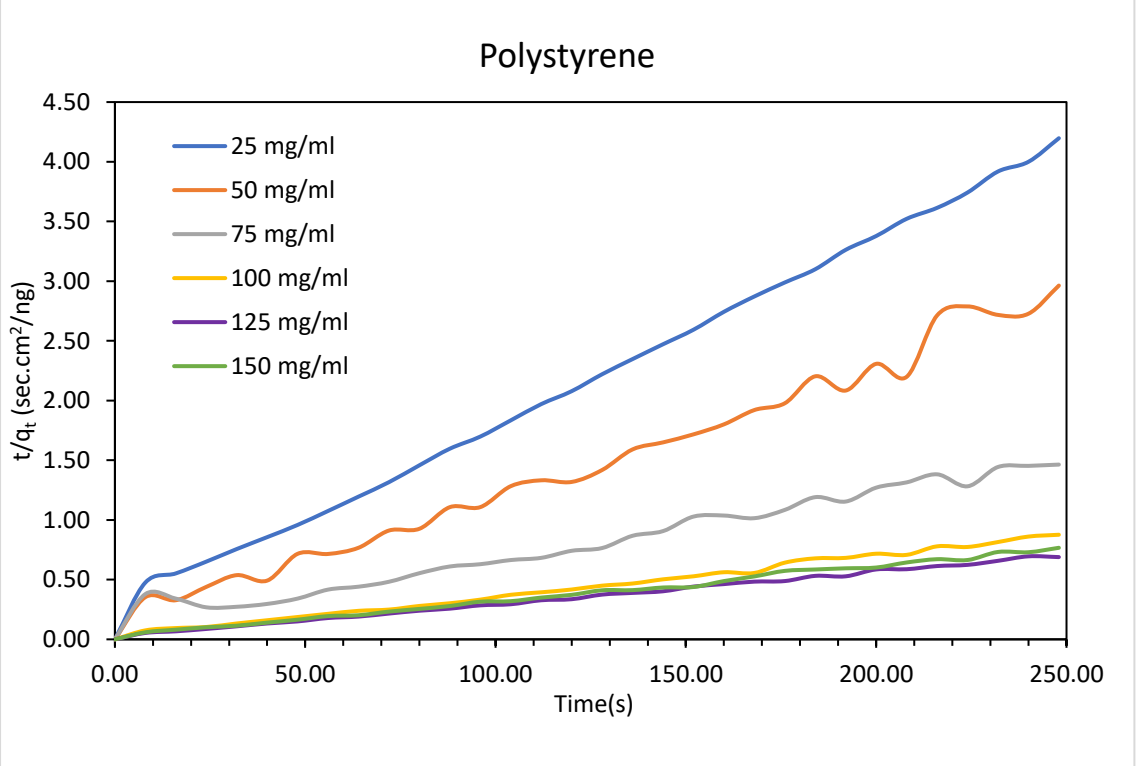


Figure 3.6 Pseudo-second-order kinetics of Linoleic acid on Polystyrene at various initial concentrations.

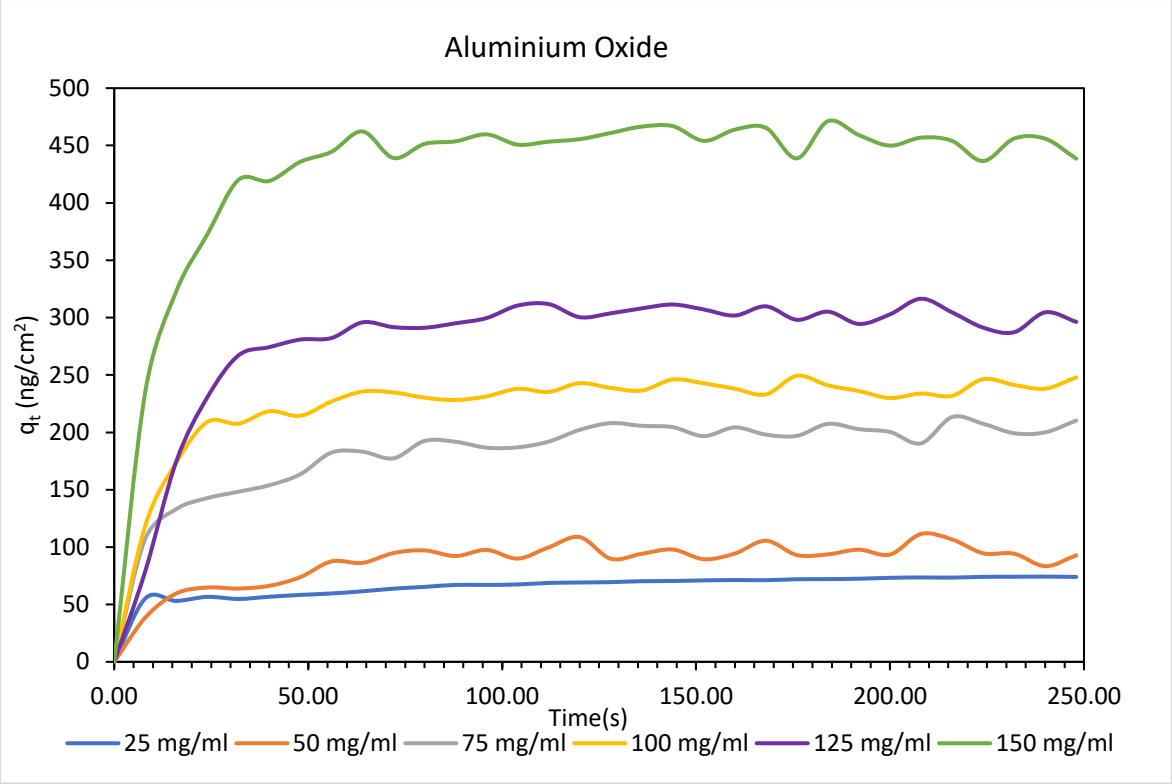


Figure 3.7 Plot of the adsorption capacity versus time for the effect of concentration on the adsorption kinetics of Linoleic acid onto Aluminum Oxide.

Figure 3.7, Figure 3.8 and Figure 3.9 presents the adsorption capacity of linoleic acid at q_t = t until q_t=q_e for all the three substrates. Figure 3.7 showed that linoleic acid reached adsorption equilibrium faster at 25mg/ml and 75mg/ml initial concentrations. Equilibrium was reached with 8 seconds at 25mg/ml and 16 seconds at 75mg/ml. It took 24 seconds to reach equilibrium at 50mg/ml. The time required to reach equilibrium increased with increasing concentration. This suggests that linoleic acid at these initial concentrations had a higher affinity for aluminium oxide. The equilibrium time here was the time at which the fluctuations in q_t started. Tran (2023) reported that the initial region before the plateau gives useful information the adsorption rate and the rate constant.

Linoleic acid was also adsorbed in larger quantities on aluminium oxide at higher initial concentrations. This highlights the importance of initial concentration of linoleic acid for adsorption onto aluminium oxide. Lundgren et al. (2006) had reported that linoleic acid never reached a plateau i.e. equilibrium in the concentration range between 0 and 1.2 weight percent. However, the linoleic acid did reach equilibrium in the concentration ranges here where the smallest concentration by weight percent (3.1%) was much higher than the highest concentration they tested. Another reason for this might be that aluminium oxide was a better

adsorbent for linoleic acid than steel. However, it is not possible to conclude this as testing with their concentration range was outside the scope of this work.

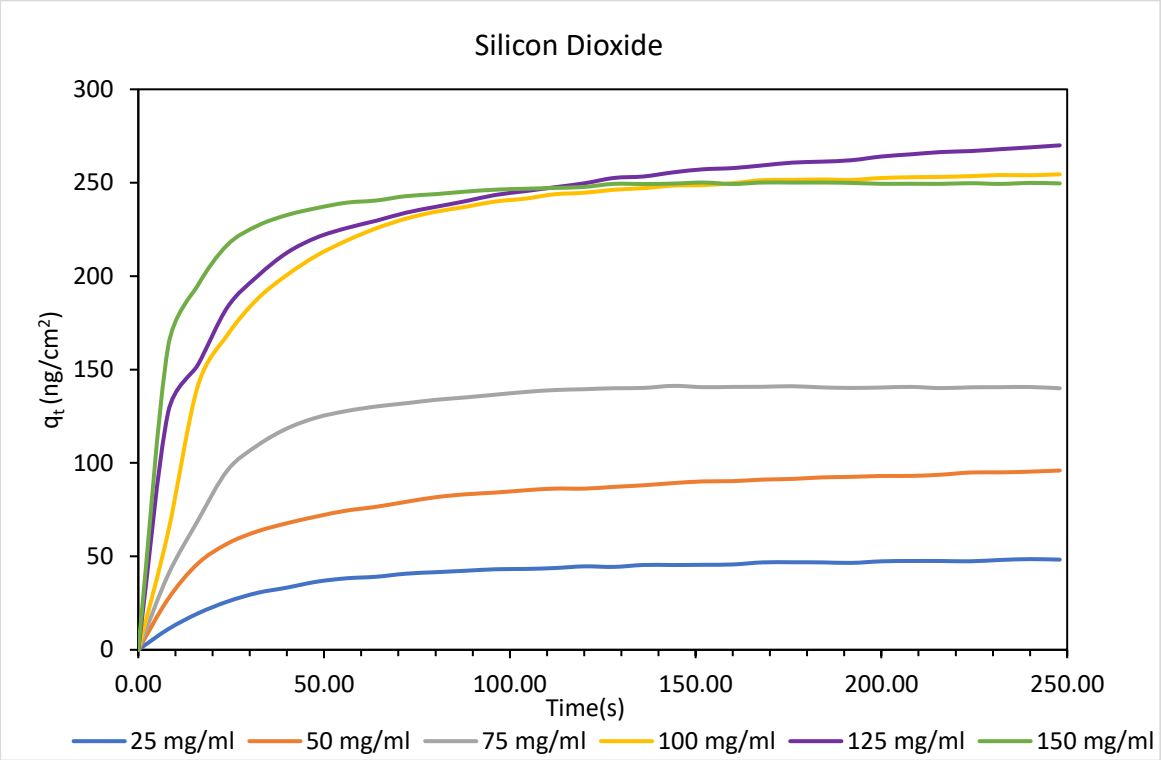


Figure 3.8 Plot of the adsorption capacity versus time for effect of concentration on the adsorption kinetics of linoleic acid onto Silicon dioxide.

Fast kinetics were observed for adsorption of linoleic acid onto silicon dioxide within the first 10 seconds were the rate of adsorption increased with the concentration of linoleic acid. Much slower kinetics were observed at low concentrations e.g. it took. Linoleic acid reached adsorption equilibrium with q_e values decreasing in the order 150mg/ml > 75m/ml > 25mg/ml> 50mg/ml> 100mg/ml. The results showed that at 125mg/ml, linoleic acid never reached equilibrium. Dissipation data from QCMD showed a positive shift followed by a gradual negative shift at 125mg/ml. Lundgren et al. (2006) already mentioned that linoleic acid adsorbs in an extended state thereby coupling solvent, however, the continued negative shift in the dissipation and positive shift in the frequency until the experiment was terminated after 2 hours suggested that linoleic acid was desorbing from the surface. The fluctuations at equilibrium highlight possible conformation changes in the adsorbed monolayer. Linoleic acid tends to extend perpendicular to the surface thereby coupling more solvent. Another possible explanation for this is that linoleic acid was reordering on the surface as equilibrium, this was recorded as fluctuations in frequency and dissipation change by the QCMD.

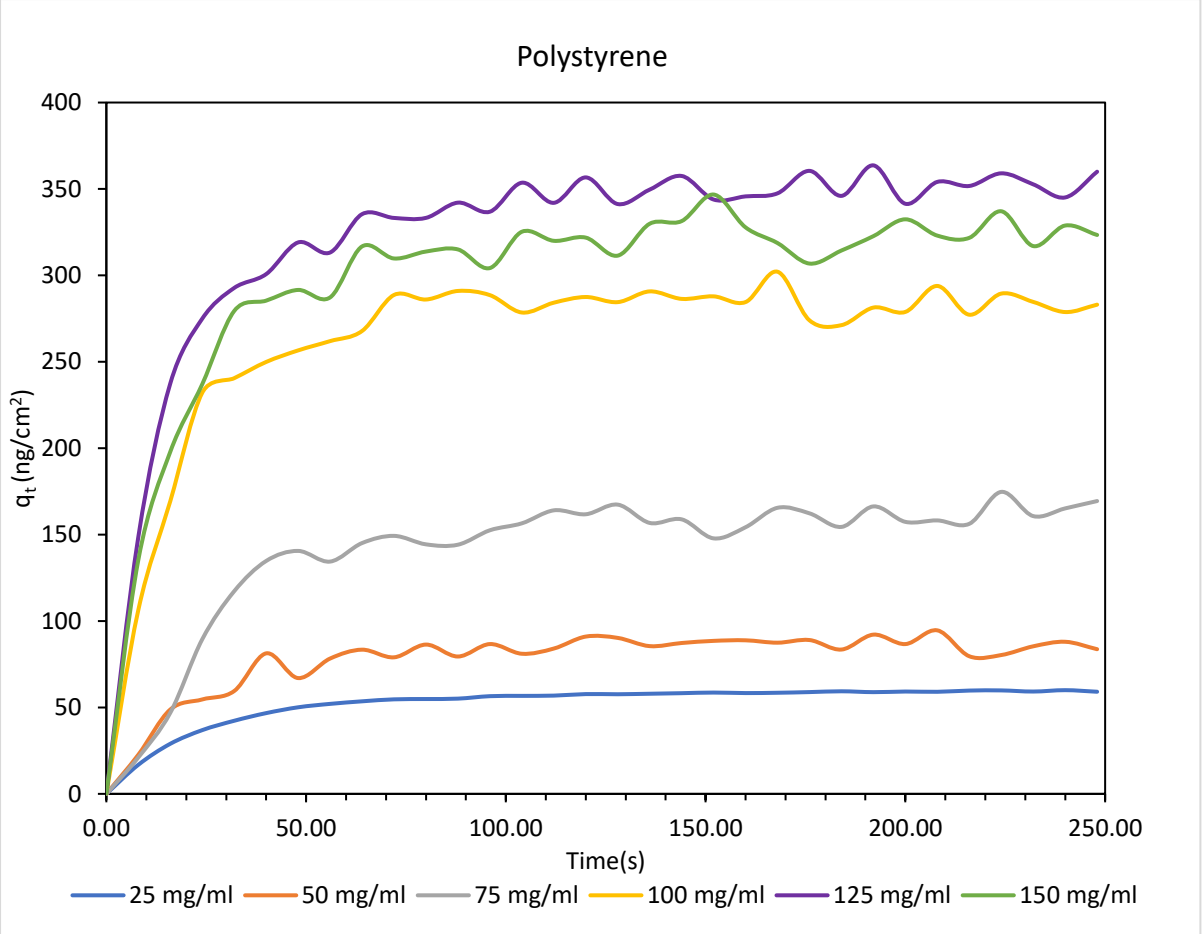


Figure 3.9 Plot of the adsorption capacity versus time for effect of concentration on the adsorption kinetics of linoleic acid onto Polystyrene.

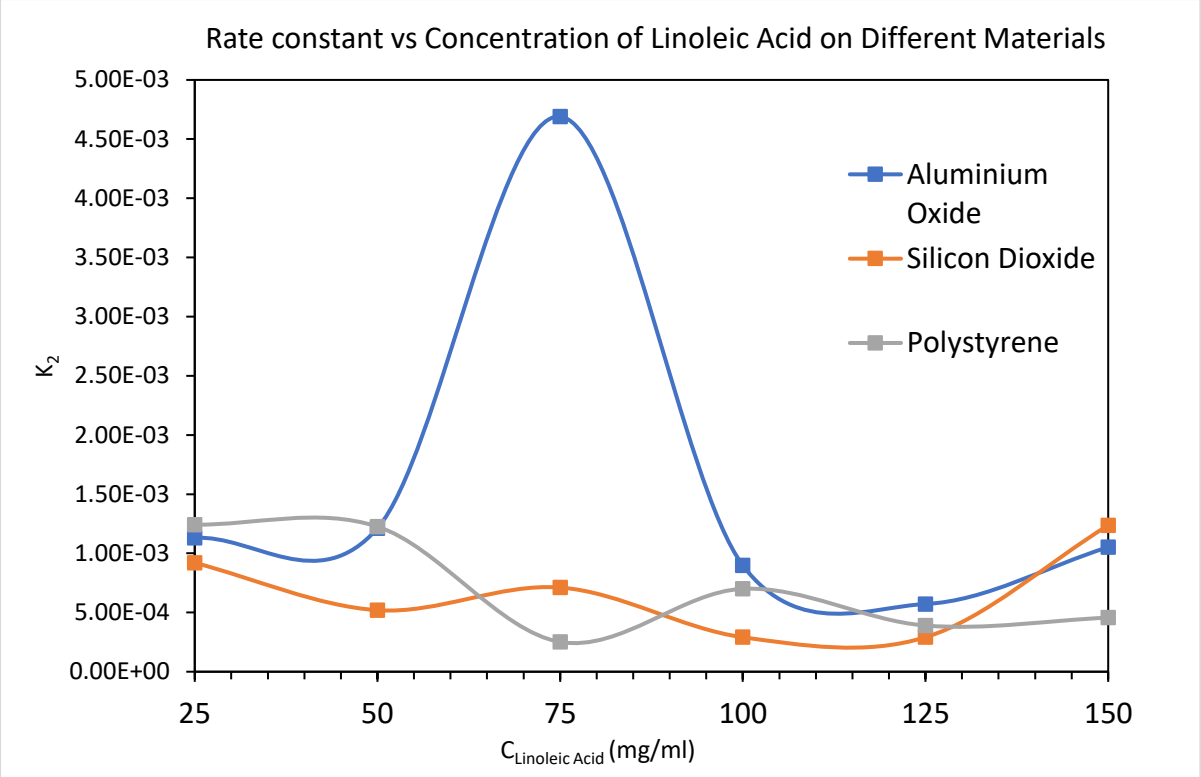


Figure 3.10 Pseudo second order rate constant of linoleic acid adsorption at different concentrations.

Figure 3.10 reports the rate constants k_2 determined for the linear plots t/q_t vs t for linoleic acid at different concentrations. k_2 represents how quickly linoleic acid was adsorbed onto the three surfaces as the adsorption progressed to equilibrium. The results show that the smaller the value of k_2, the faster it took for linoleic acid to reach equilibrium. The rate constants were important as they provided insight into the adsorption of linoleic acid. The overall rate of adsorption fluctuated as the concentration increased for polystyrene and silicon dioxide. The lowest rate of adsorption was also recorded at 75mg/ml for linoleic acid onto aluminium oxide. The rate of adsorption at 50mg/ml was similar for both silicon dioxide and aluminium oxide.

P-values for normality testing were > 0.15 for k_2 values for all materials. Therefore, the normality assumption could not be rejected. Two sample t-tests revealed that there was no significant difference between the mean of k_2 values on all materials. However, Figure 3.10 indicates that at 75mg/ml Aluminium oxide exhibits a higher k_2 value. The number of samples were less than 30 for each data set therefore the validity of the t-test relied on the assumption of normality.

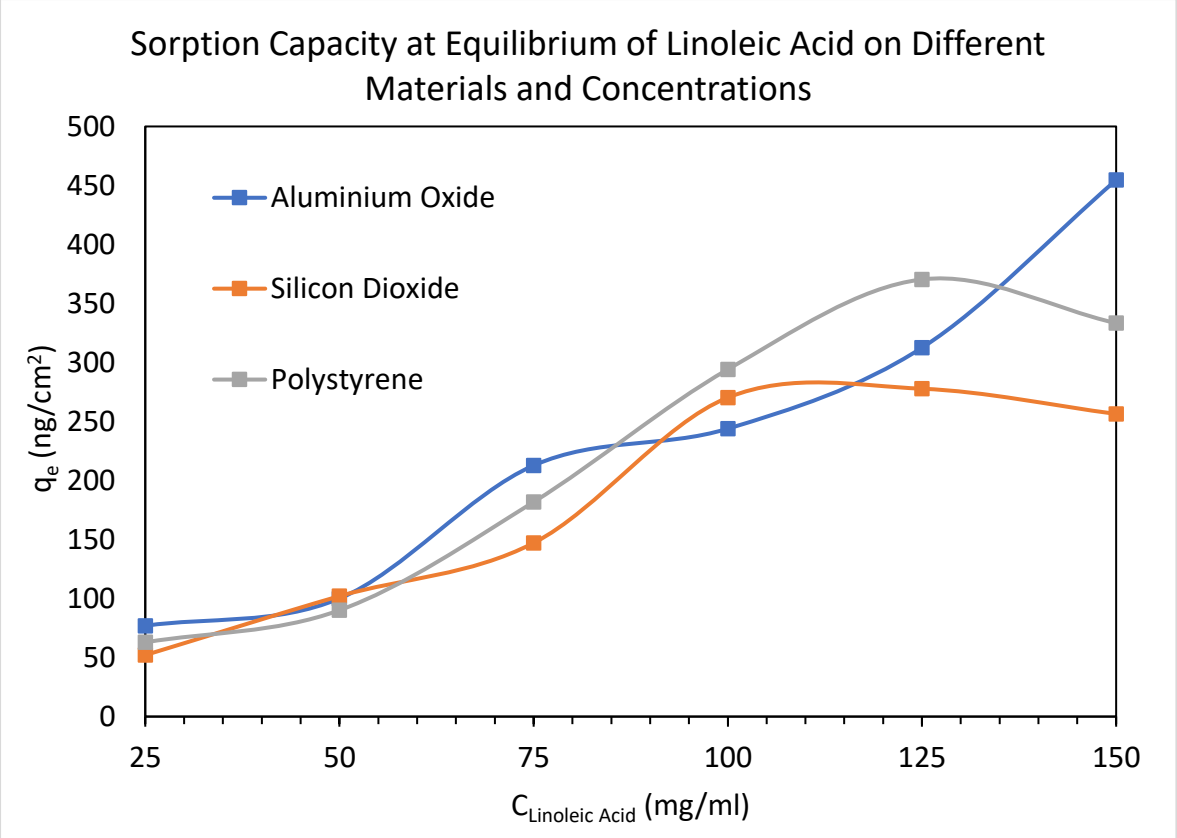


Figure 3.11 shows plot of the areal mass density at equilibrium versus concentration for the adsorption kinetics of linoleic acid onto Polystyrene, Aluminium oxide, and Silicon Dioxide.

Figure 3.11 shows the adsorption capacity /areal mass density of linoleic acid of the different substrate sensors at different concentrations. Below 75mg/ml, the data suggests that aluminium oxide is the better substate having overall a higher adsorption capacity than silicon dioxide and polystyrene. The performance of silicon dioxide was competitive to aluminium oxide at 50mg/ml as shown by the overlap in Figure 3.11. At 100mg/ml and 125mg/ml, polystyrene is a better adsorbent shown by the higher adsorption capacity in this range. Silicon dioxide was a better adsorbent than aluminium oxide only at 100mg/ml. At 150mg/ml, aluminium oxide has the best adsorption capacity followed by polystyrene and lastly silicon dioxide. The results also suggest that multilayer adsorption occurs for aluminium oxide as it never reaches a plateau within the concentration range tested as compared to silicon dioxide and polystyrene. The graphs of polystyrene and silicon dioxide also start to slightly decrease suggesting desorption of linoleic acid from the surface with the dip occurring much faster on the polystyrene substrate. Based off this, the results suggest that the maximum adsorption capacity of linoleic acid on polystyrene is approximately 333.33 ng/cm^2 while it is much lower for silicon dioxide at 227.78 ng/cm^2. Two sample t-test revealed there was no significant difference in the mean of q_e for linoleic acid adsorption onto the surface.

3.2.2.1.2 Kinetics of Oleic Acid adsorption

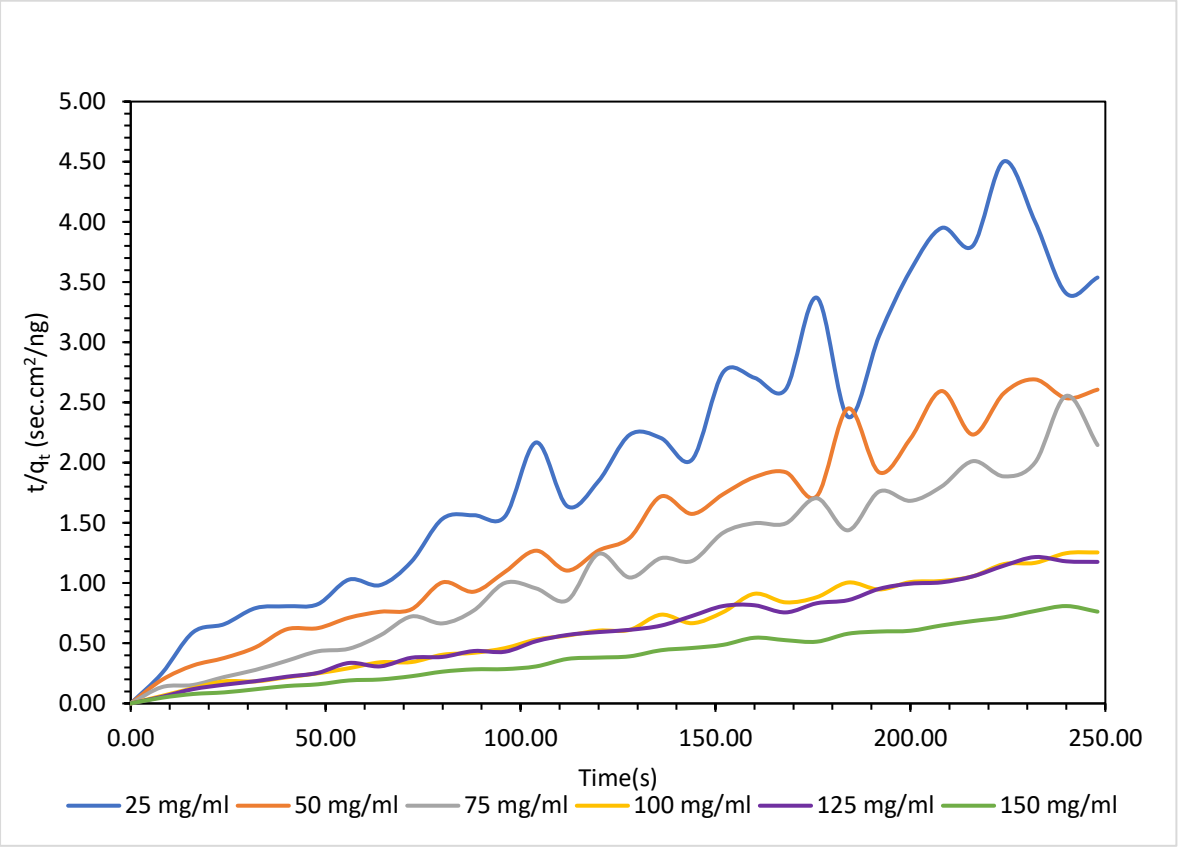


Figure 3.12 Adsorption kinetics (PSO) of Oleic acid on Aluminium Oxide at different concentrations from experimental data.

Figure 3.12, Figure 3.14 and Figure 3.16 show the application of the pseudo second order equation t/q_t onto the experimental adsorption data of oleic acid onto the substrate sensors aluminium oxide, silicon dioxide and polystyrene. The data fit shows linear profiles all concentrations however more fluctuation in the data is observed compared to adsorption of linoleic acid onto the same substrates. Concentrations of 25mg/ml, 50mg/ml and 75mg/ml all show the most fluctuations in the model fit for all substrates. Despite the fluctuations, the PSO model can be used to explain the results due to a high correlation coefficient R^2. However, the data from the plot of polystyrene for 25mg/ml was excluded as it did not fit the pseudo second order equation well with an R^2 of 0.0011 and q_e of 43.29ng/cm^2 and k_2 constant of 0.000372 sec^{-1}. Figure 3.12 showed that at 100mg/ml and 125mg/ml the data fit is similar shown by the overlap of the plots for all concentrations. However, Figure 3.14 shows that the difference is the model fit is not that different for silicon dioxide at 125mg/ml and 150mg/ml.

Apart from the model fit of concentration of 25mg/ml on polystyrene, most of the data has a good fit with R^2 values above 0.9358. Table 3.2 also suggests that R^2 increases with increasing

concentration and Figure 3.18 supports this by showing that higher areal mass density/ adsorption capacity has better model fits. Figure 3.19 shows that 75mg/ml has the highest rate constant when oleic acid was adsorbed onto aluminium oxide which is consistent with the results obtained for linoleic acid adsorption onto the same substrate sensor. However, overall, in the case of oleic acid adsorption, silicon dioxide appears to be a better adsorbate although based on the rate constant k_2 the performance of all substrates is very similar although second after silicon dioxide aluminium oxide has a better performance.

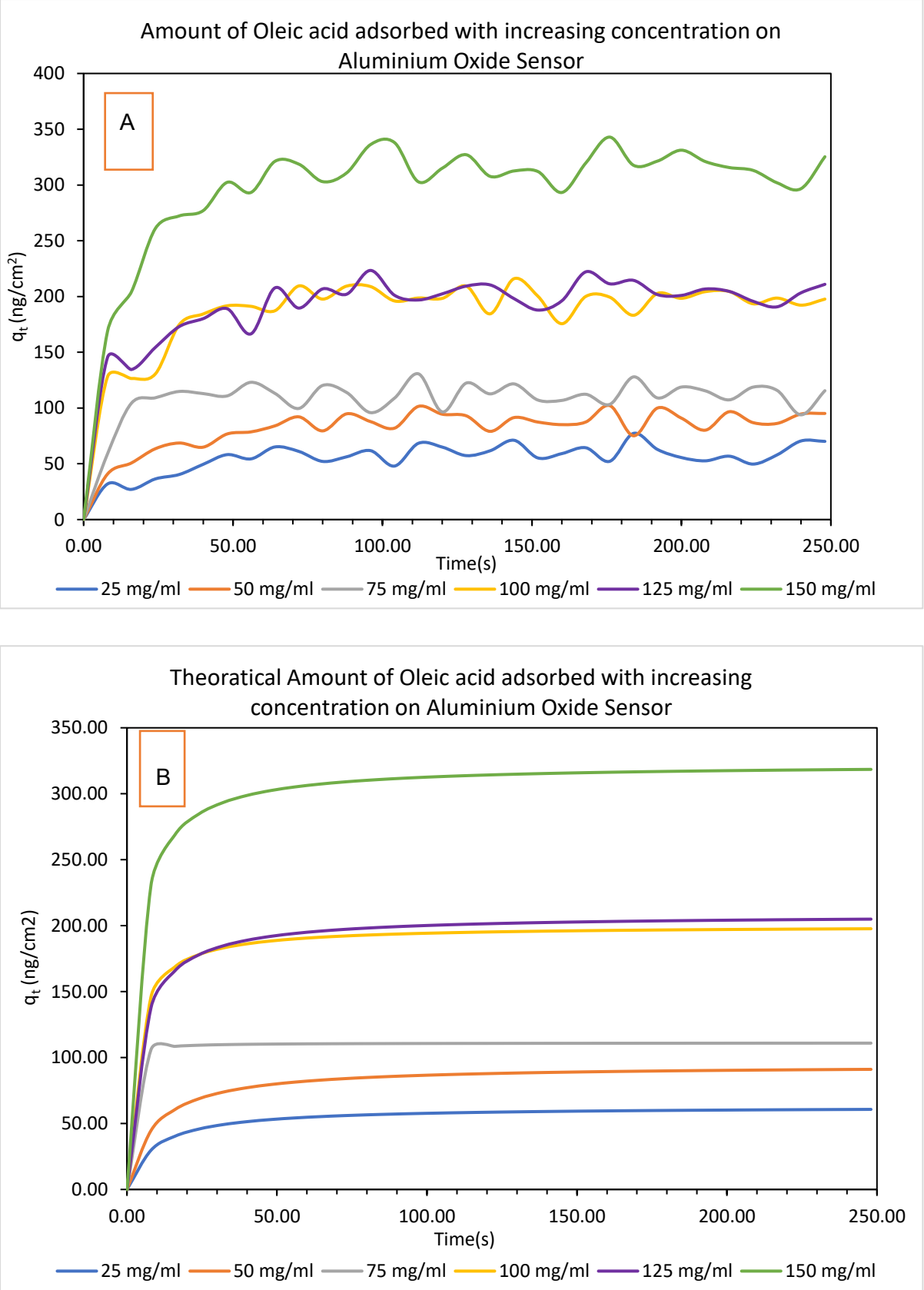


Figure 3.13 Adsorption capacity versus time for effect of concentration on the adsorption kinetics of Oleic acid onto Aluminium oxide (A) Experimental (B) Theoretical.

Figure 3.13, Figure 3.15 and Figure 3.17 (A) show experimental data plots of q_t the areal mass density/ adsorption capacity of oleic acid onto the three substrate sensors. The plots shows that q_t increases with time. When $q_t = q_e$, a lot of fluctuations are observed for the model fit on all the substrate sensors. This differs from linoleic acid particularly for adsorption onto silicon dioxide sensor where the graphs were smooth for all concentrations for the same time.

Figure 3.13, Figure 3.15 and Figure 3.17 (B) show the theoretical plots of q_t versus time. Theoretical values of q_t were calculated using Equation 3.2, the non-linear pseudo second order equation and by using the values obtained from k_2 and R^2 from the linear pseudo second order Equation 3.3. The graphs suggests that the difference between the theoretical and experimental data for q_t is very small despite the experimental data showing much more fluctuations than the theoretical data which is smooth. Figure 3.18 also highlights that increasing concentration on oleic acid increases the amount adsorbed thereby suggesting that multi-layer adsorption of oleic acid occurs on the different substrates. Lundgren et al. (2007) found similar results when investigating effect of concentration on adsorption of oleic acid from alkane solutions onto stainless steel surfaces. Aluminium oxide shows that increasing concentration beyond 125mg/ml results in more adsorption while Silicon dioxide and Polystyrene show a decrease in the amount adsorbed at equilibrium as concentration surpasses 125mg/ml suggesting that desorption from the surface is triggered as the sensors have reached capacity for adsorption.

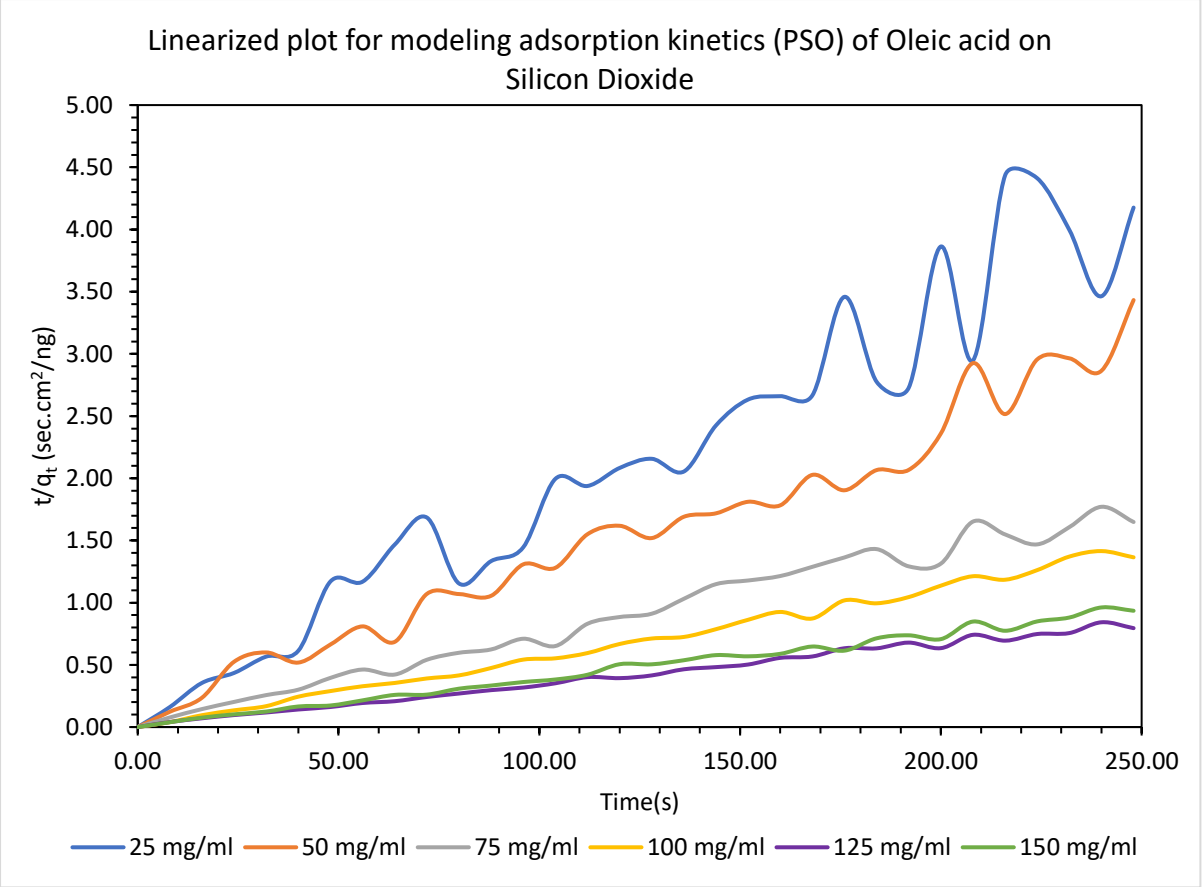
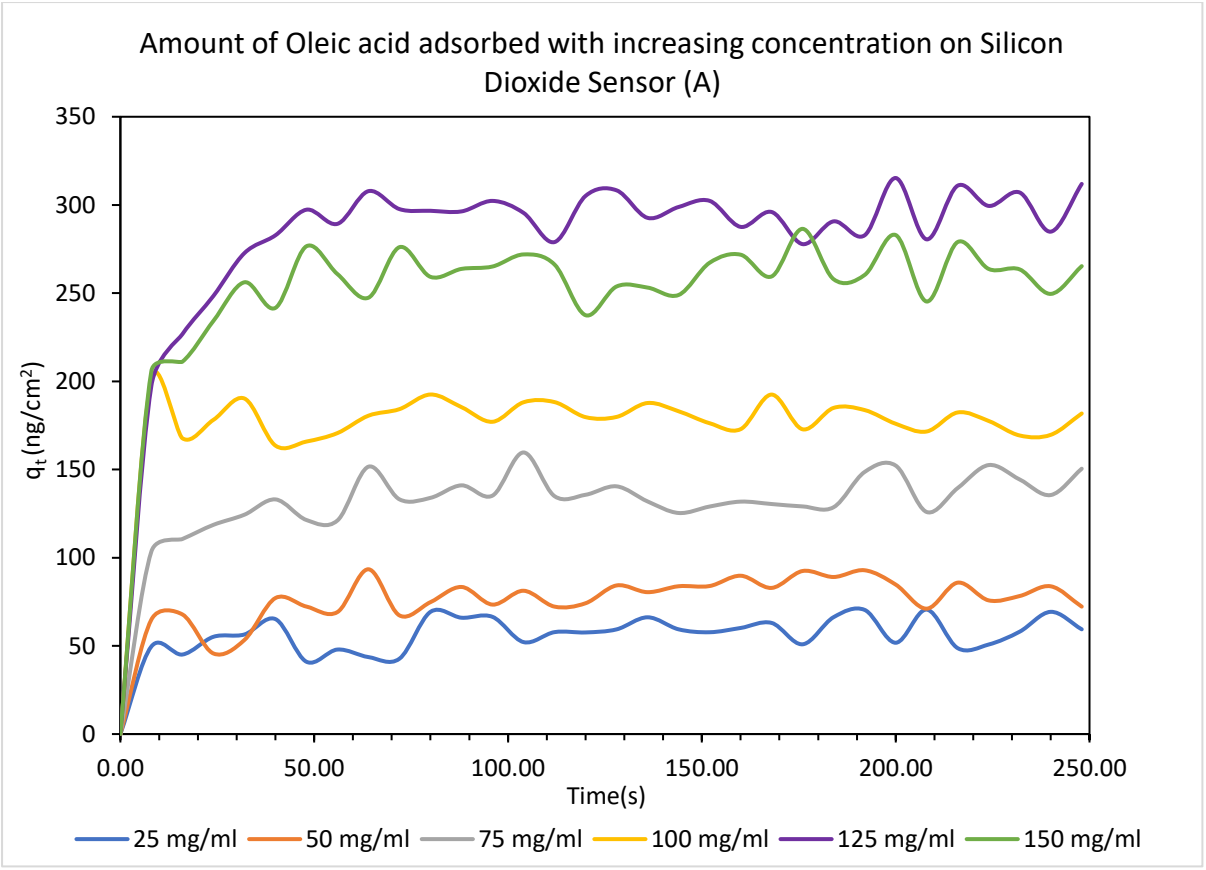


Figure 3.14 Adsorption kinetics (PSO) of Oleic acid on Silicon Dioxide.



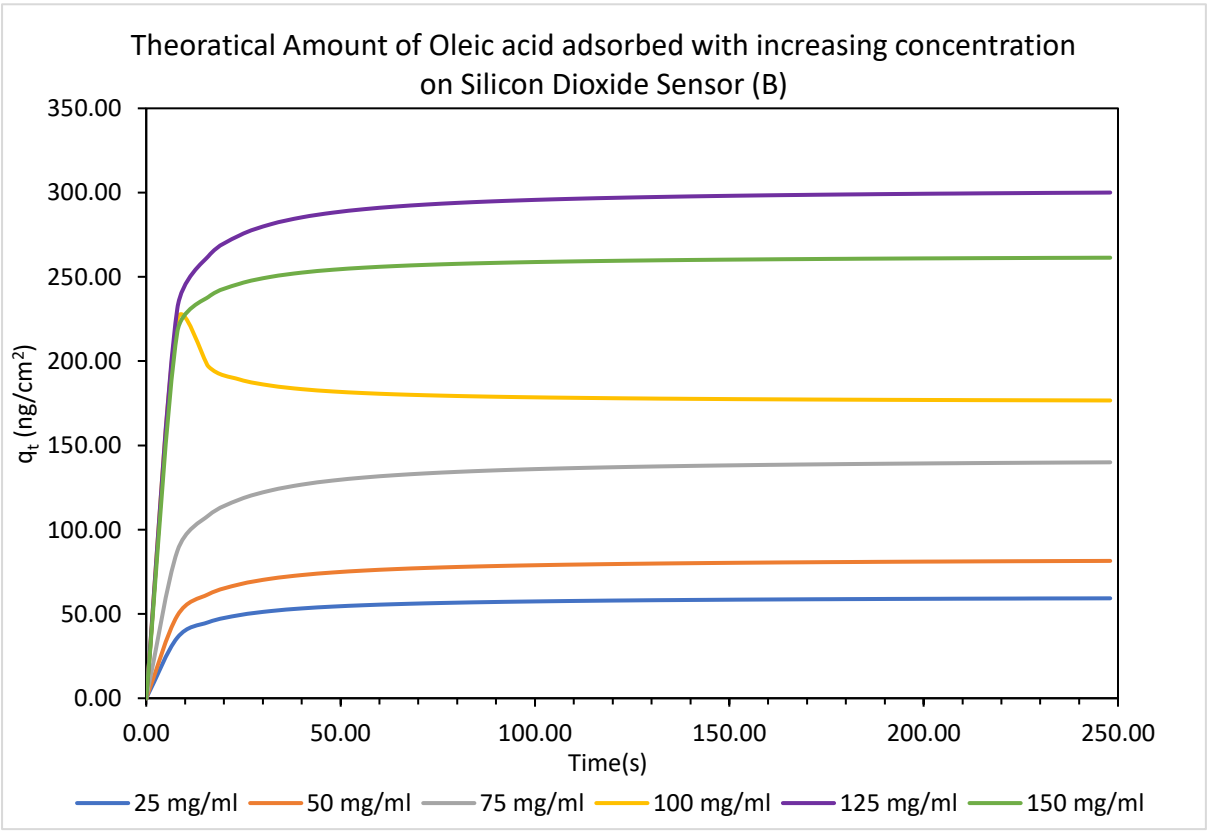


Figure 3.15 Adsorption capacity versus time for effect of concentration on the adsorption kinetics of Oleic acid onto Silicon dioxide oxide (A) Experimental (B) Theoretical.

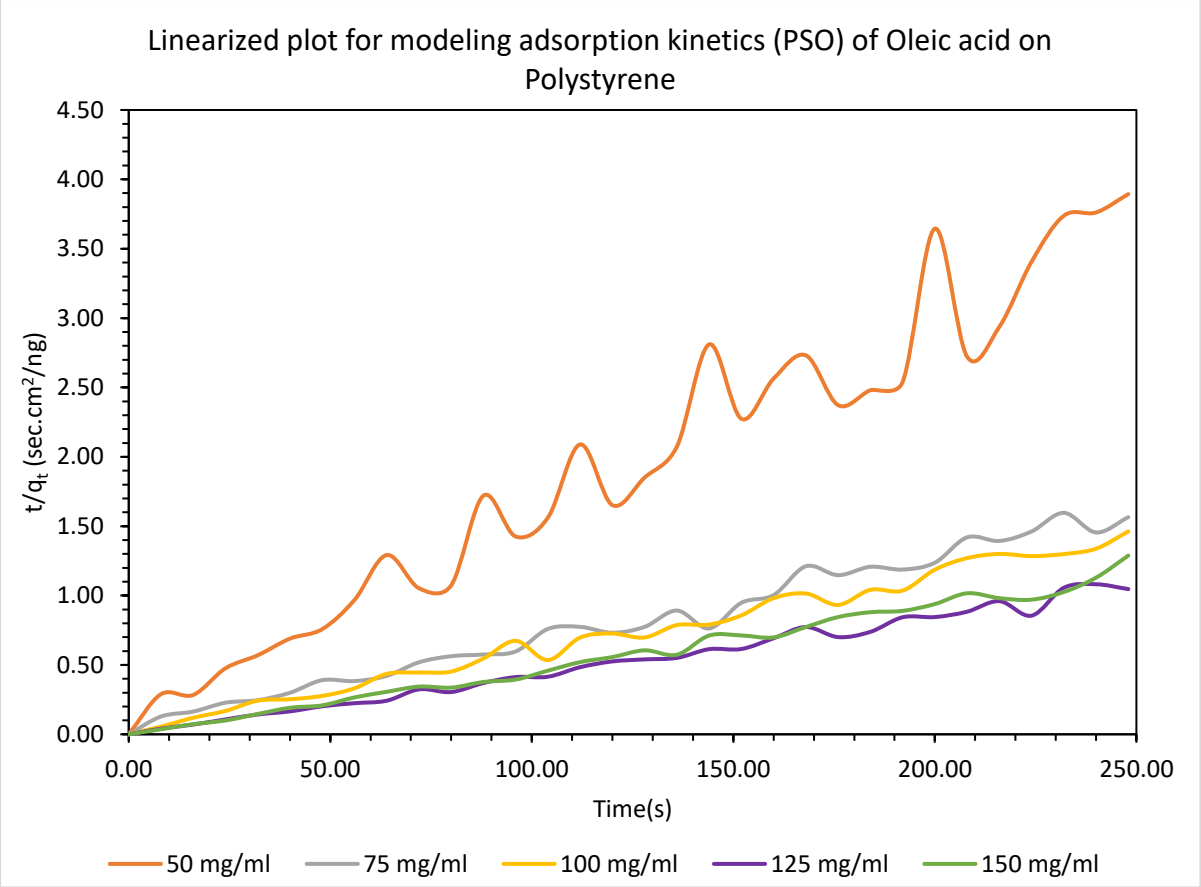
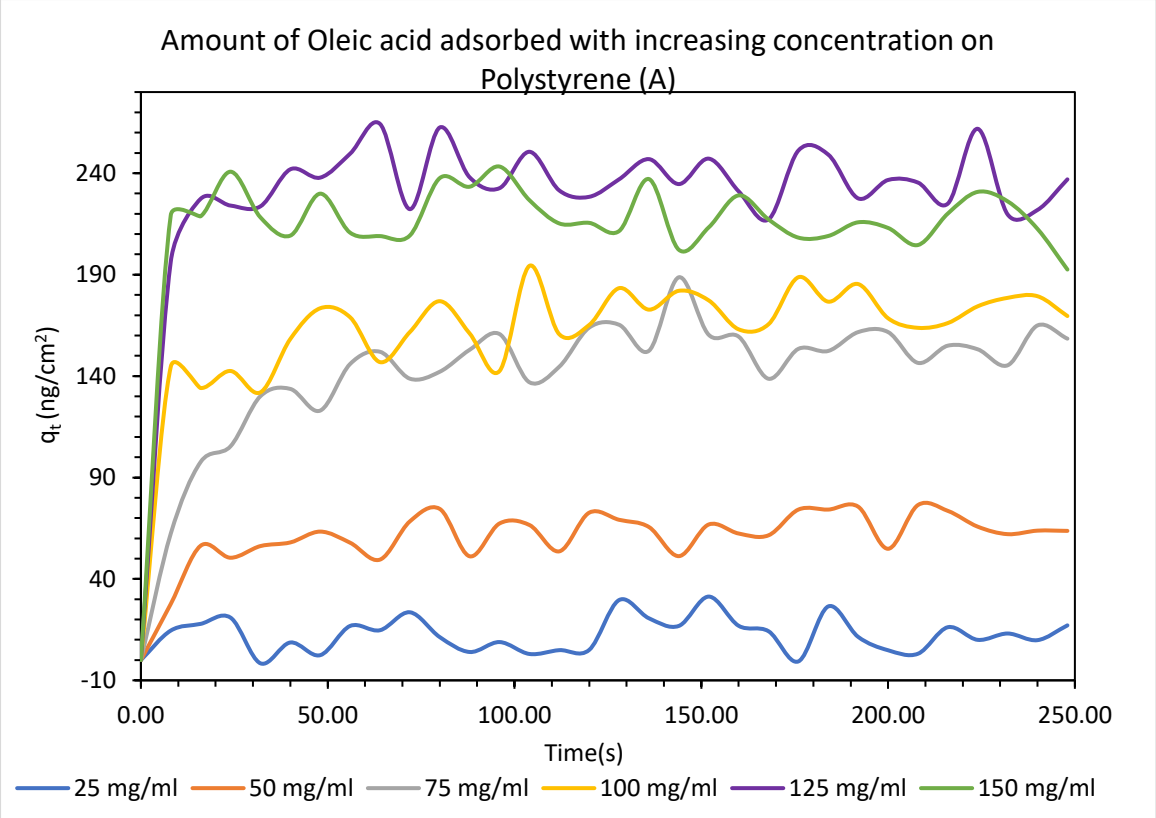


Figure 3.16 Adsorption kinetics (PSO) of Oleic acid on Polystyrene.

Figure 3.15 presents graphs of theoretical and experimental q_t vs time. The experimental qt was obtained from experimental results while the theoretical qt was obtained from Equation3.3. Figure 3.17 showed that values of qt fluctuated a lot particularly after reaching equilibrium. Oleic acid adsorption onto polystyrene had particularly high fluctuations. This might suggest that a more complex mechanism occurred. This was supported by R^2 being very low and not suitable to be presented by PSO equations. This suggests that potential physical adsorption of oleic acid through van der Waals forces of attraction with polystyrene at 25mg/ml were the driving force for adsorption. The limitation of this work was that only PSO kinetics were considered. While they modelled the rest of the data well, outliers such as the one discussed cannot be explained by it. It remains for future research to explore the adsorption mechanisms of adsorption of oleic acid onto polystyrene at low concentrations particularly at 25mg/ml to extend the work presented here.



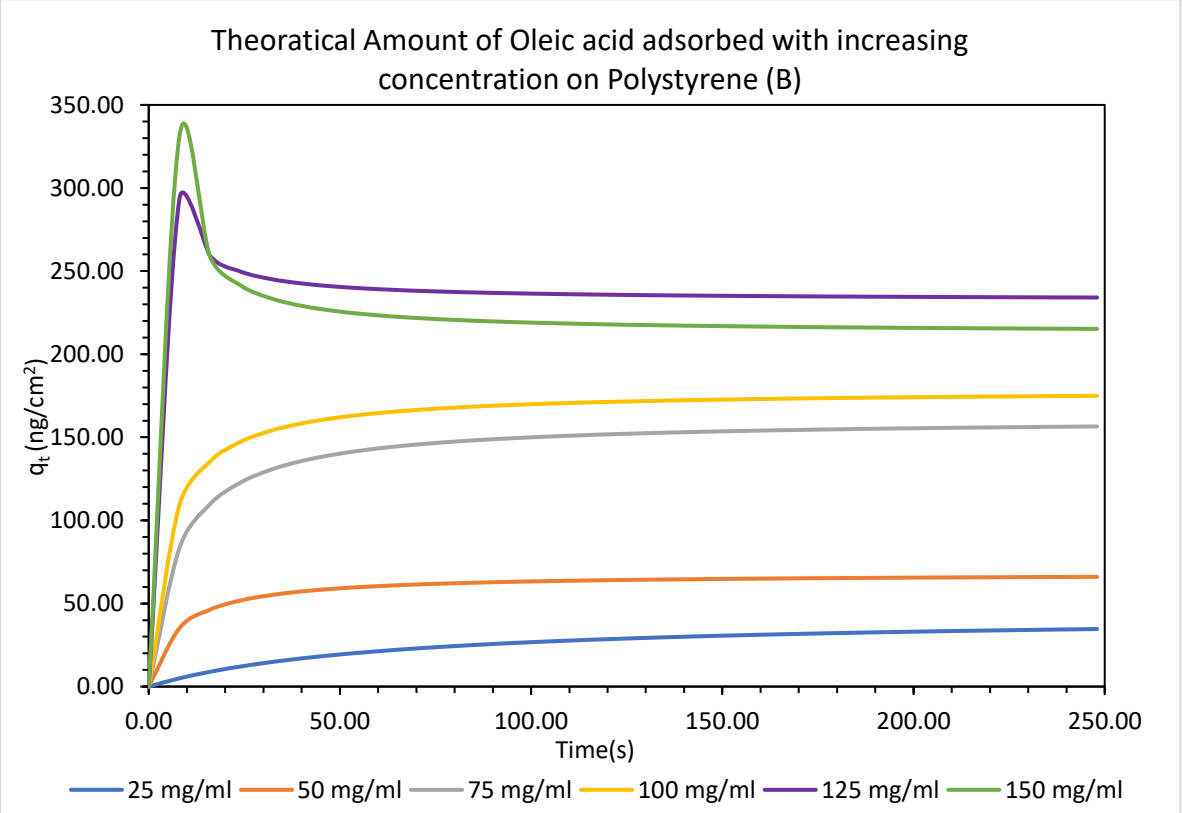


Figure 3.17 shows plot of the adsorption capacity versus time for effect of concentration on the adsorption kinetics of Oleic acid onto Polystyrene (A) Experimental (B) Theoretical.

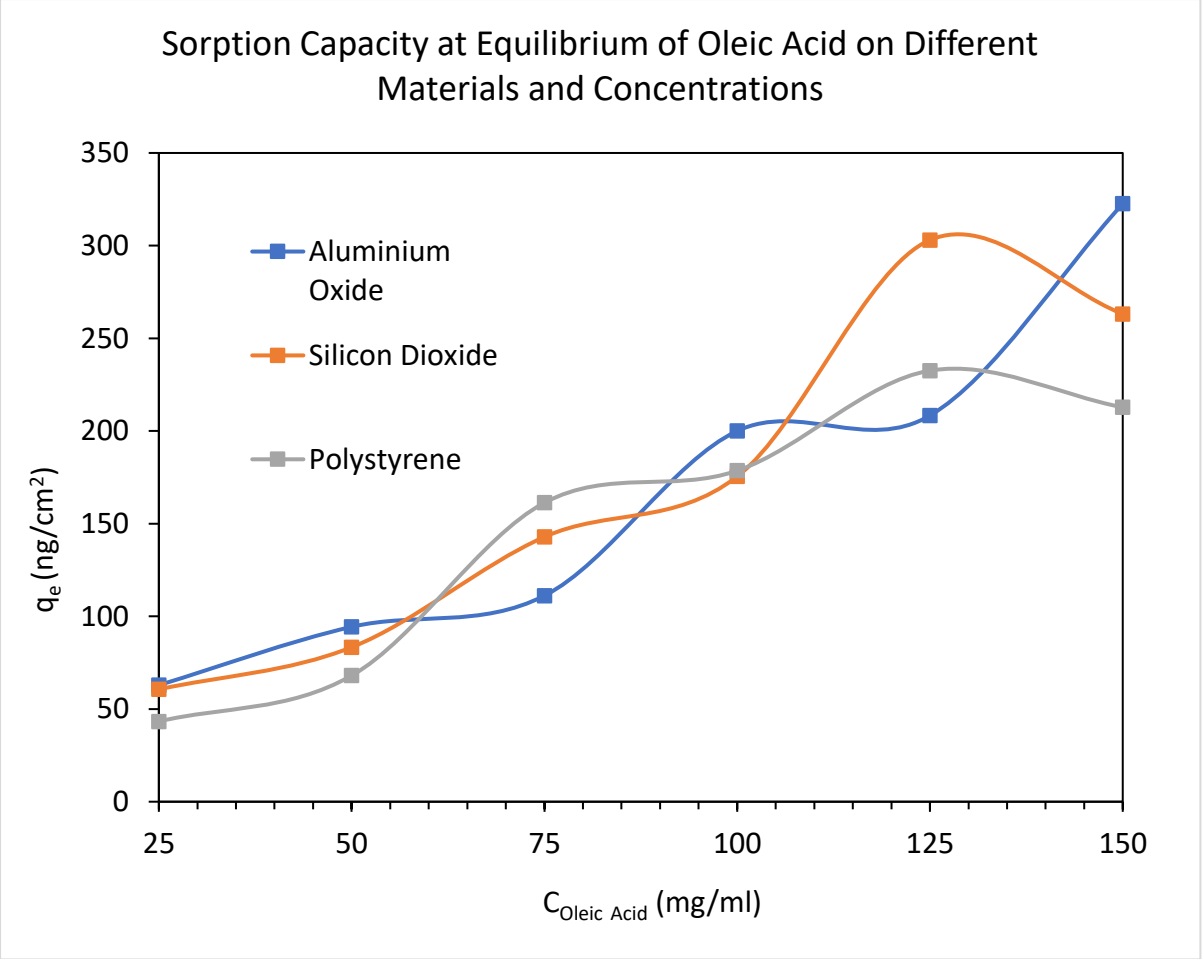


Figure 3.18 Plot of the areal mass density at equilibrium versus concentration for the adsorption kinetics of Oleic acid onto Polystyrene, Aluminium oxide, and Silicon Dioxide.

Given that at 25mg/ml oleic acid adsorption onto polystyrene could not be explained by the PSO model, the value of q_e presented in Figure 3.18 cannot be taken as accurate. Zhang (2019) argued that nonlinear regression models were more trusted and recommended for fitting kinetic and isotherm data. While this was true for most of the results presented here, it was evident that this method has its limitations. It was highlight that the physical meaning of the PSO and PFO equations need more understanding.

Many researchers in literature opt to apply PSO model over PFO model. They reason being that the PFO model only effective at the start of adsorption. The flexibility to apply PSO model at any time makes it much more preferred. Revellame et al. (2020) argued the use of R^2 is not enough to explain linearly transformed results especially when using them as a measure to confirm a nonlinear model fit. However, while this point has its merits, in this case, QCMD data is inherently nonlinear. Therefor application of the PSO model equation to understand the kinetics of adsorption in this work was appropriate.

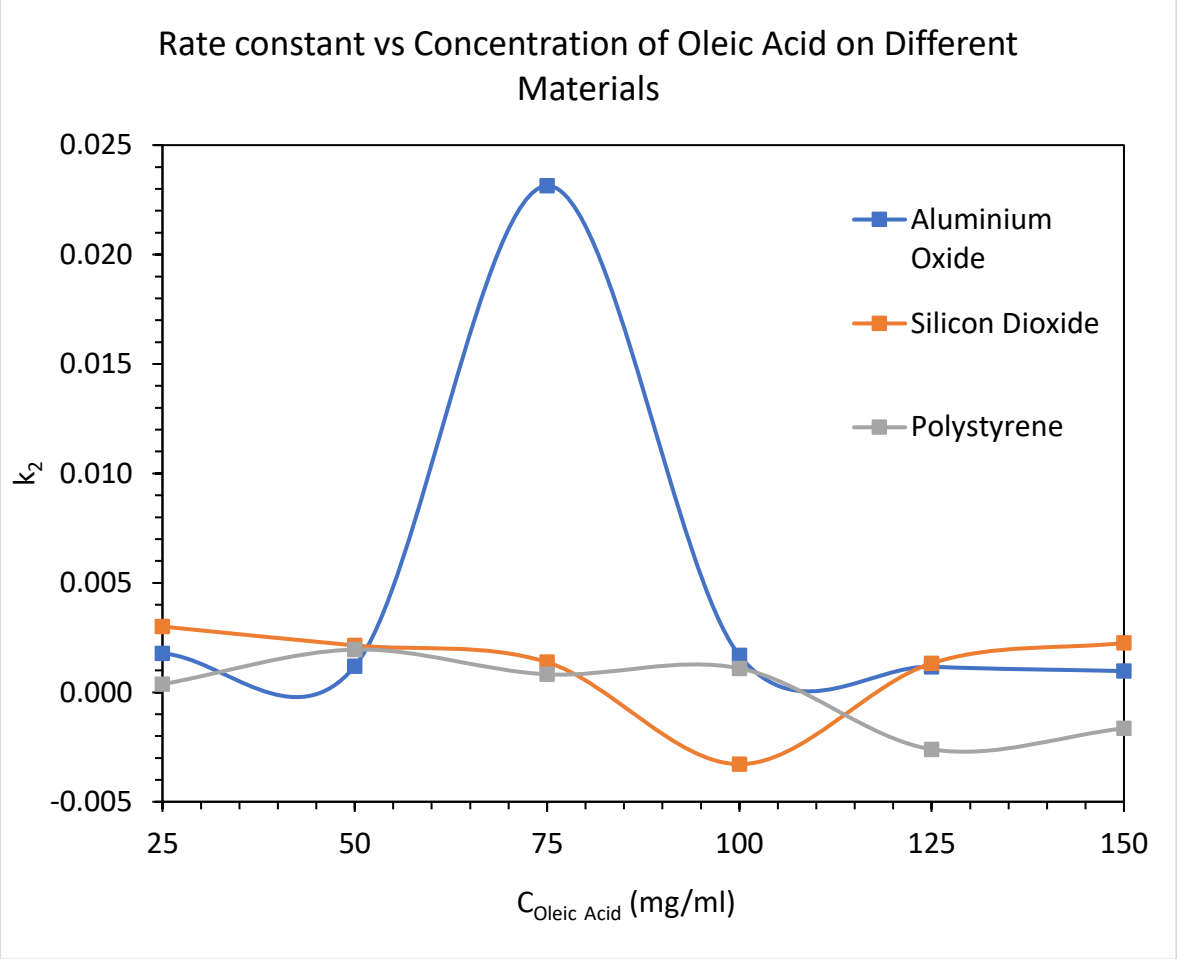


Figure 3.19 Pseudo second order rate constant (Oleic acid) at different concentrations on the three substrate sensors.

Table 3.2 shows R^2 values for the different plots of t/q_t vs time for the pseudo second order equation for Oleic Acid.

Substrate Sensor Material	Concentration (mg/ml)	25	50	75	100	125	150
Aluminium Oxide	R^2	0.9358	0.9719	0.9730	0.9918	0.9921	0.9931
Silicon Dioxide	R^2	0.9359	0.9689	0.9820	0.995	0.9936	0.9922
Polystyrene	R^2	0.0011	0.9507	0.9844	0.9888	0.9897	0.9892

3.2.2.2 Xray photoelectron Spectroscopy

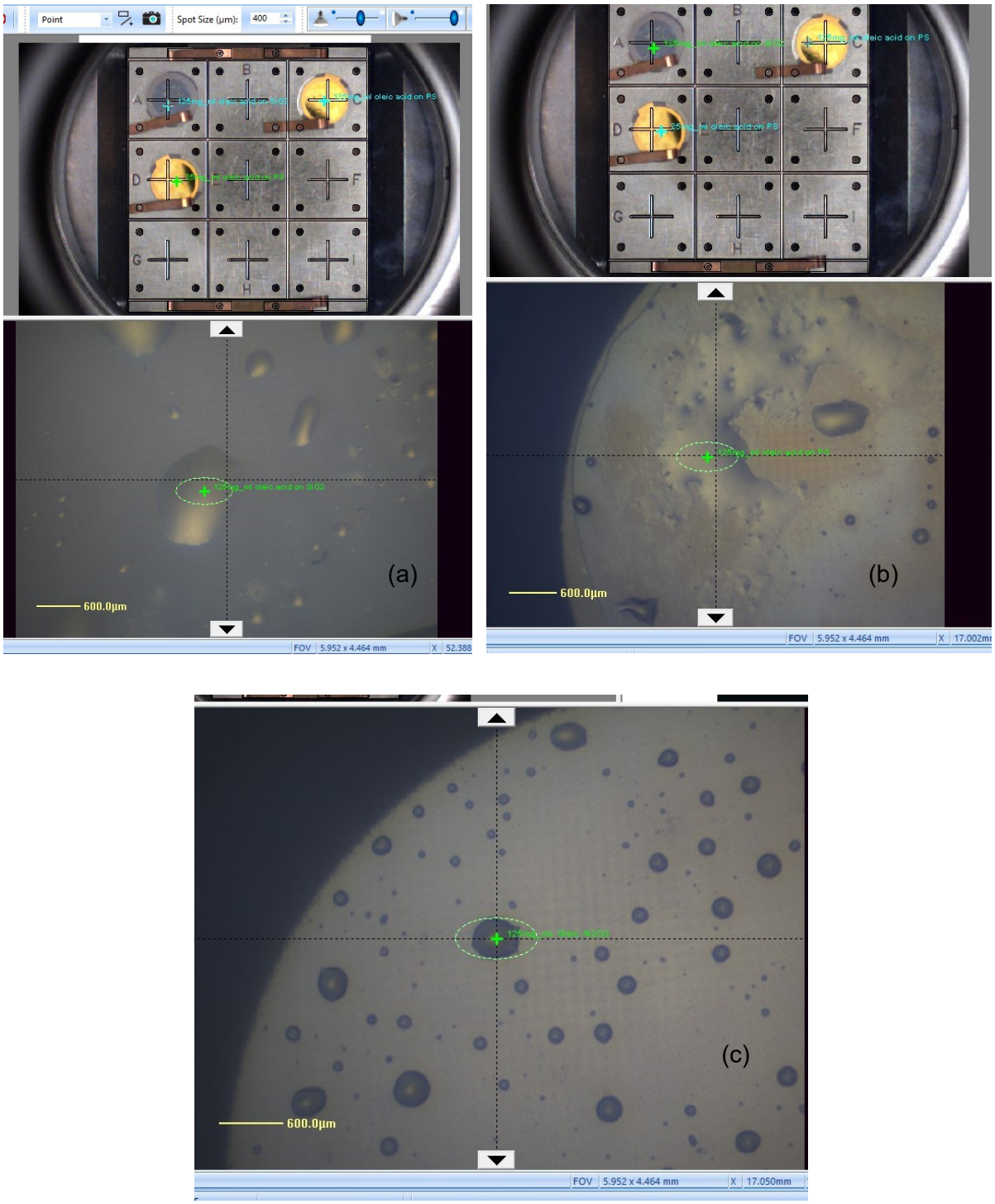


Figure 3.20 Shapes of oleic acid adsorbed onto (a) polystyrene (b) Silicon dioxide (c) Aluminium Oxide shown of the measurement window of the K-Alpha XPS Machine and operated using the Avantage software.

Images taken from the analysis chamber of the K-alpha XPS machine are presented here. The image shows the quartz sensors was secured onto the sample holder while the bottom

image shows the measurement point (spot size 400μm) on all surfaces. Figure 3.20 shows oleic acid formed different shapes when adsorbed to the three materials. Irregular shapes were formed on polystyrene and silicon dioxide however more spherical islands were observed on aluminium oxide (although it appears the size of the molecule was different at each site). Garland et al. (2008) reported observing islands formed due to the self-associating nature of oleic acid onto silica and polystyrene surfaces. They proposed that strong hydrogen bonding between chains as well as dispersion forces along the alkane chain many have been responsible for the island formations. It was unclear what caused the mix of shapes adsorbed of oleic acid on silicon dioxide (Figure 3.20 (b)) (spherical and irregular shapes were observed). However, Garland et al. (2008) found that when oleic acid molecules did not cover the surface evenly, molecules /formed islands congregated. Surface morphology of oleic acid on different materials is important as this can affect the adsorption kinetics particularly when designing adsorbents to remove fatty acids from wastewater. This remains an area for future research.

3.2.2.2.1 Oleic acid

3.2.2.2.1.1 Polystyrene

Figure 3.21 shows survey spectra of polystyrene sensors at 25mg/ml and 125mg/ml of oleic acid ss adsorbed onto the substrate. Improved signal to noise ratio resulted in increased peak intensity of C1s and O1s and reduced background noise as more oleic acid was adsorbed on polystyrene (comparison between unused polystyrene sensor in section 2.4.2.3.1 and Figure 3.21).The intensity of the C1s peaks showed a decrease in the count number/ intensity with increasing amount of oleic acid adsorbed. This corresponded to a transition from four to three peaks in the C1s region. Figure 3.22 shows the deconvolution of Si2p , C1s and O1s regions. The Si2p region at 25mg/ml has three peaks at 101.49eV , 102.02eV and 102.61eV respectively while the same region at 125mg/ml of oleic acid had two peaks at 101.47eV and 102.11eV. The increased intensity of Si2p peaks suggest that covalent bonding resulted in the siloxane bond at 102.11eV.

Figure 3.21 and Figure 3.22 showed the presence of the COOH- group from the adsorption of oleic acid. Deconvolution of the O1s at 125mg/ml revealed peaks at 531.72eV and 533.31eV corresponding to has C-O and C=O (FWHM 1.35 for both). The same peaks were found at 531.70eV and 533.21eV (FWHM 1.29 for both). Adsorption onto polystyrene confirmed the presence of COOH- , C-O and C=O peaks on C1s. This region revealed three peaks (FWHM 1.03 for all) at 289.03eV corresponding to COOH (from oleic acid) and C-C at 284.46eV and 284.24eV for adsorption at 125mg/ml oleic acid. The COOH peak was at 288.94eV (FWHM

0.89) while three C-C peaks were resolved at 283.50eV , 284.16eV and 284.65Ev with FWHM of 1.33,1.02 and 1.21 respectively. The disappearance of the peak at 283.5eV might be due reduction due to charging effects (accumulation of positive charge due to emission of electrons from an insulating material) by the adventitious carbon which is particularly common in insulating materials such as polystyrene (Goodson et al., 2022). Higher concentrations of oleic acid meant that electrons were emitted from the oleic acid layer and not polystyrene thus resulting in 'loss' of the 283.5eV. Because of this, charge calibration of shifting the 283.5eV C-C/ C-H to 284.8eV was not done. The objective was investigating whether increasing the concentration of oleic acid resulted in more adsorption. The results showed that the atomic percentage of the -COOH group increased from 0.93% to 1.64% as more oleic acid was adsorbed via van der Waals forces of attraction between the -COOH end of the fatty acid and polystyrene corresponding to a larger ΔF measured in QCMD experiments (Peter Esser , 2014). Hence oleic acid was adsorbed onto polystyrene with more oleic acid adsorbed at 125mg/ml.

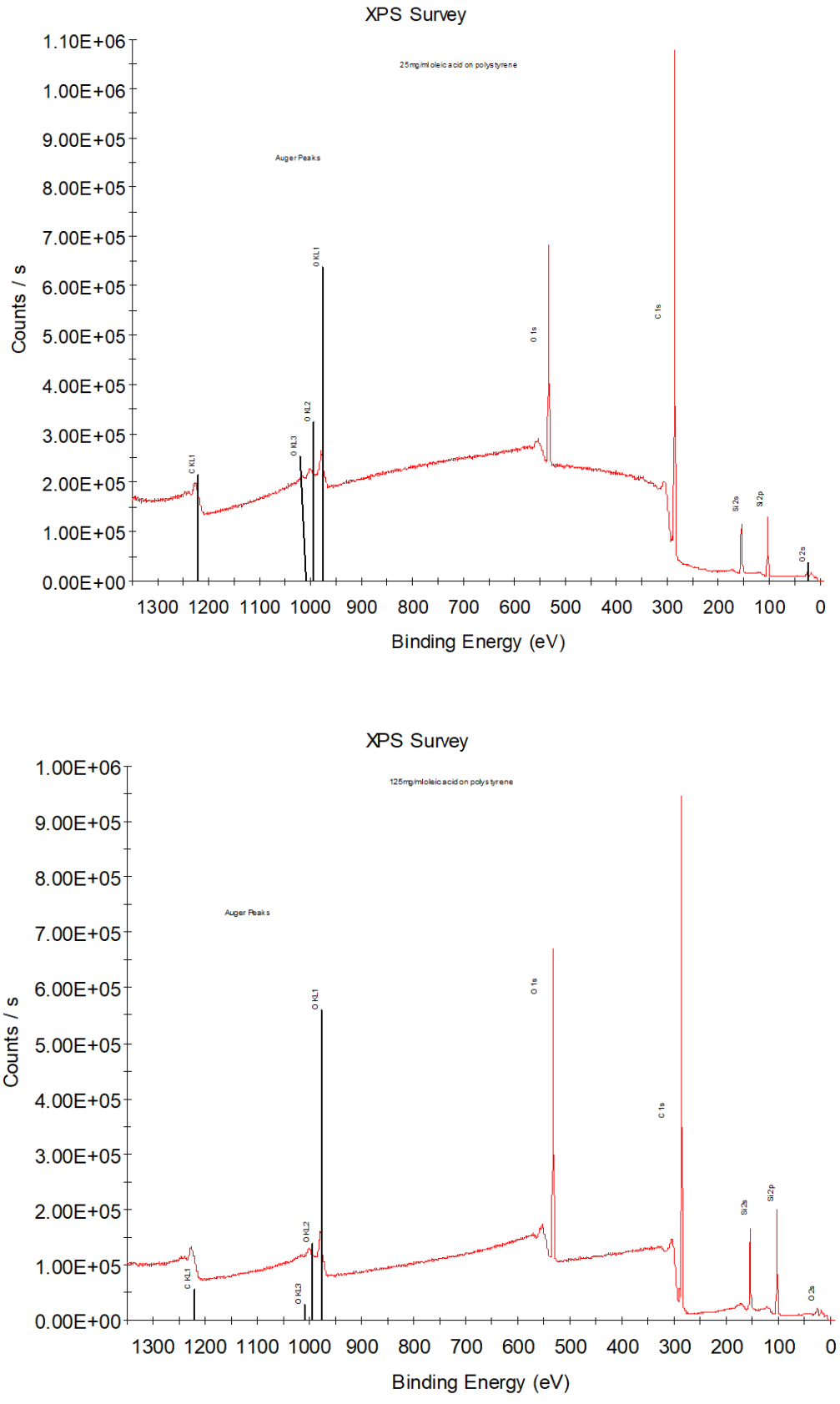


Figure 3.21 Survey spectra of 25mg/ml and 125mg/ml oleic acid adsorbed on polystyrene.

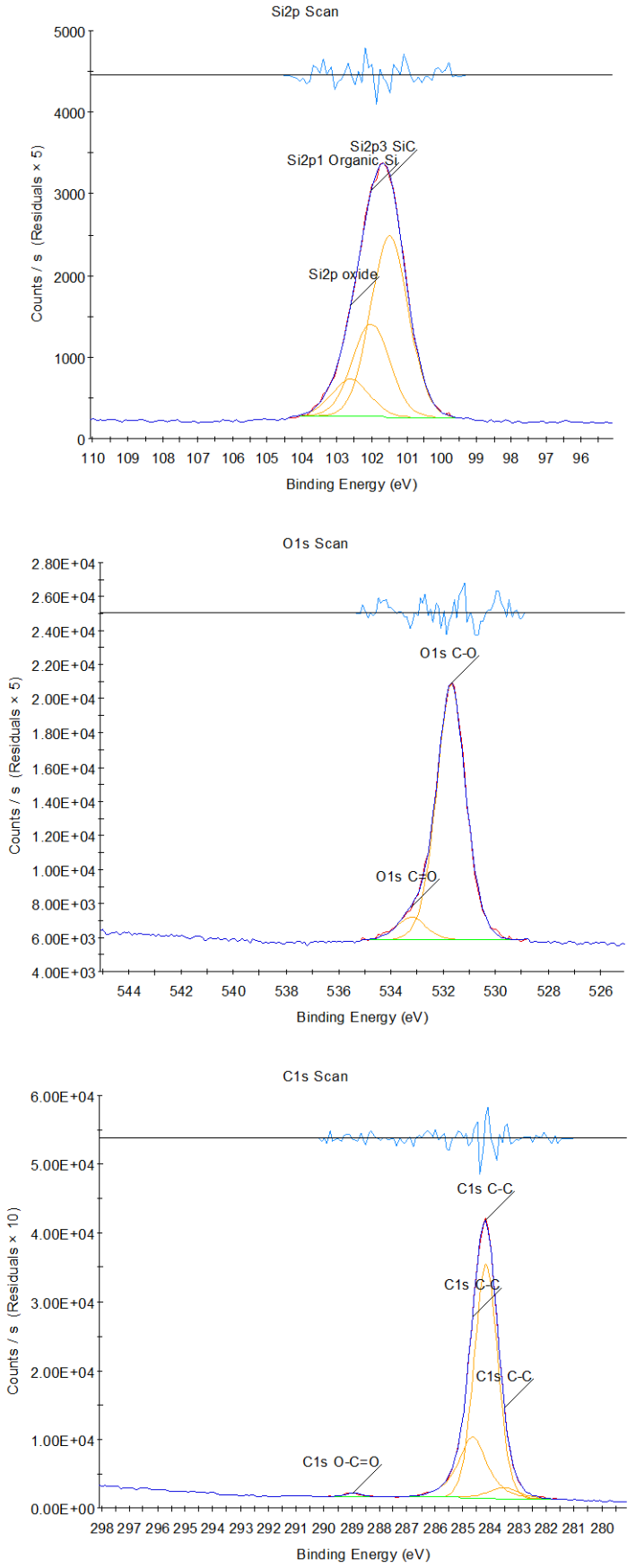


Figure 3.22 Deconvolution of Si2p, C1s and O1s scans of 25mg/ml oleic acid on polystyrene.

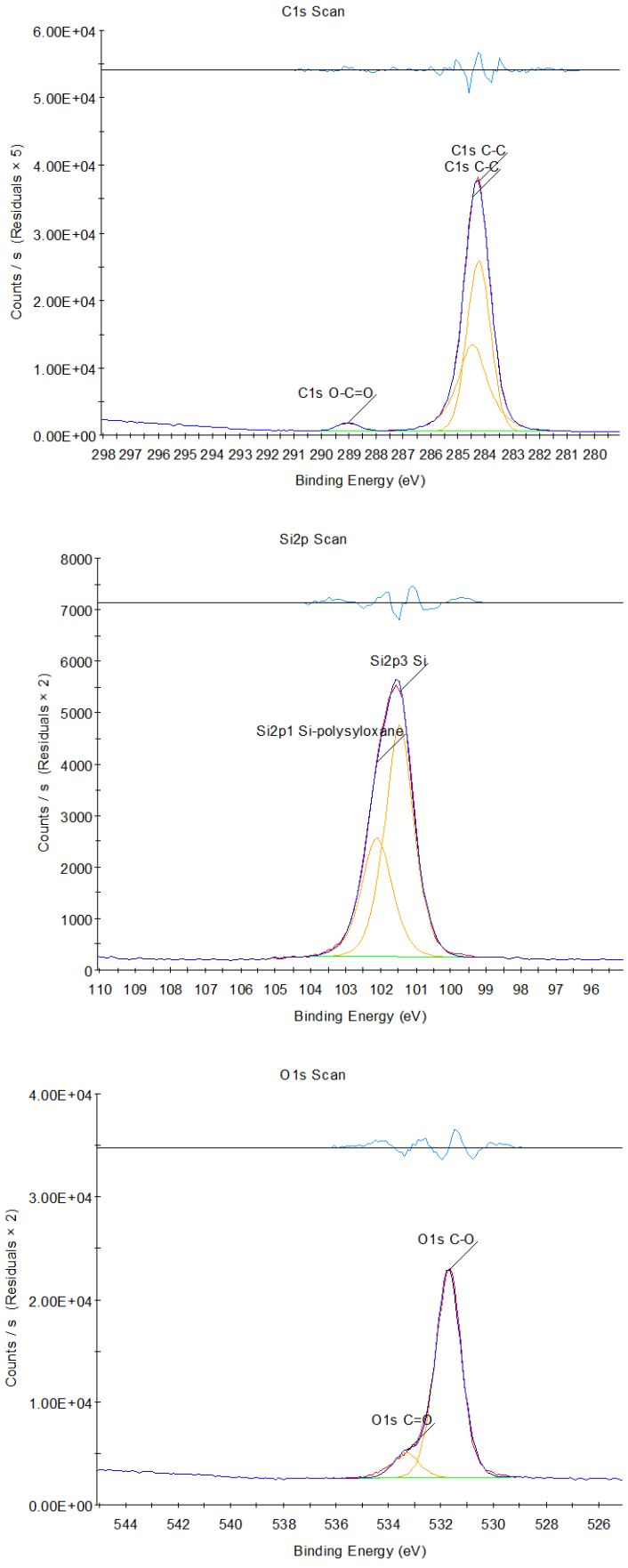


Figure 3.23 Deconvolution of Si2p, C1s and O1s scans of 125mg/ml oleic acid on polystyrene.

3.2.2.2.1.2 Silicon Dioxide

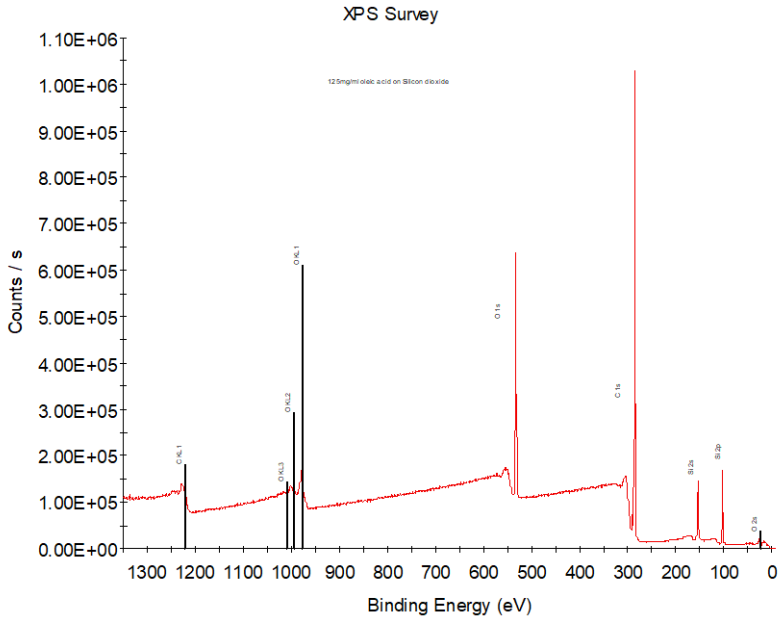


Figure 3.24 Silicon dioxide substrates and survey scan for adsorption of 125mg/ml oleic acid on SiO2.

Figure 3.24 shows survey scans as well as C1s, O1s, Si2p scans. The results suggest oleic acid had adsorbed onto the surface as can be seen by the presence Si-O-Si peaks in the Si2p scan and COOH- group in C1s and C=O, C-O peaks in O1s scan.

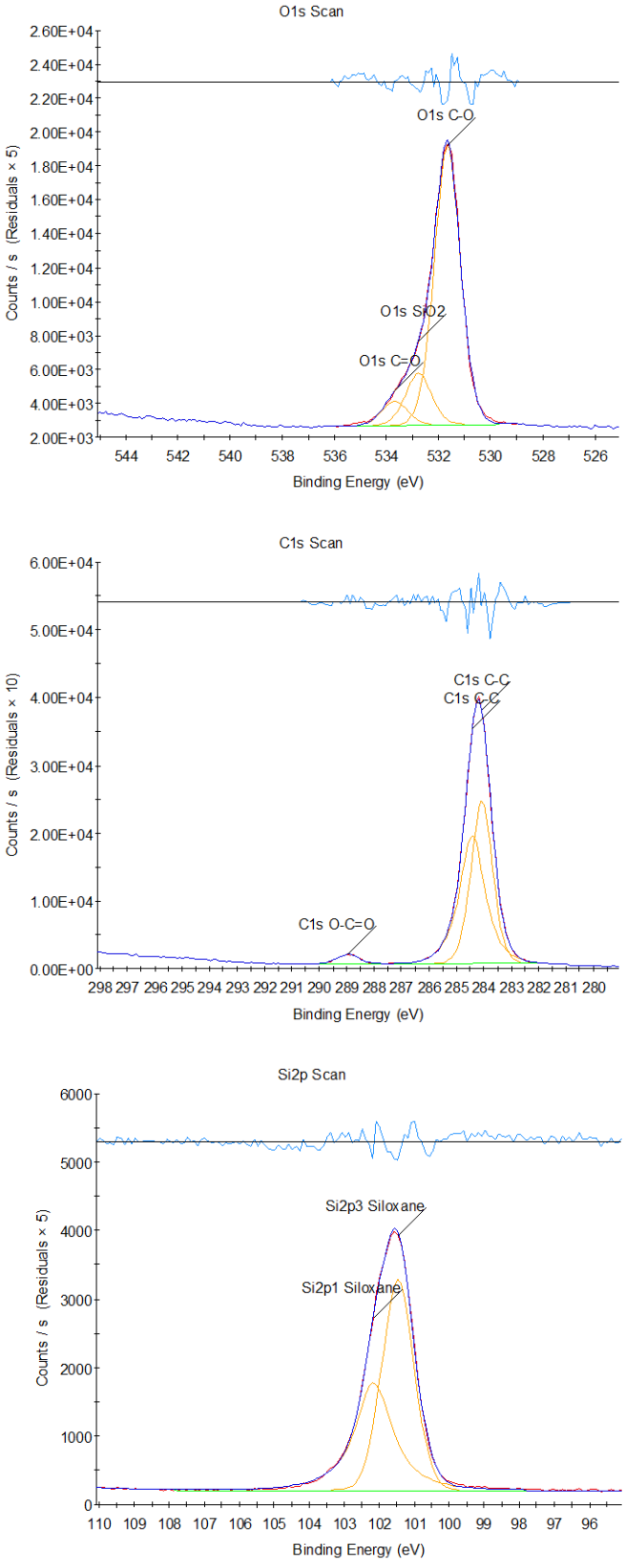


Figure 3.25 Deconvolution of O1s , C1s and Si2p scans or adsorption of 125mg/ml oleic acid on SiO2.

3.2.2.2.1.3 Aluminium oxide

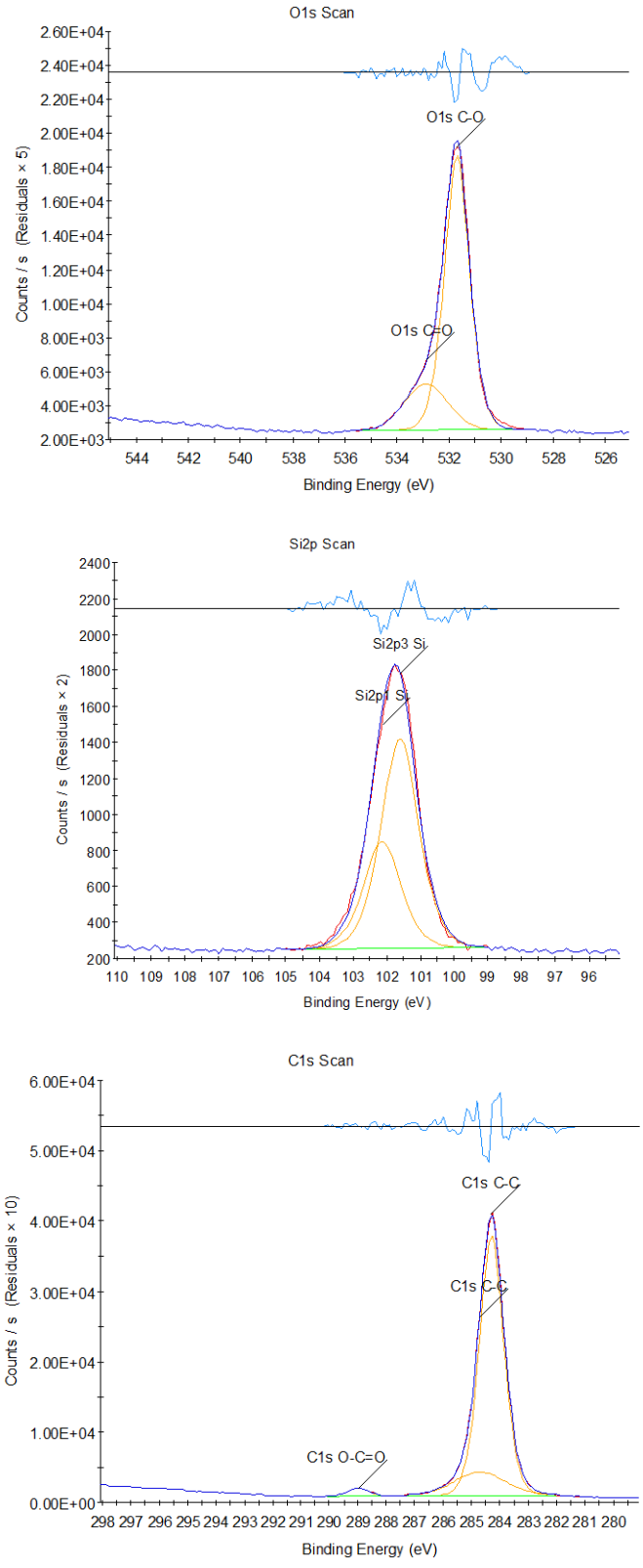


Figure 3.26 Deconvolution of O1s , C1s and Si2p scans and of aluminium oxide substrate sensor at 125mg/ml oleic acid adsorption.

Aluminium oxide substrate sensors were tested, and the result show the presence of COOH-group, C=O , C-O and Alumina silicate confirming the presence of oleic acid absorbed by the substrate sensors. The intensity of C1s and O1s peaks reduced with increasing concentration of oleic acid in the QCMD experiments. Figure 3.20 shows that oleic acid adsorbed onto aluminium oxide has circular shapes while onto polystyrene it appears to form a variety of shapes.

3.2.2.2.2 Linoleic acid

3.2.2.2.2.1 Polystyrene

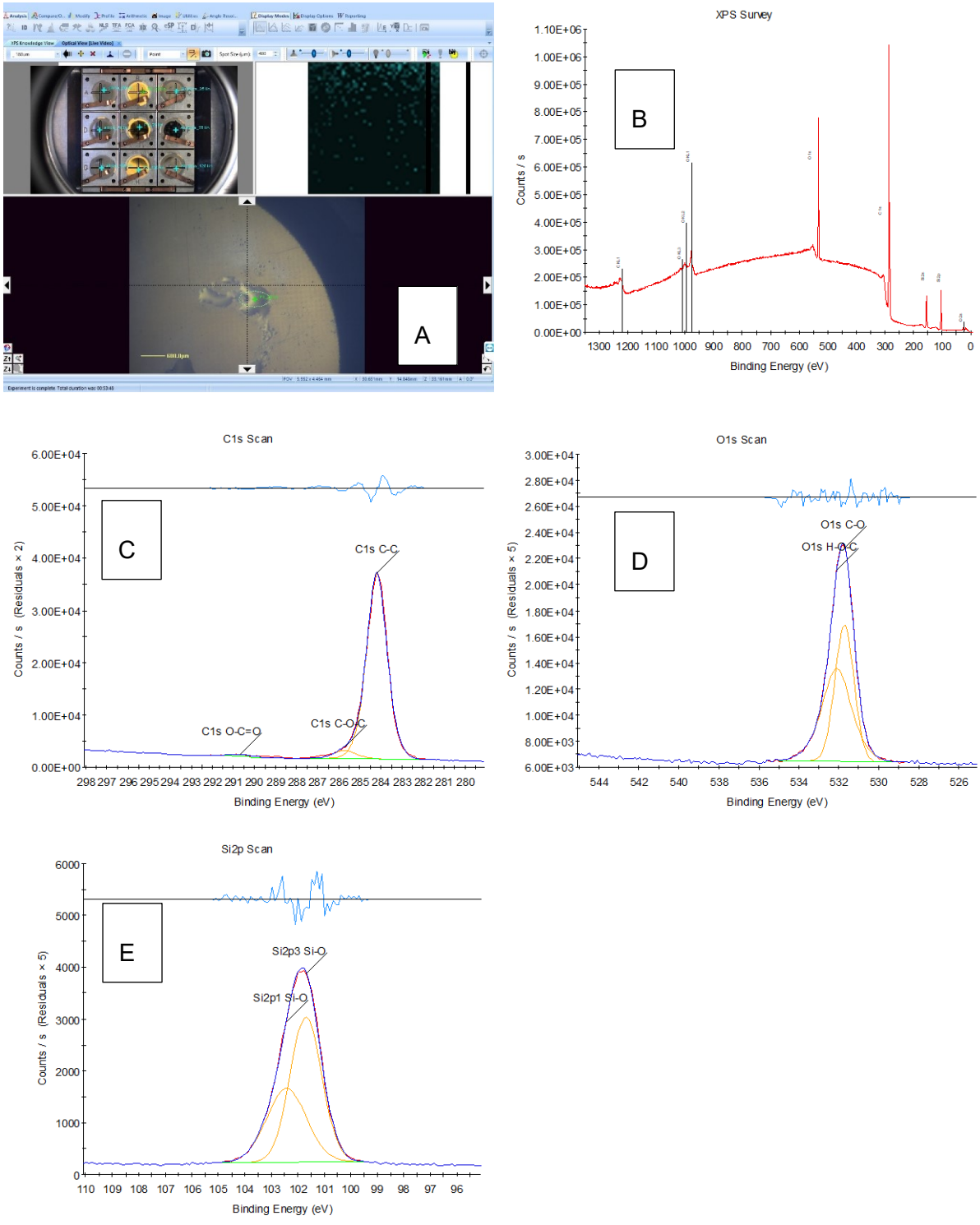


Figure 3.27 Deconvolution of peaks on polystyrene substrate. (A) analysis window of silicon substrates with linoleic acid adsorption (B) Survey scan with 75mg/ml linoleic acid adsorbed (C) C1s scan (D) O1s scan (E) Si2p scan.

3.2.2.2.2.2 Silicon Dioxide

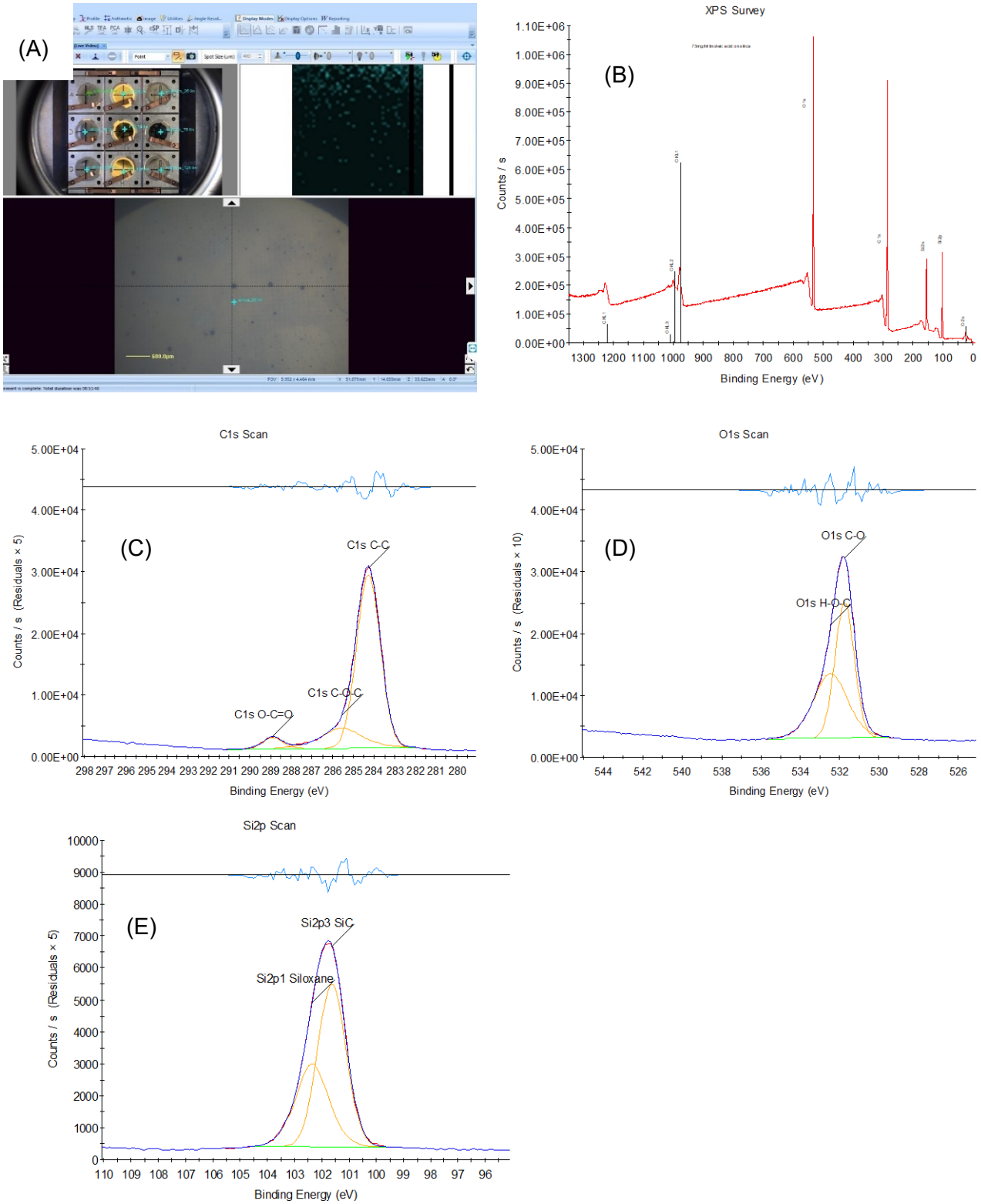


Figure 3.28 shows deconvolution of peaks on silicon dioxide substrate. (A) analysis window of silicon substrates with linoleic acid adsorption (B) Survey scan with 75mg/ml linoleic acid adsorbed (C) C1s scan (D) O1s scan (E) Si2p scan.

3.2.2.2.3 Aluminium Oxide

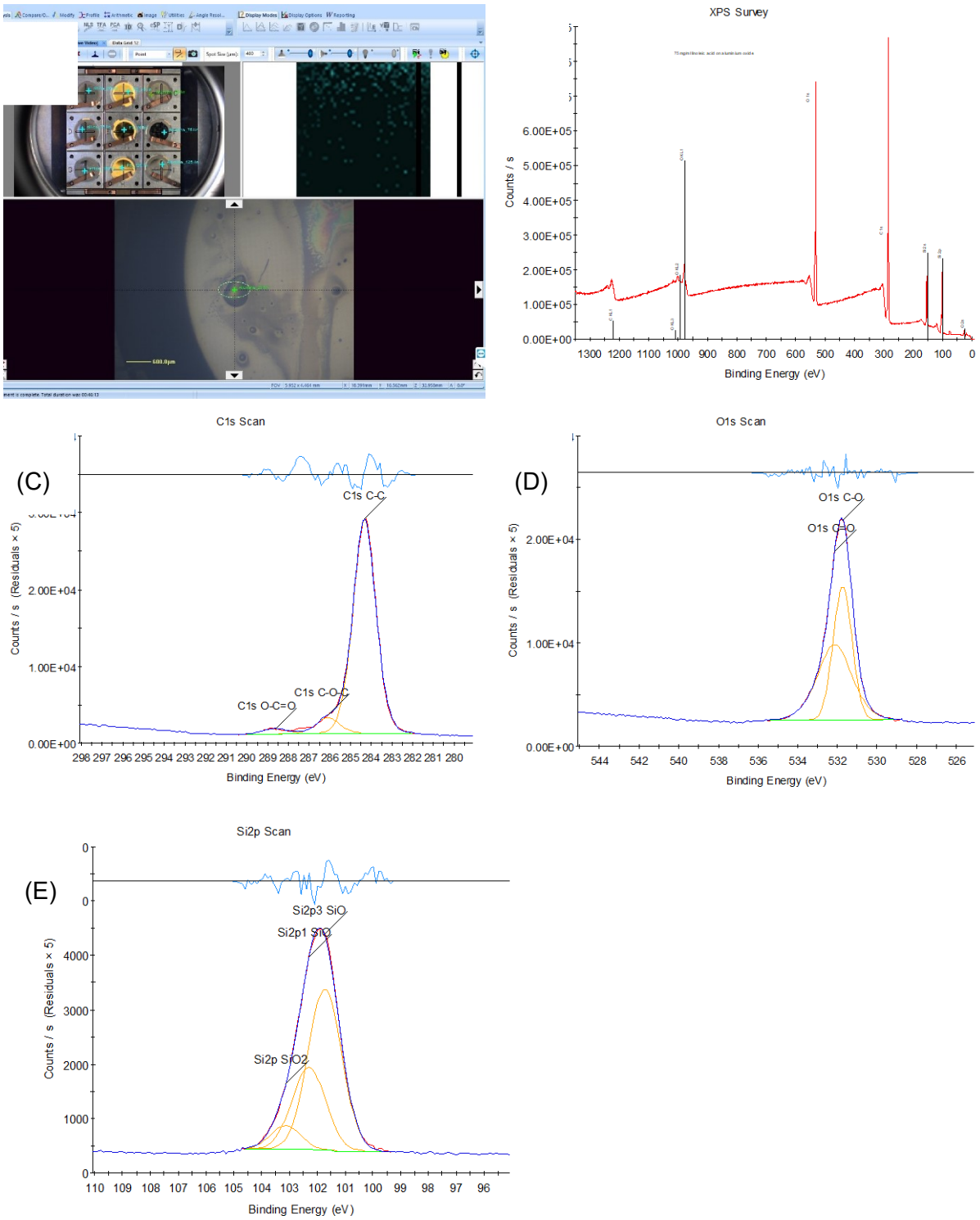


Figure 3.29 deconvolution of peaks on aluminium oxide substrate. (A) analysis window of silicon substrates with linoleic acid adsorption (B) Survey scan with 75mg/ml linoleic acid adsorbed (C) C1s scan (D) O1s scan (E) Si2p scan.

Figure 3.27, Figure 3.28 and Figure 3.29 show the XPS surveys and peaks deconvolutions of C1s, O1s and Si2p.The deconvolution of the C1s scan shows the presence of three peaks C-C at 284eV to 284.34eV, C-O-C at 258.56eV to 286.09eV and O-C=O at 288.61eV to 290.68eV. The C1s peak shows all peaks shifted depending on the adsorbent as shown in Figure 3.32. The Si2p scans shows the presence of siloxane bonds from the silicon present in the substrates with the fatty acid. O1s scan shows the presence of C-O and C=O between 531.5eV and 533eV (Thermo Fisher Scientific Inc. , 2024). The atomic percentages of the O-C=O peak is 0.66% for polystyrene,2.48% in silicon dioxide and 1.36% in aluminium oxide. More detail of the atomic percentages and fit data is in the appendix section 8.1.3.

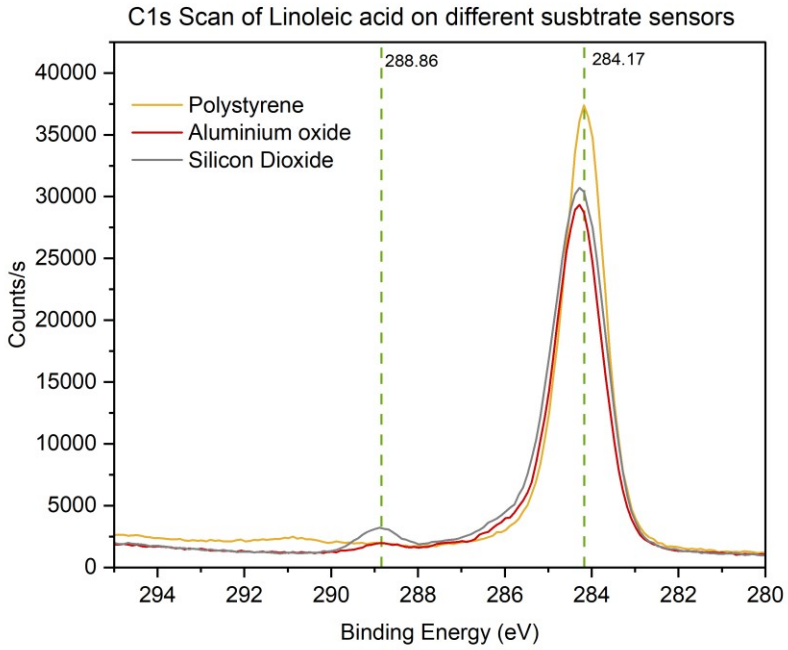


Figure 3.30 C1s region of linoleic acid adsorbed onto different materials.

XPS characterization of polystyrene was previously reported by (Goodson et al., 2022). Apart from the slight chemical shift at 284.17eV of the C-C/C=C region, there is a shift of the O-C=O peak particularly in polystyrene to 290.88eV (Thermo Fisher Scientific Inc., 2006). The shift of this peak from 291.18eV discussed in section 2.4.2.3.1 290.88eV confirms the adsorption of linoleic acid onto the polystyrene.

3.2.2.3 Contact Angle

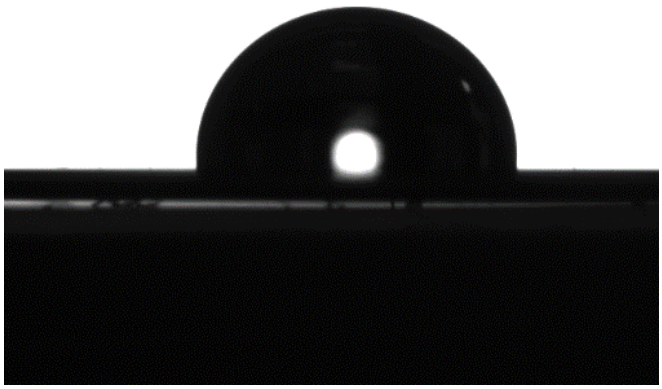


Figure 3.31 static contact angle measurement on an unused Hydrophobic polystyrene sensor

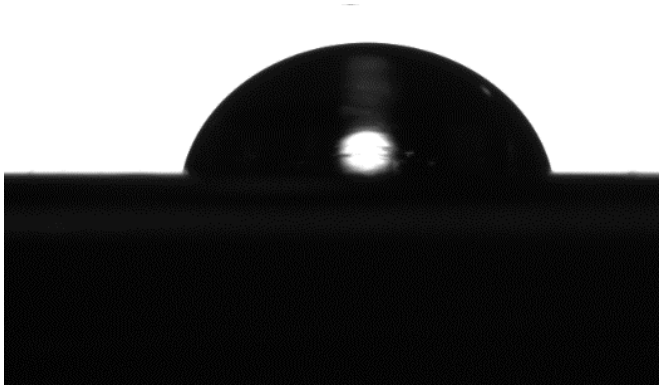


Figure 3.32 static contact angle measurement on used Hydrophobic polystyrene sensor

Contact angle measurements of the sensors before and after the experiments were measured to further determine if the fatty acids adsorbed onto the surface modified the substrate's surface properties. Before the experiment, the mean contact angle of the hydrophobic polystyrene was 95. 2 ° ± 2 °. This reduced to 77.7° ± 2 ° after fatty acid adsorption. The reduction in the contact angle may have been caused by van der Waals interaction between the fatty acid and polystyrene (Peter Esser , 2014). During contact angle measurement, carbonyl groups from the fatty acid formed hydrogen bonds with the water molecules (Farmer et al., 2024). This resulted in increasing the wettability of polystyrene. Shen et al. (2020) has already studied the adsorption and wettability of unsaturated fatty acids such as oleic acid and linoleic acid on Rhodochrosite. They were able to determine that Rhodochrosite hydrophobicity increased as concentration increased. They suggested that oleic and linoleic acid showed a higher maximum contact angle as compared to the saturated stearic acid however their results showed this value decreased as the number of double bonds increased. They argued this is of importance particularly in flotation processes. An extensive study of

contact angle measurements on polystyrene , aluminium oxide and silicon dioxide sensors was not covered in this work and remains for future research. Given the role of the adsorbents if FFA adsorption such a study could extend knowledge in removal of FFA from wastewater and potentially how the FFA could be recovered.

3.3 Conclusion

The PSO equations were able to predict that chemisorption was the rate limiting step and that oleic and linoleic acid adsorbed to the surfaces (onto silicon dioxide, aluminium oxide and polystyrene) forming a monolayer (Liu, 2006).The correlation coefficient R^2 was >0.997 for all surfaces involved in the adsorption of linoleic acid while R^2 was > 0.93 for the adsorption of oleic acid. Different concentrations had different rate constants k_2 for all materials at different concentrations. This confirms that linoleic acid and oleic acid adsorbed to the different surfaces at different rates. However, the results showed that linoleic acid adsorbed to aluminium oxide and polystyrene at the same rate at 50mg/ml before reaching adsorption equilibrium. At 75mg/ml the rate constants for aluminium oxide higher than the rest. It remains unclear why this was the case.

XPS was able to confirm the adsorption of the unsaturated fatty acids onto the sensors. The deconvolution of C1s region revealed the presence of adventitious carbon at 2835. eV which is common in insulating materials such as polystyrene (Goodson et al., 2022). The presence of the C-O,C=O groups in O1s suggested that oleic acid and linoleic acid had formed chemical bonds with polystyrene. XPS analysis of the same C1s region revealed that the adventitious carbon disappeared when more oleic acid was adsorbed. Silicon dioxide and aluminium oxide also had the presence of the acid group. This confirms that the PSO model was able to predict the adsorption of the fatty acids through use of R^2. The low R^2 of 0.0011 (Table 3.2) value for 25mg/ml of polystyrene also highlighted that at 25m/ml, oleic acid had only adsorbed to polystyrene in very low amounts. Hence the presence of background noise and the adventitious carbon when the surface was characterized. The same was not observed for silicon dioxide and aluminium oxide. This means that at low concentrations of oleic acid, silicon dioxide and aluminium oxide were better adsorbents.

Chapter 4 Investigation of Palmitic acid, Oleic Acid and Linoleic adsorption using QCMD: effect of sequencing

4.1 Abstract

This work explored the competitive adsorption of palmitic acid , linoleic acid and oleic acid onto silicon dioxide, aluminium oxide and polystyrene. The results showed that palmitic acid introduced rigidity to the adlayer and the extent of this dependent on its position in the sequence. Linoleic acid was reported to adsorb in an extended state while oleic acid adsorbed parallel to the quartz sensors, however, this effect was affected by the position of both fatty acids in the sequence thus resulting in different conformational changes of the adlayers. Raman microscopy and FTIR characterised the surfaces following adsorption and showed the increased intensity of C=C in Raman microscopy and -C=H in FTIR suggest increased adsorption of the unsaturated fatty acid. However, the presence of C=C at about 3009 cm^{-1} suggested increased linoleic acid adsorption while at 1656 cm^{-1} suggested presence of both oleic acid and linoleic acid.

4.2 Introduction

Free fatty acids are often found forming parts of oils such as olive oil and other oil/fat-based products. Different authors have studied the role of FFA in many different applications. Crespo et al. (2018) explored how different degrees of unsaturation of FFA affected adsorption and their ability to form films on different surfaces. Lundgren et al. (2006) studied the effect of degree of unsaturation from alkane solutions onto steel surfaces using QCMD. Other studies explored how fatty acid adsorption onto minerals such as calcium affected their flotation (Filippova et al., 2018). He et al. (2013), Sultana et al. (2022) and Hu et al. (2025) studied mechanisms involved in the formation of fats oils and grease deposits in sewers and highlighted the role played by FFA.

The aim of this work was to explore competitive adsorption of fatty acids (oleic acid, linoleic acid and palmitic acid) and how sequencing of the fatty acids affected their interaction with each other as well as other surfaces (polystyrene , silicon dioxide and aluminium oxide) using QCMD. This could assist in the adsorbent designs for removing FFA from wastewater.

This work involved the use of a confocal Raman microscope to identify the structure and bands intensities of the free fatty acids on different substrate sensors. Generally, confocal microscopes have the added advantage to conventional microscopes in that they have a high intensity laser beam and a scanner which allows the beam to move in a rectangular area (i.e.

movement in the x-y directions of all related planes as well as all vertical directions) while taking measurements of the sample (microscopic area). This ensures that 3D images of the sample are formed and displayed to the user on the interface (computer screen) Leng (2013) as was shown in this chapter.

Berezina et al. (2018) as part of their work were able to determine the concentration of oleic and linoleic acid by correlating this to the intensities of the bands from sunflower seed oil and olive oil. They however reported that they found Raman spectroscopy to be a non-destructive method of analysis, however in this work, given the sensitive nature of the quartz sensors, some destruction was observed during measurements and analysis owing to the use of the Raman microscope as shown in Figure 4.16 (B). As such the laser power had to be adjusted appropriately (typically kept below 12.5mW) to avoid destruction of the sample and the sensor. To the best of my knowledge, the competitive adsorption of Palmitic acid, oleic acid and linoleic acid onto silicon dioxide, aluminium oxide and polystyrene sensors studied with QCMD is reported here for the first time. This work did not consider sewer like conditions as it was beyond scope.

4.2.1 Materials and Methods

4.2.1.1 Stock solutions.

Table 4.1 Shows proportions used to make Oleic Acid stock solutions.

Sample	1	2	3	4
Oleic Acid (mg)	500	1000	1204	1400
Ethanol (ml)	10.00	10.00	10.00	10.00
Concentration (mg/ml)	50.00	100.00	120.40	140.00

Table 4.2 Shows proportions used to make Linoleic Acid stock solutions.

Sample	1	2	3	4
Linoleic Acid (mg)	502	1006	1200	1200
Ethanol (ml)	10.00	10.00	10.00	8.00
Concentration (mg/ml)	50.200	100.600	120.00	150.00

Table 4.3 Shows proportions used to make Palmitic Acid stock solutions.

Sample	1	2	3	4
Palmitic Acid (mg)	500	1000	1200	1500
Ethanol (ml)	10.00	10.00	10.00	10.00
Concentration (mg/ml)	50.00	100.00	120.00	150.00

4.2.1.2 QCMD Sequencing Tests

Competitive adsorption experiments were conducted on the hydrophobic polystyrene, aluminium oxide, and silicon dioxide sensors. The free fatty acids (FFA) stock solutions were prepared as presented in Table 4.1, Table 4.2 and Table 4.3. 0.2 ml of the FFA stock solutions were added sequentially to the system and the frequency shift observed to determine which FFA adsorbed more onto the sensor surface. Six sequencing experiments were conducted in the orders; OLP, LPO, PLO, POL, OPL and LOP. At the start of the experiment, an unused sensor was run for 30 minutes to determine the initial resonance frequency (baseline determination). After 30 minutes, 0.2ml of ethanol was added and the frequency allowed to stabilize for a further 30 minutes after which 0.2ml FFA stock solution of each FFA was then added every 10 minutes. This was done to observe the interaction of each fatty acid with the surface of the sensor and with other fatty acids using the Qsoft 401 software.

The experimental procedure for sequence Oleic acid Linoleic acid and Palmitic acid is shown below.

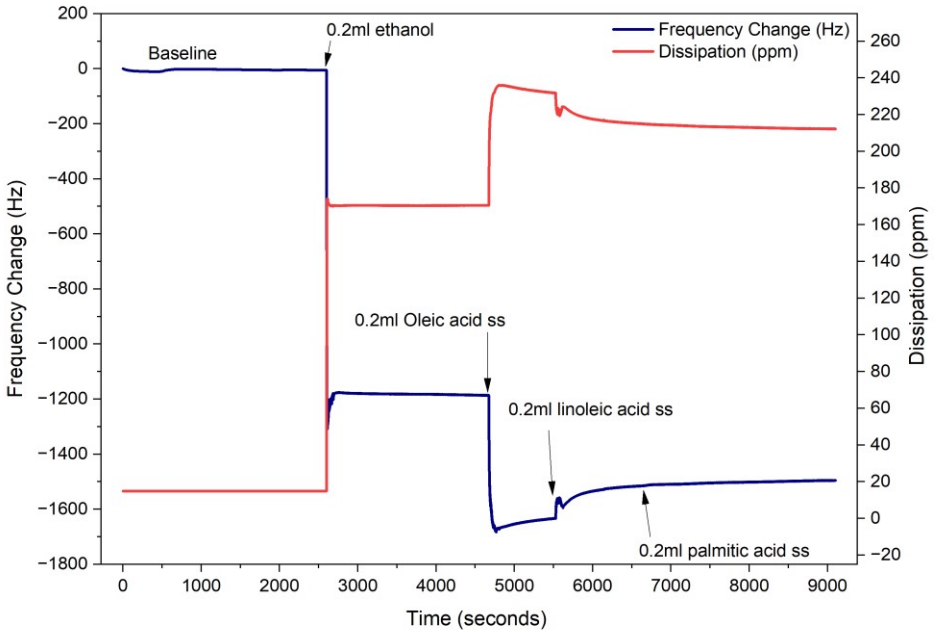


Figure 4.1 Oleic acid Linoleic acid and Palmitic acid injection sequence on a Polystyrene substrate sensor.

Figure 4.1 presents a plot of changes in frequency and dissipation for injection sequence oleic acid, linoleic acid and palmitic acid on a polystyrene sensor. The plots for order of injection are in the Appendix 8.2.1.

4.2.1.3 Characterization of samples

The surfaces were further characterized using Raman microscopy and Fourier transform infrared spectroscopy (FTIR). The confocal Raman microscope SENTERRA II was used with a wavelength of excitation laser beam of 532nm and laser power of 12.5mW and the magnification varied between 10 and 20. The settings were also adjusted to allow for better resolution and magnification depending on the sample. The spectral resolution of 4cm^{-1} and a spectral range of 50 – 4260 cm^{-1} were used to carry out the Raman measurements. 18 samples (6 for each material of the quartz sensor as shown in Appendix 8.2.1) were selected after QCM experiments for further testing and characterization of the evolution of the functional groups on the surface.

FTIR was also used for testing of fatty acids adsorption on a polystyrene substrate and assessing the evolution in the functional groups. The Agilent technologies Cary 630 FTIR spectrometer with an attenuated total reflectance (ATR) accessory was used. The spectral range was from 650-4000 cm^{-1} with a scan resolution of 2 cm^{-1}. The surface of the sample stage was wiped with wipes or Isopropyl alcohol (IPA) to ensure it was clean before and after

loading each sample for measurement. The FTIR tests involved a cocktail of the FFA in equal portions of 100mg/ml. Following this, the substrate sensors were rinsed with ethanol to remove any loosely bound FFA and allowed to dry in a petri dish. The sensors were characterized following drying in the petri dishes at room temperature and pressure. The waste solvent from rinsing of the sensor was also tested to confirm if any fatty acids were removed.

4.2.2 Results and Discussion

4.2.2.1 Effect of sequencing on different substrates

4.2.2.1.1 Polystyrene

The Figure 4.2 below presents ∆F measurements for the different FFA sequences. The experimental results showed that oleic acid gave the greatest change in resonance frequency indicating that more oleic acid adsorbed onto polystyrene than the other two fatty acids as shown in Figure 4.2. Palmitic acid was only adsorbed more onto the sensor only when it was added after oleic acid, otherwise linoleic acid is the second highest FFA to be adsorbed onto the surface of the sensor. The change in frequency was determined as follows:

$$\Delta F = F_{ethanol} - F_{FFA}$$

Equation 4.1

Appendix 8.2.1.1 presents the raw data for experiments involving polystyrene. The experiment with sequence PLO showed a step change with each addition of the fatty acids. However, for experiments with sequence OPL and LPO, a decrease in frequency was observed followed by and a positive shift in frequency. This shows that when palmitic acid was the second layer of fatty acid added, it started to displace some of the ethanol in the adsorbed film. This was accompanied by reduction in the dissipation for OPL and in LPO the dissipation and frequency remained the same. Oleic and linoleic acid are unsaturated hence were more fluid whereas palmitic acid is saturated and was more rigid (Kanicky & Shah, 2002). The physical interaction (van der Waals forces, hydrogen bonding, hydrophobic interactions) between palmitic acid and either oleic or linoleic acid in these sequences resulted in palmitic acid introducing its rigidity to the system. The third layer upon interacting with palmitic acid also had a reduction in dissipation and positive shift in frequency which suggested that the FFA were being desorbed from the surface. The same was not observed when palmitic acid was the last to be added in which very small changes in frequency was observed in the positive direction as when as small reductions in the dissipation. This meant the number of adsorption sites had already been filled hence addition of more fatty acid resulted in very negligible change/ no

change in the adsorption. This suggested that the interaction between fatty acids also affected adsorption as studied using QCMD.

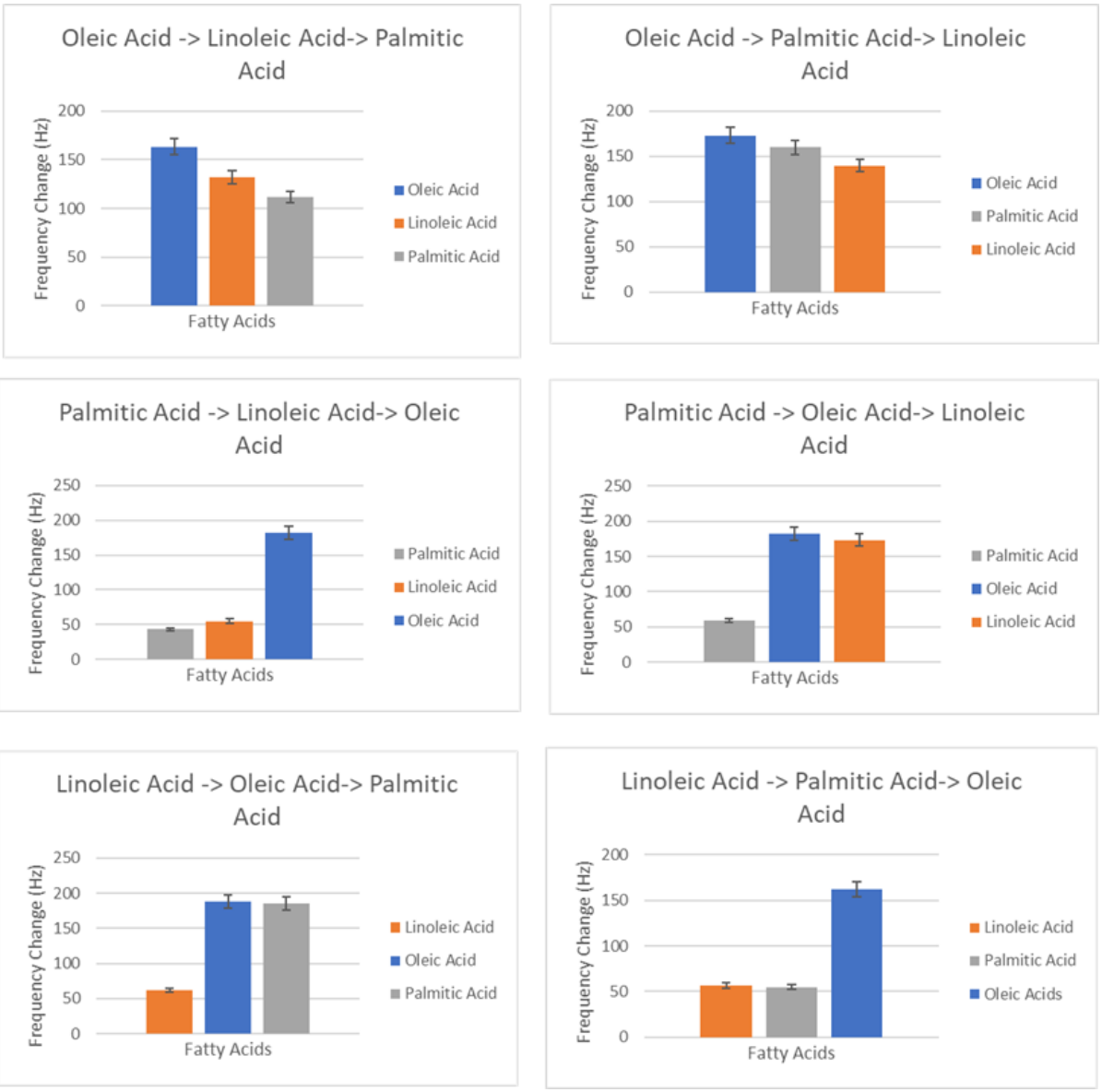


Figure 4.2 Shows ΔF for sequential addition tests of FFA on Polystyrene sensor substrate.

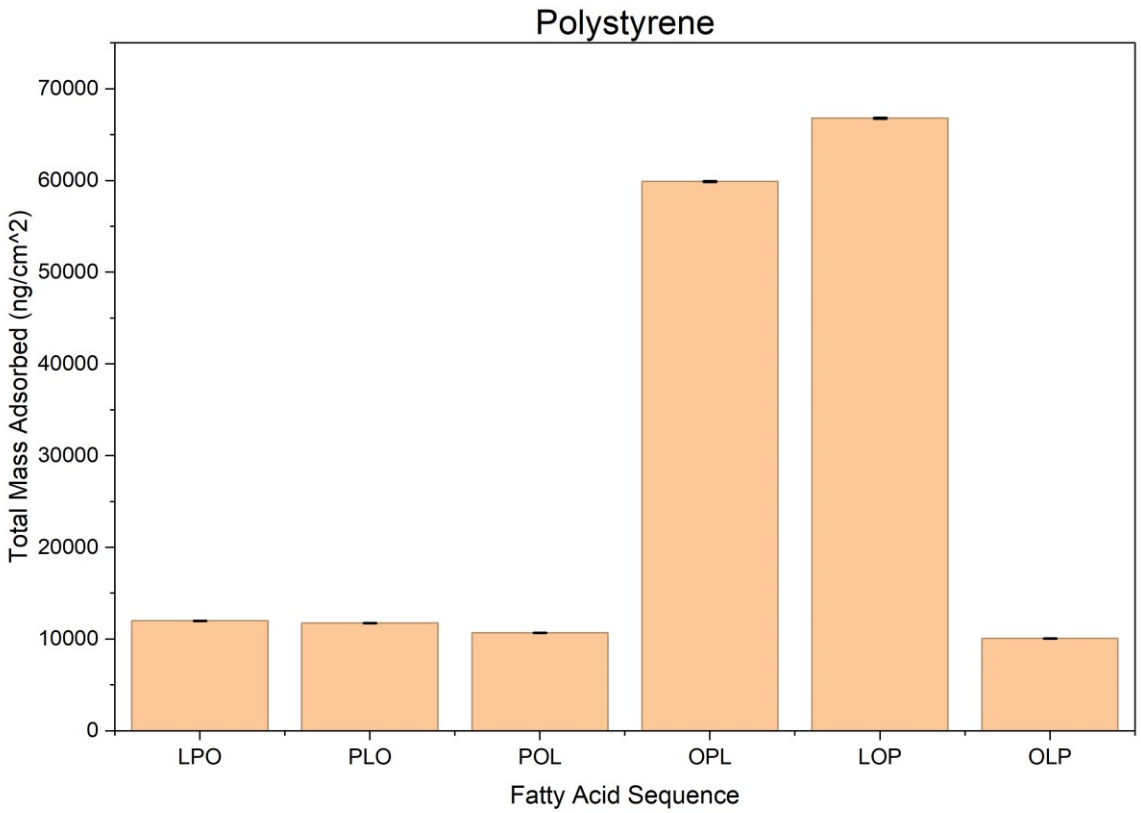


Figure 4.3 shows total mass adsorbed on Polystyrene sensor substrate at the end of each experiment

The Voight model was used to fit the data shown in Figure 4.2 to calculate the total mass adsorbed onto the polystyrene sensor at the end of each experiment. The results showed that sequence OPL and LOP adsorbed the most onto the sensor surface. However, during modelling, it was important to understand how well the data fit the Voight model. Some assumptions made by this model is that the adsorbed film formed a single homogeneous layer and had the same thickness. This may not clearly represent data where multilayer adsorption had taken place. The mass adsorbed shown in Figure 4.3 is the sensed mass not the absolute or dry mass of the fatty acids. This is because QCMD measures mass as hydrated mass which included the mass of ethanol coupled in between the fatty acid chains.

4.2.2.1.2 Silicon dioxide

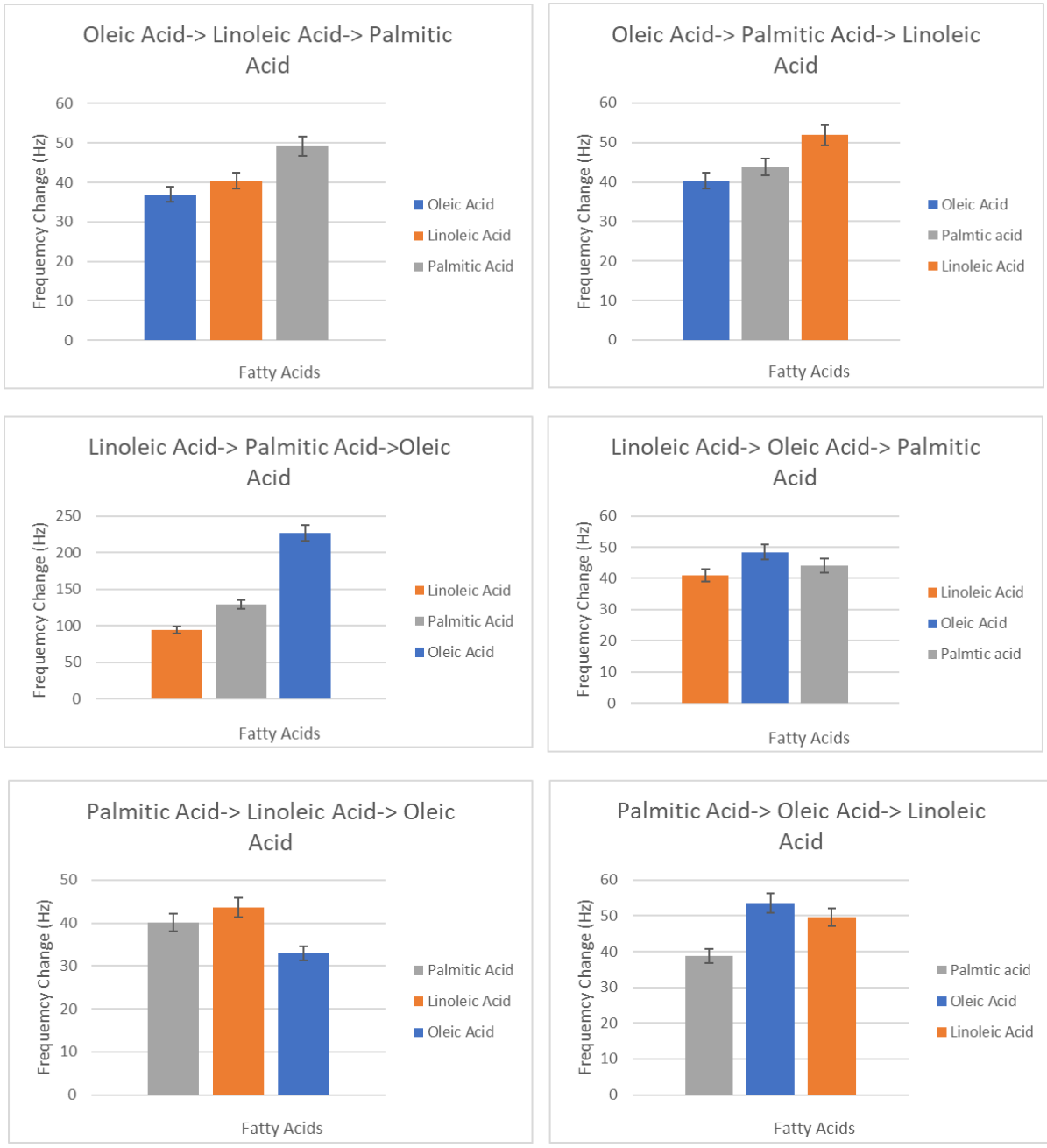


Figure 4.4 shows the total change in frequency of sequential addition of FFA onto Silicon Dioxide

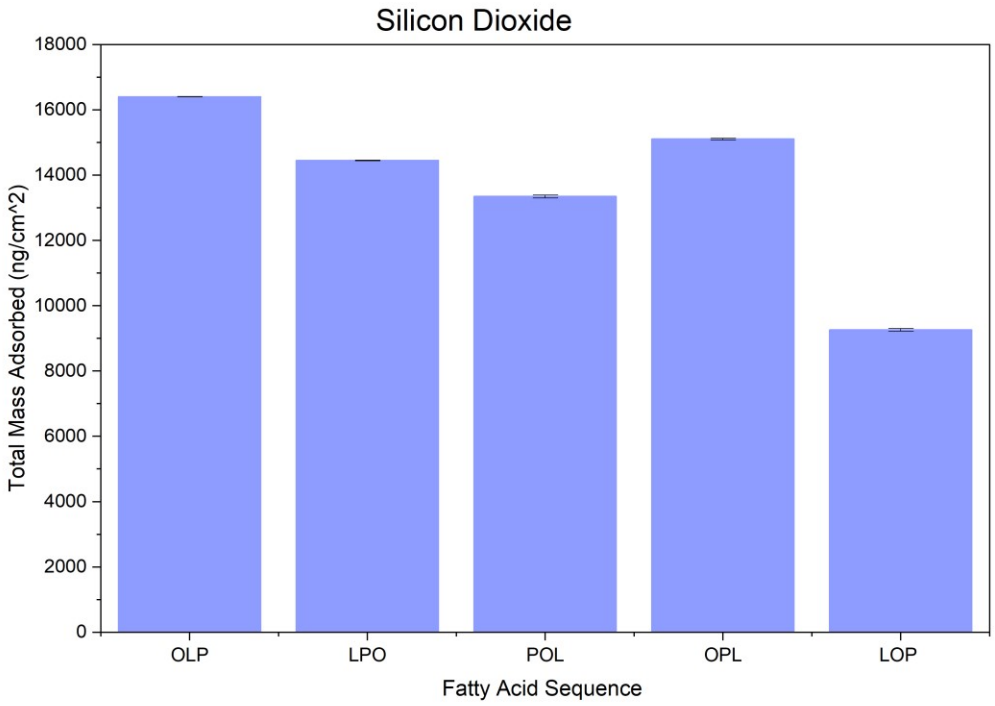


Figure 4.5 shows the total mass adsorbed due to sequential addition of FFA onto Silicon Dioxide.

The results for sequencing tests on a silicon dioxide surface have shown that on average, the frequency change is below 60Hz except for the sequence LPO as shown in Figure 4.4. The concentration used for silicon dioxide and polystyrene was 100mg/ml for each fatty acid. Hence as shown is the previous work on effect of concentration on adsorption, it was expected that reduced concentration would result in a decreased overall frequency change. The raw experimental results can be found in Appendix 8.2.1.2. The baseline for these tests was determined by starting the experiment with a clean sensor, this was followed by the addition of ethanol. Once the frequency of ethanol had stabilised, the experiment was reset to establish the baseline of ethanol as 0Hz. This shift in the position of ethanol enabled the change in frequency to be calculated from the baseline.

The stock solutions are made by dissolving fatty acids in ethanol. However, the fatty acids are amphiphilic i.e., having a carboxyl group which is hydrophilic and a hydrocarbon chain that is hydrophobic. This meant that fatty acids were only partially soluble in ethanol. The mixing and solubility of ethanol was promoted by hand shaking the mixture. Higher concentration of the fatty acids required more mixing time particularly palmitic acid as it is a solid at room temperature. For the esterification reaction in Equation 4.2 to occur, high temperatures e.g. at 80ºC and a catalyst would be needed (Cannilla et al., 2018). This was not the case for this work. The experiments were operated at room temperature and without the presence of a catalyst. It is assumed that there was no presence of any esters in the system.

$$C_8H_{17}CH = CH(CH_2)_7COOH + CH_3CH_2OH \leftrightarrow C_8H_{17}CH = CH(CH_2)_7COOC_2H_5 + H_20$$

(Cannilla et al., 2018)

FFA + Ethanol ↔ Ethyl Esters + Water

Equation4.2

LPO results were particularly interesting as they showed frequency change never stabilized after addition of each fatty acid. It also had the highest change in both overall frequency and dissipation as shown in Figure 4.6. On addition of linoleic acid, the fatty acid chain started to stretch out. This allowed it to trap more solvent(ethanol) between the chain thus making the layer softer. The addition of palmitic acid showed a similar profile. The fatty acid interacted with linoleic acid however since palmitic acid is a bit rigid ∆F for this step was not as large as for step 1 when linoleic acid was added. Addition of oleic acid showed a very large change in frequency and showed that the fatty acid chain was also stretching out and coupling more solvent creating a softer/thicker layer. All these were supported by the mirroring results of the dissipation. Increases in energy losses showed that the film became thicker and softer (Biolin Scientific, 2020). This was the reason for higher frequency changes as opposed to the other sequences because of more coupling of solvent contributing to the stretching out of the fatty acid chain to form brush-like conformation. Similar results have been obtained in polymer grafting studies onto surfaces (Biolin Scientific, 2020). Three slopes indicated the three steps with each fatty acid addition onto the previous layer (multilayer coverage).

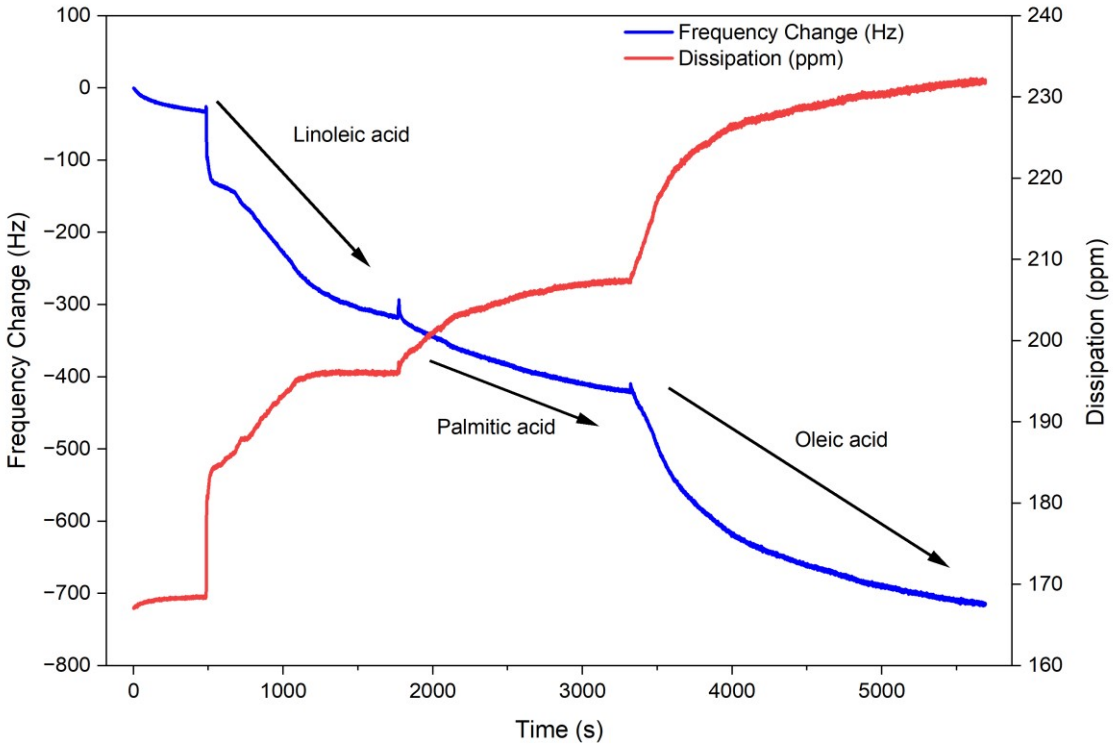


Figure 4.6 Shows sequencing of Linoleic acid Palmitic acid and Oleic acid QCMD experimental results.

The sequences OLP and OPL also showed a step increase in frequency change on addition of each fatty acid into the system. The last fatty acid added was found to contribute to the largest change in frequency thus mass adsorbed. Depending on the order of addition, all three free fatty acids (including LPO) had a significant impact on the adsorption onto the silicon dioxide surface. The results suggest that given a longer time, more adsorptions would take place. LOP has two layers. The addition of palmitic acid did not result in frequency change suggesting oleic acid and palmitic were just reordering themselves in that layer. POL has two layers followed by a desorption. The desorption was because of the expelling of ethanol trapped within the adlayer. This caused the film to collapse, and this was measured as the positive shift in frequency and a reduction in dissipation energy. This also meant the top layer was less soft that the previous layer. PLO had a single layer (monolayer coverage). The signal fluctuated by about 10Hz for the entire experiments which also suggested the fatty acids just reordered themselves on the substrate surface. Bearing in mind palmitic acid is relatively rigid, this also contributed to less of the other fatty acids being adsorbed.

4.2.2.1.3 Aluminium Oxide

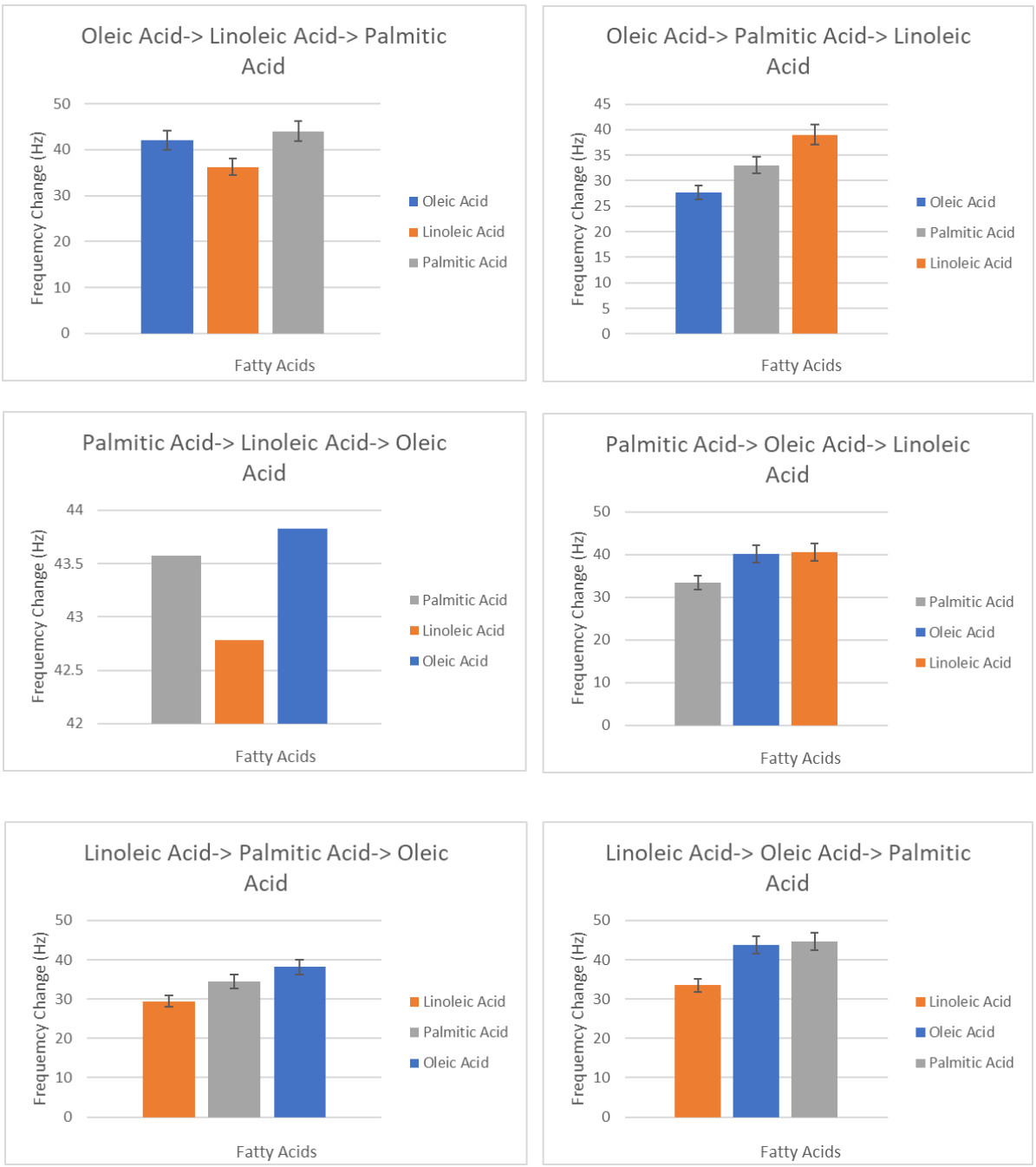


Figure 4.7 shows ΔF for sequential addition of FFA onto Aluminium Oxide.

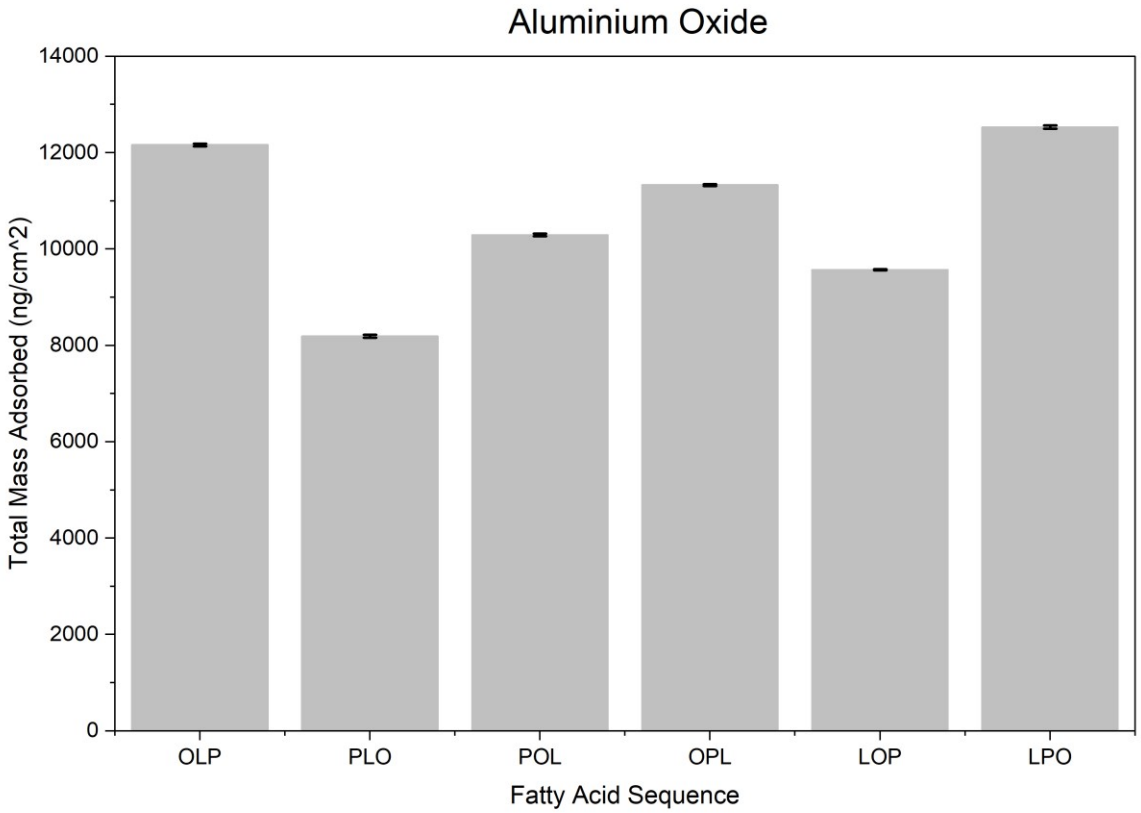


Figure 4.8 Total mass adsorbed due to sequential addition of FFA onto Aluminium Oxide.

Aluminium oxide sensor substrate was used to examine the sequential addition of oleic acid linoleic acid and palmitic acid and how this would affect the adsorption/binding of the fatty acids to the surface and to the adlayer. A step increase in the total frequency change was observed for sequences OPL and LPO as shown in Figure 4.7. Sequence LPO exhibited a different step change to OPL as shown in Appendix 8.2.1.3. The frequency decreased rapidly on addition on linoleic acid for sequence LPO. Within the 10min before addition of palmitic acid, linoleic acid started to reorganize on the surface as shown by a positive shift in frequency. This suggested that the layer was less soft. Addition of palmitic acid and oleic acid saw the signal also exhibiting the same behaviour as linoleic acid. Sequences LOP and POL showed that addition of the last layer of FFA did not result in a change in the total frequency while sequences OLP and PLO showed that addition of the second layer of FFA resulted in a desorption as shown by a positive shift in frequency (the mechanism for this has already been explained with silicon dioxide substrate tests).

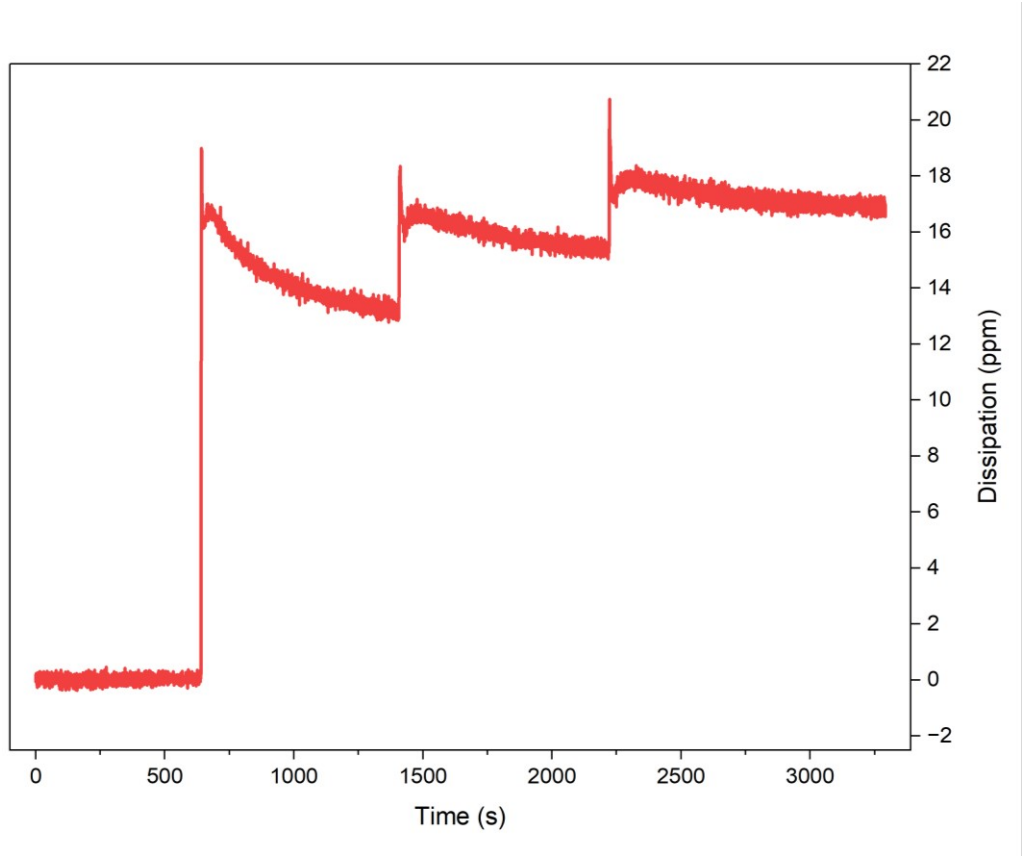


Figure 4.9 shows Changes in dissipation energy for LPO.

The dissipation energy losses of the sequence LPO on addition of each fatty acid are shown in Figure 4.9. Changes in frequency do not always directly correlate to information about the materials properties such as viscosity, elasticity , density etc. It was important to then focus on the dissipation energy as it tends to be more sensitive and can give a better insight about changes within each adlayer particularly for layers falling outside of the Sauerbrey model as shown Dunér et al. (2013) on their work on growing Poly(acrylic acid) films where the Voight model was used to study the changes from the QCM data obtained. Like this work, the spread in the overtones (Figure 4.10) indicated that the layer was soft and required different approach from Sauerbrey.

D-find software was used to model changes in the adlayers using experimental data and application of the Voigt model. The software was configured using Table 4.4. The baseline and bulk fluid were set to that of ethanol at room temperature and pressure. Period borders were placed when the first change in frequency and dissipation was observed for the 3rd, 5th and 7th overtone. The period borders represent the point at which a change occurred. Changes in frequency and dissipation do not always indicate adsorption or desorption i.e. for thick hydrated films, ΔF can be nonlinear therefore it is much better to monitor changes in dissipation due to its sensitivity to thick films (Dunér et al., 2013; Poitras & Tufenkji, 2009).

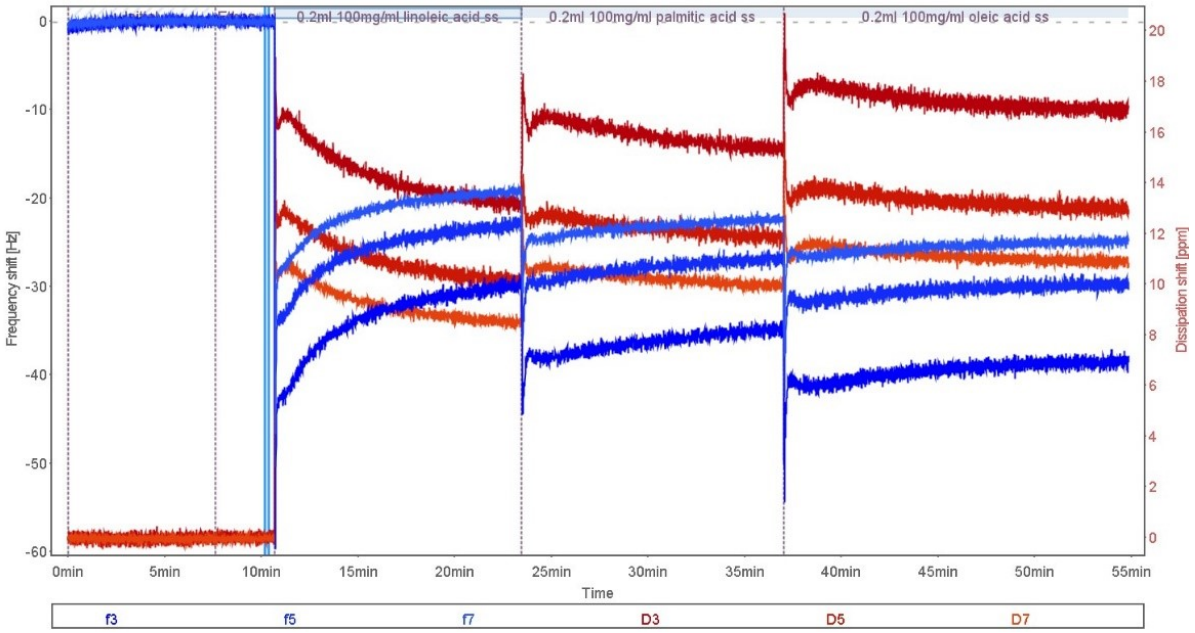


Figure 4.10 shows frequency and dissipation over different harmonics for sequence LPO.

Table 4.4 shows configuration settings for LPO on D-find.

Period	Name	Type	Layer	Bulk Liquid
1	Ethanol	Reference	No layer changes	
2	0.2ml 100mg/ml Linoleic acid	Fit	Linoleic acid (902g/L)	Ethanol 25ºC (784g/L)
3	0.2ml 100mg/ml Palmitic acid	Fit	Palmitic acid (853g/L)	Ethanol 25ºC (784g/L)
4	0.2ml 100mg/ml Oleic acid	Fit	Oleic acid (890g/L)	Ethanol 25ºC (784g/L)

Figure 4.10 showed that an instantaneous decrease (∆F 60.0Hz) in frequency was observed upon the addition of linoleic acid ss. The fast change in ∆F might suggest fast kinetics however, a positive shift frequency to about 45.0Hz was observed. The initial sharp decrease in frequency at the start of each period suggests that the linoleic acids had a high affinity to the surface. At 45.0Hz, the frequency continued to shift gradually in the positive direction to 30±0.0426Hz.The dissipation energy also increased (∆D 19.0ppm) rapidly upon addition of linoleic acid and then gradually decreased to a ∆D value of 13.2±0.0172ppm. This suggests that while linoleic acid had initially quickly adsorbed to the surface forming a formed thick soft viscoelastic and solvent rich layer (Nanoscience Instruments, 2025), the decrease in ∆D indicated that the layer became less soft as reordering of linoleic acid chains gradually resulted in the expulsion of the ethanol coupled between the chains. Kou et al. (2010) reported that

change in orientation of molecules may result in expulsion of solvent resulting in a more rigid layer thus explaining the changes in frequency and dissipation.

Addition of palmitic acid saw ∆D increase to 15.4±0.0185pmm and then to 16.8±0.0169ppm once oleic acid was added. The dissipation energy remained relatively stable within the layers for both palmitic acid and oleic acid layers while a slight increase in frequency within the layers was observed. Kou et al. (2010) at the end of the remaining periods, ∆F was 35.0±0.0416Hz for palmitic acid and ∆F 38.6±0.0428Hz for oleic acid. The ∆D between layers of fatty acid added became smaller with each fatty acid layer added e.g. ∆D between palmitic acid and oleic acid was 1.47±0.03ppm suggesting that the adsorbed layers became increasingly more rigid.

The changes described above meant that the classic Sauerbrey could not be used to explain or calculate these changes. Thus, the more complex Voigt model was used through D-find Smartfit. The fitting of this model has already been described elsewhere in literature (Voinova et al., 1999).The mass adsorbed when linoleic acid ss was added was 12637.1±45.6ng/cm^3 which then reduced to 11862.4±41.1ng/cm^3 for the palmitic acid layer. The adsorbed mass increased further to 12141.4±35.7ng/cm^3 once the third layer of oleic acid was adsorbed. The mass calculated in D-find is the hydrated mass and not the absolute dry mass of the fatty acid films. As explained above, the structure of the fatty acids affected the sensed mass. Linoleic acid was very flexible due to the presence of two double bonds; this made it easier for ethanol to be trapped in the monolayer, hence having the highest sensed mass. Palmitic acid is a saturated fatty acid hence was tightly packed together (Kanicky & Shah, 2002). This expelled solvent from the adsorbed film resulting in a lower sensed mass than before. When Oleic acid ss was added, the mass increased indicating again that the adsorbed layer became more fluid.

For most sequences, palmitic acid was adsorbed the least to the surface, the exception being when it was added first in the sequence as shown in appendix 8.2.2.3. Figure 4.8 compares the total mass adsorbed from all sequences and confirms that sequences starting with palmitic acid ss had the lowest mass adsorption as compared to when an unsaturated fatty acid started the sequence. One of the main concerns when calculating the mass adsorbed of viscoelastic materials using QCMD is whether the sensed mass is because of viscous effects caused by the bulk fluid or the mass of the adsorbed film onto the substrate sensor. Hodges et al. (2020) in their work were able to show that when the measured frequency shifts for multiple overtones were there the same, the bulk fluid was being measured and not the adsorbed species at the sensor surface. This of course was not the case in this work where the frequency measurements over multiple overtones were not the same as shown in Figure 4.10. This

helped to assert that the measured frequency and dissipation shifts were because of the adsorbed fatty acid layers at the surface.

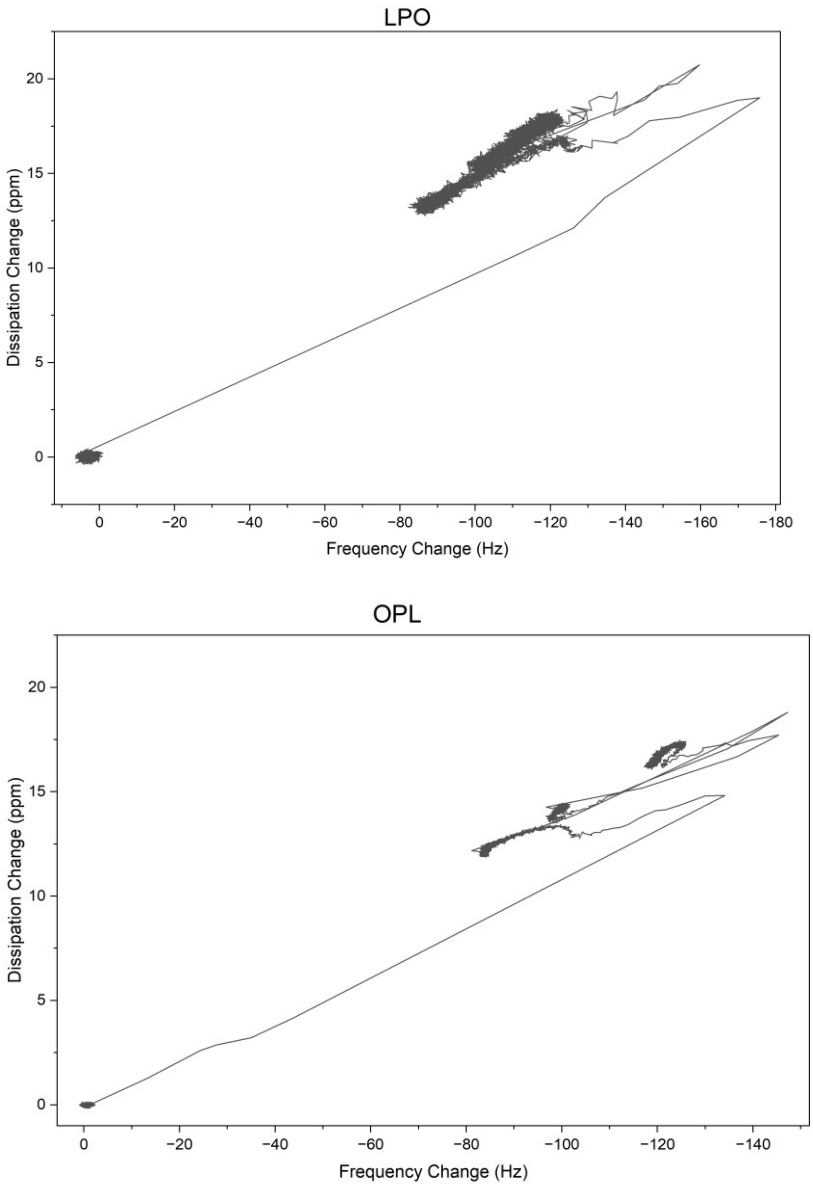


Figure 4.11 Dissipation vs Frequency plots for sequence LPO and OPL on aluminium oxide.

Figure 4.11 shows the graph for dissipation vs frequency. They provide information on the energy dissipated per unit mass added to the sensor (Paul et al., 2008; Kou et al., 2010). These graphs are important for explaining conformational change that occurred during the experiments (Paul et al., 2008; Yang et al., 2024). The slope of the graphs has been defined as K where $K=\Delta D/\Delta F$. A small K value is associated with a more rigid layer while a large K value is associated with a soft hydrated layer. From literature, it is understood that one slope is associated with the adsorption process. More slopes are indicative of a change in the orientation or coupled solvent to the adsorbed layer (Rodahl et al., 1997; Paul et al., 2008;

Kou et al., 2010). The results show three slopes on the graphs. Each line represents each fatty acid during the sequential addition of the fatty acid for LPO and OPL. The first slope showed the adsorption of the fatty acid onto aluminium oxide. The value of K was larger for the first slope in sequence OPL than LPO. This was expected as the dissipation data showed gradually reduced following the adsorption of linoleic acid onto aluminium oxide. Lundgren et al. (2006) reported that oleic acid adsorbed parallel to a steel sensor while linoleic acid adsorbed perpendicular. This meant more solvent was expelled from the adlayer as linoleic acid re-ordered on the surface. This explains why the K value was slightly lower for linoleic acid than oleic acid thus oleic acid had a more dissipated layer than linoleic acid. The K value for Oleic acid was slightly higher than for linoleic acid as oleic acid adsorbed parallel to the sensor making it less flexible to expel or couple more ethanol than linoleic acid. The K values of the second slope showed palmitic was less rigid when added to oleic acid than linoleic acid. Lastly, the K value was largest for slope three in the sequence OPL than LPO suggesting linoleic acid coupled more solvent than oleic acid resulting in a softer layer more dissipated layer.

Table 4.5 K values calculated from the slope of ΔD /ΔF at the 3rd overtone.

Sequence	Slope 1	Slope2	Slope3
LPO	0.39	0.29	0.27
OLP	0.40	0.09	0.32
LOP	0.38	0.38	O.40
POL	0.40	0.44	0.35
PLO	0.40	0.29	0.34
OPL	0.40	0.33	0.38

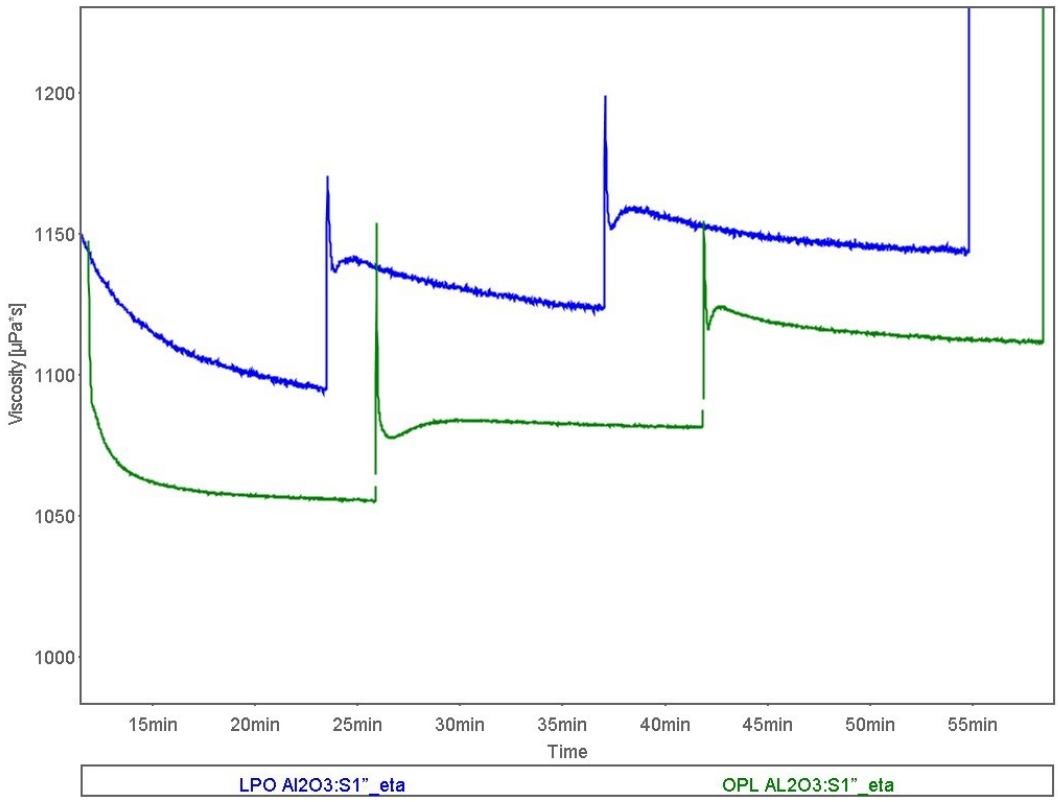


Figure 4.12 Viscosity changes of the sequences LPO and OPL as calculated by Voight.

Table 4.6 Total Viscosity of Adsorbed layer calculated using the average viscosity of shift of the last fatty acid added.

Sequence	Viscosity (µPa*s)
OLP	45.590 ± 0.045
PLO	19.066 ± 0.256
POL	5.864 ± 0.104
OPL	30.371 ± 0.037
LOP	6.825 ± 0.073
LPO	18.374 ± 0.068

Application of the Voight model to analyse changes in frequency and dissipation during film formation on the quartz sensors has been used in literature for extracting information of the shear viscosity and elastic modulus of the adsorbed film (Dunér et al., 2013; Hodges et al., 2020; Setiowati et al., 2021). Figure 4.12 showed the viscosity changes within the adlayer as a function of time during FFA addition. The results presented here show that viscosity changes followed the same trend as the dissipation from the measurements of sequential addition of the FFA. The viscosity did not remain the same throughout the experiments which was expected due to the presence of fatty acids which behave as non-Newtonian fluids. This

change in viscosity also suggests that the measured mass was primarily due to the influence of the fatty acids and not the bulk.

The acoustic ratio was 0.45 for LPO and remained relatively constant throughout the experiment. Suggesting that soft hydrated layers were adsorbed onto the surface. The highest viscosity was measured for sequences starting with oleic acid reported in Table 4.6 with the lowest viscosity of the layer measured when oleic acid was second in the sequence. Lundgren et al. (2007) had suggested that oleic acid having a higher viscosity than linoleic acid affected the corrections they made to bulk effects by a greater extent allowing for calculation of the true sensed mass. In this case it remains unclear why the total viscosity of the adsorbed layers was highest for sequences starting with oleic acid as palmitic acid has the highest viscosity followed by oleic acid and lastly linoleic acid. However, I was able to deduce that the order of adsorption of the fatty acids affects the overall viscosity by varying amounts. Why specific orders resulted in higher measured viscosity remains for future research.

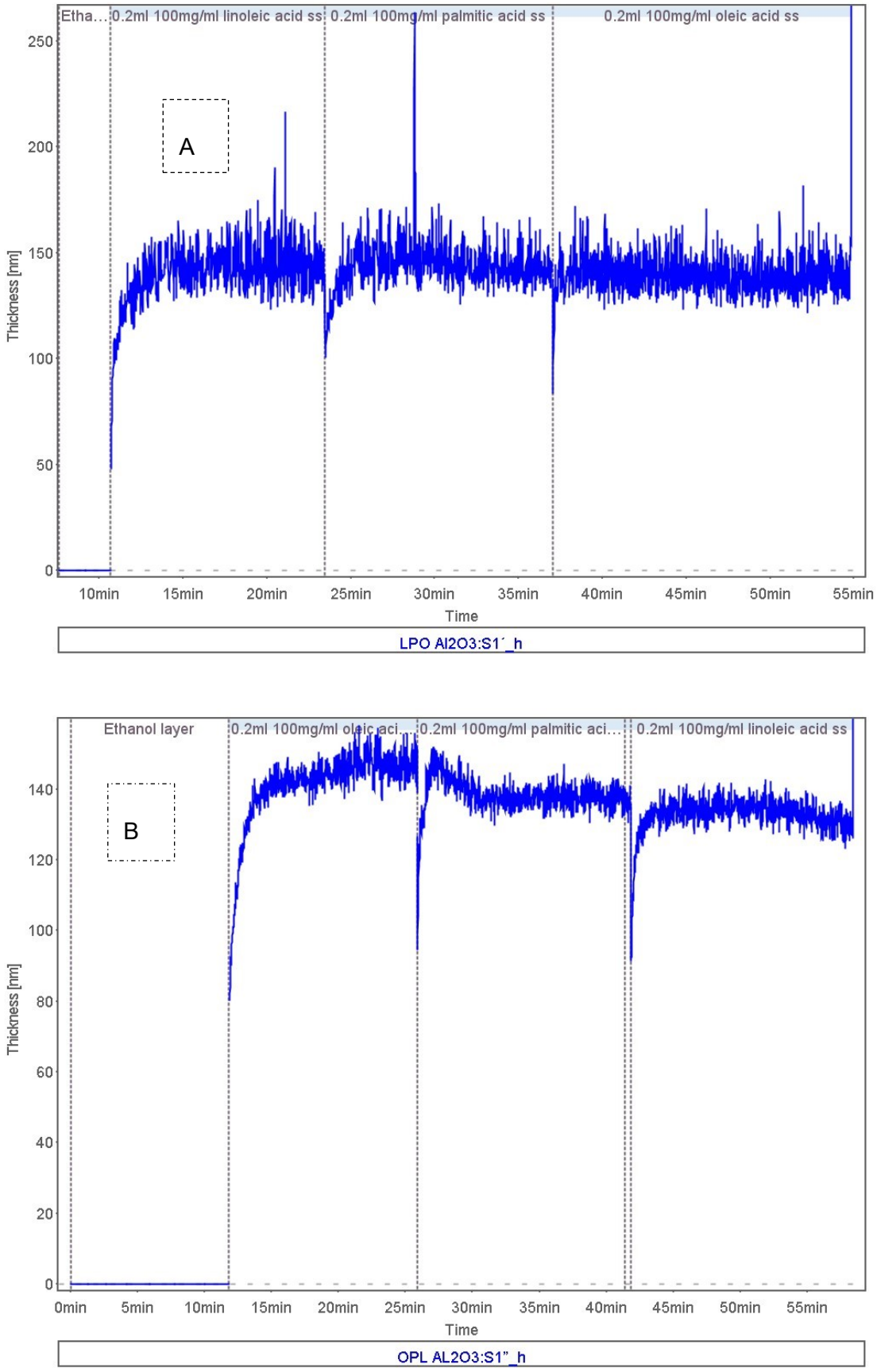


Figure 4.13(A) and (B) show the Voigt thickness of the adlayer for sequence LPO and OPL

The thickness of the adsorbed layer as calculated by Voight it presented in Figure 4.13. The results shows that three layers have been added onto aluminium oxide sensor. For sequence LPO, the average thickness within each layer was 146.21±0.60nm , 143.62 ±0.42nm and 140.79±0.41 nm. Figure 4.13 (B) showed that the thickness within each layer was 137.24±0.23nm, 131.76±0.22 and 125.60±0.22nm for oleic acid, palmitic acid and linoleic acid respectively. The total thickness (Figure 4.140 of the adsorbed layers showed that more fatty acid was adsorbed for sequence OLP and LPO with the lowest thickness recorded for sequences starting with palmitic acid probably due to its tendency to pack closely together. Lundgren et al. (2007) reported that linoleic acid at high concentrations had adsorbed perpendicular to the surface thus forming and extended layer while oleic acid on extended slightly from the surface influencing more mass to be measured for linoleic acid than oleic acid. However, when the unsaturated fatty acids are adsorbed sequentially, sequence OLP formed a thicker layer than LOP. When linoleic acid was first in the sequence, the effect of palmitic acids nature for close packing was much less than when palmitic acid followed oleic acid in the sequence. This was because of linoleic acids ability to form a more extended layer coupling more solvent than oleic acid. Generally, the results showed that when unsaturated fatty acids started the sequence, a thicker layer was formed on aluminium oxide than when palmitic acid started the sequence because of more solvent (ethanol) being coupled in between the fatty acid chains.

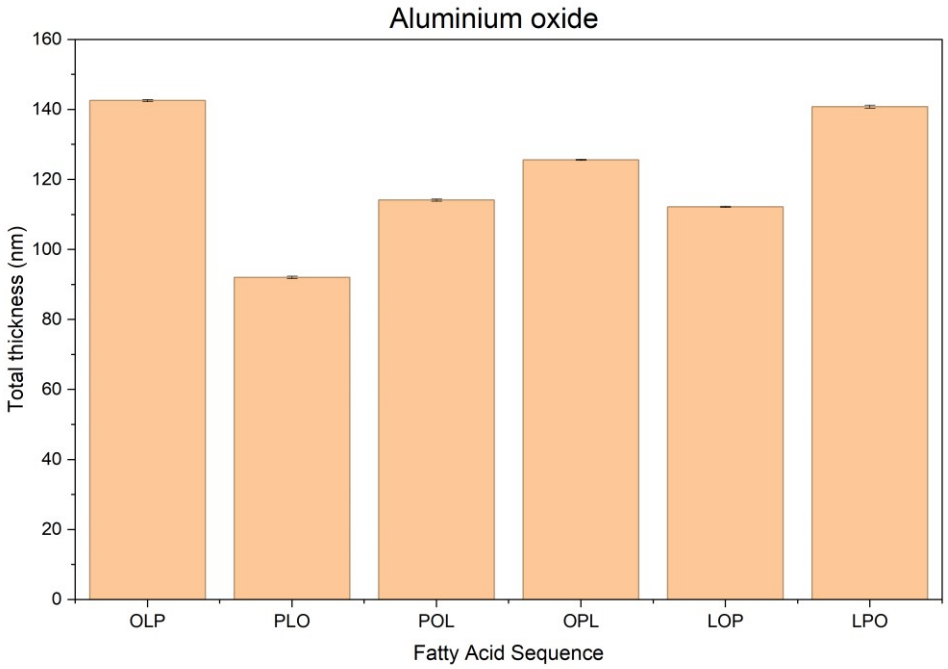


Figure 4.14 Total thickness of FFA adsorbed calculated as the average shift of the last period i.e. fatty acid added.

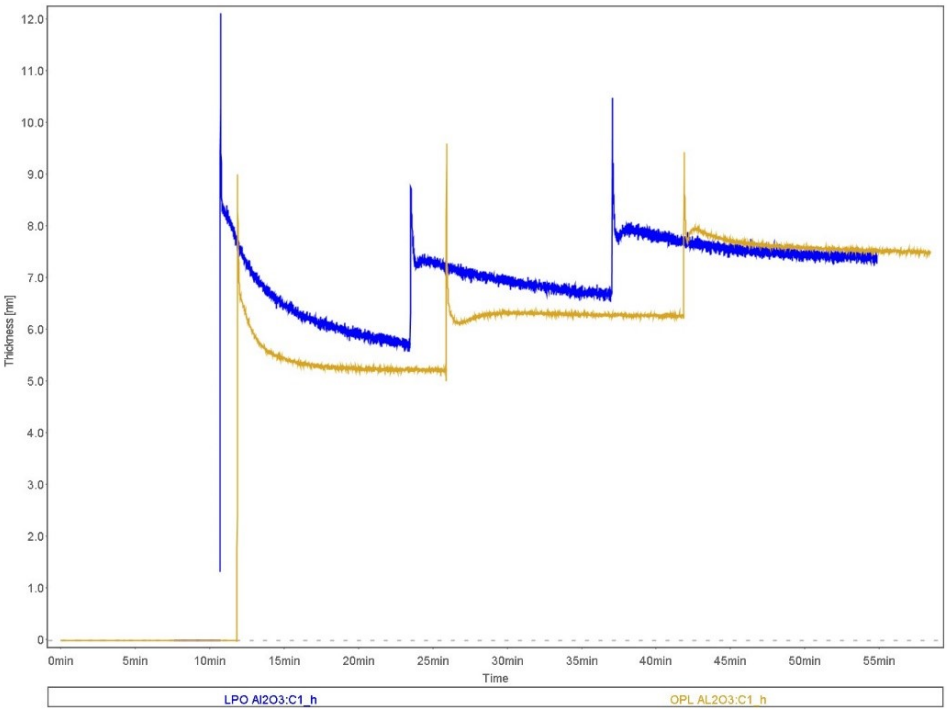


Figure 4.15 shows Sauerbrey mass for LPO and OPL.

Table 4.7 Total thickness of adsorbed layer calculated by Sauerbrey equation at the 3rd overtone.

Fatty Acid Sequence	Thickness (nm)
OLP	9.363 ± 0.006
PLO	9.054 ± 0.006
POL	8.275 ± 0.007
OPL	7.759 ± 0.002
LOP	9.414 ± 0.003
LPO	7.75 ± 0.006

The Sauerbrey model was used to calculate the thickness of the layer to compare with the thickness calculated by the Voight model. From the results shown in Figure 4.15, it was evident that Sauerbrey model underestimated the thickness (Table 4.7). Many authors in literature reported that the Sauerbrey model is not suitable for modelling measurements where $\Delta D > 0$ and the layers are soft thick and hydrated (Setiowati et al., 2021; Dunér et al., 2013; Plikusiene et al., 2022). As this was the case in this work, the application of Sauerbrey to model the data was abandoned.

4.2.2.2 Raman microscopy

Raman microscopy was used to investigate the surface heterogeneity and composition of silicon dioxide and aluminium oxide following the sequencing tests. The 'Fingerprint' method was used by comparing the Raman spectra obtained from the sample to a reference spectrum which was possible as the energy of the light is proportional to the wavenumber hence the vibrational states of a molecule (Anton Paar, 2024).

4.2.2.2.1 Silicon dioxide

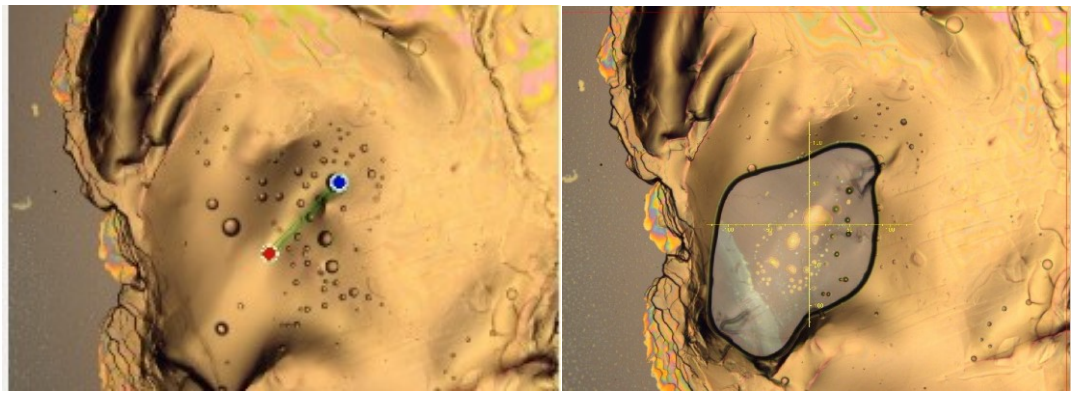


Figure 4.16 Images taken by the Raman microscope during analysis of Silicon dioxide sensor flowing sequencing experiment OLP (A) before analysis (B) shows degradation of the sample after analysis.

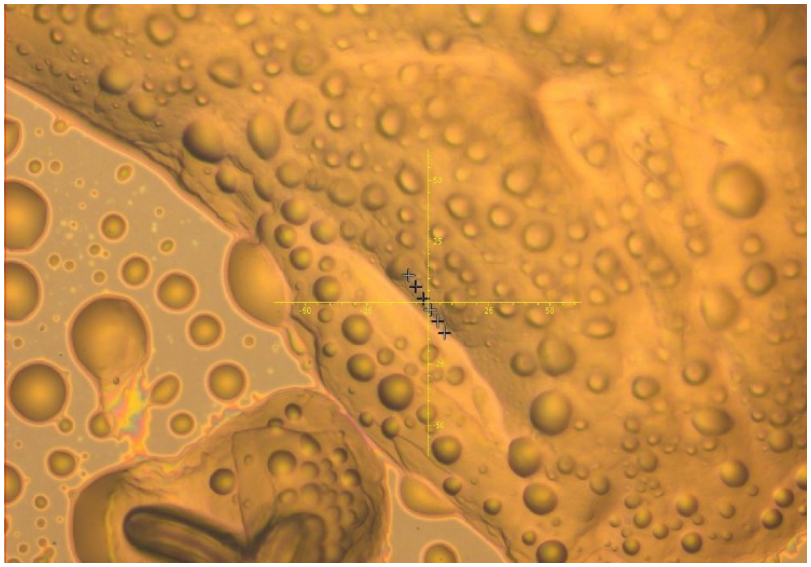


Figure 4.17 Raman microscope image of sequence POL on Silicon dioxide surface

The microscopic images were captured by the Raman microscope during analysis of silicon dioxide. It was determined in section 2.4.1.1 that palmitic acid adsorbed to surfaces via

chemisorption of -COOH from palmitic acid with the surface. At higher concentrations, aggregates of palmitic acid were observed on the sensor. Analysis of silicon dioxide during sequencing experiments revealed palmitic acid aggregates formed hills on the surface appearing as platelike structures alongside round deposits (oleic and linoleic acid). They highlight how the topography of the substrate sensor changes owing to the adsorption of the fatty acids. Figure 4.16 shows that the plate like structures dominated when palmitic acid was added last in the sequence as compared to Figure 4.17 where irregular shapes of fatty acids and some spherical shaped droplets are observed on the sensor. The morphology of silica nanoparticles modified by adsorption of oleic acid has been presented elsewhere in literature (Li & Zhu, 2003). While the shape of the adsorbed film was able to be observed using Raman microscopy, studies of the surface roughness owing to adsorption were beyond scope of this work. To the best of my knowledge, the chemical composition of silicon dioxide and aluminium oxide modified by adsorption of oleic acid linoleic acid and palmitic acid in competitive adsorption studies is presented here for the first time.

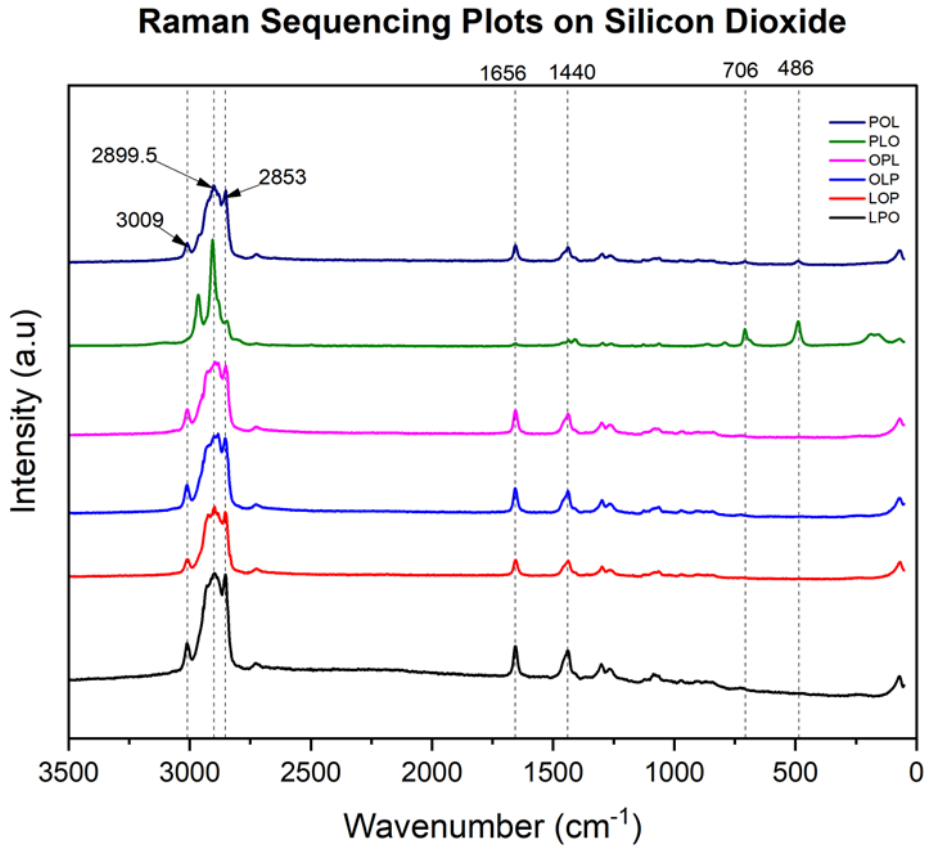


Figure 4.18 Raman spectra for adsorbed sequences on silicon dioxide sensor.

Figure 4.18 shows the Raman shift measurements of the silicon dioxide substrates sensors. Key bands identified were the 1440 cm^{-1} indicating a CH_2 bend peak for the saturated parts of

the fatty acid chains. The shape of this bend was dependent on the environment/ fatty acid being adsorbed. For example, pure palmitic acid tablet Raman spectra had this moiety present, however, the shape of the band was different compared to when the fatty acid was part of the sequencing test and adsorbed onto silicon dioxide surface as shown by the yellow region in Figure 4.19.The region 1400-1500cm^{-1} also has 3 peaks for palmitic acid but only has 1 peak for the sequencing test.

All sequences contained the 1440cm^{-1} peak excluding the PLO sequence where the intensity of this peak is very low. Bands 1656 cm^{-1} and 3009 cm^{-1} are also well-known fatty acids markers with vibrational modes relating to the C = C double bond (HORIBA Jobin Yvon , 2017; Traces Centre, 2021). In the case of adsorption onto silicon dioxide, the bands were not present again for sequence PLO. The other peaks 486 cm^{-1} which the Si-O-Si peak and 706 cm^{-1} C-C aliphatic were present in PLO and not in the other sequences. Using the palmitic acid spectrum as a 'fingerprint' , it is evident from the green highlighted regions that some bands present in pure palmitic acid are not present when all the fatty acids are adsorbed onto silicon dioxide substrates as shown in Figure 4.19.

The intensity of all the spectrum from the sequencing test were also very low compared to the pure fatty acid. Chiu et al. (2017) argued that the 2850cm^{-1} band (CH_2) is a better reliable indicator for a fatty acid however, considering the nature of the substrate (solid silicon dioxide sensor with oleic acid and linoleic acid (liquid) and palmitic acid which comes out of ethanol solution upon contact with a surface (solid), the band was slightly shifted and also considering that the carbonyl band tends to be a lot weaker in Raman than in the Infrared spectra, the peak is usually found between 1625cm^{-1} to 1687cm^{-1} (C=O) in Raman (Lin-Vien et al., 1991). The presence of bands 2853 cm^{-1}, 1656cm^{-1} and 1440 cm^{-1}, are indicators of the presence of fatty acid chains especially in this case when their intensity was weaker compared to the pure fatty acid. The OH stretching is typically found between 2800 and 3100cm^{-1} in this case.

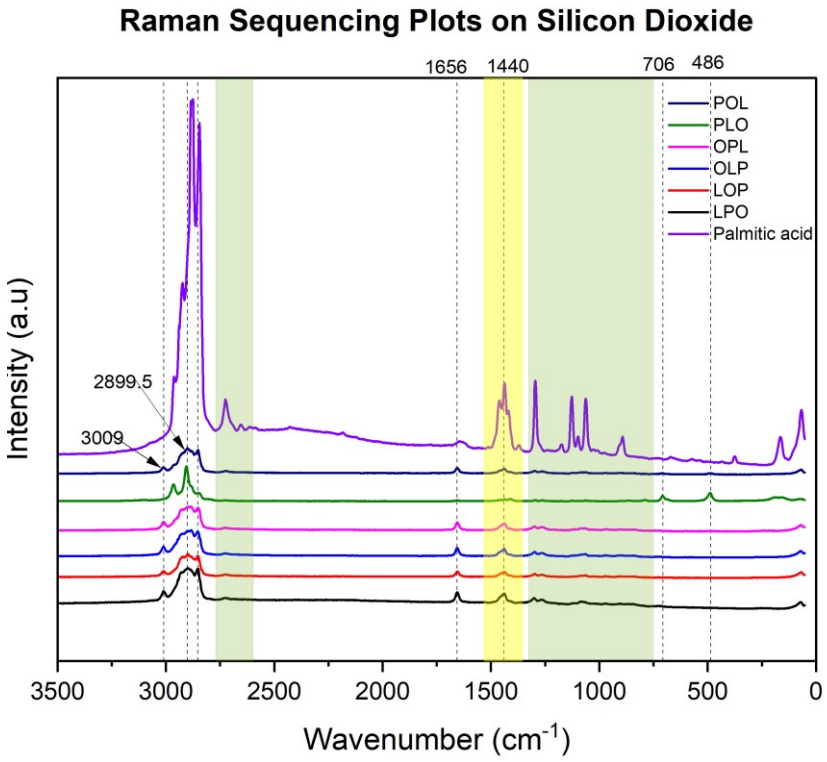


Figure 4.19 Raman Spectra of Palmitic Acid with those of the sequencing tests.

4.2.2.2.2 Aluminium Oxide

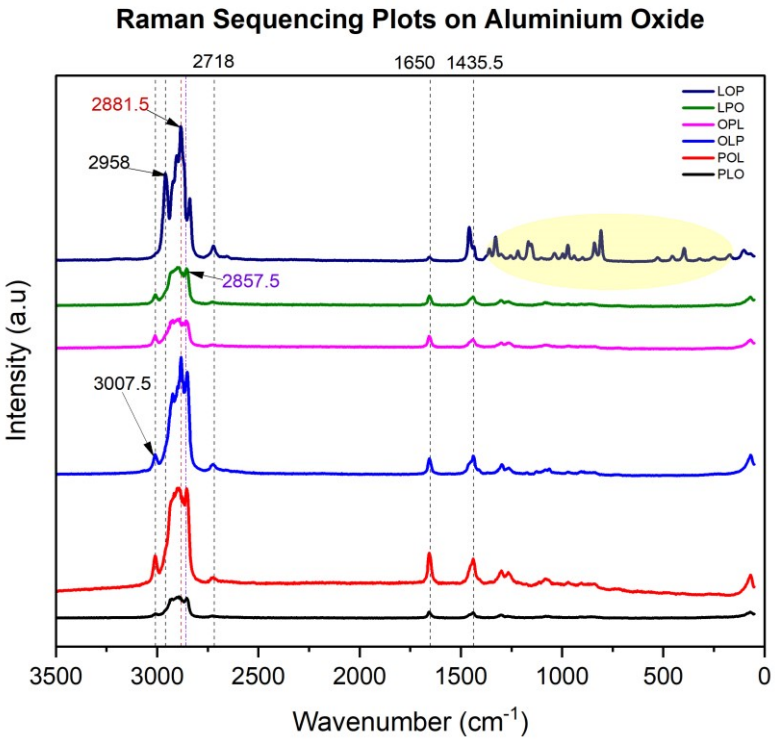


Figure 4.20 Raman shift sequencing plots on Aluminium oxide sensor substrates.

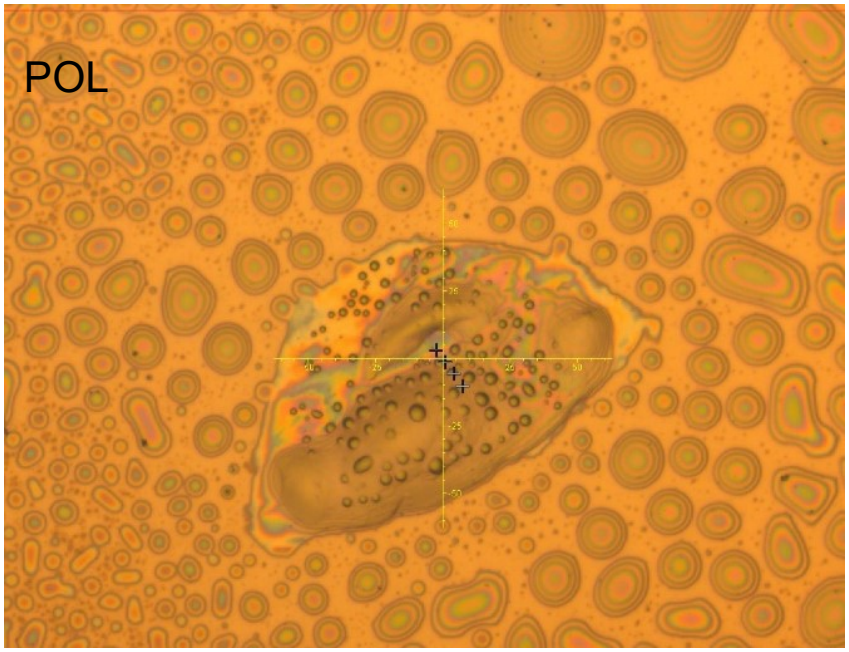


Figure 4.21 shows the Raman microscope image sequence POL.

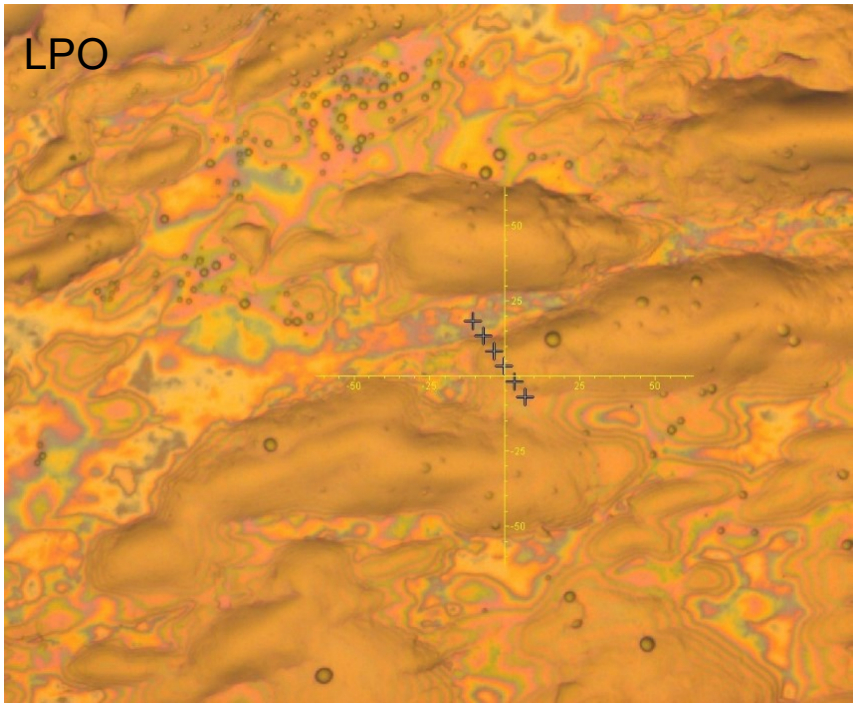


Figure 4.22 shows the Raman microscope image sequence LPO.

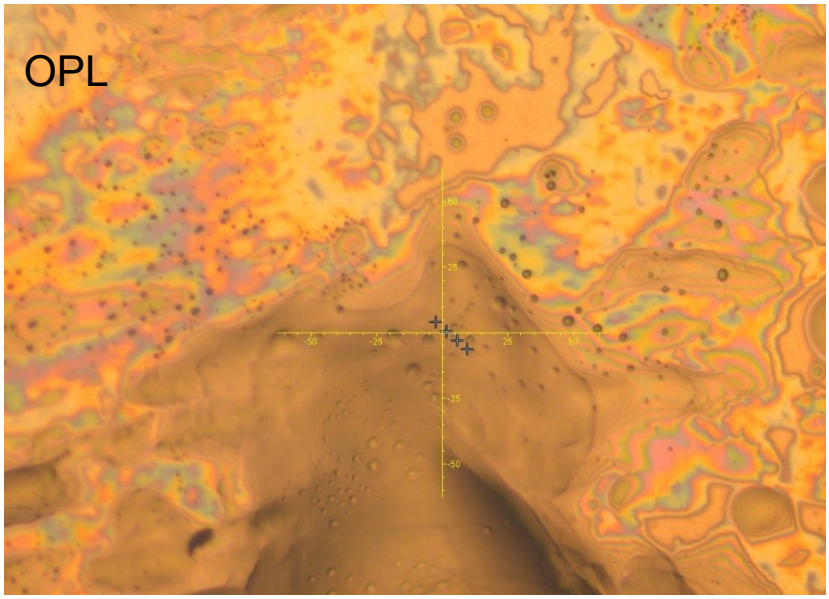


Figure 4.23 shows the Raman microscope image sequence OPL.

Figure 4.20 shows the Raman shifts of all sequences when adsorbed onto aluminium oxide while figures Figure 4.21 to Figure 4.23 show the Raman microscope images of 3 sequences studied. As with those for silica we can see the surface topological changes due to adsorption of the fatty acids. Some spherical particles can be seen as well as the bulkier mass of particles that appear to have formed hill like structures on the surface of the aluminium oxide substrate. Figure 4.20 shows that band 1650cm^{-1} and 1435.5 cm^{-1} are present for all sequences although the intensity of these bands is slightly higher for sequences OLP and POL. Another difference is that sequence LOP has a slightly broader band with two peaks as shown in Figure 4.24 in the range 1400 cm^{-1} to 1500 cm^{-1} compared to silica which had 1 band in that region. The band at 1650cm^{-1} is associated with a cis C=C stretching from oleic acid. However, the higher intensity of this band has been associated with increased degree of unsaturation (Jamieson et al., 2018). The Raman shift at 1435.5 cm^{-1} is associated with CH_2 which shows a shift of 4.4 cm^{-1} as compared to the 1440 cm^{-1} reported by Jamieson et al. (2018), Canzano et al. (2012) and Reitzenstein et al. (2007) for oleic acid for the same assignment. The Raman spectra reported here confirms that all fatty acid were adsorbed onto the sensors due to the presence of C=C between 3005 and 3010 cm^{-1} and C=O at 1656 cm^{-1} for palmitic acid while the same peak is C=C for oleic acid.

Aluminium oxide was a better adsorbent for palmitic acid in sequence LOP. This is because the Raman spectra does not show the presence of the C=C at about 3009 cm^{-1}. However, it is also known that this peak exists at 1656cm^{-1}. However, as this peak was very low in this sequence it led to conclusion that for sequence LOP, palmitic acid had the highest contribution to the adsorbed mass measured using QCMD. Silicon dioxide showed it was overall the better

adsorbent due to the presence of C=C (at 3009cm^{-1} and 1656cm^{-1}) while the other peaks are contributions from the aliphatic chain. The intensity of the C=C group higher in all sequences was very low for sequence PLO at 1656cm^{-1} and no peak at 3009cm^{-1}.

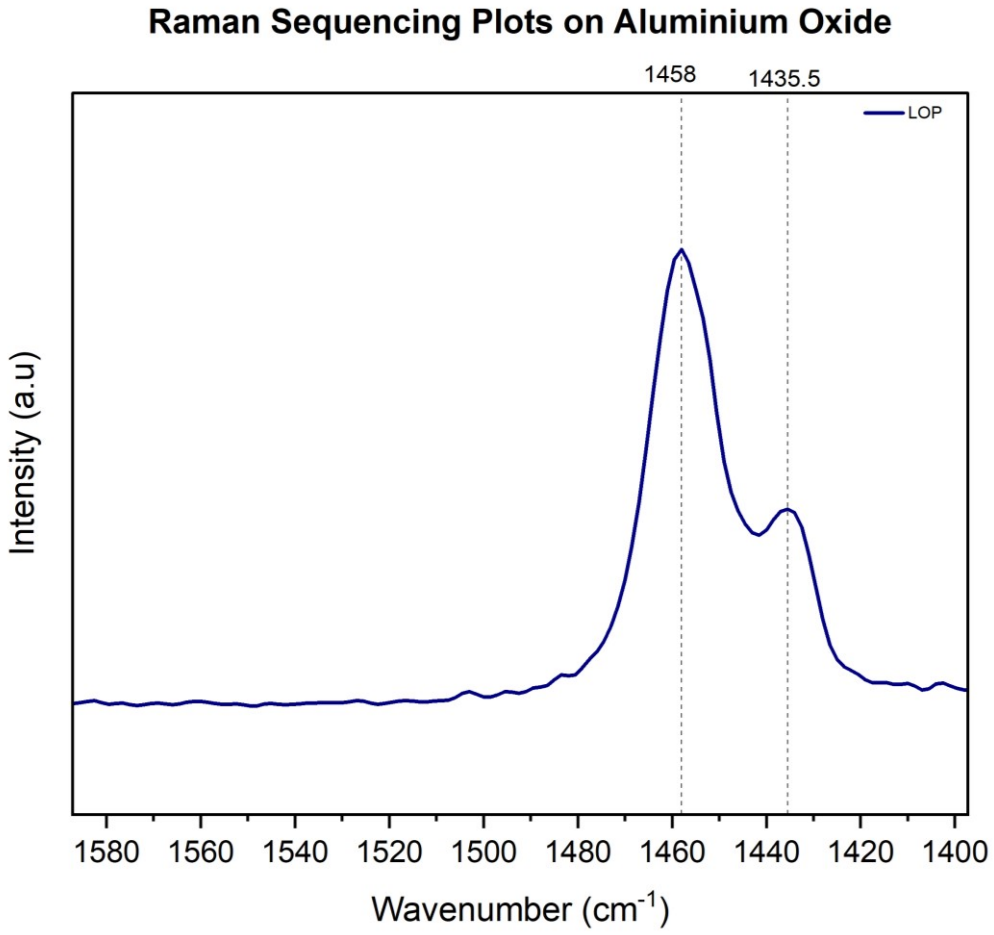


Figure 4.24 shows the Raman spectra between 1400 and 1500cm^{-1} in sequence LOP.

4.2.2.2.3 Raman Peak Area

The Raman peak area was used to give a quantitative representation of the concentration of specific molecular vibrational states (Renishaw plc, 2025). This was done through deconvolution of Raman band in the range 2500 and 3500 cm^{-1} to resolve overlapping peaks contributing to the broad bands. The Lorentzian distribution was used on Origin Pro to do the deconvolution. The is Lorentzian distribution a continuous probability distribution with a bell-shaped curve that has broader wings (Statistics How To, 2025). The gaussian distribution was usually suitable for dealing with solids while Lorentzian distribution was suitable for gases and liquids. Given that the sequencing test involved both solid (palmitic acid) and liquids (linoleic acid and oleic acid), the Voigt distribution would have been suitable. However, the Voigt distribution in Origin Pro is not the sum on the Lorentzian and Gaussian distribution but a

convolution (Lassègues et al., 2006). The other issue encountered while attempting to fit Voigt is that the half-width and area were not defined/fixed, thus making it unsuitable for use in this case. The Lorentzian fit however gave more favourable results and thus proceeded with this method of deconvolution.

The deconvolution showed the number of peaks fitted under the bands of interest and the R^2 values for the band of each sequence are given in the corresponding tables. Figure 4.25 and Table 4.7 show the results of the deconvolution of the peaks in range 2600 to 3100cm^{-1} for sequence LOP on aluminium oxide. The area under the peaks corresponds to the intensity of the peaks fitted with the value of R^2 as 0.94287. These are CH_2 peaks associated with a CH_2 stretch in the region between 2800 and 2958cm^{-1}. The Figure 4.26 shows the intensity/concentration of the Raman peaks based of the calculated peak areas. The most intense peak is found at 2882 cm^{-1} which is symmetric and broad. Kaneko et al. (1994) found similar results with their most intense and broad peak for CH_2 stretching of between 2850 and 2950 cm^{-1} in their work on using IR and Raman techniques to study polymorphism of erucic and palmitoleic acid.

The correlation of the Raman peak area with the degree of unsaturation has already been described elsewhere for peaks at 3013 cm^{-1}, 1663 cm^{-1} and 1264 cm^{-1} (Baeten et al., 1998). While Jamieson et al. (2018) correlated the peak are ratios with structural properties specifically the chain length and degree of unsaturation. Deconvolution of the Raman peaks with the range 2500 and 3100 cm^{-1} for sequencing tests on aluminium oxide was done to investigate what contributed to the broadening of the peak in this range. It is known from literature that the peak at 1656cm^{-1} is a cis C=C bond in oleic acid (Jamieson et al., 2018; Reitzenstein et al., 2007).

Figure 4.27 presents the deconvolution of sequence LOP on aluminium oxide substrate sensor. The results presented here in the region 2800-3100 cm^{-1} show the presence of 7 bands with different Raman shifts: 2958 ,2924, 2904, 2882, 2886, 2842 and 2836 cm^{-1} which are characteristic of the symmetric and asymmetric v(C-H) vibrations of the CH_2 and CH_3 groups in the fatty acid (Baeten et al., 1998; Jamieson et al., 2018). Baeten et al. (1998) presented four shifts in this region. The main difference is that the Raman spectral measurements were for edible oils rather than pure fatty acids. Another contribution could be the presence of more than one type of fatty acid influencing varied concentrations of different moieties due to their interaction with each other. The contribution of the band at 2721cm^{-1} was from palmitic acid as shown in Figure 4.19. The C=C bond that is usually at 3010 cm^{-1} was not present in this region for sequence LOP, suggesting purely aliphatic chain contributions to the broadening of the Raman peak in that region.

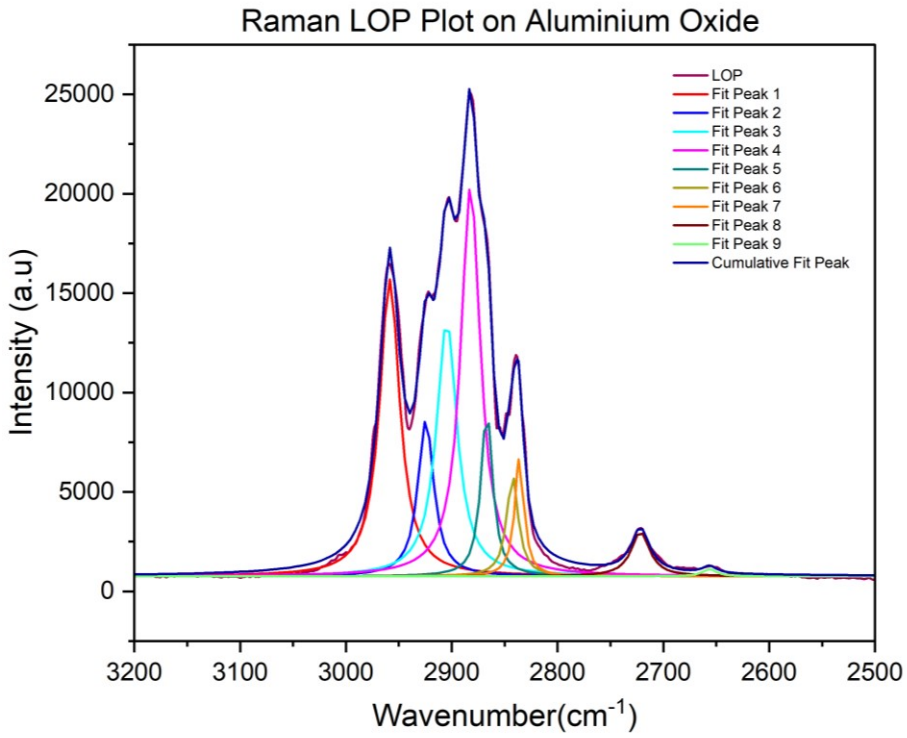


Figure 4.25 shows the number of peaks fitted for LOP.

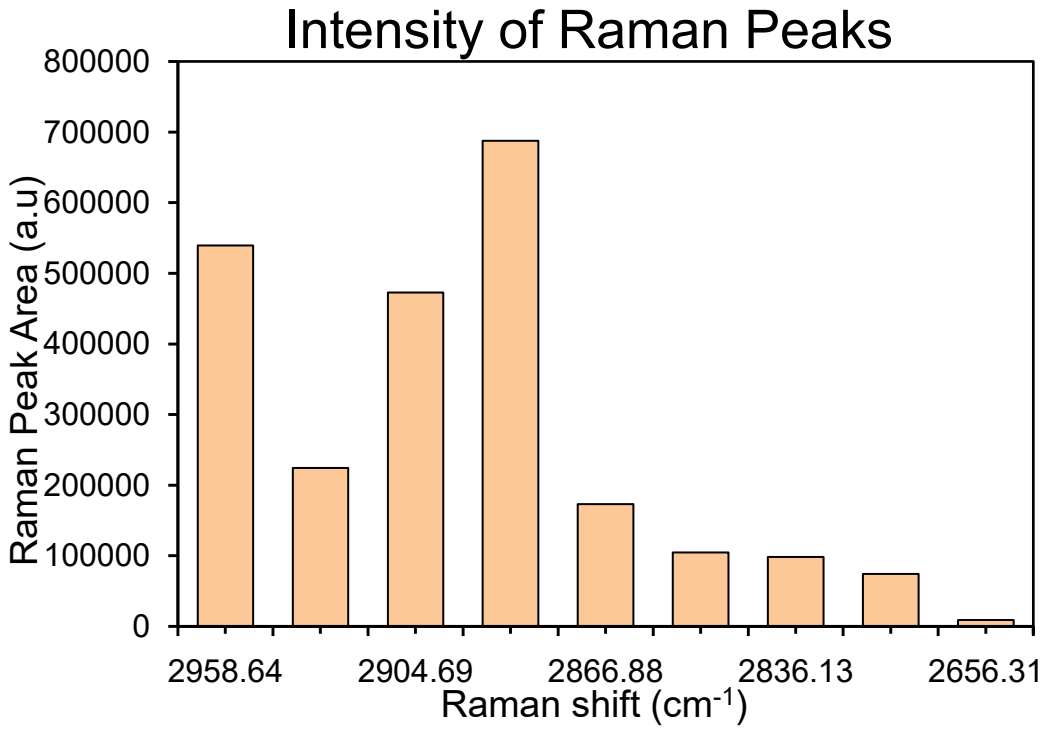


Figure 4.26 shows Intensity of Raman peaks for sequence LOP.

Table 4.8 Show deconvolution of bands between 2600 cm^{-1} and 3100 cm^{-1} for LOP.

Model	Lorentz								
Equation	y = y0 + (2*A/pi)*(w/(4*(x-xc)^2 + w^2))								
Plot	Peak1	Peak2(	Peak3	Peak4	Peak5	Peak6	Peak7	Peak8	Peak9
y0	754.57137 ± 13.14449	754.57137 ± 13.14449	754.57137 ± 13.14449	754.57137 ± 13.14449	754.57137 ± 13.14449	754.57137 ± 13.14449	754.57137 ± 13.14449	754.57137 ± 13.14449	754.57137 ± 13.14449
xc	2958.63621 ± 0.23014	2924.42311 ± 0.62773	2904.69086 ± 0.5299	2882.22374 ± 0.37043	2866.87724 ± 0.47958	2842.55853 ± 2.64676	2836.12572 ± 1.4183	2721.70767 ± 1.35316	2656.30526 ± 7.20823
w	22.95861 ± 0.73593	18.00274 ± 2.31241	23.44267 ± 3.14564	22.19404 ± 2.18855	13.03291 ± 2.06695	13.16004 ± 4.39996	10.46584 ± 3.25205	21.34932 ± 3.96559	16.17464 ± 20.96308
A	539276.87617 ± 14540.25547	224233.75597 ± 42133.39109	472634.68787 ± 90086.03332	687759.59055 ± 95878.19147	173255.56977 ± 43008.31804	104837.00536 ± 90207.40375	98170.60024 ± 81310.86426	74141.49646 ± 9915.38747	9170.53088 ± 8550.97796
Reduced Chi-Sqr	436944.0173								
R-Square (COD)	0.94287								
Adj. R-Square	0.94231								

Figure 4.27 and Table 4.8 present the deconvolution of sequence LPO which had a broader peak than LOP. As mentioned above the region 2800-3100 cm^{-1} presented symmetric and asymmetric v(C-H) vibrations of the CH_2 and CH_3 groups. LPO has six Raman shifts at : 3009, 2931,2906, 2890,2871 and 2852 cm^{-1}. The peak at 3009 cm^{-1} is associated with (=C-H) stretch due to the presence of C=C from linoleic acid (Jamieson et al., 2018; Traces Centre, 2021). Sequences POL and OPL have 6 Raman shifts in this region while OLP has 5 Raman peaks in this region. All sequences presented the presence of C=C bond at around 3005-3010 cm^{-1} excluding sequence LPO where the broad peak was purely because of the aliphatic chains of the fatty acids. Jamieson et al. (2018) reported that increased unsaturation resulted in increased intensity of the C=C. This suggests that more linoleic acid had chemically adsorbed during QCMD experiments for these sequences. The identification of which fatty acid adsorbed more by using peak area ratios was outside scope of this work and remains for future research.

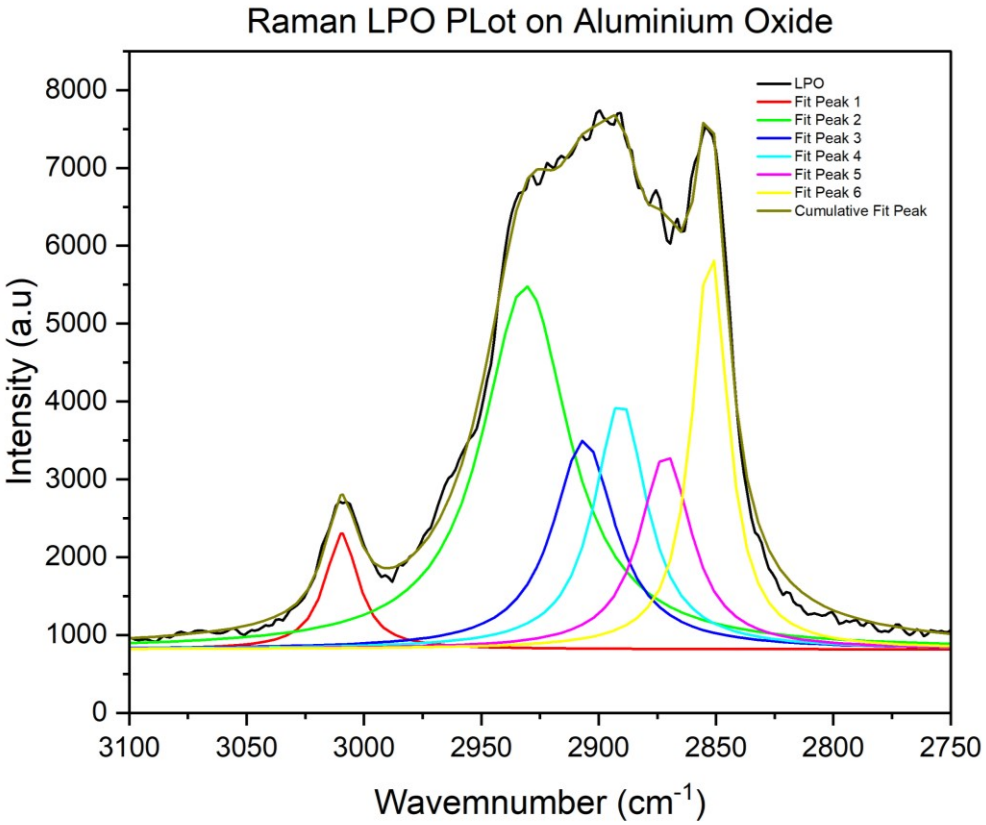


Figure 4.27 shows the number of peaks fitted for LPO.

Table 4.9 Show deconvolution of bands between 2600 cm^{-1} and 3100 cm^{-1} for LPO.

Model	Lorentz					
Equation	y = y0 + (2*A/pi)*(w/(4*(x-xc)^2 + w^2))					
Plot	Peak1(LPO)	Peak2(LPO)	Peak3(LPO)	Peak4(LPO)	Peak5(LPO)	Peak6(LPO)
y0	816.27082 ± 4.88206	816.27082 ± 4.88206	816.27082 ± 4.88206	816.27082 ± 4.88206	816.27082 ± 4.88206	816.27082 ± 4.88206
xc	3009.50157 ± 0.67184	2931.09325 ± 2.3021	2906.24164 ± 6.90135	2890.65398 ± 3.51483	2871.48166 ± 2.62117	2852.49078 ± 0.43465
w	17.27399 ± 2.11325	44.7711 ± 3.35469	32.39698 ± 23.78243	27.28223 ± 20.44902	26.94226 ± 12.98349	18.12837 ± 1.68525
A	40429.75939 ± 3883.97113	328122.29755 ± 84799.3998	136648.80663 ± 255864.57879	136299.22883 ± 245094.99564	106126.69608 ± 103152.37332	147412.42878 ± 25786.19007
Reduced Chi-Sqr	59827.25254					
R-Square (COD)	0.93996					
Adj. R-Square	0.93958					

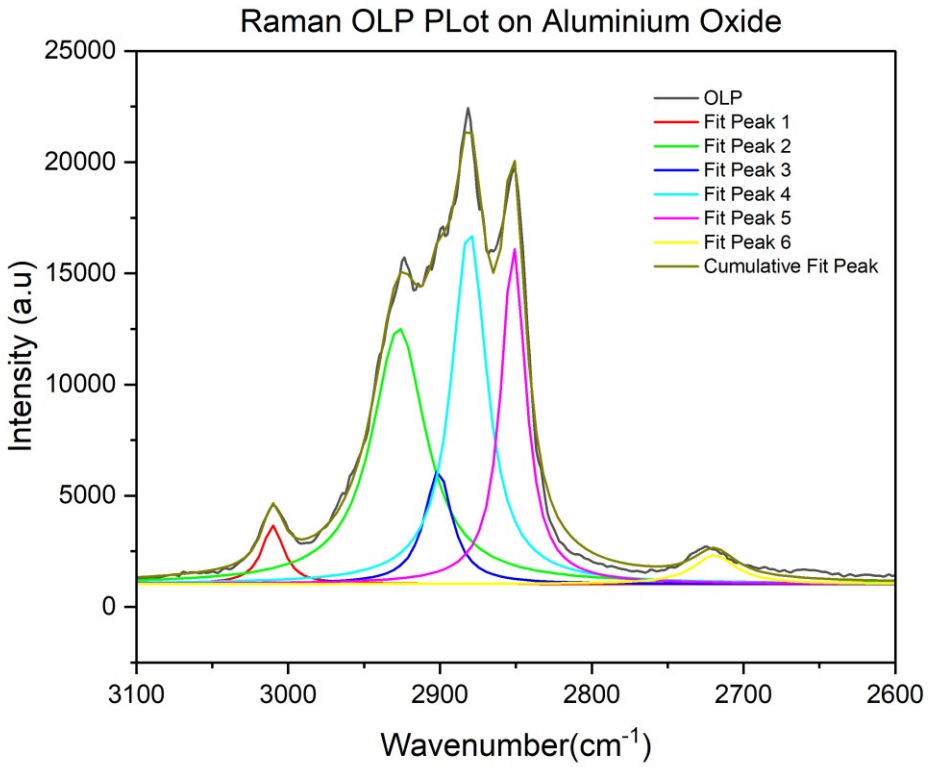


Figure 4.28 shows the number of peaks fitted for OLP.

Table 4.10 Show deconvolution of bands between 2600 cm^{-1} and 3100 cm^{-1} for OLP

Model	Lorentz					
Equation	y = y0 + (2*A/pi)*(w/(4*(x-xc)^2 + w^2))					
Plot	Peak1(OLP)	Peak2(OLP)	Peak3(OLP)	Peak4(OLP)	Peak5(OLP)	Peak6(OLP)
y0	1030.4484 ± 9.25352	1030.4484 ± 9.25352	1030.4484 ± 9.25352	1030.4484 ± 9.25352	1030.4484 ± 9.25352	1030.4484 ± 9.25352
xc	3010.12696 ± 0.71629	2927.02479 ± 0.72951	2901.18735 ± 0.91676	2880.74213 ± 0.41637	2851.57311 ± 0.17316	2719.22282 ± 2.05367
w	17.30868 ± 2.19673	42.7768 ± 1.4632	21.97769 ± 4.69924	28.10131 ± 1.669	19.55483 ± 0.64015	34.27961 ± 5.9554
A	71363.6018 ± 6918.90777	773675.93581 ± 40058.21178	176289.0539 ± 61299.50609	702780.89805 ± 59774.94327	466148.42244 ± 18830.4183	69116.32691 ± 8668.40983
Reduced Chi-Sqr	211926.47714					
R-Square (COD)	0.96625					
Adj. R-Square	0.96603					

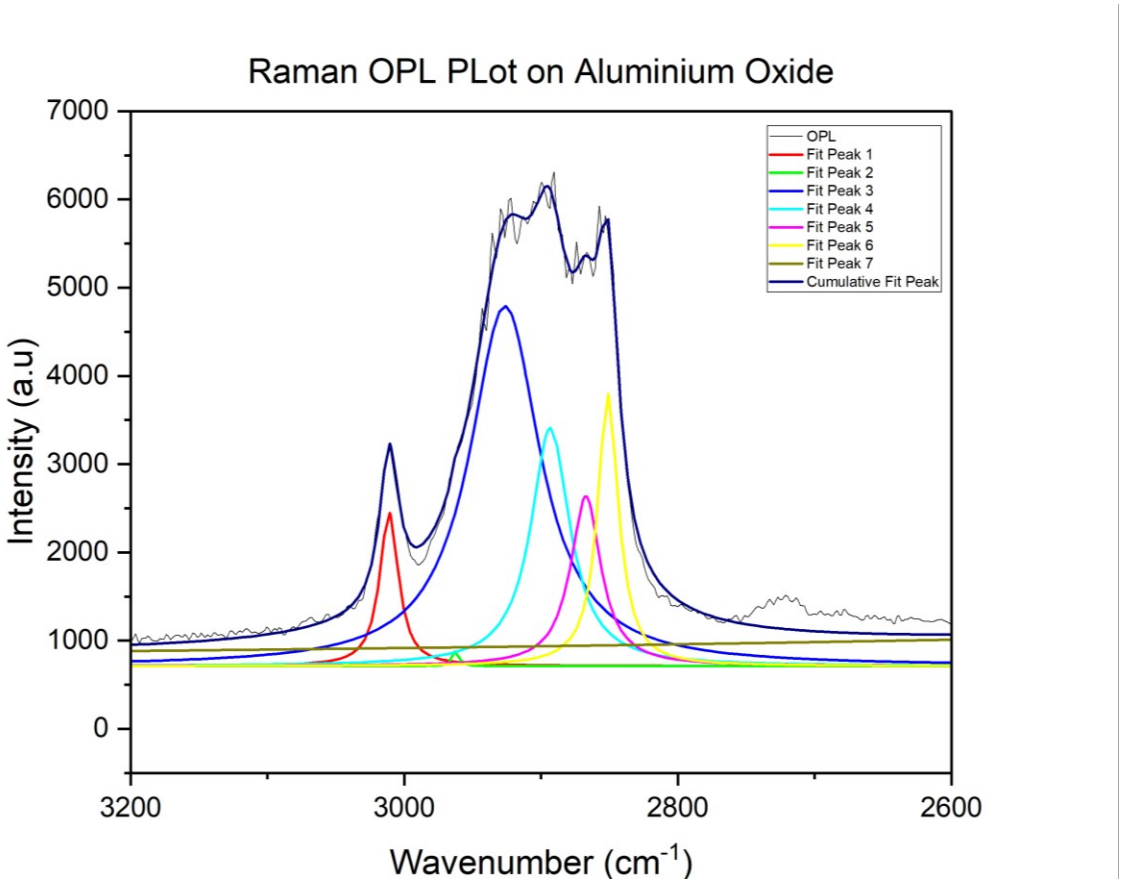


Figure 4.29 shows the number of peaks fitted for OPL.

Table 4.11 Show deconvolution of bands between 2600 cm-1 and 3100 cm-1 for OPL.

Model	Lorentz						
Equation	y = y0 + (2*A/pi)*(w/(4*(x-xc)^2 + w^2))						
Plot	Peak1(OPL)	Peak2(OPL)	Peak3(OPL)	Peak4(OPL)	Peak5(OPL)	Peak6(OPL)	Peak7(OPL)
y0	712.10184 ± 19.9114	712.10184 ± 19.9114	712.10184 ± 19.9114	712.10184 ± 19.9114	712.10184 ± 19.9114	712.10184 ± 19.9114	712.10184 ± 19.9114
xc	3011.09396 ± 0.51878	2962.09387 ± 2.58292	2926.4222 ± 1.8561	2893.20128 ± 1.54168	2867.35803 ± 2.1366	2851.05284 ± 0.84226	1630.50804 ± 20.27867
w	16.23741 ± 1.75045	4.99792 ± 8.95447	62.65812 ± 3.57699	34.63953 ± 8.34068	26.73657 ± 11.55299	18.52235 ± 2.85962	2088.33232 ± 135.29093
A	44583.19168 ± 4091.78341	1519.63224 ± 2348.3643	401635.8133 ± 44065.67652	146994.99749 ± 60922.56645	80873.67881 ± 59421.87287	89839.74972 ± 28950.16939	1824543.44108 ± 159609.77172
Reduced Chi-Sqr	52177.51166						
R-Square (COD)	0.91621						
Adj. R-Square	0.91558						

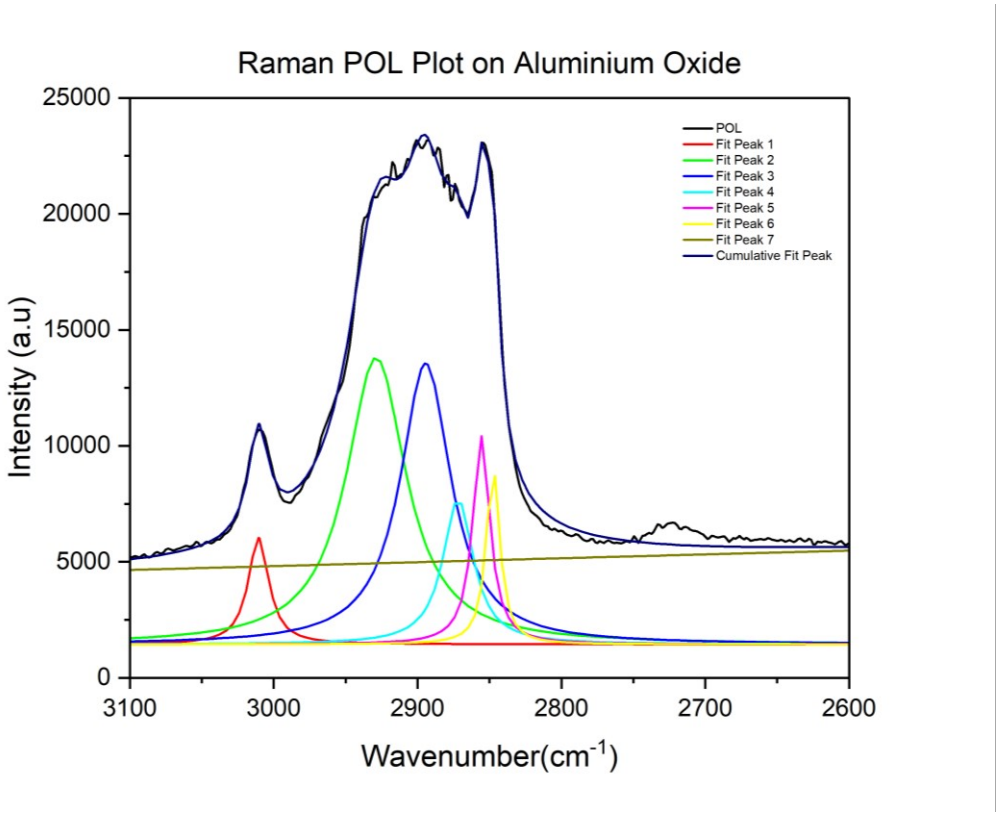


Figure 4.30 shows the number of peaks fitted for POL.

Table 4.12 Show deconvolution of bands between 2600 cm^{-1} and 3100 cm^{-1} for POL.

Model	Lorentz						
Equation	y = y0 + (2*A/pi)*(w/(4*(x-xc)^2 + w^2))						
Plot	Peak1(POL)	Peak2(POL)	Peak3(POL)	Peak4(POL)	Peak5(POL)	Peak6(POL)	Peak7(POL)
y0	1441.63722 ± 205.12606	1441.63722 ± 205.12606	1441.63722 ± 205.12606	1441.63722 ± 205.12606	1441.63722 ± 205.12606	1441.63722 ± 205.12606	1441.63722 ± 205.12606
xc	3010.57173 ± 0.55929	2928.78901 ± 1.29716	2894.42607 ± 2.06253	2871.81162 ± 1.8993	2855.62162 ± 1.25211	2847.49653 ± 1.0014	1858.33365 ± 10.59222
w	17.34675 ± 1.75305	50.30559 ± 2.84633	42.62504 ± 7.77761	25.66126 ± 13.38261	14.41195 ± 5.9238	11.10295 ± 2.64711	3615.34741 ± 160.39708
A	125298.76805 ± 9907.21112	978504.40499 ± 126233.60521	811783.51503 ± 292792.51908	252792.74342 ± 246249.80731	203491.02542 ± 157334.33627	135068.63009 ± 81472.4507	2.68152E7 ± 2267393.1401
Reduced Chi-Sqr	393907.6149						
R-Square (COD)	0.95211						
Adj. R-Square	0.95175						

4.2.2.3 Fourier Transform Infrared Spectroscopy

FTIR was used to characterize a polystyrene substrate sensor following adsorption of a cocktail of all three fatty acids in QCMD experiments. The sensor was washed with ethanol to remove loosely bound fatty acids. The solvent i.e. the 'waste wash' and polystyrene before and after washing were characterized to detect the presence of FFA.

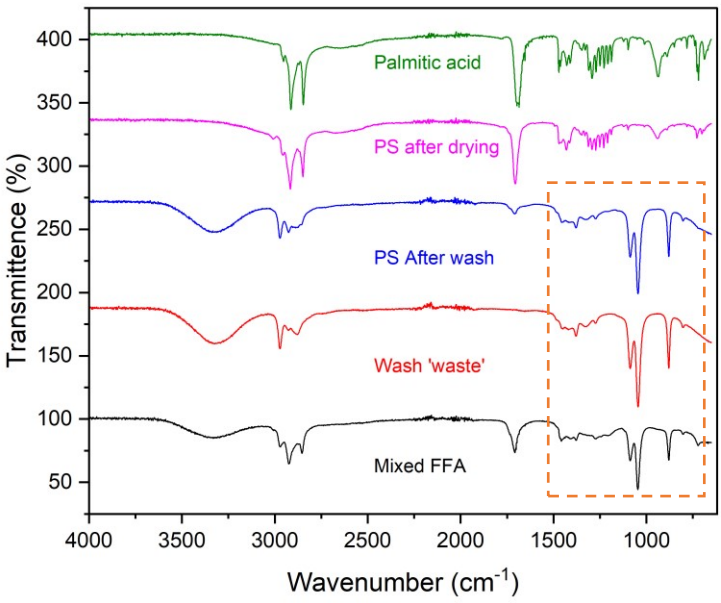


Figure 4.31 shows FTIR spectrum from sequencing tests on polystyrene substrate sensor.

The results from Figure 4.31 presents a spectrum of a palmitic acid tablet. The results showed a peak at 3337 cm^{-1} which is not present on the polystyrene substrate after drying. From Nandiyanto et al. (2019) it shows that the 2500-4000 cm^{-1} is a single bond region. The is a broad peak between 3084–3576 cm^{-1} which shows the presence of the OH group from alcohol functional group (LibreTexts, 2015; Bradley, 2015; Kim, 2024). This is because ethanol is the solvent used in cleaning the sensors and it is also a component is making the fatty acid stock solutions which is why the peak was not present after the polystyrene substrate sensor has dried off and not present in the pure palmitic acid. There are also C-H stretching peaks between 2500-3000 cm^{-1}. A sharp and narrow peak at 1709 cm^{-1} and 1695 cm^{-1} in the case for palmitic acid was identified. The 1709 cm^{-1} peak was not as intense/ sharp for polystyrene after wash. All the spectra apart from the wash waste have the peak between 2000-2500 cm^{-1} which corresponds to the C=O for the carboxylic acid (Kim, 2024; Ibarra et al., 2016).

The region below 1500 cm^{-1} is described as the fingerprint region from literature (Nandiyanto et al., 2019). In this region, the region circled in the orange dashed line has near identical peaks in this region. The same was observed for the palmitic acid spectrum and polystyrene substrate after drying. There was a peak at 939 cm^{-1} for palmitic acid and polystyrene substrate after drying. This peak was the -OH group out of plane (Krishna et al., 2020). The peak at 880 cm^{-1} in the other three spectra are C-H bending peaks. 1045 cm^{-1} and 1090 cm^{-1} are C-O stretching. The peak at 3011cm^{-1} showed presence of =C-H from the unsaturated region of oleic and linoleic acid. Azmi et al. (2022) in their work also found a similar peak at 3010cm^{-1} for oleic acid spectrum. The presence of the =C-H , C=O CO confirmed the adsorption of the FFA onto polystyrene using QCMD. This suggests that polystyrene could potentially be used as an adsorbent for FFA. Currently, there are concerns of polystyrene microplastics in wastewater Falco et al. (2024), however, these results highlight that polystyrene has the potential to be recycled and repurposed for FFA adsorption.

4.3 Conclusions

This work explored the interactions of sequential addition FFA with each other and different substrate sensors which was achieved using the QCMD. By exploring changes in the dissipation, conformational changes were explored. The results showed that palmitic acid introduced rigidity to the adlayers with the extent of the effect dependent on where it appeared in the sequence. The total mass adsorbed for each sequence was determined by the Voight model with sequence OPL and LOP having the highest recorded mass adsorbed in polystyrene. Sequence OLP and LPO had the highest mass adsorbed on aluminium oxide while in silicon dioxide sequence OLP and OPL had the highest mass adsorbed.

Raman microscopy and FTIR were used to study the modifications on the substrate sensors which showed the changes such as the presence of C=C, OH and C=O groups reaffirming the adsorption of these FFA onto the different sensors. Exploration of the Raman peak area revealed that some groups such as CH_3,CH_2 were more intense for sequences LOP, OLP and POL on aluminium oxide. The C=C group was most intense in sequences POL on aluminium oxide. Increased intensity of C=C at about 3009 cm^{-1} and 1656 cm^{-1} was associated with increased adsorption of unsaturated fatty acids i.e. oleic acid and linoleic acid.

Chapter 5 Effect of pH, Temperature and Inserts on adsorption using QCM

5.1 Abstract

The effect of pH, temperature and presence of inserts was investigated using QCMD. It was determined that adsorption of oleic acid, palmitic and linoleic acid was highest around the pKa values of 9.85, 9.24 and 8.6 respectively with palmitic acid forming the thickest layer. Calculation of the thermodynamic parameters revealed that the adsorption of all FFA onto a Gold quartz sensor was an endothermic process with a great degree of spontaneity. The introduction of secondary surface (pure copper and tinned copper) to the QCMD batch system resulted in increased adsorption of palmitic acid particularly for pure copper. Introducing the inserts altered the surface chemistry and surface area in the system thus affecting adsorption of the FFA by different degrees. This helped understand the behaviour of FFA under conditions discussed in this chapter.

5.2 Introduction

The effect of temperature was explored using QCMD. The Gibbs free energy (G) is a thermodynamic parameter that defines the spontaneity of a reaction in a closed system at constant temperature and pressure. It is defined by:

$$G = H - TS$$

Equation 5.1

Where H is the enthalpy ,T is the temperature in Kelvin at S is the entropy. The change in the Gibbs free energy (∆G°) of the system for each experiment was calculated as :

$$\Delta G° = -RTln(Keq°)$$

Equation 5.2

(Himawan et al., 2006)

Where R is the universal gas constant [8.3144 J/(mol×K)], T is temperature in Kelvin, Keq° is the thermodynamic equilibrium constant.

Keq° was determined by:

$$Keq° = \frac{q_e}{ce}$$

Equation 5.3

Where q_e is the adsorption capacity of the pseudo second order kinetics (Langmuir isotherm) (Romero-González et al., 2005). The equilibrium concentration after adsorption $ce \approx F_e$ after adsorption where F_e is the frequency at equilibrium where no more change is the resonance frequency is observed. The enthalpy change ΔH° and the change in entropy ΔS° of the system was determined as shown in Equation 5.4. ΔH °and ΔS° were assumed to be independent of temperature (Tran et al., 2021).

$$\Delta G° = \Delta H° - T\Delta S°$$

Equation 5.4

The effect of pH was explored using QCMD as well as the impact of inserts. The pH is defined by:

$$pH = -\log_{10}[H^+]$$

(Katoch, 2022)

Equation 5.5

The ionization of fatty acid chains is affected by the pH which affects the distance between the fatty acid chains thereby affecting adsorption and the sensed mass by QCMD. This is because, ionization refers to the process by which electrons from molecules (fatty acids in this case) or atoms are gained or lost thereby resulting in a net positive or negative charge. The electrostatic forces of repulsion thereby influenced the distance between the fatty acid chains (Kanicky & Shah, 2002; Lowe et al., 2022).

The aim of this work is to determine the effect of pH on adsorption of fatty acids on different materials and determination of the thermodynamic parameters. The other aim was to also explore the impact of foreign inserts on adsorption of the fatty acids. Characterization on the inserts and sensor surface after adsorption experiments was beyond the scope of this work.

5.2.1 Materials and methods

5.2.1.1 Effect of pH experiments

0.1M sodium bicarbonate-sodium carbonate buffer were prepared using sodium carbonate (≥99.5) CAS: 497-19-8 from Sigma- Aldrich and sodium hydrogen carbonate CAS: 144-55-8 from Avantor VWR International. Buffer solutions resist pH changes upon addition of an eternal components which may be either basic or acidic in nature (Katoch, 2022; Beynon & Easterby, 1996). This buffer was chosen as it has a buffering range within 2 pH units of the fatty acids e.g oleic and linoleic acid pKa in this work (Salwan et al., 2023). The other benefits of this buffer were that it was easy to prepare, very cost effective and had an excellent shelf life reducing the amount of time required to prepare a fresh buffer. A weighing boat and scale were used to measure out the powder buffer constituents which were dissolved in DI water (PURELAB Chorus 1 (ELGA LabWater) to make the buffer solutions. The SciQuip pH meter was calibrated for applicable ranges to the buffer pH which was used to determine the final pH of each buffer. 0.1 M hydrochloric acid and sodium hydroxide were used to adjust the buffer pH accordingly (drop at a time). The pH range tested was based on the pKa (referenced from literature) (Kanicky & Shah, 2002) of the FFA (oleic acid, palmitic acid, and linoleic acid). Table 6.1 shows the ranges tested for the FFA. The green areas highlight the testing range while the red slash (**/**) symbol shows the pKa of the specific fatty acid tested. Another test was done to test well below the pKa of all the fatty acids as shown on the first row of Table 6.1. The buffer used was 0.1M Citric Acid – Sodium Citrate Buffer. The buffer was made from citric acid monohydrate (≥99%) CAS:5949-29-1 and Sodium citrate tribasic dihydrate (≥99%) CAS: 6132-04-3 both from Merk.

For sodium bicarbonate-sodium carbonate buffers, the QSX 301 Gold sensors from Biolin scientific were used in this work. The sensors were used as received and no modification was done to the surface before the experiments. A batch module was used for these experiments. To start, a stable baseline of the gold sensor substrate was determined at the start of the experiment followed by addition of 0.1ml of the buffer solution. Once the frequency was stable, 0.1ml of 50mg/ml of the fatty acid stock solution was added, and the experiment allowed to run until the substrate sensor was saturated with no more significant changes in the final resonance frequency.

The substrate sensors used for Citric Acid – Sodium Citrate Buffer were QSX 301 Gold, QSX 303 Silicon Dioxide and QSX 309 Aluminium Oxide. 0.1ml of 100mg/ml of FFA stock solution was used. All experiments were conducted at 25 ± 0.04 ºC.

Table 5.1 Shows the pH ranges tested for the FFA.

pH	Linoleic acid	Oleic acid	Palmitic acid
3.75	✓	✓	✓
8.20			✓
8.40			✓
8.60			✓
8.80	✓		✓
9.00	✓		✓
9.24	✓		
9.40	✓	✓	
9.60	✓	✓	
9.85		✓	
10.00		✓	
10.20		✓	

5.2.1.2 Temperature Experiments

The effect of temperature on adsorption of fatty acid stock solutions was investigated using the QCMD. A Gold QSX 301 sensor from Biolin scientific was used throughout these experiments. To start the experiment, the temperature of the sensor was set to 15 ºC, 25 ºC or 35ºC using the Qsoft401 software. The temperature of the bulk solution was controlled using a water bath circulator from Julabo and set to the same temperature as the sensor. Once the temperature was set, the baseline was determined followed by addition of 0.2ml absolute ethanol ≥99.8% from Sigma Aldrich (CAS:64-17-5). Once the frequency was constant, 0.2ml of 50mg/ml stock solution was added. The experiment was terminated once no significant change in frequency was observed for the last step. The fatty acids tested remain the same (Oleic acid, Linoleic acid, and Palmitic acid). The experimental setup is shown in Figure 5.1. The experiments were repeated twice, and all conducted using a batch module which is double walled.

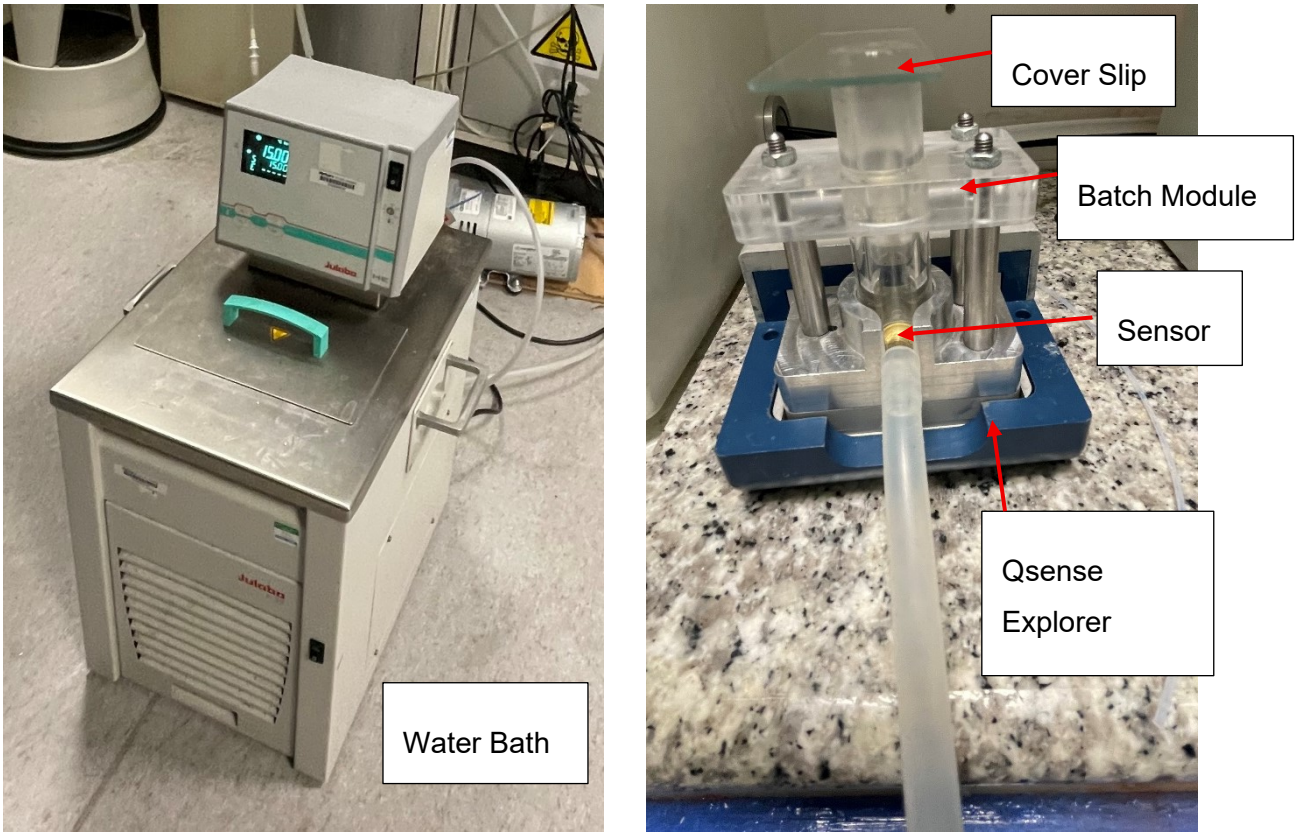


Figure 5.1 shows the QCMD setup for temperature experiments.

5.2.1.3 Contact Angle Measurements

Contact angle measurements were conducted using the Contact Angle Goniometer with DROPimage (Rame-Hart). Following adsorption on FFA at pH 3.75, contact angle measurements conducted on the sensor substrates. The sample was mounted on the sample stage and the stage levelled. The focus on the sample was also adjusted to ensure a sharp image is taken during the measurement and a suitable baseline for measurement is established. A water droplet placed on the sample by an auto syringe using controls from the DROPimage software was measured to determine the contact angle of the surfaces.

5.2.1.4 Experiments Involving Use of Inserts

Tinned copper wire TWC 20 from Rowan Cables Products Ltd was used in this work. Two inserts were used. A pure tinned copper insert used as provided by the manufacturer and one which processed to expose the inner copper layer. The inserts were used as a secondary surface to investigate the impact of this on adsorption of the fatty acids. For the second insert, tinned copper was smoothed down by sanding using sanding paper to expose the inner copper layer. The wire diameter is 0.91mm inches ± 0.1%. The wires were then coiled using a Ball-Plus 5/32 inches Allen key by Allen®. The size of the coils of the wires was assumed to be of

the same size as the Allen key. The setup involving the inserts is as shown in Figure 5.2. The cross-sectional area of the wire is given by:

$$A = \pi r^2 = \pi \times \left(\frac{0.91}{2}\right)^2 = 0.650mm$$

Equation 5.6

The experiment follows the same procedure for QCM experiments with ethanol ≥99.8% added once a stable baseline has been established. The fatty acids are added to the system as the last step.

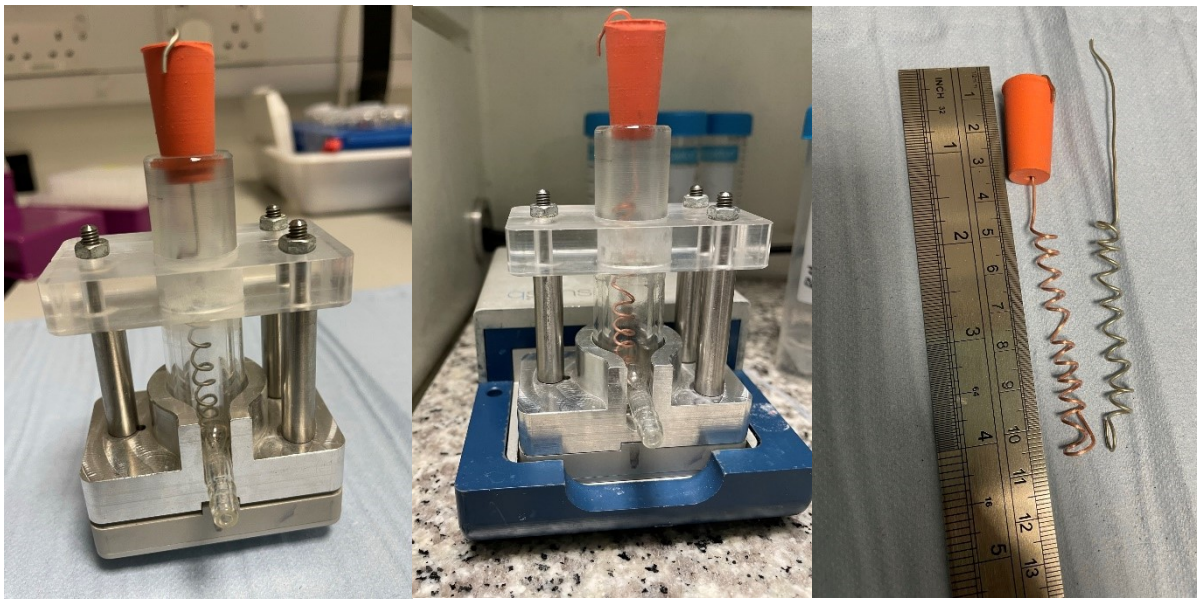


Figure 5.2 shows copper and tinned copper inserts used as secondary surface.

5.2.2 Results and Discussion

5.2.2.1 Effect of pH on adsorption of FFA

A gold substrate sensor was used to investigate the impact of changes in pH on the amount on the adsorption of FFA using QCMD. The pKa value of the fatty acid is dependent on the solution environment and is identified as the point where half the hydrogen ions from the carboxyl group of the fatty acid have been removed. Previous studies highlighted the effect of unsaturation of fatty acids on the pKa i.e. more saturated fatty acids presented with higher pKa values due to closer packing distance between fatty acid chains (Kanicky & Shah, 2002).The study also highlighted that the presence of a C=C double bond results in bends in the chain (near the position of the double bonds) (Clayden et al., 2012) making it difficult to tightly pack the fatty acid chains (Kanicky & Shah, 2002; Kanicky et al., 2000). Linear saturated fatty acids i.e. palmitic acid in this case would have closely packed chains in a monolayer thus increasing the pKa of fatty acid. The closely packed nature of linear fatty acids prevents deprotonation by the hydroxide ions in the fatty acid monolayer (Kanicky et al., 2000).

Short chain fatty acids (those with carbon chain length between 2 and 6) normally have a low pKa values between 4.5 and 5 (Quast, 2016). As an example, some factors affecting this value include: the ionic environment of the solution , presence of an oxidising or reducing agent and the carboxylic acid chain length. Kanicky et al. (2000) in their work explored the effect of chain length on the pKa where they determined that beyond a chain length of 4 carbons, electronic effects between the carboxylate ion on the carbon chain and the rest of the alkyl group were not significant resulting in the pKa values remaining relatively stable. Therefore, increasing the chain length from 5 to 7 carbons increases the pKa from 4.82 to 4.83 (Kanicky & Shah, 2002). This phenomenon however did not apply to longer chain fatty acids as the increase in chain length did in fact affect the pKa. The driving factor being that increasing the chain length increased the van der walls forces in the fatty acid monolayer thus resulting in reduced distance between fatty acid chains due to closer packing.

For Oleic (cis double bond is located in position 9) and Linoleic acid some bending was expected due to the presence of the unsaturated double bond with linoleic acid having two C=C double bonds located at position 9 and 12 thus affecting the packing in a monolayer and fluidity (Spector & Yorek, 1985; Kanicky & Shah, 2002; Arisawa et al., 2016). As such linoleic acid molecules had larger packing distance than oleic acid hence having a lower pKa. The lowest pKa was for palmitic acid due to its chain length. Previous work explored the effects of the saturation or unsaturation of fatty acids on factors such as packing density, fluidity, chain flexibility however to the best of my knowledge, non-have explored the effect of pH on

adsorption of the fatty acids using QCM. It is also important to note that the previous work by other researchers on the behaviour of the fatty acids will help explain some of the patterns observed as the FFA adsorbed onto the gold quartz substrate sensor.

The thickness of the layer adsorbed was calculated by dividing the Sauerbrey mass by the effective density, ρ_{eff} of the FFA as shown in Equation 5.7.

Thickness, δ_f :

$$\Delta\delta_f = \frac{\Delta m}{\rho_{eff}}$$

(Irwin et al., 2005)

Equation 5.7

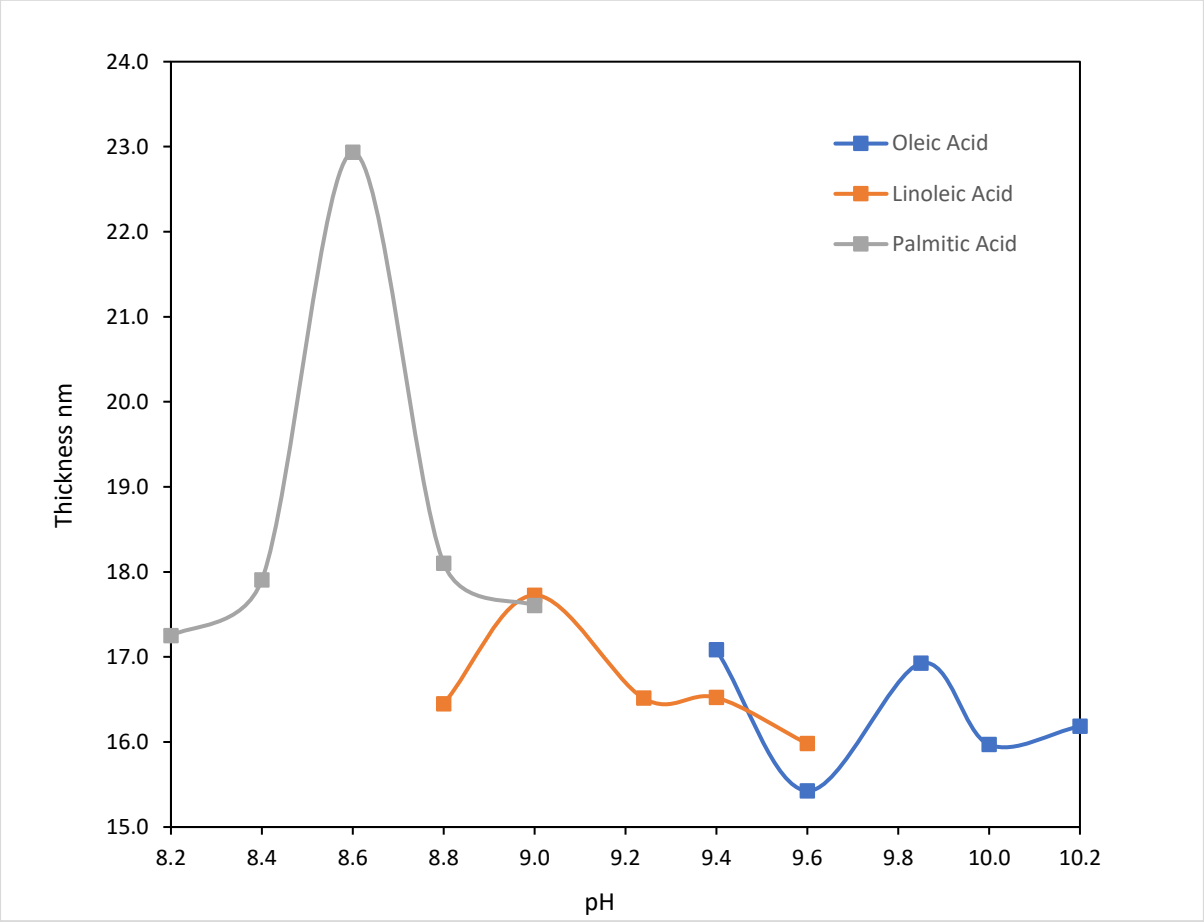


Figure 5.3 Shows the effect of pH on the thickness of the fatty acid layer adsorbed onto Gold.

The thickness of the adsorbed layers of the FFA are as shown in Figure 5.3. The testing range of the distinct FFA was close to the pKa of the respective FFA. Figure 5.3 showed that palmitic

acid formed the thickest layer during adsorption followed by linoleic acid and the lastly oleic acid. The thickest layer recorded for palmitic acid was at pH 8.6 while linoleic acid formed the thickest layer at pH 9. Oleic acid had the thickest layer recorded at pH 9.4. The plot for palmitic acid showed that the thickness of the adsorbed layer increases rapidly until pH 8.6 beyond this pH the amount adsorbed reduces hence thickness of the layer reduces. Previous studies have found fatty acid monolayers/ bilayers became ionized with increasing pH (Lowe et al., 2022). At pH values below the apparent pKa of the fatty acid, the fatty acids were not ionized. However, as the pH increased to a value near the pKa of the fatty acid, 50% of the fatty acid molecules were ionised leading to ion dipole interactions between the polar group of the fatty acid resulting in reduced intermolecular distances between adsorbed fatty acid chains. This suggests that a stable layer at the sensor- fatty acid interface was formed as this phenomenon supported closer packing resulting in a thicker adsorbed layer. However, previous studies also showed that this layer weakens with further increase in pH due to the fatty acid being completely ionised. Hence increasing pH beyond the pKa of the fatty acids results in ionic repulsion forces between the polar group leading greater distances between fatty acid chains thus allowing the solvent from solution in between the chains (Lowe et al., 2022; Kanicky et al., 2000). This may have led to instability resulting in breakdown of the adsorbed palmitic acid layer which was observed by the reduced thickness of the adsorbed layer. This supports the results of work by Kanicky & Shah (2002) where they determined that the closest packing of fatty acids is close to the pKa value. Palmitic acid thus favoured more adsorption at pH 8.6. Also, because it is linear more palmitic acid molecules could be adsorbed from the bulk solution.

As pH increases, the thickness of linoleic acid adsorbed increases. As the pH increases past 9, the amount of linoleic acid reduces which is shown in Figure 5.3 by reduction in the thickness of the layer with the lowest thickness of 15.98nm at pH 9.60. Oleic acid shows no clear trend as pH is increased in Figure 5.3. It starts off with a reduction in the thickness of the layer as pH is increased to 9.60 followed and increase in adsorption leading up to the pKa (9.85) and beyond this pH the thickness of the layer adsorbed decreases. Ionic repulsion between fatty acid molecules tends to increase at high pH values. This coupled with the presence of the double bonds in both oleic and linoleic acid explains why the thickness of the adsorbed layers were considerably lower than that of palmitic acid.

Linoleic acid has two double bonds while oleic acid has one. Looking at the structural differences, the distance between linoleic acid chains is larger than distance between oleic acid chains (Kanicky et al., 2000). This allows for more solvent to couple between the molecules of the monolayer thus resulting in a thicker recorded layer as QCMD measures

hydrated mass. This will result in an overestimation of the actual thickness of the adsorbed layer. At pH 9.24, Figure 5.3 and Figure 5.4 showed a decrease in thickness of the adsorbed layer and a decrease in the dissipation. This is indicative of a collapse in the monolayer thereby expelling any coupled solvents resulting in reduced viscosity of the adsorbed monolayer. This can be seen by a change in the dissipation of the experimental data in Figure 5.5 and in the appendix 8.3 at pH 9.24 to pH 9.60. Upon addition of the linoleic acid to the system, the dissipation increased in all three instances followed by a decrease at which the dissipation remained constant at pH 9.24. Following the decrease in dissipation for pH 9.40 and pH 9.60, the dissipation increased further indicating the change in viscosity of the adsorbed layer as the experiment progressed.

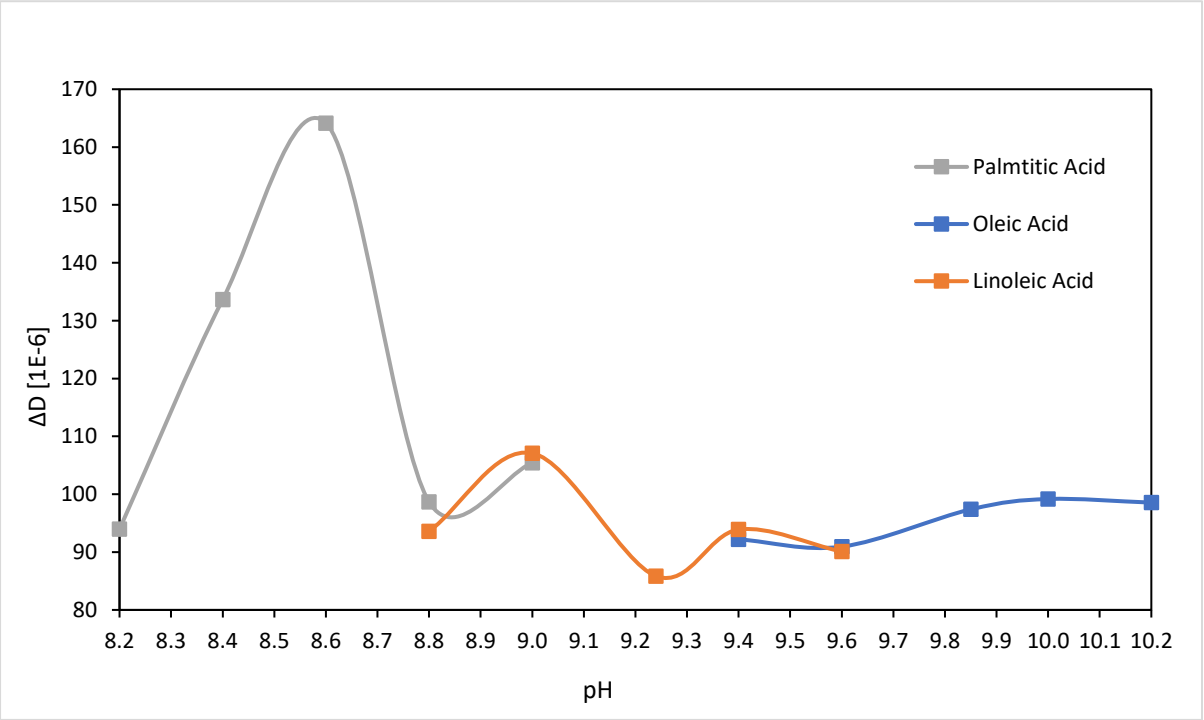
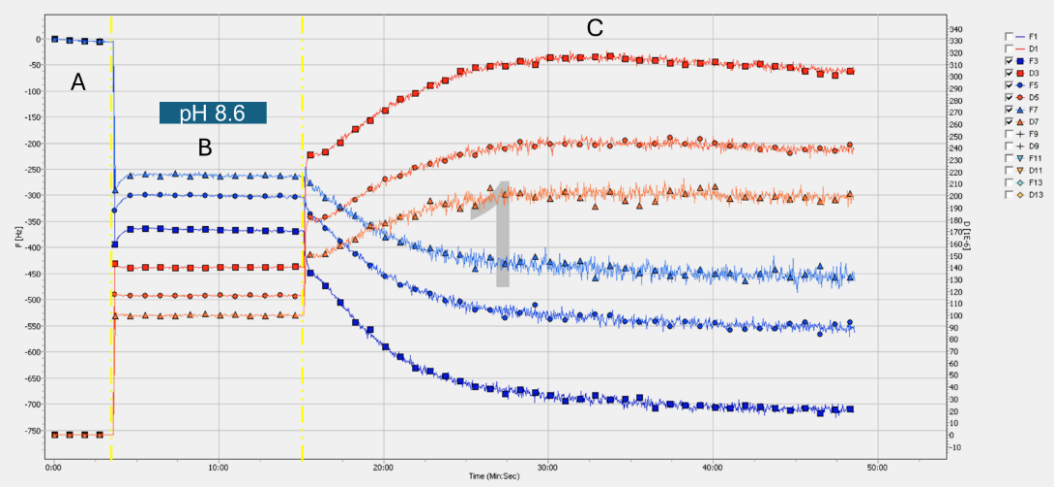
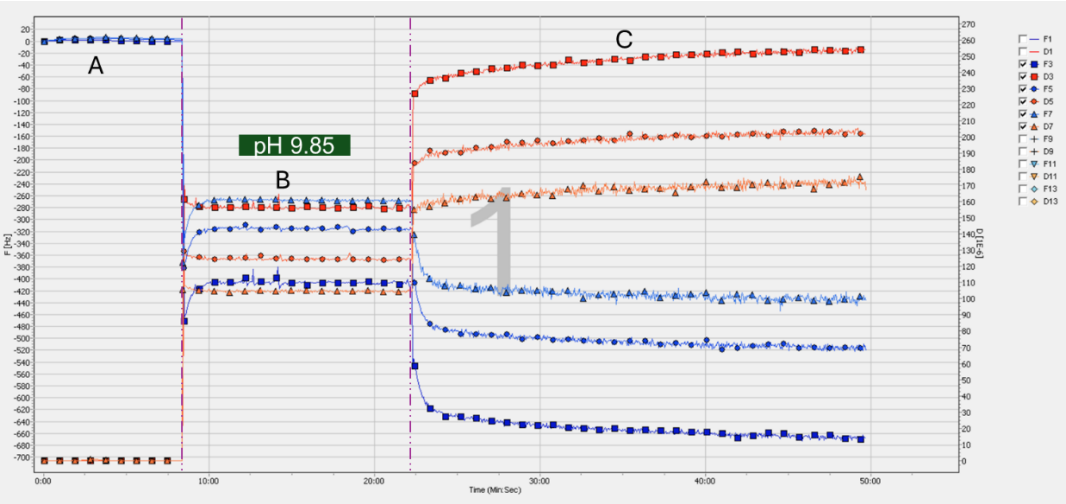


Figure 5.4 Effect of pH on Dissipation for adsorption onto gold substrate sensors.

The dissipation changes due to changes in pH are highlighted in Figure 5.4. Palmitic acid showed that the dissipation or rather the extent of the viscoelastic nature of palmitic acid is dependent on the pH. The flexibility of the adsorbed palmitic acid monolayer increases as the pH increases from 8.2 to 8.6. Further increase in the pH results in a reduction in the dissipation energy meaning the layer becomes more rigid. At pH 9, the dissipation energy increases again indicating that the layer becomes more fluid again however the thickness of the layer still reduces as shown in Figure 5.3. Oleic acid shows a gradual increase in dissipation with pH in Figure 5.4 however, the dissipation remains constant beyond pH 9.85. This shows that for oleic acid, changes thickness of the oleic acid monolayer is not proportional to the dissipative energy losses. Thickness of the linoleic acid monolayer is proportional to the energy dissipation. Experimental data of all FFA are in the appendix 8.3.

5.2.2.2 QCM experimental results





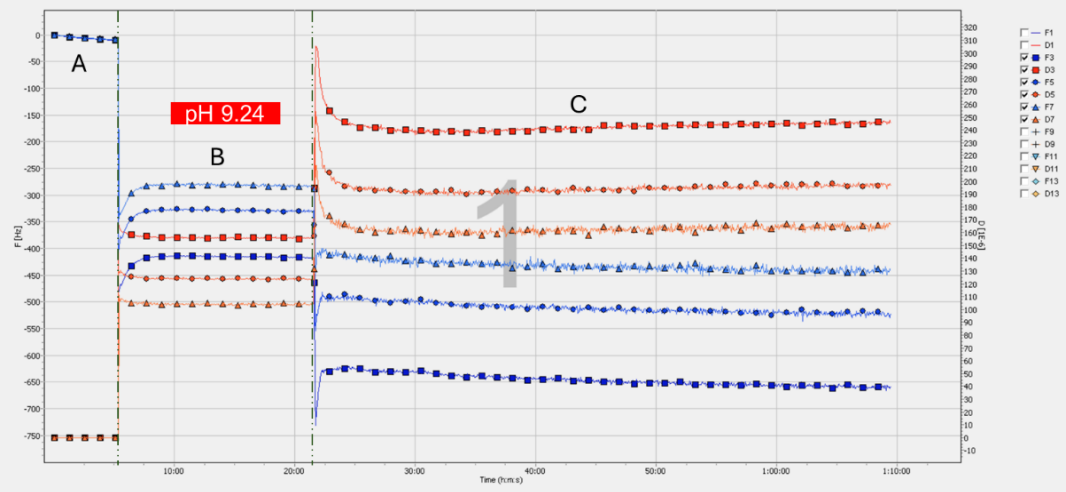


Figure 5.5 shows frequency and dissipation plots for Palmitic acid (pH 8.6), Oleic acid (pH 9.85) and Linoleic acid (pH 9.24). The plots show different overtones and (A) Baseline (B) buffer added (C) Fatty acid ss added

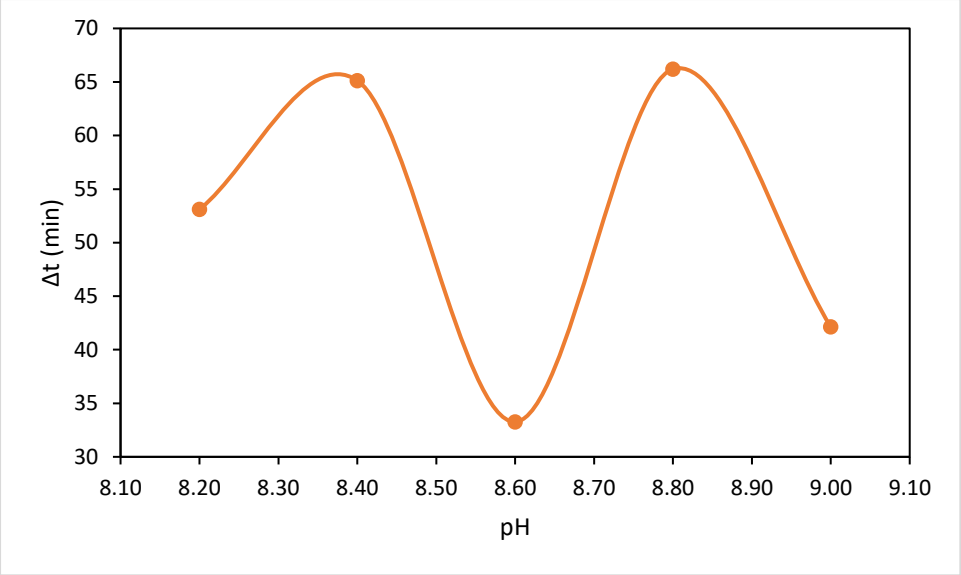


Figure 5.6 Rate of palmitic acid adsorbed at different pH.

Figure 5.5 shows the negative changes in frequency and positive shift in dissipation for the 3rd , 5th and 7th overtones. This is true for the tested pH range. The results found in Figure 5.5 and appendix 8.3 shows time it takes for the gold substrate sensor to be fully saturated at different pH. The highest rate of adsorption was observed at pH 8.6 as it took 33 min for the sensor to be saturated. This is supported by the frequency and dissipation graphs in Figure 5.5 where in the third phase C, between 20 and 30 minutes the rate of adsorption is higher seen by a steep curve both in F and D. The curves then level out.

Frequency and dissipation plots of palmitic acid at the third, fifth and seventh overtone. Measurement at multiple overtones allows for the best signal which are more to be analysed. In the case of palmitic acid , the third overtone is the most sensitive as it has the highest change in both frequency and dissipation during the adsorption of palmitic acid. The adsorption kinetics in Figure 5.9 and Figure 5.6 show that the rate of frequency change for palmitic acid was higher at pH 9 within the first 8 minutes. However, beyond this time, while the frequency appeared to stabilise at other pH, the adsorption rate increased at pH 8.6. At pH 8.8, the frequency continues to increase and never stabilises, suggesting that although the rate of adsorption was slowest, more palmitic acid can be adsorbed at this pH although not exceeding the other pH values. Oleic acid has the fastest adsorption rate at pH 9.0 as shown in Figure 5.7 while linoleic acid has the fastest adsorption at pH at both pH 8.8 and pH 9.0. The capacity of adsorption is reached very quickly with approx. 2.5 minutes (Figure 5.8) for linoleic acid at the pKa of 9.24 with the frequency remains stable after this suggesting that the capacity of adsorption has been reached. The other pH values within this time show

fluctuations in the frequency suggesting adsorption and desorption during this time while at pH 9.24 linoleic acid has reached the adsorption equilibrium capacity.

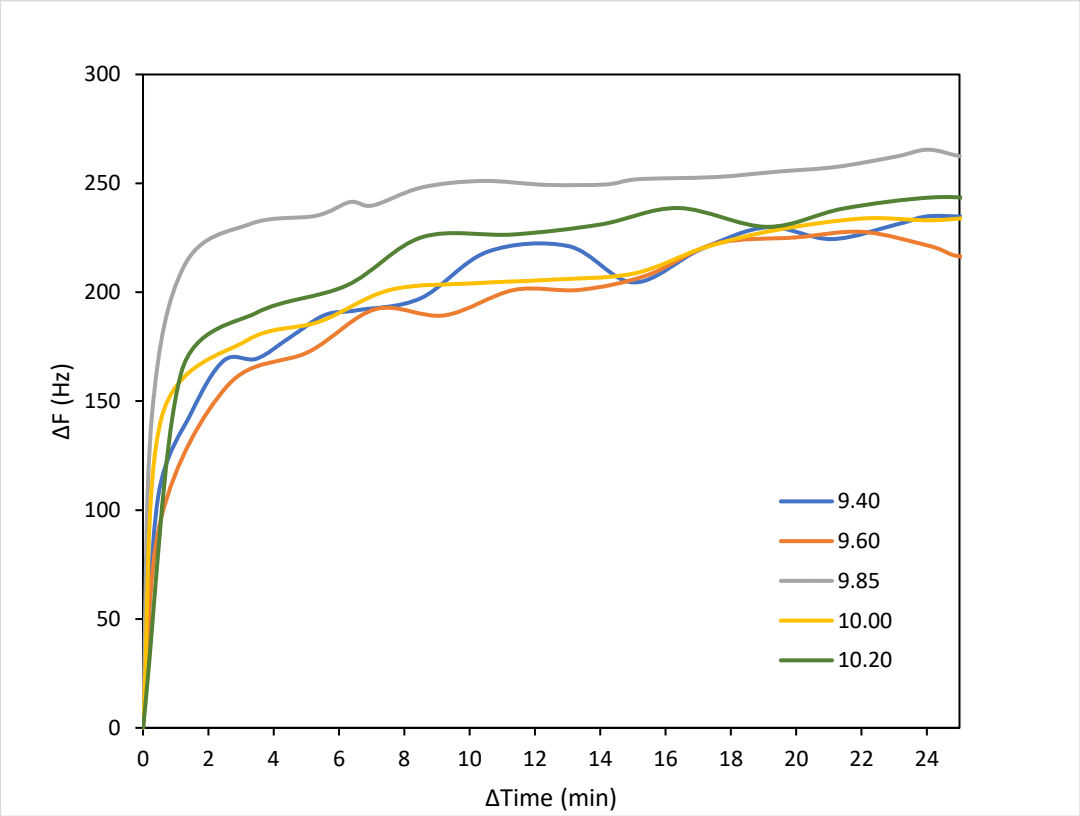


Figure 5.7 Rate of adsorption of Oleic acid on Gold at different pH.

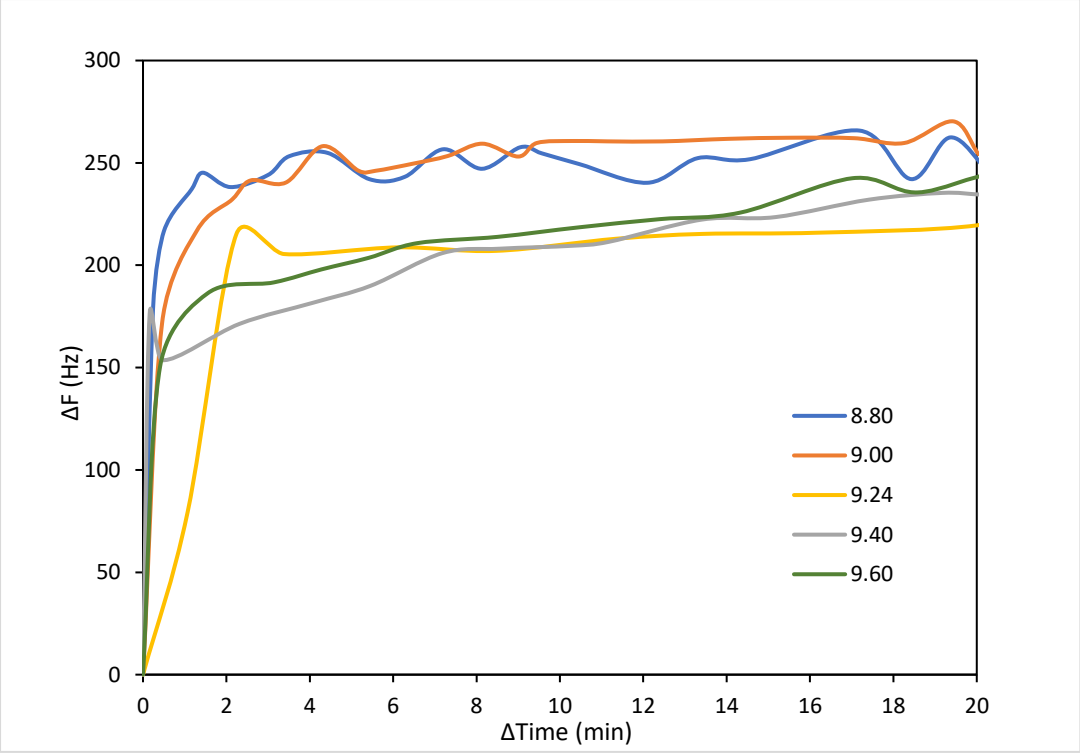


Figure 5.8 Rate of adsorption of Linoleic acid on Gold at different pH.

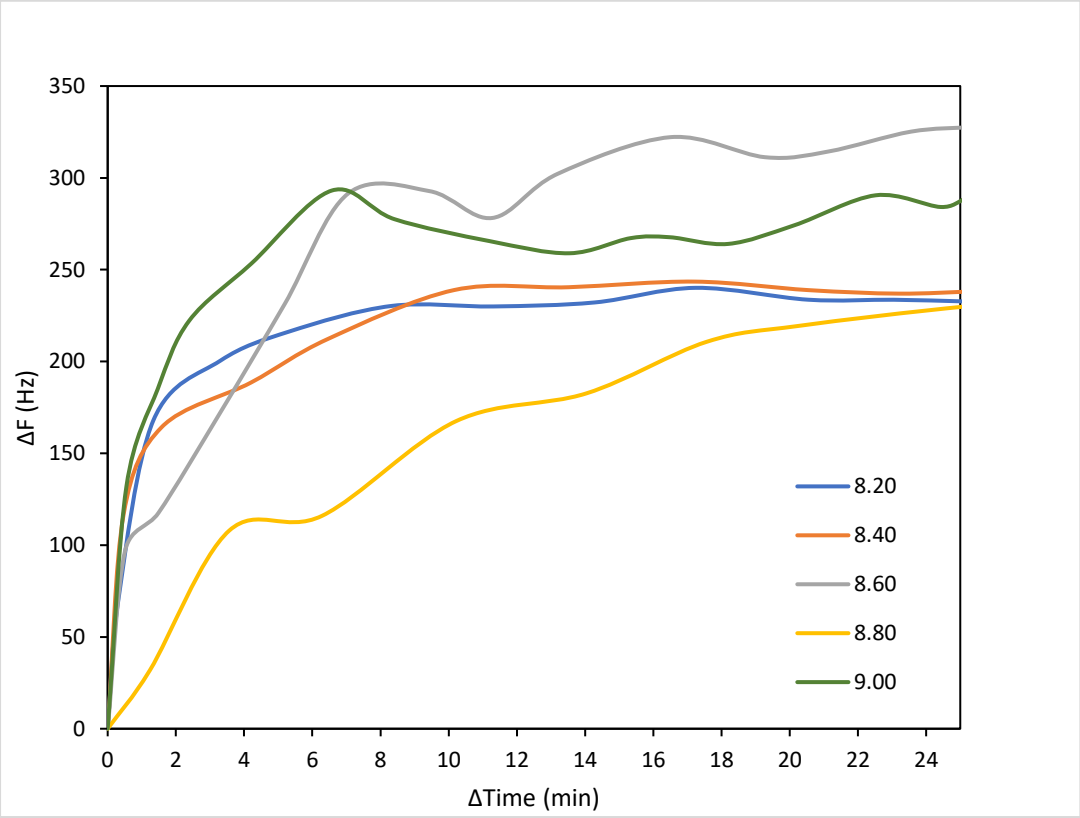


Figure 5.9 Rate of adsorption of Palmitic acid on Gold at different pH values

5.2.2.3 Contact Angle

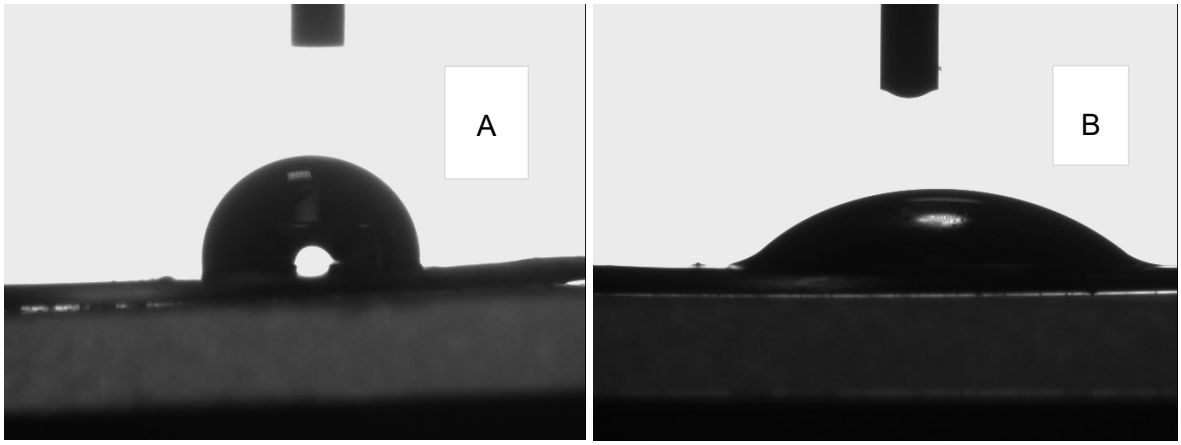


Figure 5.10 Oleic acid on aluminium oxide (A) and silicon dioxide (B)

Table 5.2 shows contact angle measurements after adsorption of FFA using QCM at pH 3.75

	Palmitic Acid	Oleic Acid	Linoleic acid
Gold	71.20 ± 0.56	135.00 ± 0.00	38.05 ± 1.48
Silicon dioxide	90.00 ± 0.00	77.40 ± 1.84	88.05 ± 2.75
Aluminium oxide	83.95 ± 0.35	30.95 ± 0.21	90.50 ± 0.71

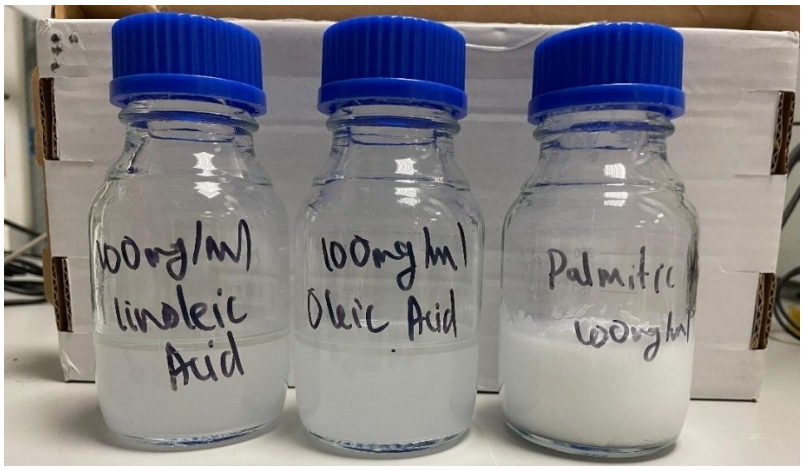


Figure 5.11 Effect of pH 3.75 on FFA

Table 5.2 and Figure 5.10 show contact angle measurements of the different FFA on different sensors. Contact angle measurements give an idea of the wettability of the sensors after the experiments. Figure 5.11 shows how the FFA interact with the citrate buffer used. The figure show that Oleic acid and linoleic acid separated from the bulk solution while palmitic acid formed precipitates with the citrate buffer. This led to the abandonment of testing for adsorption at very low pH. The results obtained from QCM of frequency change might have

been misleading for this pH as changes in frequency would not be only due to adsorption of the fatty acids but also formation of precipitates on the surface of the sensor. In the case of oleic and linoleic acid, the efficiency of adsorption would be hindered by non-polar nature of the fatty acids. The fatty acid chains at such low pH are not ionised contributing further to the already existing energy barrier between water molecules in the citrate buffer and the oleophilic fatty acid chain. This explains the discontinuity in the testing range seen in Table 5.1 as the new focus was testing adsorption around the pKa of the fatty acids.

5.2.2.4 Effect of Temperature

The temperature-dependence of adsorption of FFA was investigated using QCMD. The temperatures tested were 15ºC, 25ºC and 35ºC. Figure 5.12 shows that the temperature of the sensor surface was set to 15ºC however the experimental data shows that the Qsense explorer struggled to reach the set temperature as such, an external water bath was used to try to get the temperature as close as possible to the desired temperature. After a few repeats, the water bath was set to 5ºC as this was the lowest temperature that could be reached by the water bath without it freezing. Temperatures higher than this failed to get than 18ºC. The viscosity of ethanol was reported to decrease with temperature (Kaye & Laby, 2024). However as shown in Figure 5.12 by the dissipation of all plots of the three fatty acids, the dissipation remained the same thereby suggesting the viscosity of ethanol remained the same within the temperature range 16ºC and 18.4 ºC and $\Delta T < 2.5$ºC for all the experiments because of interactions with the FFA.

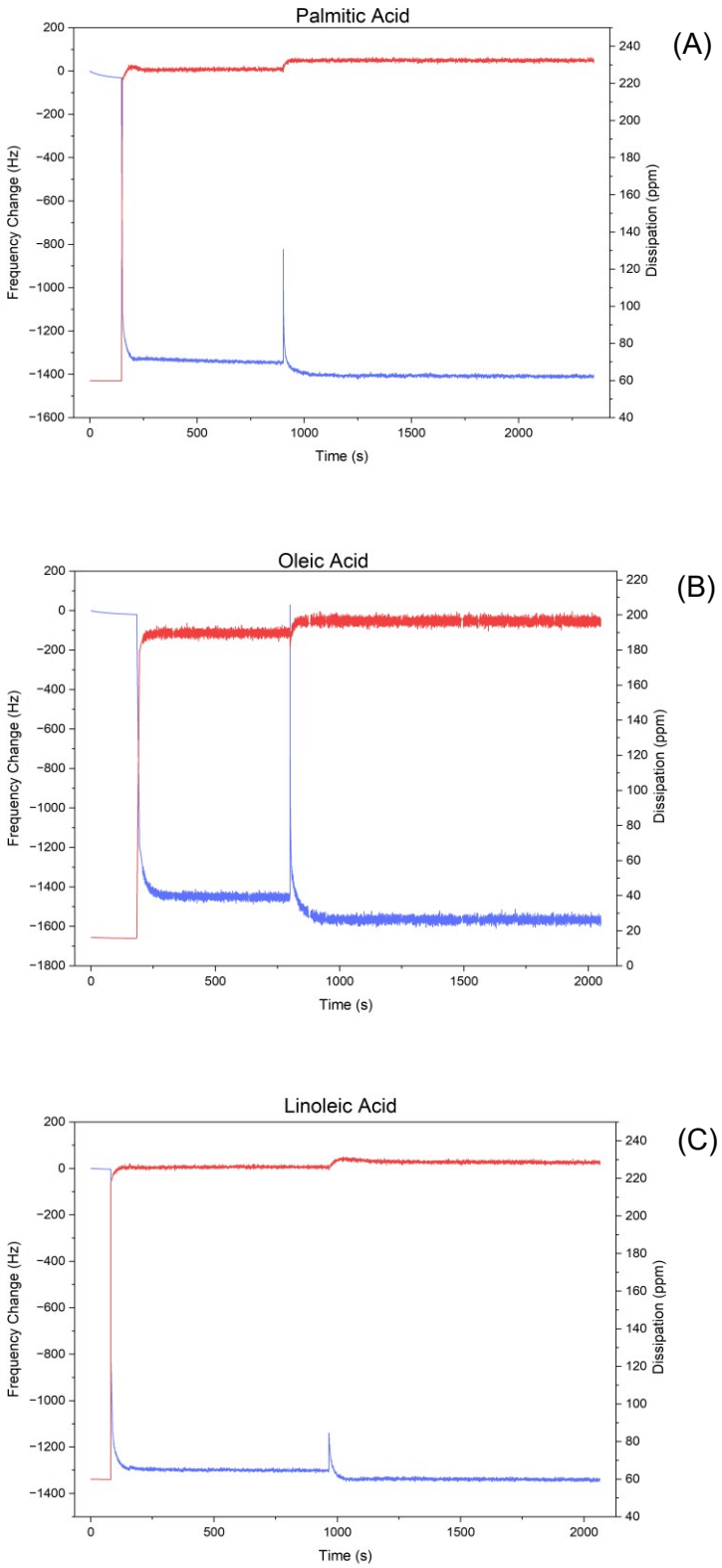


Figure 5.12 Effect of temperature on adsorption of 50mg/ml ss of fatty acid onto gold sensor at 15ºC (A) Palmitic Acid (B) Oleic Acid (C) Linoleic Acid

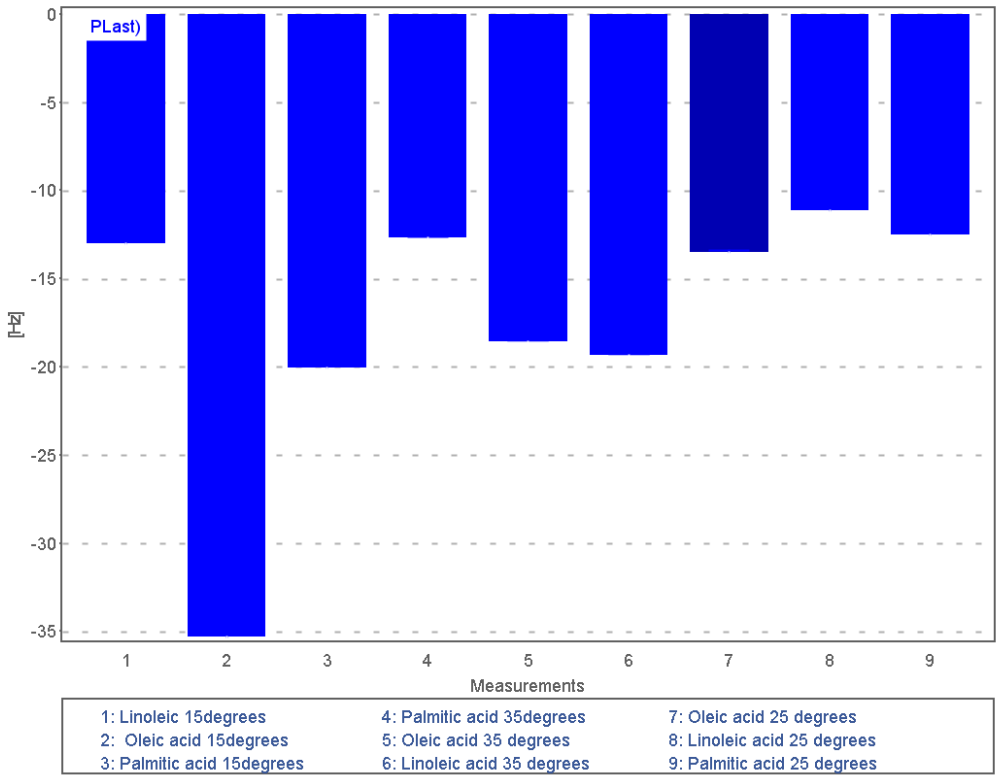


Figure 5.13 Shows influence of temperature on ΔF (Hz) of FFA.

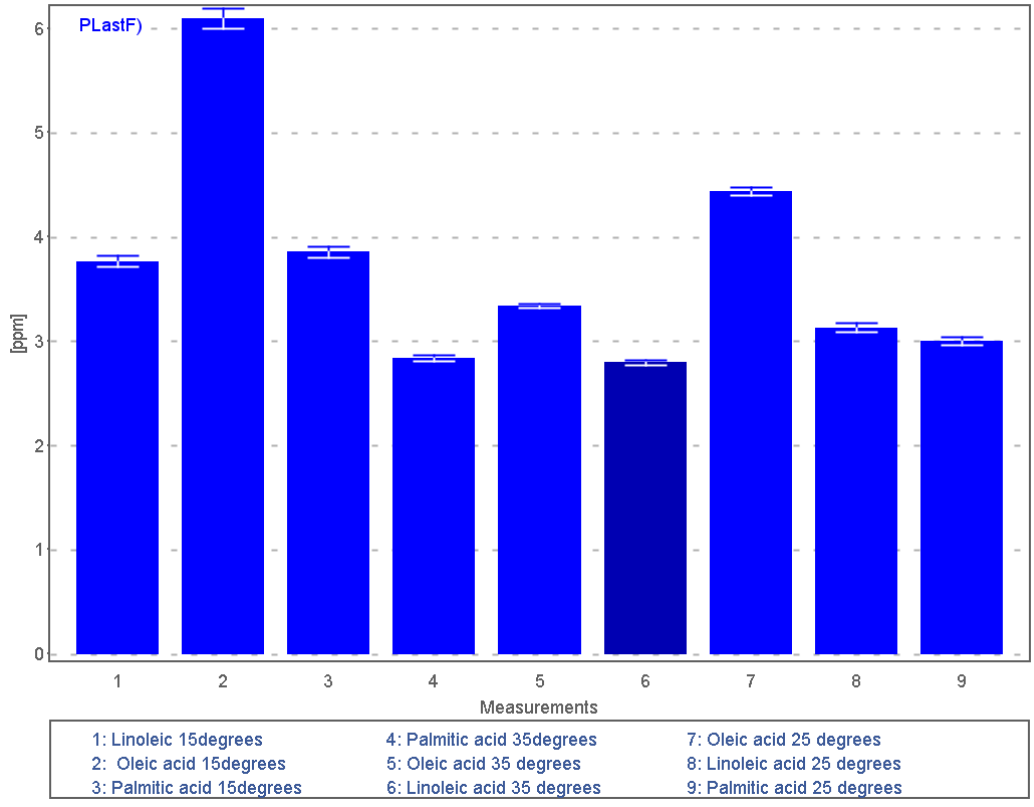


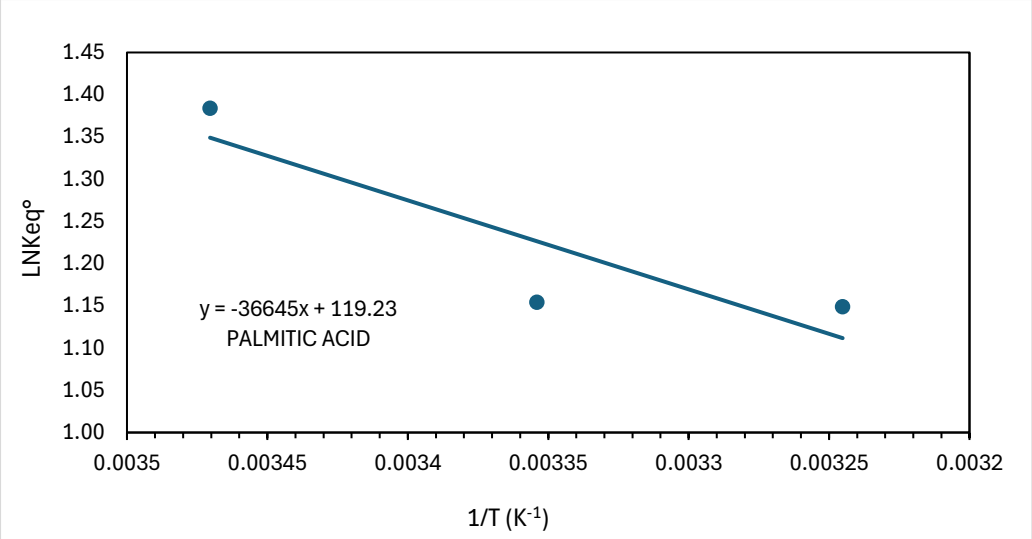
Figure 5.14 Effect of temperature on ΔDissipation (ppm) of FFA.

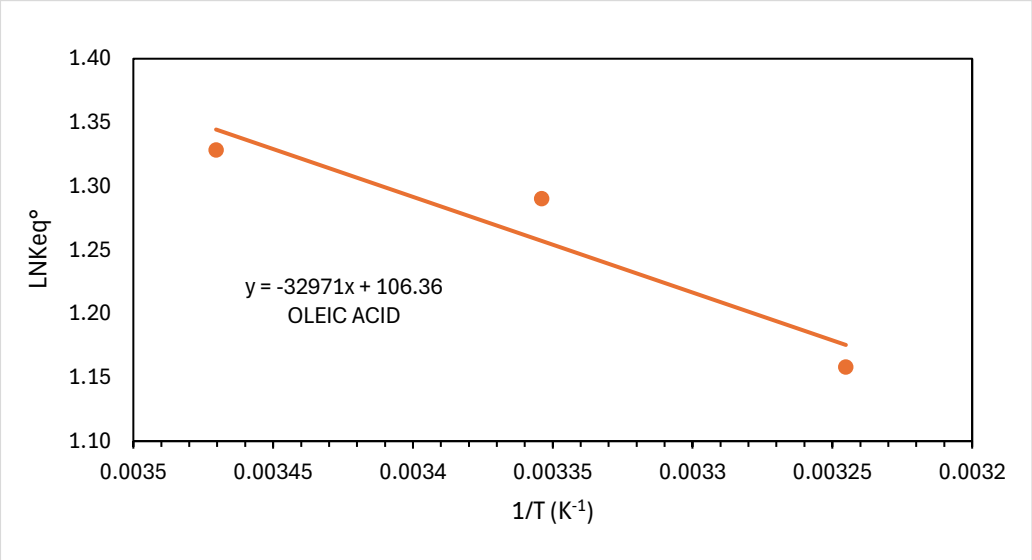
Figure 5.13 shows the effect of temperature on changes in frequency during adsorption of the FFA. At 15ºC, Oleic acid has the highest frequency change of 35Hz followed by palmitic acid at 20Hz and linoleic acid at about 13Hz. Linoleic acid adsorption on gold only caused a 11Hz frequency change making it the least adsorbed at 25ºC. However, at 35ºC, the results suggest more linoleic acid was adsorbed more (∆F at 19.3Hz) as compared to oleic acid (∆F at 18.6Hz) and palmitic acid (∆F at 12.7Hz). Palmitic acid showed a reduction in frequency change as the temperature was increased while oleic acid showed an increase in adsorption highlighted by an increase in frequency change between 25ºC and 35ºC.

Figure 5.14 shows that the dissipation change reduces with increasing temperature for adsorption of all the fatty acids suggesting the fatty acid become less viscous as temperature increases. Gusain et al. (2021) reported that increasing temperature resulted in reduction in the viscosity due to changes in the diffusion of the adsorbate thus resulting in a shift in the position of equilibrium of adsorption. However, oleic acid has the highest change in dissipation changes implying larger changes in viscosity at all the temperatures tested as compared to palmitic and linoleic acid.

Table 5.3 Thermodynamic parameters for FFA on Gold.

Adsorbate	Temp (K)	Keq°	∆G° (KJ mol^{-1})	∆H° (KJ mol^{-1})	∆S° (KJ^{-1} mol^{-1})	R^2
Palmitic Acid	288.15	3.9907	-3.3156	304.6765	991.2782	0.9846
	298.15	3.1719	-2.8614			
	308.15	3.1552	-2.9438			
Oleic Acid	288.15	3.7753	-3.1826	274.1209	884.2770	0.9235
	298.15	3.6337	-3.1983			
	308.15	3.1847	-2.9677			
Linoleic Acid	288.15	4.9295	-3.8217	364.7518	1197.2160	0.7666
	298.15	3.2258	-2.9032			
	308.15	3.2092	-2.9873			





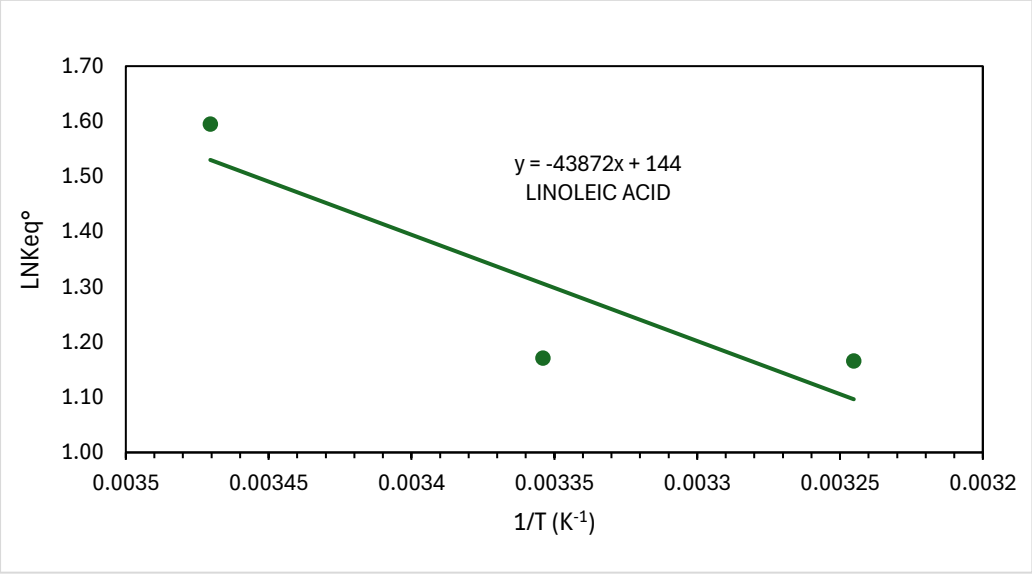


Figure 5.15 Endothermic reaction as calculated by Van´t Hoffs equation FFA adsorption on Gold.

Figure 5.15 is a plot of LNKeq° against 1/T. The entropy of the system ∆S° and enthalpy ∆H° are calculated by (Romero-González et al., 2005):

$$\Delta S° = intercept \times R$$

Equation 5.8

$$\Delta H° = -slope \times R$$

Equation 5.9

Table 5.3 show the thermodynamic parameters of the FFA on a gold surface. Figure 5.15 shows that the adsorption the was endothermic as shown by the positive enthalpy values. The values of the enthalpy also suggest that chemisorption was favoured at all the temperatures as the enthalpies were all above $\pm 80KJ$ (Savara et al., 2009). The enthalpy of the systems ranged from 274.12KJ mol^{-1} to 364.75KJ $mol^{-}1$. This suggests that chemisorption was due to the hydrogen bonds (Au-O=C) between the COOH- and the Au from the sensor surface (Maity et al., 2024; Schmidbaur et al., 2014). This also supports that monolayer adsorption occurred during all instances. The entropy also suggests that there was increased randomness in the adsorption at the interface between the bulk solvent and the sensor surface thereby promoting adsorption (Sahmoune, 2019).

The entropy is highest for linoleic acid followed by palmitic acid. The Gibbs free energy was found to be -ve and decreased with increasing temperature thereby also supporting the adsorption of the FFA on gold. R^2 was found to be higher than 0.9235 for oleic acid and palmitic acid. However, a lower R^2 of 0.7666 for linoleic acid was determined. This is because the highest frequency change measured for linoleic acid was at 35°C and below this temperature the results from Figure 5.3 suggest at lower temperature less linoleic acid is adsorbed. However, the values of entropy and enthalpy are the highest suggesting greater disorder/ spontaneity and thereby increased adsorption. This is contrary to the results obtained from QCM experiments. The application of Langmuir isotherm (used to determine q_e and therefore Keq°) for linoleic acid was not as favourable as seen for palmitic and oleic acid. The raw data for all fatty acids can be found in appendix 8.3.

5.2.2.5 Effect of inserts on adsorption

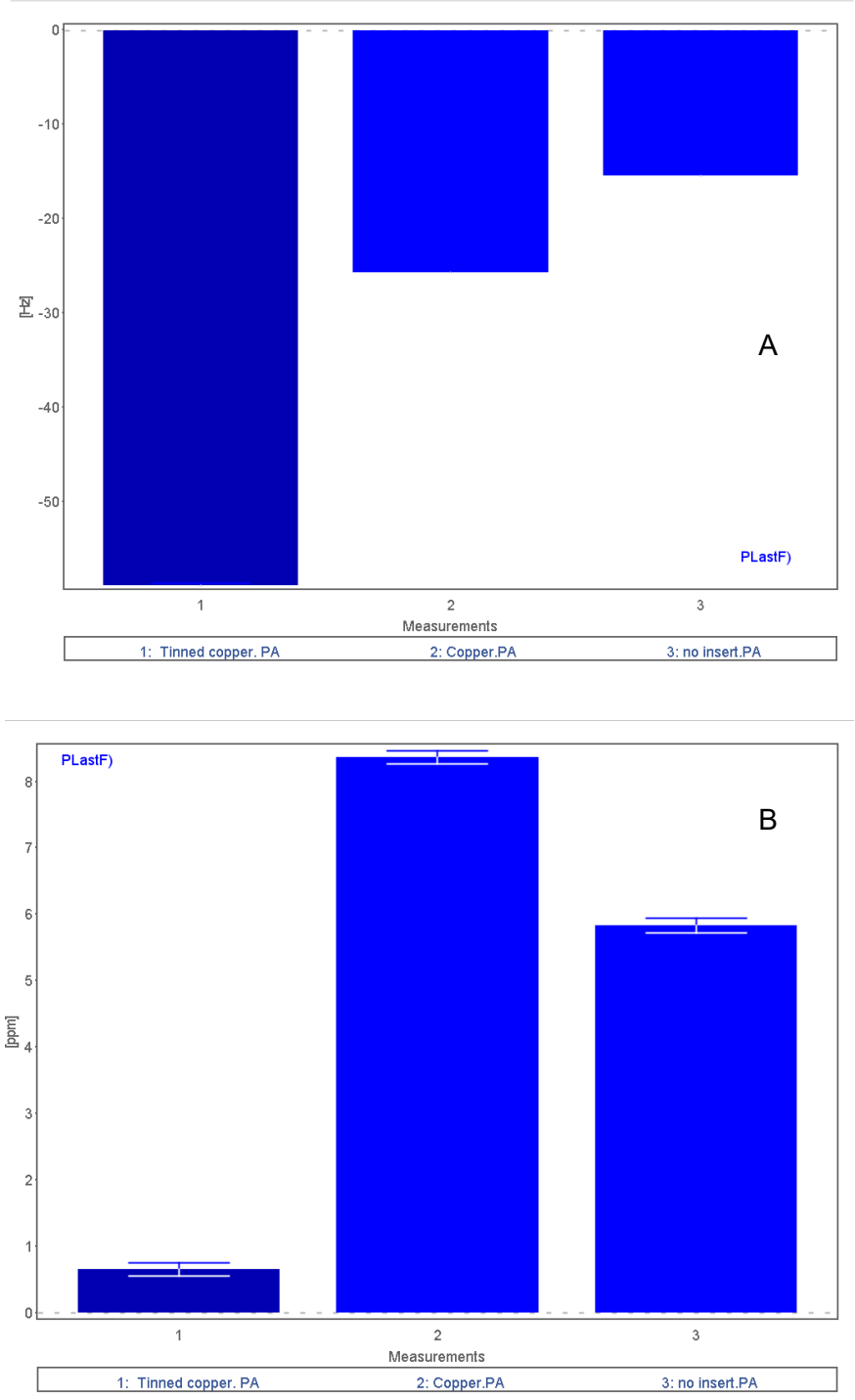


Figure 5.16 Effect of inserts on palmitic acid adsorption [A] Frequency (Hz), [B] Dissipation (ppm).

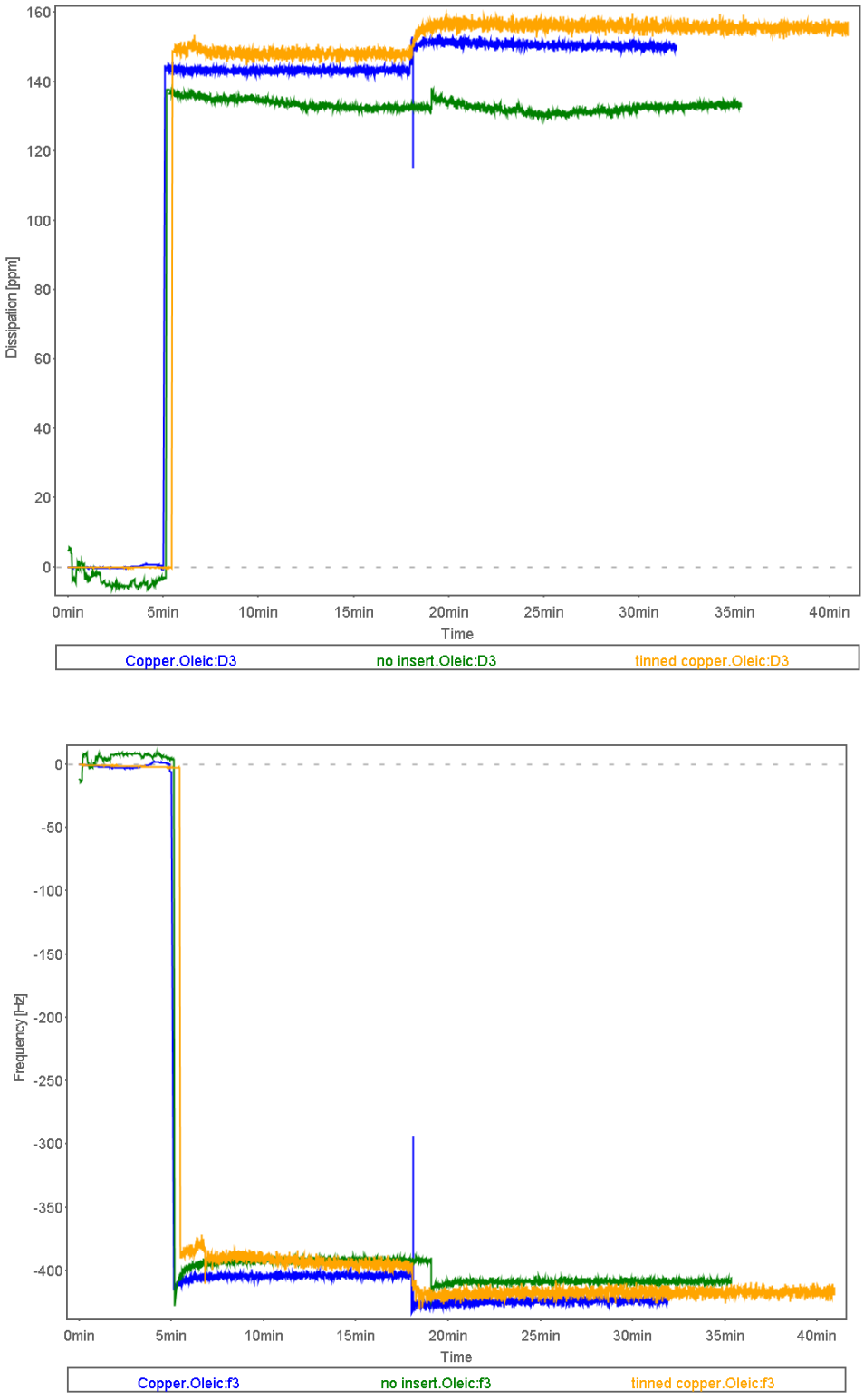
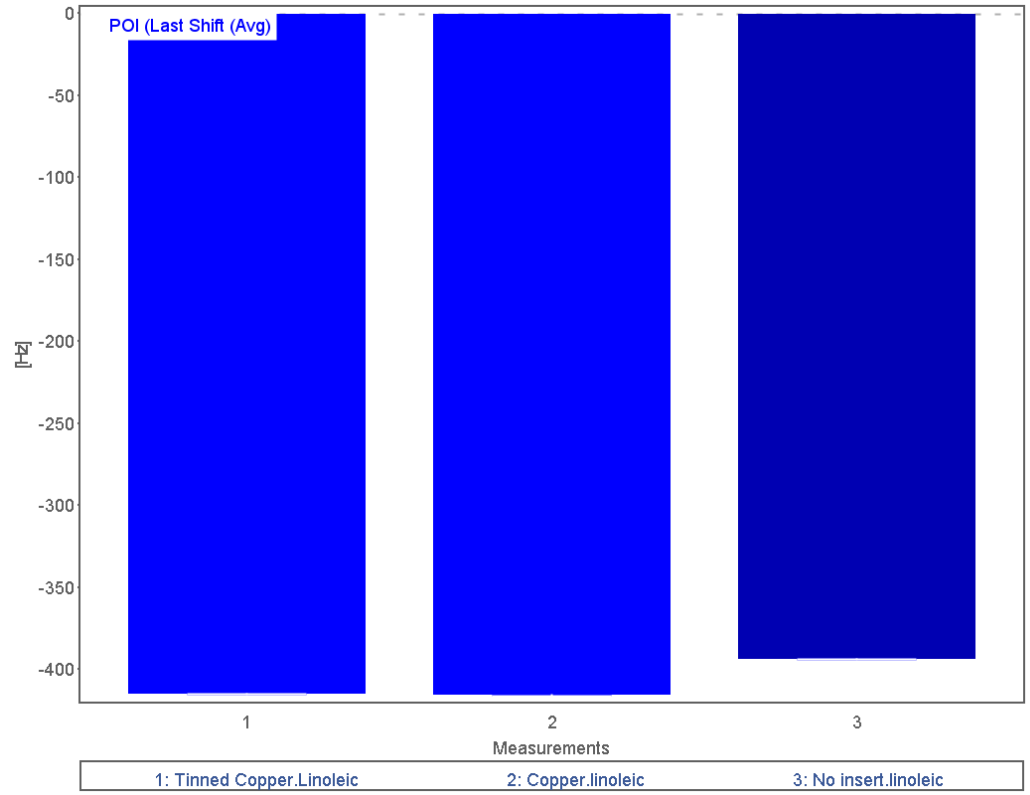
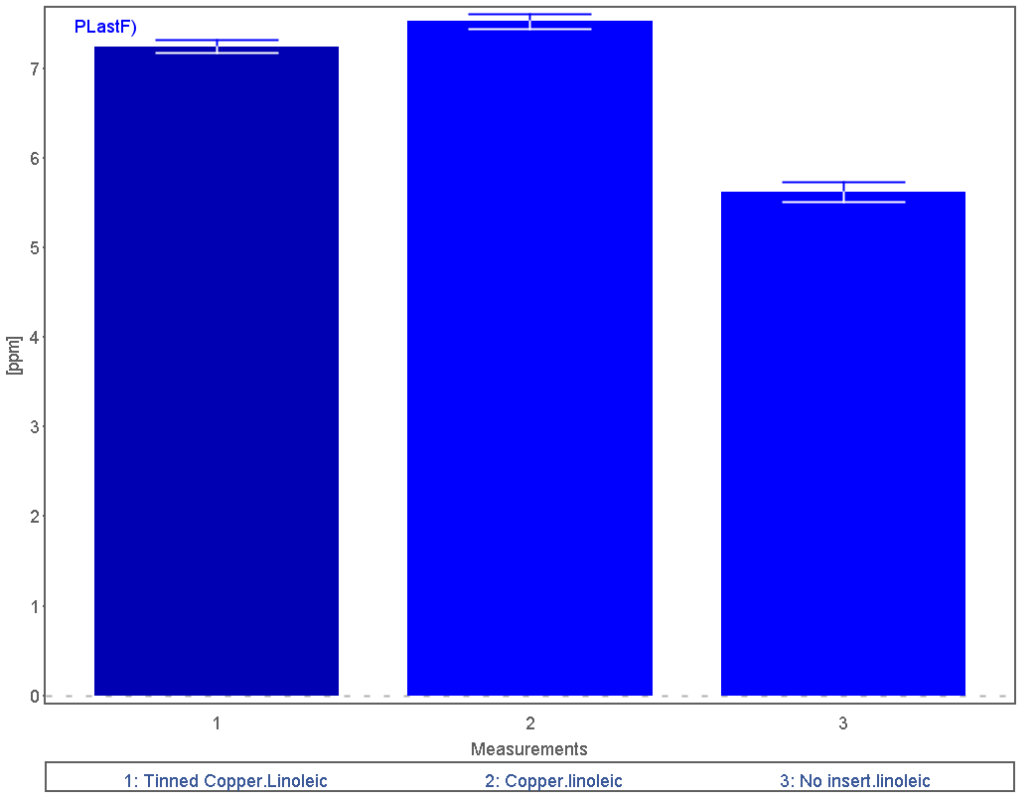


Figure 5.17 Effect of inserts on adsorption of oleic acid.



A



B

Figure 5.18 Effect of inserts on adsorption of linoleic acid. [A] Frequency (Hz), [B] Dissipation (ppm).

Figure 5.16, Figure 5.17 and Figure 5.18 showed the effect of introducing inserts on adsorption of FFA on Gold. Figure 5.16 shows that the highest frequency change was for tinned copper followed by copper. This suggest that there was less adsorption when the was no insert and that tinned copper promoted the adsorption of palmitic acid. The dissipation change was highest for copper and lowest for tinned copper. For oleic acid adsorption, having no inserts supported more adsorption while tinned copper supported more adsorption than the pure copper insert. The difference in frequency for linoleic acid for both inserts is very small (ΔF =1.1Hz) with the copper insert having a slightly higher frequency change. The system with no inserts had the least adsorption in this case. For linoleic acid, the change in frequency is proportional to the change in dissipation while there is no clear correlation between frequency and dissipation changes for oleic acid and palmitic acid systems with inserts.

The results showed that introducing inserts has an impact on adsorption due to the difference in the surface chemistry and surface area in the system (Yang et al., 2017). The increased surface area and number of adsorption sites affected the amount adsorbed. Tinned copper is protected from corrosion whereas the copper insert had ionic interactions with the bulk solution. The dissipation also suggests copper forms ionic bonds with palmitic acid thereby resulting in a change in the viscosity of the adlayer. The results of both frequency and dissipation for all the fatty acids suggest that a different mechanism is present as well as different species. The exploration of the mechanism at the sensor-solvent interface and at the insert-solvent interface have not been explored in this work as the focus was to establish whether introduction of foreign inserts affect the adsorption.

5.2.3 Conclusion

The investigation of pH on adsorption of FFA has highlighted that the adsorption of the FFA in highest around the pKa values of individual fatty acids. Testing for adsorption at very low pH with a citrate buffer resulted in repulsion forces between water molecules in the buffer and the hydrophobic fatty acid tail resulting in the unsaturated fatty acid forming a layer above the buffer. Palmitic acid formed precipitates with the citrates buffer. The observations were not observed where testing was done near the pKa, and a different buffer (sodium bicarbonate-sodium carbonate) used. Calculation of the thermodynamic parameters determined that the adsorption of all FFA was an endothermic process with a great degree of spontaneity. This was supported by the -ve $\Delta G°$ which decreased with increasing temperature for all the fatty acids and that monolayer adsorption was favoured. The addition of inserts to the batch system affected adsorption with tinned copper performing better than pure copper inserts. The viscoelastic properties of the adlayer were greatly affected by the presence of inserts due to

introduction of new species such as Cu^{2+} into the system. This was observed by the extent of change in dissipation using QCM.

Chapter 7 Main conclusion

Adsorption of palmitic acid linoleic acid and oleic acid have been investigated using the QCM. The advantage of this method is that it is quick and does not require lots of materials thereby being an environmentally friendly method of investigating adsorption. The drawback of this method is that the quartz sensors are expensive (a pack of five cost approximately £500.00) and as recommended by the manufacturer the sensors can only be used once. The sensors were cleaned with ethanol before and after the experiments as it was effective at dissolving any physiosorbed fatty acids as highlighted by the results from X-ray photoelectron spectroscopy.

The quartz sensor is the centre of this work. By using this method, it was possible to determine the areal mass capacity of adsorbed FFA onto different materials. The effect of pH, concentration and temperature were all investigated, and it was determined that the adsorption was an endothermic process, which was very spontaneous as shown by the Gibbs free energy of the systems at different temperatures. By changing the concentration, adsorption isotherms of frequency against concentrations were determined. The general trend being adsorption increased with increasing concentration however, there were some slight variations depending on the adsorbent.

It was found that the influence of pH on adsorption of the fatty acids onto the sensors was more favoured around the pKa of the fatty acids. Another phenomenon was the effect or order of injection on adsorption. This was studied by tracing both frequency and dissipation shifts. Oleic acid in this case proved to contribute to higher adsorption. The other fatty acids were adsorbed more depending on whether they were injected first or last and on the substrate sensor used. The introduction of inserts also highlighted that adsorption increased when either tinned copper or copper inserts were introduced into the system.

The quartz sensor as mentioned is highly sensitive, hence the difficulty was finding a suitable method for characterizing the surface. In-situ methods of characterization are always desirable as it is possible to measure the change in real time as adsorption occurs. However, due to the associated high cost the sensors were analysed either before or after the QCM experiments. X-ray photoelectron spectroscopy proved invaluable as it was possible to determine the surface modification by looking for the COOH group to confirm adsorption. Raman microscopy was also used however, as contact is required between the probe and the sensor, extra care was required. It should be noted that high power settings above 12.5mW can degrade the sample as shown in this work. Despite this, the bonds formed on the surface were determined successfully without causing damage to the sensor in most cases. FTIR was also used

however, the extent of use was limited to end-of-life sensors as greater force between the probe and sensor was required which resulted in breakage of the sensor in most cases. The thesis discussed the adsorption kinetics of adsorption of the FFA with application of the Langmuir model. The adsorption kinetics together with the application of the Vant Hoffs equation resulted in determination of the adsorption equilibrium constants K, and the thermodynamic constant Keq° resulting in confirmation of monolayer adsorption in various instances.

Chapter 6 Further Work

In this work, the densities of the adsorbate and solvent have been assumed to be similar for ease of calculation, thus Sauerbrey model used for calculating ∆m which would be the same as ∆m for the Voight model under this assumption.

For increased accuracy,

$$m_{film} = m_{ads} + m_{solvent}$$

Equation6.1

where a secondary technique such as ellipsometry could be used to determine the mass of the adsorbent.

This could then be used to calculate the thickness of the film h_f.

$$h_f = \frac{1}{\rho_{solvent}}\left[m_{film} - m_{ads}\left(1 - \frac{\rho_{solvent}}{\rho_{ads}}\right)\right]$$

Equation6.2

(Reviakine et al., 2011)

Characterization of the adsorbent sensors by Raman microscopy revealed the presence of FFA. However, quantifying which fatty acid adsorbed more by using peak area ratios was outside scope hence for future research. That would help in being able to predict which fatty acids could more during sequencing as well support the results from QCMD presented in this work.

QCMD experiments were conducted under laboratory conditions described in this work. To increase relevance in the field of adsorbents for FFA removal from wastewater, real life sewer conditions could be explored to assess how well the materials investigated in this work perform as adsorbents.

Application of different adsorption isotherms e.g. Langmuir, Freundlich etc to QCMD data from adsorption of oleic and linoleic acid could help extend the work presented in this thesis thereby helping predict adsorption capacities of the adsorbents.

6.1 Spin Coating

Attempts were made to spin coat synthesised silica particle however this was unsuccessful as shown in Figure 6.1. More work is required in the method development of coating the quartz sensor. Much research has been done in control the properties such as particle size, and functionalization of the silica particles in literature. Combined with QCM and successful coating/ formation of a top layer for use in QCM experiments for FFA adsorption could help in tailoring the highest adsorption and recovery of the fatty acids. Because of the sensitivity of the quartz crystal microbalance, it is important to consider best practices to achieve this such as effect of sensor mounting, temperature etc (Fredrik Pettersson, 2025). This method might be more cost effective than ordering sensors of different materials from the supplier. More work is required to develop a robust method of coating the quartz sensors. Exploration of other techniques for characterizing the quartz sensor such as AFM could also be used for surface coverage studies for adsorption of fatty acids. Kenneth Olesen (2024) had already created an standard operating procedure for spin coating materials onto the quartz sensors. This highlights increased need for researchers to control surface properties including those offered by the QCMD.

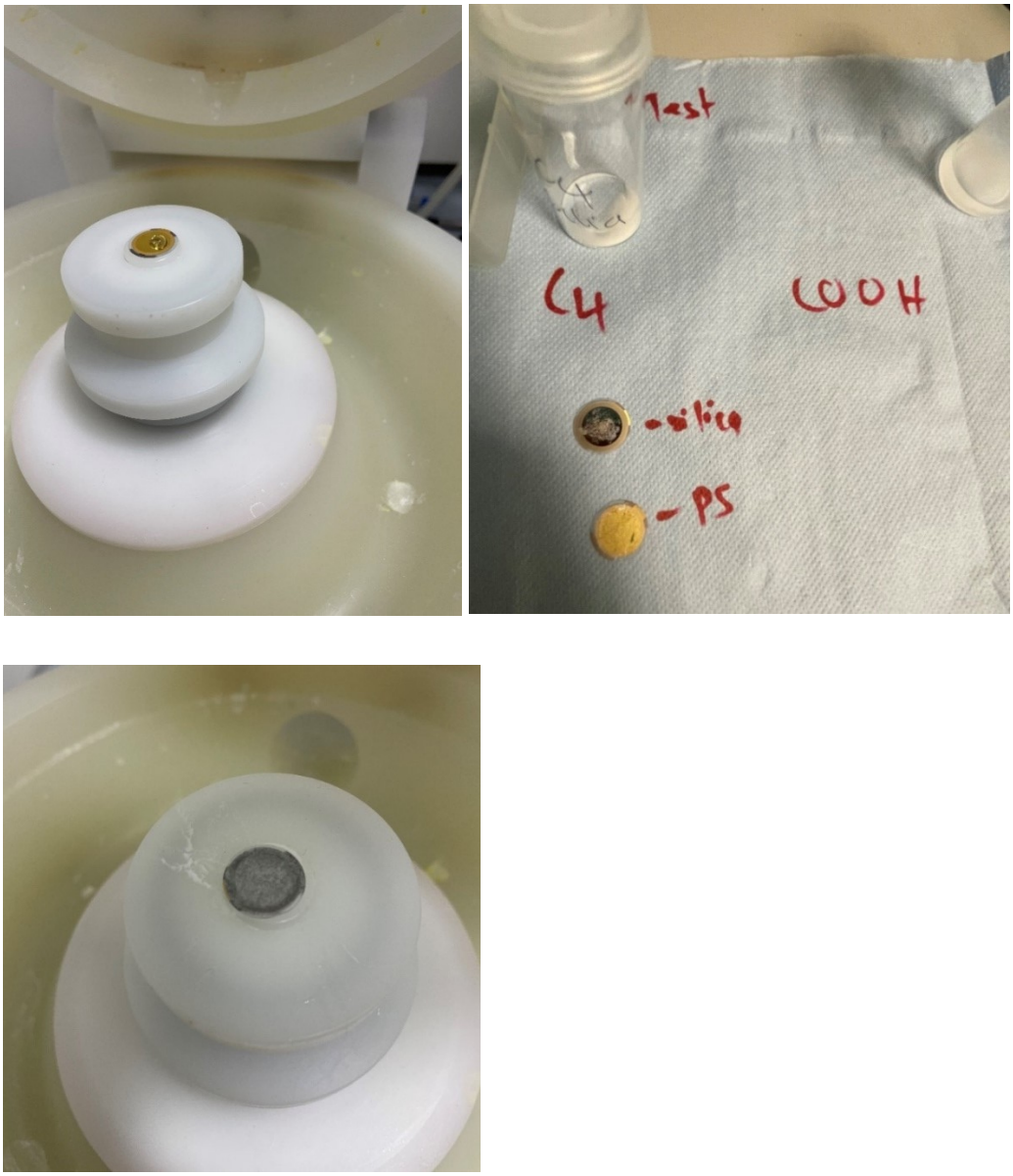


Figure 6.1 Spin coating of particles with different functional groups on quartz sensors.

6.2 Proof of concept

The first objective of this work was to synthesize silica particles and to determine whether the QCM-D was a good technique for determining the kinetics of adsorption. The synthesis of silica nanoparticles was done following the Stober method of synthesis. SEM was used to determine if spherical particles were synthesised. The ability of the gold-plated quartz crystal to be used for adsorption was investigated by using octadecane.

6.2.1 Experimental Methods

6.2.1.1 Silica Synthesis and particle size distribution

The Stober method was followed to synthesize silica nanoparticles. The experimental procedure is as shown in Figure 6.2. This method was adapted from the work done by Rao et al. (2005) as shown in Figure 1.3. However, in this work, the ultra-sonicator was replaced by using a magnetic stirrer. Ethanol was mixed with deionised water in a round bottom flask and put on a magnetic stirrer for 10 minutes. Tetraethoxysilane (TEOS) was then added to the mixture of ethanol and DI water. The pH was then measured using a pH meter which was then washed with DI water after use. After 10 minutes, 28% ammonium hydroxide solution was added dropwise to the mixture. Table 6.1 shows the quantities of each substance used in the experiments conducted. The mixture was left overnight on a magnetic stirrer set to 750rpm at room temperature. The mixture was then centrifuged for 10 minutes at 6000rpm to recover synthesised Stober nanoparticles. The recovered particles were then dried at room temperature in a fume hood.

Image J was used to measure the diameter of particles generated from the SEM images. Minitab was then used for plotting the histogram of average length (diameter) of the synthesised particles.

Table 6.1Shows the material and Equipment list needed for Experiments

Experiment	Materials and Equipment
Silica Synthesis	• TEOS from Aldrich • De-ionised (DI) Water • Ethanol • 28% ammonium hydroxide • Magnetic stirrer • pH meter • scale • round bottom flask • centrifuge
QCM-D	• Gold plated quartz crystal (QSX 301) from Qsense. • Octadecane from Acros organics, CAS: 593-45-3 • Spatula • Tweezers • Soft tissue paper • Cyclohexane • Qsense Explorer • Qsense open module

Table 6.2 shows the amounts of each regent used in the experiment

Experiment	pH	Ammonia (ml)	TEOS (ml)	DI Water (ml)	Ethanol (ml)	Mass of ammonia (g)	Total Volume (ml)	Molarity
1	13.76	8.00	6.00	14.00	96.00	7.20	124.00	1.66
2	13.65	3.80	6.00	14.00	96.00	3.42	119.80	0.81
3	13.65	10.00	6.00	14.00	96.00	9.00	126.00	2.04

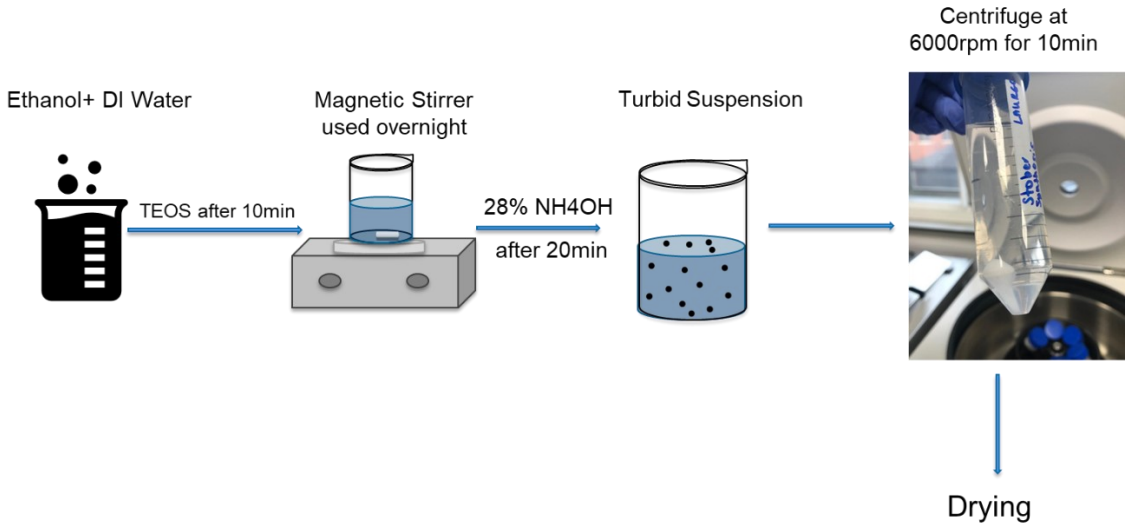


Figure 6.2 Procedure for synthesis of silica nanoparticles using the Stober method.

6.2.2 QCM-D

An alkane, Octadecane was used to test if the quartz crystal microbalance (QCM-D) could be used to measure adsorption on a gold-plated quartz crystal. The first step was to prepare the quartz crystal by cleaning and drying. After which it was mounted onto the QCM-D flow cell. A simple method of cleaning was used which involved washing the quartz crystal in hexanol then rinsing it with deionised water. Since the quartz crystal is extremely sensitive, it was dried with a soft paper towel to avoid scratches and then further dried with nitrogen gas. To test if no damage to the crystal was made during cleaning, the empty crystal was loaded onto the QCM-D flow cell and the experiment conducted to assess whether any resonance frequencies could be picked up. After the crystal was deemed fit for use, a sample in this case octadecane was

loaded onto the centre of the crystal. A small sample is used as the QCM-D sensor is very sensitive to any change mass. The experiment is then run following the standard operating procedure set as described below.

6.2.2.1.1 Standard Operating Procedure

Octadecane is a solid at room temperature. To test how temperature affects adsorption, a procedure was devised involving heating octadecane from 27°C to above its melting point of 28°C and then cooling it back from 31°C to the start temperature. The temperature was increased by 1°C in each step. The time increments at each step were set to 10 minutes except at the end of the experiment where the sample was cooled for 20 minutes to ensure it fully solidifies.

In the second stage of investigations, the temperature was increased from 25°C to 31°C to ensure the sample was fully melted before cooling it back to room temperature. The temperature was increased by 1°C in each step just as in the previous test. The time increments at each step remain the same at 10minutes and at the end of the experiment where the sample was cooled for 20 minutes. The same experiment was then repeated multiple times to test if the octadecane polymorph does not change on subsequent heating cooling and reheating.

6.2.3 Results and Discussion

6.2.3.1 Silica Synthesis

The Stober method was used to synthesise silica nanoparticles. Concentration of ammonium hydroxide(28%) solution was varied to see the effect this would have on the synthesised particles. Figure 6.3 and Figure 6.5 shows the results of the SEM images. SEM is a characterization technique used for morphological studies of materials giving information of the size, pore structure, shape and particle size distribution of the material under test (Seetala et al., 2013; Abdelaal et al., 2014). Figure 6.3 shows silica particles synthesised at 0.81M and Figure 6.5 shows particles synthesised at 1.66M. It is seen that in both figures, spherical particles were synthesised. Table 6.3 showed that the mean diameter of the 0.81M particles is 0.4575μm while the diameter of the 1.66M particles is 1.0409 μm. The particle size increased with increasing concentration of ammonium hydroxide(28%) which is contrary to the results obtained by Zulfiqar et al. (2016) described in section 1.2.2.4.2. This may be because while the particles were synthesised and the experiment being run overnight, evaporation occurred. Ethanol may have evaporated resulting in a decrease in its concentration hence reducing the particle size as shown in Figure 6.3. Another factor that is

observed is that sub particles also formed resulting in having different sized particles in Figure 6.3. Figure 6.5 on the other hand shows spherical particles and in some cases the particles seemed to have been nucleating thus affecting the shape of some of the particles. Figure 6.4 and Figure 6.6 show histograms of particle size distribution of the sober particles. Figure 6.4 shows a bimodal particle size distribution. This is highlighted by the two peaks indicating that there are two main modal particle sizes which are particles of diameters 0.452μm and 0.575μm. This also suggests that the particles were formed via aggregation as suggested in section 1.2.2.3. Figure 6.6 on the other hand shows a normal distribution of particles with modal diameter being about 1.05μm.

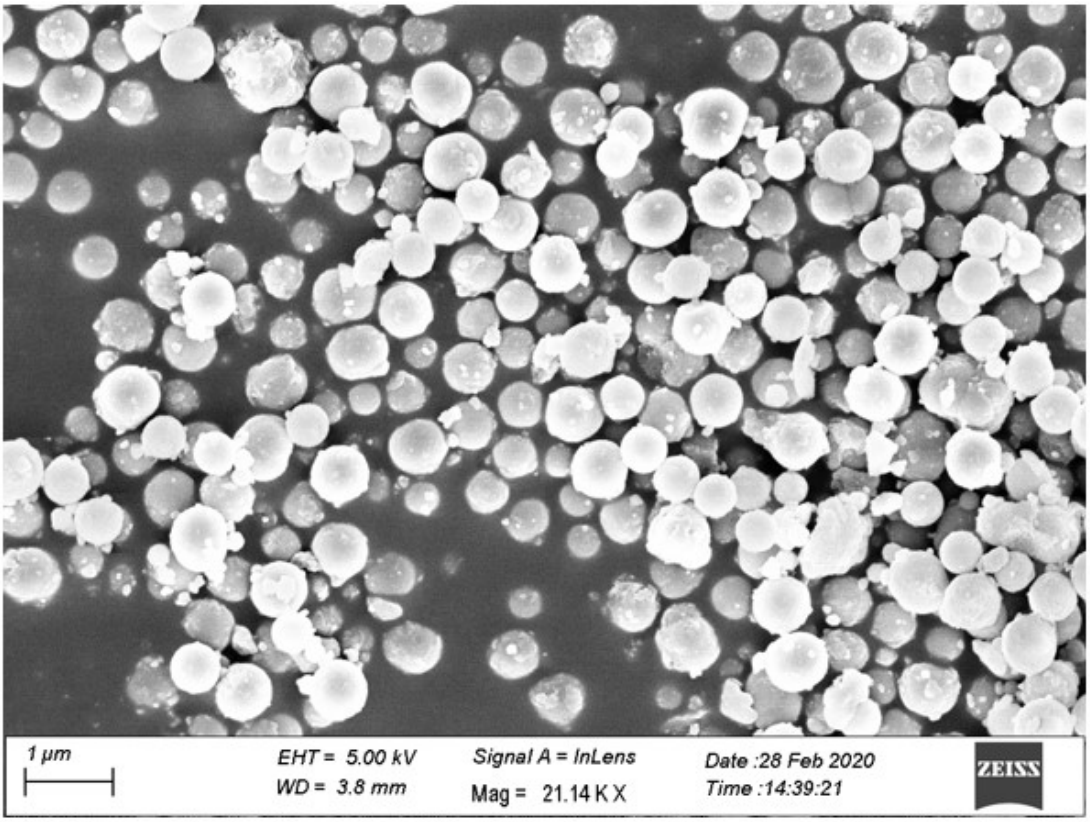


Figure 6.3 shows the Scanning Electron Microscopy image of silica made at 0.81M of ammonium-hydroxide(28%)

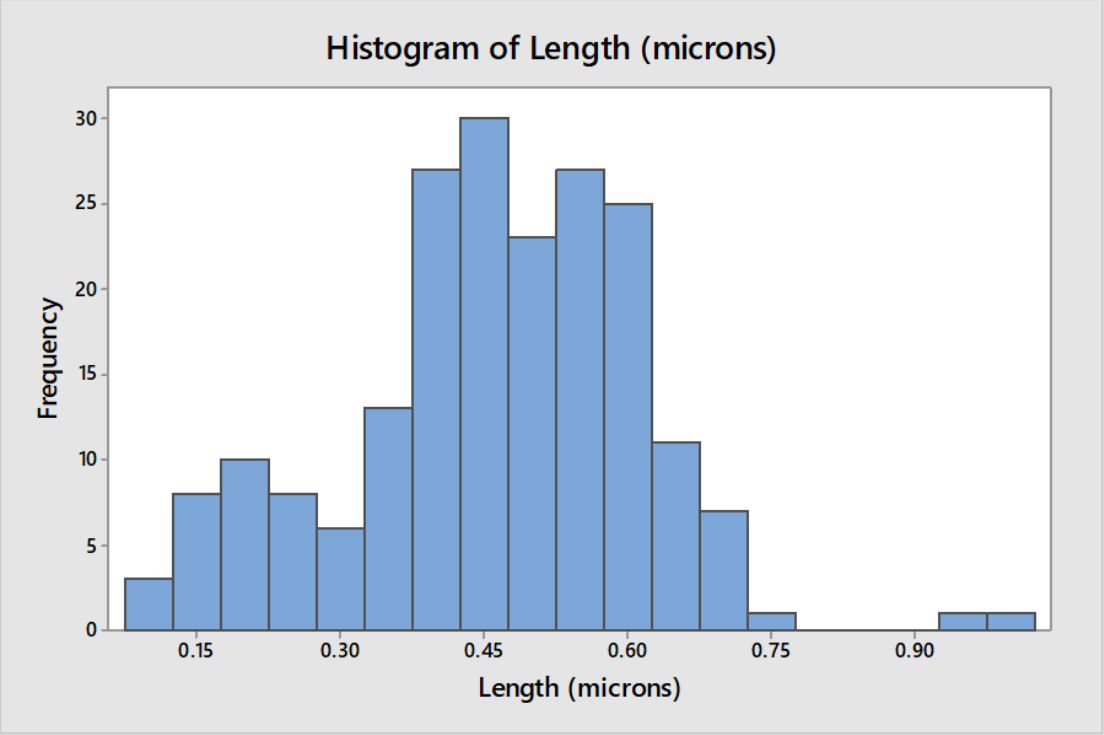


Figure 6.4 A histogram of the particle size distribution of silica made at 0.81M of ammonium-hydroxide(28%)

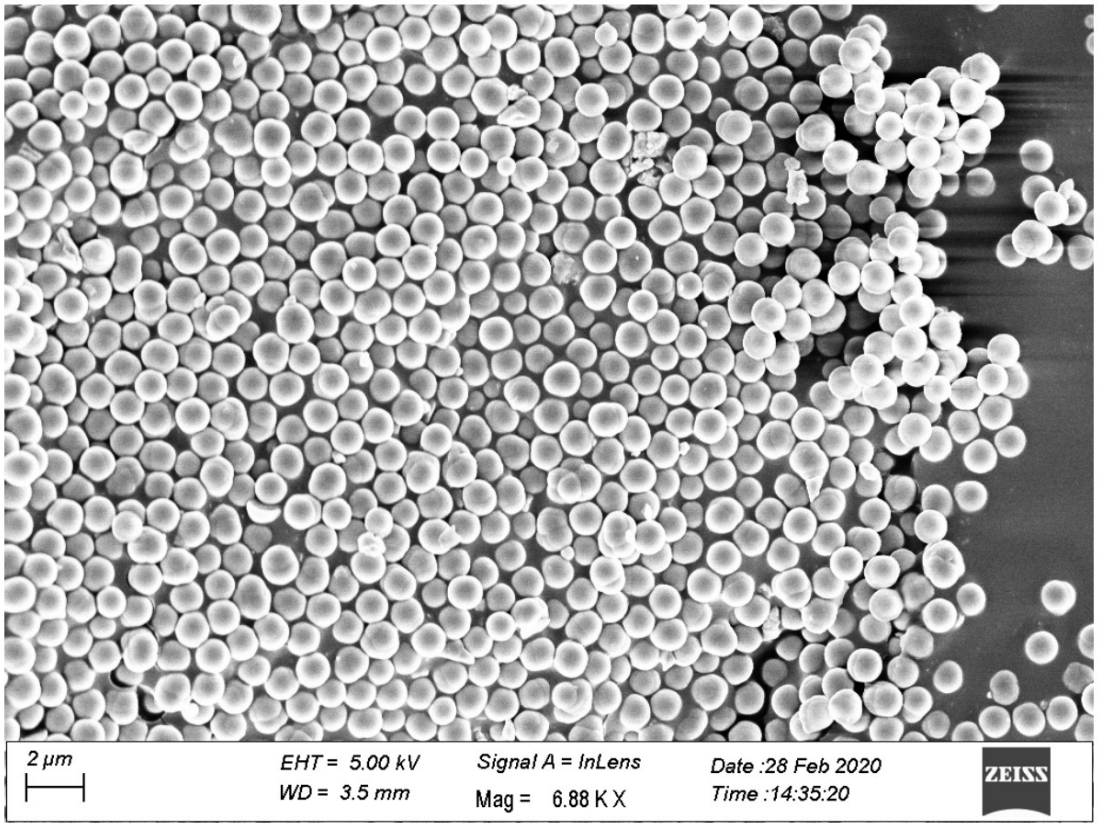


Figure 6.5 Scanning Electron Microscopy image of silica made at 1.66M of ammonium-hydroxide(28%)

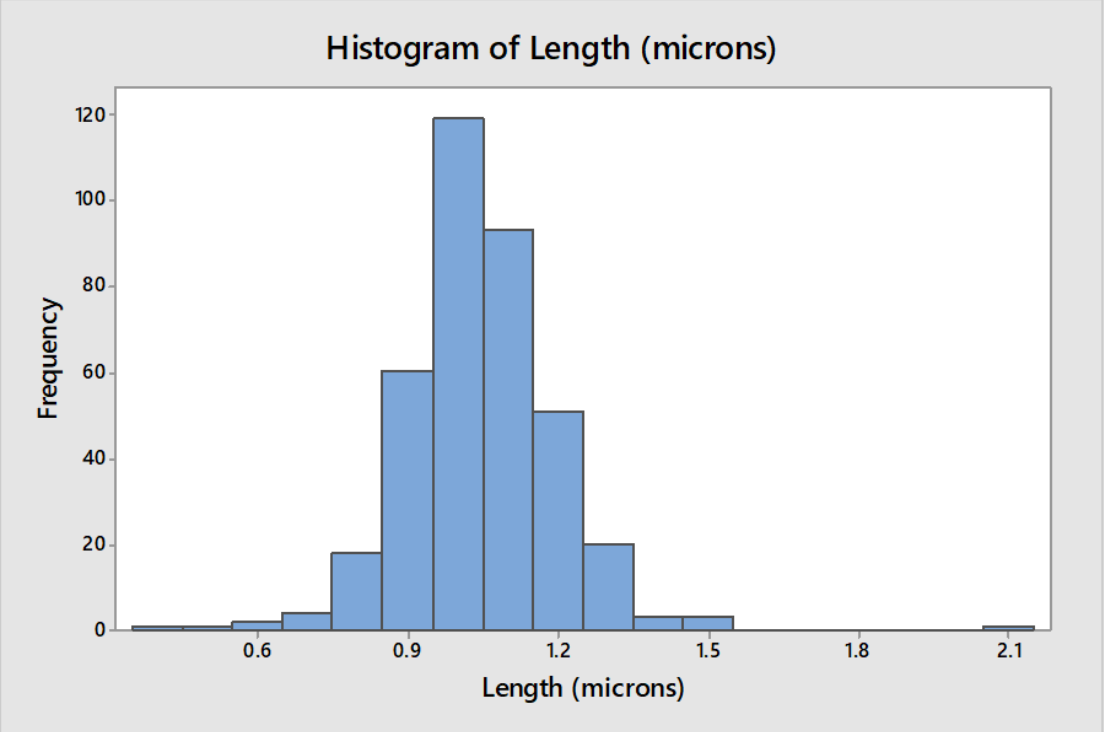


Figure 6.6 A histogram of the particle size distribution of silica made at 1.66M of ammonium-hydroxide(28%)

Table 6.3 shows the statistical output from Minitab of the SEM images

Length (microns)	**Silica (0.81M)**	**Silica (1.66M)**
Minimum (μm)	0.1020	0.4290
Maximum(μm)	0.9900	2.1020
Mean(μm)	0.4575	1.0409
Median(μm)	0.4690	1.0230
St Deviation	0.1527	0.1542
Standard Error of the mean	0.0108	0.0080

6.2.3.2 Quartz Crystal Microbalance

Figure 6.7 shows the output of the adsorption of Octadecane onto a gold-plated quartz crystal. Octadecane melts between 26°C and 28.2°C (European Chemicals Agency, 2020). The temperature is gradually increased until Octadecane is fully melted. While the temperature is increased and Octadecane begins to melt, a frequency shift is observed. At about 23min, a sharp drop in the resonance frequency is observed which is the time at which Octadecane will have fully melted. The temperature profile showed that the temperature at this point will be about 28°C.This change in frequency from -50Hz to -400Hz shows that physical adsorption of Octadecane will have occurred. The frequency and dissipation remain constant for about 50min. During this time the temperature is increased to 31°C to ensure it has fully melted and then the temperature is reduced until fully solid again.

The frequency and dissipation do not return to the original values at the start of the experiment but rather remain constant further supporting the theory that octadecane has been adsorbed onto the surface. This is like results obtained by Erzuah et al. (2018) when studying adsorption on crude oil using the QCM-D technique. This experiment was repeated over 5 loops to study if adsorption and desorption occur in the system. Figure 6.8 clearly shows the results of this system. Figure 6.8 shows that adsorption and desorption both occur in the system. Adsorption is indicated by the negative shift in frequency and by the positive shift in the dissipation. Desorption is shown by the increase in the frequency which occurs once Octadecane has fully solidified. The first three cycles show that adsorption and desorption remain the same in each cycle. This suggests that as Octadecane melts, chemisorption does not occur with the gold surface of the quartz crystal. Hence this method can be extended to other alkanes and fatty acids to test if the same would apply for them and thus enabling the kinetics of adsorption to be studied. Since QCM-D can only give details of physical changes e.g. change in mass of a system, other techniques such as X-ray Photoelectron Spectroscopy and Raman microscopy would need to be used to fully study what happens at the interface between the crystal surface ,air and the fatty acids.

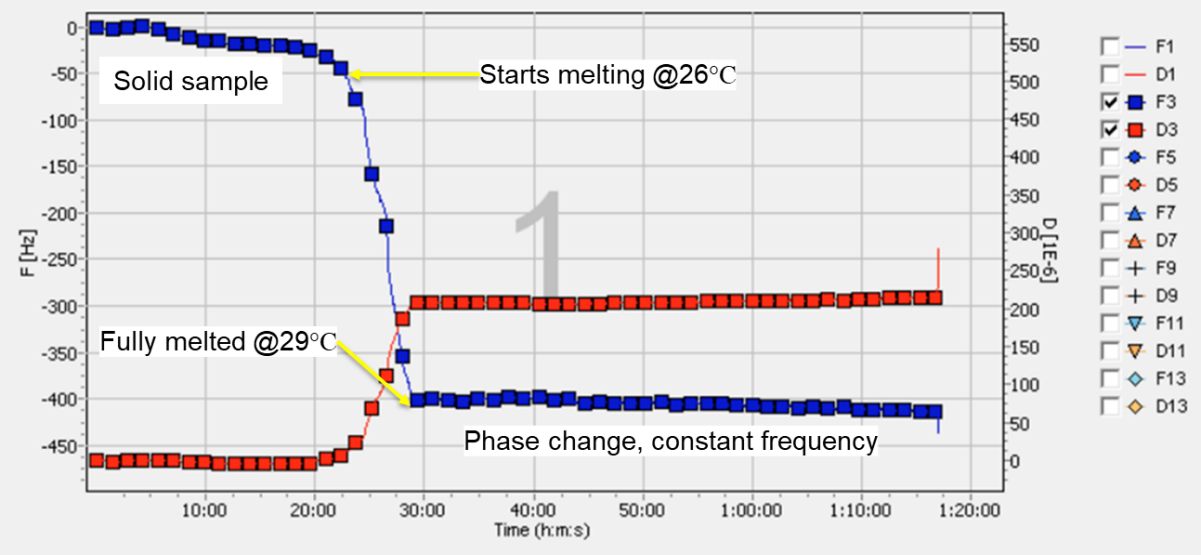


Figure 6.7 shows the QCM output for adsorption of Octadecane

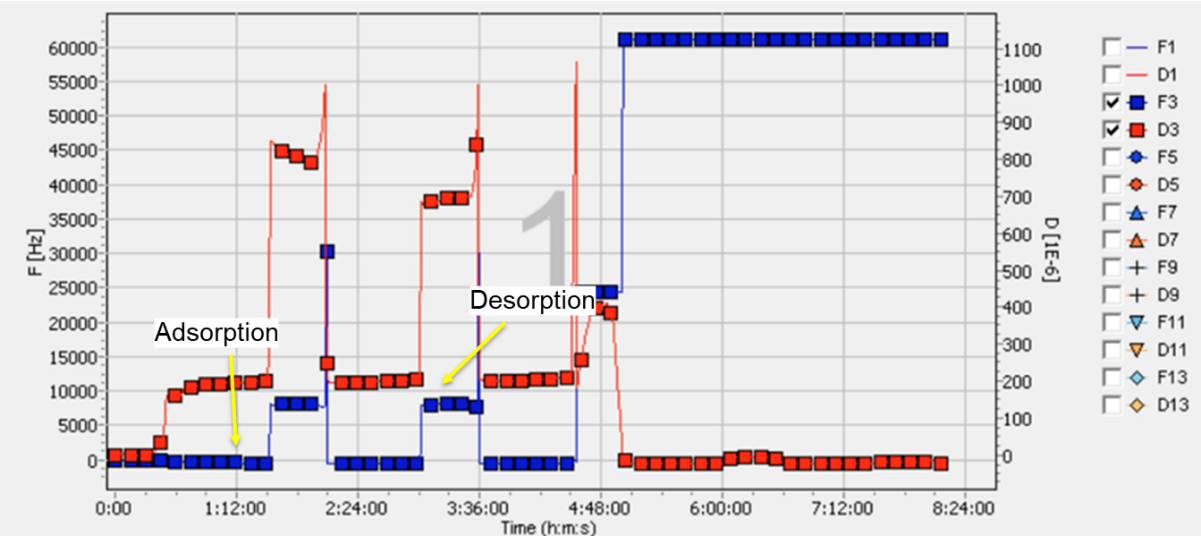


Figure 6.8 shows the adsorption behaviour of Octadecane when melted then cooled and the process repeated.

Chapter 7 References

Abdelaal, H. M., Zawrah, M. F. & Harbrecht, B., 2014. Facile One-Pot Fabrication of Hollow Porous Silica Nanoparticles. *Chemistry European Journal,* Volume 20, p. 673 – 677.

Adam Bushell, Paul Mack,East Grinstead, 2019. *Identifying structures on a plasma-modified.* [Online]
Available at: https://documents.thermofisher.com/TFS-Assets/MSD/Application-Notes/AN52333-identifying-structures-plasma-modified-polymer-surface.pdf

Adamczyk, Z., Sadowska, M. & Żeliszewska, P., 2020. Applicability of QCM-D for Quantitative Measurements of Nano- and Microparticle Deposition Kinetics: Theoretical Modeling and Experiments. *Analytical Chemistry,* 92(22), pp. 15087-15095.

Ahmed, H. R., Kayani, . K. F., Ealias, . A. M. & Aziz , . K. . H. H., 2025. A Comprehensive Review of Forty Adsorption Isotherm Models: An In-depth Analysis of Ten Statistical Error Measures. *Water, Soil and Air Pollution,* 236(346).

Alsharif, M. A., 2025. Understanding Adsorption: Theories, Techniques, and Applications. In: *Adsorption - Fundamental Mechanisms and Applications.* s.l.:s.n.

Anderson, H. et al., 2007. Quartz crystal microbalance sensor design I. Experimental study of sensor response and performance. *Sensors and Actuators B,* Volume 123, pp. 27-34.

Anderson, H. et al., 2007. Quartz crystal microbalance sensor design I. Experimental study of sensor response and performance. *Sensors and Actuators B,* 123(1), p. 27–34.

Anton Paar, 2024. *Basics of Raman spectroscopy.* [Online] Available at: https://wiki.anton-paar.com/be-en/basics-of-raman-spectroscopy/

Appel, J., 1973. FREUNDLICH'S ADSORPTION ISOTHERM. *SURFACE SCIENCE,* Volume 39, pp. 237-244.

Arisawa, K. et al., 2016. Saturated fatty acid in the phospholipid monolayer contributes to the formation of large lipid droplets. *Biochemical and Biophysical Research Communications,* 480(4), pp. 641- 647.

Arkles, B., 2006. Hydrophobicity, Hydrophilicity and Silanes. *Paint & Coatings Industry,* 22(10), pp. 114-135.

Azizian, S., 2004. Kinetic models of sorption: a theoretical analysis. *Journal ofColloid and Interface Science,* 276(1), p. 47–52.

Azmi, I. S., Jalil, M. J. & Hadi, A., 2022. Epoxidation of unsaturated fatty acid–based palm oil via peracid mechanism as an intermediate product. *Biomass Conversion and Biorefnery.*

Baeten, V., Hourant, P., Morales, M. T. & Aparicio, R., 1998. Oil and Fat Classification by FT-Raman Spectroscopy. *Journal of Agricultural and Food Chemistry,* 46(7), p. 2638–2646.

Bayrak, Y., 2006. Application of Langmuir isotherm to saturated fatty acid adsorption. *Microporous and Mesoporous Materials,* 87(3), p. 203–206.

BBC News, 2017. *Monster' fatberg found blocking east London sewer.* [Online] Available at: https://www.bbc.co.uk/news/uk-england-london-41238272 [Accessed 20 April 2020].

Bere, K. et al., 2025. Adsorption Mechanism of a Perfluorinated Carboxylic Acid on Charged Polystyrene Surfaces in Aquatic Environment: A Combined Experimental and Computer Simulation Investigation. *The Journal of Physical Chemistry B,* 129(32), pp. , 8244−8253.

Berezina, K. V. et al., 2018. The Use of Raman Spectroscopy and Methods of Quantum Chemistry for Assessing the Relative Concentration of Triglycerides of Oleic and Linoleic Acids in a Mixture of Olive Oil and Sunflower Seed Oil. *Optics and Spectroscopy,* 125(3), p. 297–303.

Beula, C. & Sai, P. S. T., 2013. Kinetics of Esterification of Palmitic acid with Ethanol-Optimization Using Statistical Design of Experiments. *International Journal of Chemical Engineering and Applications,* 4(6), pp. 388-392.

Beynon, R. J. & Easterby, J. S., 1996. *Buffer Solutions The Basics.* New York: Oxford University Press Inc..

Biolin Scientific, 2018. *Characterization of biomolecular interactions.* [Online] Available at: https://www.biolinscientific.com/hubfs/Content%20Offer/QSense/EN/QSense%20Overview%20Characterization%20of%20biomolecular%20interactions%20w%20QSense.pdf [Accessed 28 May 2020].

Biolin Scientific, 2019. *QSense Sensors.* [Online] Available at: https://www.biolinscientific.com/qsense/sensors [Accessed 7 February 2024].

Biolin Scientific, 2020. *Characterization of polymer based systems : Analyse layer build-up, conformation and molecular interaction with QSense QCM-D.* [Online] Available at: https://www.biolinscientific.com/hubfs/Content%20Offer/QSense/EN/Characterization%20of%20polymer%20based%20systems%20w%20QSense.pdf [Accessed 5 April 2023].

Biolin Scientific, 2020. *Measurements QCM-D.* [Online] Available at: https://www.biolinscientific.com/hubfs/Pdf/QSense/Technology%20Notes/QS-TN-1-Quartz-Crystal-Microbalance-with-Dissipation.pdf?t=1540827501590 [Accessed 18 May 2020].

Biolin Scientific, 2020. *Measurements QCM-D.* [Online] Available at: https://www.biolinscientific.com/measurements/qcm-d [Accessed 18 May 2020].

Biolin Scientific, 2023. *How to optimize the QCM-D baseline stability.* [Online] Available at: https://www.biolinscientific.com/hubfs/Content%20Offer/QSense/EN/QSense%20Guide%20How%20to%20optimize%20the%20baseline%20stability.pdf?hsLang=en

BioNavis, 2024. *How to Analyze Quartz Crystal Microbalance with Dissipation (QCMD) Data?.* [Online]
Available at: https://bionavis.com/article/how-to-analyze-quartz-crystal-microbalance-with-dissipation-qcmd-data/
[Accessed 2025].

Bournel, F., Laffon, C., Parent, P. & Tourillon, G., 1996. Adsorption of acrylic acid on aluminium at 300 K: a multi-spectroscopic study. *Surface Science,* Volume Volumes 352–354, pp. 228-231.

Bradley, M., 2015. *FTIR Basic Organic Functional Group Reference Chart.* [Online] Available at: https://www.thermofisher.com/blog/materials/a-gift-for-you-an-ftir-basic-organic-functional-group-reference-chart/
[Accessed 18 2 2024].

Britannica, 2025. *How Does Metal Rust?.* [Online] Available at: https://www.britannica.com/science/How-Does-Metal-Rust [Accessed November 2025].

Browne, M. M., Lubarsky, G. V., Davidson, M. R. & Bradley, R. H., 2004. Protein adsorption onto polystyrene surfaces studied by XPS and AFM. *Surface Science,* 553(1-3), pp. 155-167.

Butt, H.-J., Graf, K. & Kappl, M., 2003. *Physics and Chemistry of Interfaces.* Berlin: WILEY-VCH Verlag GmbH & Co..

Calvo, B., Collado, I. & Cepeda, E. A., 2008. Solubilities of Palmitic Acid in Pure Solvents and Its Mixtures. *Journal of Chemical & Engineering Data,* 54(1), p. 64–68.

Cannilla, C., Bonura, G., Costa, F. & Frusteri, F., 2018. Biofuels production by esterification of oleic acid with ethanol using a membrane assisted reactor in vapour permeation configuration. *Applied Catalysis A, General,* Volume 566, p. 121–129.

Canzano, S. et al., 2012. Use and Misuse of Sorption Kinetic Data: A Common Mistake That Should Be Avoided. *Adsorption Science & Technology,* 30(3), pp. 217-225.

Carta, G., Murru, E., Banni, S. & Manca, C., 2017. *Palmitic acid: Physiological role, metabolism and nutritional implications.* [Online] Available at: https://pubmed.ncbi.nlm.nih.gov/29167646/ [Accessed 22 February 2023].

Carta, G., Murru, E., Banni, S. & Manca, C., 2017. Palmitic Acid: Physiological Role, Metabolism and Nutritional Implications. *Frontiers in Physiology,* 8(902), pp. 1-14.

Casa Software Ltd, 2008. *Basic Quantification of XPS Spectra.* [Online] Available at: http://www.casaxps.com/help_manual/manual_updates/Basics_Quantification_of_XPS_Spectra.pdf

CasaXPS, 2008. *Depth Profiling using XPS.* [Online] Available at: http://www.casaxps.com/help_manual/manual_updates/Depth_Profiling_using_XPS.pdf

Chang, C.-C. & Shu, M.-C., 2003. The Chemical Origin of Defects on Silicon Dioxide Exposed to Ethanol. *The journal of physical chemistry B,* 107(29), pp. 7076-7087.

Chen, S.-L., Dong, P. & Yang, G.-H., 1997. The Size Dependence of Growth Rate of Monodisperse Silica Particles from Tetraalkoxysilane. *COLLOID AND INTERFACE SCIENCE,* Volume 189, p. 268–272.

Chen, W. et al., 2021. Surface hydrophobicity: effect of alkyl chain length and network homogeneity. *Frontiers of Chemical Science and Engineering,* Volume 15, pp. 90-98.

Chindam, C., Venkata, K. C., Balasubramaniam, K. & Prakash, R. V., 2013. Thermomechanical response of metals: Maxwell vs. Kelvin–Voigt models. *Materials Science and Engineering: A,* Volume 560, pp. 54-61.

Cho, N.-J., Frank, C. W., Kasemo, B. & Höök, F., 2010. Quartz crystal microbalance with dissipation monitoring of supported lipid bilayers on various substrates. *Nature Protocols,* 5(6), pp. 1096-1106.

Chu, K. H., Hashim, M. A. & Basirun, . A. A., 2025. Pseudo-First-Order Kinetics in Water Contaminant Adsorption: A Cautionary Note. *Water, Air, & Soil Pollution,* 237(55), p. 2026.

Clark , J., 2015. *ESTERIFICATION.* [Online] Available at: https://www.chemguide.co.uk/organicprops/alcohols/esterification.html [Accessed 5 june 2020].

Clayden, J., Greeves, N. & Warren, S., 2012. *Organic Chemistry.* 2nd ed. New York: Oxford University Press Inc..

Crespo, A., Morgado, N., Mazuyer, D. & Cayer-Barrioz, J., 2018. Effect of Unsaturation on the Adsorption and the Mechanical Behavior of Fatty Acid Layers. *Langmuir,* 34(15), pp. 4560-4567.

Crowther, M. W., 2008. NMR and IR Spectroscopy for the Structural Characterization of Edible Fats and Oils : An Instrumental Analysis Laboratory. *Journal of Chemical Education,* 85(11), pp. 1550-1554.

Dąbrowski, A., 2001. Adsorption — from theory to practice. *Advances in Colloid and Interface Science,* 1-3(93), pp. 135-224.

Del Mundo, D. M. N. & Sutheerawattananonda, M., 2017. Influence of fat and oil type on the yield, physico-chemical properties, and microstructure of fat, oil, and grease (FOG) deposits. *Water Reasearch,* Volume 124, pp. 308-319.

Dhopatkar, N., Park, J. H., Chari, K. & Dhinojwala, A., 2015. Adsorption and Viscoelastic Analysis of Polyelectrolyte-Surfactant Complexes on Charged Hydrophilic Surfaces. *Langmuir,* Volume 31, pp. 1026-1037.

Drummond, I. W. et al., 1996. *Spatial resolution in X-ray photoelectron spectroscopy.* [Online] Available at: https://royalsocietypublishing.org/doi/epdf/10.1098/rsta.1996.0122

Dunér, G., Thormann, E. & Dedinaite, A., 2013. Quartz Crystal Microbalance with Dissipation (QCM-D) studies of the viscoelastic response from a continuously growing grafted polyelectrolyte layer. *Colloid and Interface Science,* Volume 408, p. 229–234.

Easley, A. D. et al., 2022. A practical guide to quartz crystal microbalance with dissipation monitoring of thin polymer films. *Journal of Polymer Science,* 60(7), p. 1090–1107.

Ebelegi, A. N., Ayawei, N. & Wankasi, D., 2020. Interpretation of Adsorption Thermodynamics and Kinetics. *Open Journal of Physical Chemistry,* 10(3).

Edvardsson, M., 2018. *QCM mass and Ellipsometry mass - What is the difference?.* [Online] Available at: https://www.biolinscientific.com/blog/what-is-the-difference-between-qcm-mass-and-ellipsometry-mass
[Accessed 17 march 2022].

Erzuah, S., Fjelde, I. & Omekeh, A. V., 2018. *Wettability estimation by oil adsorption using quartz crystal microbalance with dissipation.* Copenhagen, Society of Pertroleum Engineers.

Erzuah, S., Fjelde, I. & Omekeh, A. V., 2018. *Wettability estimation by oil adsorption using quartz crystal microbalance with dissipation.* Copenhagen, Society of Pertroleum Engineers.

European Chemicals Agency, 2020. *Octadecane.* [Online] Available at: https://www.echa.europa.eu/web/guest/brief-profile/-/briefprofile/100.008.902 [Accessed 14 June 2020].

Evans, H. E. & Weinberg, W. H., 1979. The reaction of ethanol with an aluminum oxide surface studied by inelastic electron tunneling spectroscopy. *The Journal of Chemical Physics,* 71(4), p. 1537–1542.

Falco , G. et al., 2024. Promoting removal of polystyrene microplastics from wastewater by electrochemical treatment. *Journal of Water Process Engineering,* Volume 68, p. 106418.

Farmer, S., Kennepohl, . D., Morsch, L. & Reusch, W., 2024. *Structure and Properties of Carboxylic Acids.* [Online]

Available at: https://chem.libretexts.org/Bookshelves/Organic_Chemistry/Organic_Chemistry_(Morsch_et_al.)/20%3A_Carboxylic_Acids_and_Nitriles/20.02%3A_Structure_and_Properties_of_Carboxylic_Acids

Filippova, I. V. et al., 2018. Effect of calcium minerals reactivity on fatty acids adsorption and flotation. *Colloids and Surfaces A: Physicochemical and Engineering Aspects,* Volume 545, pp. 157-166.

Fraxedas, J. et al., 2021. In situ XPS analysis of the electronic structure of silicon and titanium thin films exposed to low-pressure inductively-coupled RF plasma. *Applied Surface Science,* Volume 542, p. 148684.

Fredrik Pettersson, 2022. *QCM-D data analysis - How to tell a bulk shift from an adlayer.* [Online]
Available at: https://www.biolinscientific.com/blog/qcm-d-data-analysis-how-to-tell-a-bulk-shift-from-an-adlayer

Fredrik Pettersson, 2022. *QCM-D data analysis - How to tell a bulk shift from an adlayer.* [Online]
Available at: https://www.biolinscientific.com/blog/qcm-d-data-analysis-how-to-tell-a-bulk-shift-from-an-adlayer
[Accessed 2025].

Fredrik Pettersson, 2025. *Best Practices for Measuring External Coating Thickness on QSense QCM-D Sensors.* [Online]
Available at: https://www.biolinscientific.com/blog/best-practices-for-measuring-external-coating-thickness-on-qsense-qcm-d-sensors

Gabelman, A., 2017. *Adsorption Basics: Part 1.* s.l., American Institute of Chemical Engineers.

Garland, E. R., Rosen, E. P., Clarke, L. I. & Baer, T., 2008. Structure of submonolayer oleic acid coverages on inorganic aerosol particles: evidence of island formation. *Physical Chemistry Chemical Physics,* 10(21), p. 3156–3161.

Girardeaux, C. & Pireaux, J.-J., 1996. Analysis of Polystyrene (PS) by XPS. *Surface Science Spectra,* 4(2), p. 130–133 .

Good, C. & Facey, H., 2018. *X-ray Photoelectron Spectroscopy (XPS) : How XPS Works.* [Online]

Available at: https://chem.libretexts.org/Courses/Franklin_and_Marshall_College/Introduction_to_Materials_Characterization__CHM_412_Collaborative_Text/Spectroscopy/X-ray_Photoelectron_Spectroscopy_(XPS)
[Accessed 7 July 2023].

Goodson, M. L., Lagle, R. & Guggilla, P., 2022. X-Ray Photoelectron Spectroscopy of Polystyrene Composite Films. *Journal of Advanced Materials Science and Engineering,* 2(1), pp. 1-5.

Goodson, M. L., Lagle, R. & Guggilla, P., 2022. X-Ray Photoelectron Spectroscopy of Polystyrene Composite Films. *Journal of Advanced Materials Science and Engineering,* 2(1), pp. 1-5.

Gopalakrishna, S., Langhoff, A., Brenner, G. & Johannsmann, D., 2021. Soft Viscoelastic Particles in Contact with a Quartz Crystal Microbalance (QCM): A Frequency-Domain Lattice Boltzmann Simulation. *Analytical Chemistry,* 93(21), p. 10229–10235.

Grosser, A. et al., 2017. Anaerobic digestion of sewage sludge with grease trap sludge and municipal solid waste as co-substrates. *Environmental Research,* Volume 155, pp. 249-260.

Gunter, P. L. J. & Niemantsverdriet, J. W., 1995. Thickness determination of uniform overlayers on rough substrates by angle-dependent XPS. *Applied Surface Science,* 89(1), pp. 69-76.

HEIDE, P. V. D., 2012. *X-ray photoelectron spectroscopy : an introduction to principles and practices.* 1st ed. Hoboken: John Wiley & Sons, Inc..

He, X. et al., 2013. Mechanisms of Fat, Oil and Grease (FOG) deposit formation in sewer lines. *Water Research,* 47(13), pp. 4 4 5 1 - 4 4 5 9.

He, X. et al., 2013. Mechanisms of Fat, Oil and Grease (FOG) deposit formation in sewer lines. *water research,* Volume 47, pp. 4451 - 4459.

Himawan, C., Starov, V. M. & Stapley, A. G. F., 2006. Thermodynamic and kinetic aspects of fat crystallization. *Advances in Colloid and Interface Science,* Volume 122, pp. 3-33.

Hodges, C. S., Harbottle, D. & Biggs, S., 2020. Investigating Adsorbing Viscoelastic Fluids Using the Quartz Crystal Microbalance. *ACS Omega,* 5(35), p. 22081–22090.

Hofmann , S., Han, Y. S. & Wang, J. Y., 2017. Depth resolution and preferential sputtering in depth profiling of sharp interfaces. *Applied Surface Science,* Volume 410, pp. 354-362.

HORIBA Jobin Yvon , 2017. *RAMAN DATA AND ANALYSIS.* [Online] Available at: https://static.horiba.com/fileadmin/Horiba/Technology/Measurement_Techniques/Molecular_Spectroscopy/Raman_Spectroscopy/Raman_Academy/Raman_Tutorial/Raman_bands.pdf [Accessed 10 January 2024].

Ho, Y. & Mckay, G., 1999. Pseudo-second order model for sorption processes. *Process Biochemistry,* 34(5), p. 451–465.

Huang, Y.-T., Lee, L.-C. & Shih, M.-C., 2018. A Study on the Pseudo-Second-Order Kinetic Equation for the Adsorption of Methylene Blue onto Nitric Acid-Treated Rice Husk: Comparison of Linear Methods. *International Journal of Scientific and Research Publications (IJSRP),* 8(6), pp. 509-515.

Hunter , R. J., 2001. *Foundations of Colloid Science.* 2nd ed. New York: Oxford University Press.

Hu, Y., Xing, H., Li, G. & Wu, M., 2020. Magnetic Imprinted Polymer-Based Quartz Crystal Microbalance Sensor for Sensitive Label-Free Detection of Methylene Blue in Groundwater. *Sensors (Basel),* 20(19), p. 5506.

Hu, Z. et al., 2025. Fat, oil and grease - induced sewer blockages: Mechanisms, modelling and monitoring strategies. *Water Research,* Volume 286, p. 124215.

Iasmin, M., Dean, L. O. & Ducoste, J. J., 2016. Quantifying fat, oil, and grease deposit formation kinetics. *Water Research,* Volume 88, pp. 786-795.

Ibarra, J. et al., 2016. Synthesis and characterization of magnetite/PLGA/chitosan nanoparticles. *Materials Research Express,* 2(9), p. 095010.

Ibrahim, I. A., Zikry, A. F. & Sharaf, M. A., 2010. Preparation of spherical silica nanoparticles: Stober silica. *American Science,* Volume 6, p. 11.

Irwin, E. F., Ho, J. E., Kane, S. R. & Healy, K. E., 2005. Analysis of Interpenetrating Polymer Networks via Quartz Crystal Microbalance with Dissipation Monitoring. *Langmuir,* Volume 21, pp. 5529-5536.

Irwin, E. F., Ho, J. E., Kane, S. R. & Healy, K. E., 2005. Analysis of Interpenetrating Polymer Networks via Quartz Crystal Microbalance with Dissipation Monitoring. *Langmuir,* Volume 21, pp. 5529-5536.

Jablonski, A., 2019. Evaluation of procedures for overlayer thickness determination from XPS intensities. *Surface Science,* Volume 668, pp. 14-24.

Jablonski, A. & Zemek, J., 2009. Overlayer thickness determination by XPSusing the multiline approach. *Surface and Interface Analysis,* 41(3), pp. 143-264.

Jamieson , L. E., Li, . A., Faulds, K. & Graham, . D., 2018. Ratiometric analysis using Raman spectroscopy as a powerful predictor of structural properties of fatty acids. *Royal Society Open Science,* 5(12), p. 181483.

Jensen, D. S. et al., 2013. Silicon (100)/SiO2 by XPS. *Surface Science Spectra,* 20(1), p. 36–42.

Johannsmann, D., 2015. *The Quartz Crystal Microbalance in Soft Matter Research : Fundamentals and Modeling.* s.l.:Springer.

Johnson, D., Hilal, N. & Bowen, W. R., 2009. *Basic Principles of Atomic Force Microscopy.* 1st ed. Burlington: Elsevier Ltd.

KANEKO, F., YAMAZAKI, K. & KOBAYASHI, M., 1994. Vibrational spectroscopic study on polymorphism of erucic acid and palmitoleic acid: yl+ al and y- a reversible solid state phase transitions. *Spectrochimica Acta,* 50A(8/9), pp. 1589-1603.

Kanicky, J. R., Poniatowski, A. F., Mehta, N. R. & Shah, D. O., 2000. Cooperativity among Molecules at Interfaces in Relation to Various Technological Processes: Effect of Chain Length on the pKa of Fatty Acid Salt Solutions. *Langmuir,* 16(1), pp. 172-177.

Kanicky, J. R. & Shah, D. O., 2002. Effect of Degree, Type, and Position of Unsaturation on the pKa of Long-Chain Fatty Acids. *Journal of Colloid and Interface Science,* 256(1), p. 201–207.

Karaman, M. E., Antelmi, D. A. & Pashley, R. M., 2001. The production of stable hydrophobic surfaces by the adsorption of hydrocarbon and fluorocarbon carboxylic acids onto alumina substrates. *Colloids and Surfaces A: Physicochemical and Engineering Aspects,* Volume 182, pp. 285-298.

Katoch, R., 2022. *Techniques in Forage Quality Analysis.* Singapore: Springer.

Kaye & Laby, 2024. *Viscosity of Ethanol.* [Online] Available at: https://wiki.anton-paar.com/en/ethanol/

Kenneth Olesen , 2024. *Coating QCM sensors ex-situ: How to setup the measurement and analyze the data.* [Online] Available at: https://www.biolinscientific.com/blog/coating-qcm-sensors-ex-situ-how-to-setup-the-measurement-and-analyze-the-data

Kim, T., 2024. *Typical IR Absorption Frequencies For Common Functional Groups.* [Online] Available at: https://www.niu.edu/clas/chembio/research/analytical-lab/ftir/ir-frequencies-table.shtml
[Accessed 18 2 2024].

Kou, J., Tao, D. & Xu, G., 2010. Fatty acid collectors for phosphate flotation and their adsorption behavior using QCM-D. *International Journal of Mineral Processing,* 95(1-4), pp. 1-9.

Kou, J. & Xu, S., 2016. In situ kinetics and conformation studies of dodecylamine adsorption on to zinc sulfide using a quartz crystal microbalance with dissipation QCM-D. *Colloids and Surfaces A: Physicochemical and Engineering Aspects,* Volume 490, p. 110–120.

Kou, J. & Xu, S., 2016. In situ kinetics and conformation studies of dodecylamine adsorption onto zinc sulfide using a quartz crystal microbalance with dissipation (QCM-D). *Colloids and Surfaces A: Physicochemical and Engineering Aspects,* Volume 490, pp. 110-120.

Kratos Analytical Ltd, 2025. *Importance of energy resolution in XPS.* [Online] Available at: https://www.kratos.com/helpful-article/importance-of-energy-resolution-xps/

Krishna, D. N. G. & Philip, J., 2022. Review on surface-characterization applications of X-ray photoelectron spectroscopy (XPS): Recent developments and challenges. *Applied Surface Science Advances,* Volume 12, p. 100332.

Krishna, Y. et al., 2020. *Enhancing the thermal properties of organic phase change material (palmitic acid) by doping MXene nanoflakes.* Selangor Darul Ehsan, AIP Conference Proceedings.

Krtil, P., Trojánek,, A. & Samec, Z., 2001. Kinetics of Water Sorption in NafionThin Films-Quartz Crystal Microbalance Study. *Journal of Physical Chemistry B,* 105(83), pp. 7979-7983.

Kumar, C. S., Singh, . M. M. & Krishna, R., 2023. *Advanced Materials Characterization : Basic Principles, Novel Applications, and Future Directions.* 1 ed. Boca Raton: CRC PRESS.

Kumar, K. V., 2006. Linear and non-linear regression analysis for the sorption kinetics of methylene blue onto activated carbon. *Journal of Hazardous Materials,* 137(3), pp. 1538-1544.

Kusum, S. A., Pourghaz, M. & Ducoste, J. J., 2025. Identifying surface formation and adhesion mechanisms of FOG deposits on sewer lines. *Water Research,* Volume 278, p. 123340.

Lapidot, T., Campbell, K. L. S. & Heng, J. Y. Y., 2016. Model for Interpreting Surface Crystallization Using Quartz Crystal Microbalance: Theory and Experiments. *Analytical Chemistry,* 88(9), pp. 4886-4893.

Lapidot, T., Campbell, K. S. & Heng, J., 2016. Model for Interpreting Surface Crystallization Using Quartz Crystal Microbalance: Theory and Experiments. *Analytical Chemistry,* Volume 88, p. 4886−4893.

Largitte, L. & Pasquier, R., 2016. A review of the kinetics adsorption models and their application to the adsorption of lead by an activated carbon. *Chemical Engineering Research and Design,* Volume 109, pp. 495-504.

Lassègues, J.-C., Grondin, J. & Talaga, D., 2006. Lithium solvation in bis(trifluoromethanesulfonyl)imide-based ionic liquids. *Physical Chemistry Chemical Physics,* 16 November, 8(48), pp. 5629-5632.

Leng, Y., 2013. *Materials Characterization : Introduction to Microscopic and Spectroscopic Methods.* 2nd ed. Weinheim: Wiley-VCH Verlag GmbH & Co. KGaA.

Liberman, A., Mendeza, N., Trogler, W. C. & Kummel, A. C., 2014. Synthesis and surface functionalization of silica nanoparticles for nanomedicine. *Surface Science Reports,* 69(2-3), pp. 132-158.

LibreTexts, 2015. *Infrared Spectroscopy Absorption Table.* [Online] Available at: https://chem.libretexts.org/Ancillary_Materials/Reference/Reference_Tables/Spectroscopic_Reference_Tables/Infrared_Spectroscopy_Absorption_Table
[Accessed 18 2 2024].

Li, C. et al., 2016. Effect of synthesis temperature on the ordered pore structure in mesoporous silica studied by positron annihilation spectroscopy. *Applied Surface Science,* Volume 363, p. 445–450.

Li, C., Zhang, N. & Gao, P., 2023. Lessons learned: how to report XPS data incorrectly about lead-halide perovskites. *Materials Chemistry Frontiers,* 7(18), pp. 3797-3802.

Lim, M. S. et al., 2007. Adsorption and Desorption of Stearic Acid Self-Assembled Monolayers on Aluminum Oxide. *Langmuir,* 23(5), pp. 2444-2452.

Lind, T. K. & Cárdenas, M., 2016. Understanding the formation of supported lipid bilayers via vesicle fusion—A case that exemplifies the need for the complementary method approach (Review). *Biointerphases,* 11(2), p. 020801.

Lin-Vien, D., Colthup, N. B., Fateley, W. G. & Grasselli, J. G., 1991. *The Handbook of Infrared and Raman Characteristic Frequencies of Organic Molecules.* 1 ed. s.l.:Elsevier Science & Technology.

Liu, S. X. & Ki, J.-T., 2009. Study of adsorption kinetics of surfactants onto polyethersulfone membrane surface using QCM-D. *Desalination,* 247(1-3), p. 355–361.

Liu, Y., 2006. Some consideration on the Langmuir isotherm equation. *Colloids and Surfaces A: Physicochem. Eng. Aspects,* Volume 274, p. 34–36.

Li, Y. et al., 2025. Influence of polystyrene microplastics on the structural stability of activated sludge microbial flocs in sequencing batch reactors. *Environmental Pollution,* Volume 384, p. 126949.

Li, Z. & Zhu, Y., 2003. Surface-modification of SiO2 nanoparticles with oleic acid. *Applied Surface Science,* 211(1-4), pp. 315-320.

Long, J. H., Aziz, T. N., Reyes, F. . L. d. l. & Ducoste, J. J., 2012. Anaerobic co-digestion of fat, oil, and grease (FOG): A review of gas production and process limitations. *Process Safety and Environmental Protection,* 90(3), pp. 231-245.

Lowe, L. A. et al., 2022. Subtle changes in pH affect the packing and robustness of fatty acid bilayers. *Soft Matter,* Issue 18, pp. 3498-3504.

Lowe, L. A. et al., 2022. Subtle changes in pH affect the packing and robustness of fatty acid bilayers. *Soft Matter,* Volume 18, pp. 3498-3504.

Lundgren, S. M., Persson, K., Kronberg, B. & Claesson, P. M., 2006. Adsorption of fatty acids from alkane solution studied with quartz crystal microbalance. *Tribology Letters,* Volume 22, pp. 15-20.

Lundgren, S. M., Persson, K., Kronberg, B. & Claesson, P. M., 2006. Adsorption of fatty acids from alkane solution studied with quartz crystal microbalance. *Tribology Letters,* Volume 22, pp. 15-20.

Lundgren, S. M. et al., 2007. Unsaturated Fatty Acids in Alkane Solution: Adsorption to Steel Surfaces. *Langmuir,* Volume 23, pp. 10598--10602.

Maity, S., Takano, S., Masuda, S. & Tsukuda, T., 2024. Bonding and Electronic Interactions of Hydrogen with Gold Superatoms. *The Journal of Physical Chemistry C,* 128(1), pp. 19-30.

Mai, W., 2020. *Fundamental Theory of Atomic Force Microscopy.* [Online] Available at: http://www.nanoscience.gatech.edu/zlwang/research/afm.html [Accessed 15 June 2020].

Malin Edvardsson, 2023. *QCM data analysis - When to use Viscoelastic modelling.* [Online] Available at: https://www.biolinscientific.com/blog/qcm-data-analysis-when-to-use-viscoelastic-modelling
[Accessed 2025].

Malin Edvardsson, 2025. *Exploring supported lipid membranes: Formation, characterization, and applications with QCM-D.* [Online] Available at: https://www.biolinscientific.com/blog/lipid-bilayer-characterization-with-qcm-d

Malin Edvardsson, 2025. *What is QCM-D?.* [Online] Available at: https://www.biolinscientific.com/blog/what-is-qcmd [Accessed 2025].

Mathias, J., 2020. *The Advantages and Disadvantages of Scanning Electron Microscopy (SEM).* [Online] Available at: https://www.innovatechlabs.com/newsroom/2083/advantages-disadvantages-scanning-electron-microscopy/
[Accessed 15 June 2020].

McArdle, T. et al., 2015. Optimizing the Mass-Specific Activity of Bilirubin Oxidase Adlayers through Combined Electrochemical Quartz Crystal Microbalance and Dual Polarization Interferometry Analyses. *Applied Materials Interfaces,* Volume 7, p. 25270−25280.

Nandiyanto, A. B. D., Oktiani, R. & Ragadhita, R., 2019. How to Read and Interpret FTIR Spectroscope of Organic Material Asep. *Indonesian Journal of Science & Technology,* 4(1), pp. 97-118.

Nanoscience Instruments , 2020. *Scanning Electron Microscopy.* [Online] Available at: https://www.nanoscience.com/techniques/scanning-electron-microscopy/ [Accessed 15 June 2020].

nanoScience Instruments, 2024. *Optimizing Chemical Mechanical Planarization (CMP).* [Online]
Available at: https://www.nanoscience.com/wp-content/uploads/2024/02/24NMI-02-CMP-Tech-Note.pdf

Nanoscience Instruments, 2025. *How to Interpret the Signals from QCM-D?.* [Online] Available at: https://www.nanoscience.com/blogs/how-to-interpret-the-signals-from-qcm-d/?utm_source=chatgpt.com

Nascimento, F. H. d. et al., 2023. Empirical adsorption kinetics: comparing linear and nonlinear regression analysis emphasizing the need for high throughput analysis. *Journal of Environmental Science and Health, Part B ,* 58(7), pp. 539-553.

Neves, L., Oliveira, R. & Alves, M. M., 2009. Fate of LCFA in the co-digestion of cow manure, food waste. *water research,* 43(20), p. 5142–5150.

Orsavova, J. et al., 2015. Fatty Acids Composition of Vegetable Oils and Its Contribution to Dietary Energy Intake and Dependence of Cardiovascular Mortality on Dietary Intake of Fatty Acids. *International Journal of Molecular Sciences,* 16(6), pp. 12871-12890.

Paul, S., Paul, D., Basova, T. & Ray, A. K., 2008. Studies of Adsorption and Viscoelastic Properties of Proteins onto Liquid Crystal Phthalocyanine Surface Using Quartz Crystal Microbalance with Dissipation Technique. *The Journal of Physical Chemistry C,* 112(31), p. 11822–11830.

Peter Esser , 2014. *Principles in Adsorption to Polystyrene.* [Online] Available at: https://documents.thermofisher.com/TFS-Assets/LSG/Application-Notes/D19559.pdf

Phetrungnapha, A., Wiengnak, N. & Maikrang , K., 2023. Removal of free fatty acid from waste cooking oil using an adsorbent derived from cassava peel. *Korean Journal of Chemical Engineering,* Volume 40, p. 2253–2262.

Physical Electronics, Inc, 2020. *XPS / ESCA.* [Online] Available at: https://www.phi.com/surface-analysis-techniques/xps-esca.html [Accessed 15 June 2020].

Plikusiene, I., Maciulis, V., Ramanavicius, A. & Ramanaviciene, A., 2022. Spectroscopic Ellipsometry and Quartz Crystal Microbalance with Dissipation for Assessment of Polmer Layers and for the Application of Biosensing. *Polymers,* Volume 14, p. 1056.

Poitras, C. & Tufenkji, N., 2009. A QCM-D-based biosensor for E. coli O157:H7 highlighting the relevance of the dissipation slope as a transduction signal. *Biosensors and Bioelectronics,* 24(7), pp. 2137-2142.

Punvichai, T. & Pioch, . D., 2019. Covalorization of Palm Oil-Refining by-Products as Soaps. *Journal of the American Oil Chemists' Society,* 96(3), pp. 329 - 336.

QIU, H. et al., 2009. Critical review in adsorption kinetic models. *Journal of Zhejiang University-SCIENCE A,* 10(5), p. 716–724.

Qsense DFind, 2024. *The Viscoelastic model.* [Online] Available at: file:///C:/Program%20Files/Q-Sense/Dfind/help/The_Viscoelastic_model.html

Quast, K., 2016. The use of zeta potential to investigate the pKa of saturated fatty acids. *Advanced Powder Technology,* 27(1), pp. 207-214.

Ramaswamy, S., Huang, H.-J. & Ramarao, B. V., 2013. *Separation and Purification Technologies in Biorefineries.* Sussex: John Wiley & Sons, Ltd.

Rangabhashiyam, S., Anu, N., Giri, N. M. S. & Selvaraju, N., 2014. A Novel approach of the modified BET Isotherm towards continuous column study. *Journal of Scientific and Industrial Research (JSIR),* Volume 73, pp. 489-494.

Rao, K. S. et al., 2005. A novel method for synthesis of silica nanoparticles. *Journal of Colloid and Interface Science,* 289(1), p. 125–131.

Regmi, B. P. et al., 2014. Molecular weight sensing properties of ionic liquid-polymer composite films: theory and experiment. *Materials Chemistry C,* Volume 2, p. 4867–4878.

Reimhult, K. et al., 2008. Characterization of QCM sensor surfaces coated with molecularly imprinted nanoparticles. *Biosensors and Bioelectronics,* 23(12), pp. 1908-1914.

Reitzenstein, S. et al., 2007. Nondestructive analysis of single rapeseeds by means of Raman spectroscopy. *JOURNAL OF RAMAN SPECTROSCOPY,* 38(3), pp. 301-308.

Renishaw plc, 2025. *What Raman spectroscopy can tell you.* [Online] Available at: https://www.renishaw.com/en/what-raman-spectroscopy-can-tell-you--25800?srsltid=AfmBOoo7qrHSG13hiugJu2b5iJsnTjw5moubVamRzA7xJfkekQx2dNaQ

Revellame, E. D. et al., 2020. Adsorption kinetic modeling using pseudo-first order and pseudo-second order rate laws: A review. *Cleaner Engineering and Technology,* 100032(1), p. 100032.

Reviakine, I., Johannsmann, D. & Richter, R. P., 2011. Hearing What You Cannot See and Visualizing What You Hear: Interpreting Quartz Crystal Microbalance Data from Solvated Interfaces. *Analytical Chemistry,* 83(23), p. 8838–8848.

Robati, D., 2013. Pseudo-second-order kinetic equations for modeling adsorption systems for removal of lead ions using multi-walled carbon nanotube.. *i Journal Of Nanostructure in Chemistry,* 3(55), pp. 2193-8865.

Rodahl, M. et al., 1997. Simultaneous frequency and dissipation factor QCM measurements of biomolecular adsorption and cell adhesion. *Faraday Discuss,* Volume 107, pp. 229-46.

Rodahl, M. & Kasemo, B., 1966. A simple setup to simultaneously measure the resonant frequency and the absolute dissipation factor of a quartz crystal microbalance. *Review of Scientific Instruments,* 67(9), pp. 3238-3241.

Romero-González, J. et al., 2005. Determination of thermodynamic parameters of Cr(VI) adsorption from aqueous solution onto Agave lechuguilla biomass. *The Journal of Chemical Thermodynamics,* 37(4), pp. 343-347.

RTI Laboratories, 2015. *FTIR Analysis.* [Online] Available at: https://rtilab.com/techniques/ftir-analysis/ [Accessed 15 June 2020].

Saevels, S. et al., 2004. Characterisation of QMB sensors by means of the BET adsorption isotherm. *Sensors and Actuators B,* Volume 101, p. 242–251.

Sahmoune, M. N., 2019. Evaluation of thermodynamic parameters for adsorption of heavy metals by green adsorbents. *Environmental Chemistry Letters,* Volume 17, p. 697–704.

Saleh, T. A., 2021. *Polymer Hybrid Materials and Nanocomposites.* 1st ed. s.l.:William Andrew Publishing.

Salwan, R., Rana, A. & Sharma, V., 2023. Preparations of laboratory solutions. In: *Laboratory Methods in Microbiology and Molecular Biology - Methods in Molecular Microbiology.* s.l.:Elsevier.

Savara, A., Schmidt, C. M., Geiger, F. M. & Weitz, E., 2009. Adsorption Entropies and Enthalpies and Their Implications for Adsorbate Dynamics. *The Journal of Physical Chemistry C,* 113(7), pp. 2806-2815.

Schmidbaur, H., Raubenheimer, H. G. & Dobrzańska, L., 2014. The gold–hydrogen bond, Au–H, and the hydrogen bond to gold, Au···H–X. *Chemical Society Reviews,* 43(1), pp. 345-380.

Schönwälder, S. M. S. et al., 2014. https://pubs.acs.org/doi/10.1021/bm500750v. *Biomacromolecules,* 15(5), p. 2398–2406.

Seanneng, K. A. L., 2023. Investigation of Palmitic Acid Sorption Using Quartz Crystal Microbalance. Orlando Florida, American Institute of Chemical Engineers.

Seanneng, K. A. L., 2025. Herstal: s.n.

Seetala, N. V. et al., 2013. Positron lifetime and SEM studies of porous silica. *World Journal of Engineering,* 10(3), pp. 199-204.

Setiowati, A. D., Neve, L. D., A'yun, Q. & Meeren, P. V. d., 2021. Quartz Crystal Microbalance with Dissipation (QCM-D) as a tool to study the interaction between whey protein isolate and low methoxyl pectin. *Food Hydrocolloids,* Volume 110, p. 106180.

Sharipov, A. S. & Starik, A. M., 2015. Theoretical Study of the Reactions of Ethanol with Aluminum and Aluminum Oxide. *The Journal of Physical Chemistry A,* 119(17), pp. , 3897−3904.

Shen, Z., Zhang, Q., Li, X. & Chen, Q., 2020. Adsorption Behavior and Wettability of Rhodochrosite Surface: Effect of C18 Fatty Acid Unsaturation. *Minerals,* 10(10), p. 905.

Shklyarevskii, O. I., Lysykh, A. A. & Yanson, I. K., 1976. Tunnel spectra of carboxylic acids: the transition from physical absorption to chemisorption. *Soviet Journal Low Temperature Physics,* 2(5), p. 328–333.

Soult, A. et al., 2019. *Lipids and Triglycerides.* [Online] Available at: https://chem.libretexts.org/Courses/University_of_Kentucky/UK%3A_CHE_103_-_Chemistry_for_Allied_Health_(Soult)/Chapters/Chapter_14%3A_Biological_Molecules/14.2%3A_Lipids_and_Triglycerides
[Accessed 5 June 2020].

Spector, A. A. & Yorek, M. A., 1985. Journal of Lipid Research. *Journal of Colloid and Interface Science,* 26(9), pp. 1015-1035.

Stanford, J. P. et al., 2016. Kinetic and equilibrium sorption of organic liquids and vaporsin Matrimid. *Journal of Membrane Science,* Volume 512, pp. 29-37.

Statistics How To, 2025. *Cauchy Distribution.* [Online] Available at: https://www.statisticshowto.com/cauchy-distribution/

Stein, L. & Miller, D., 2019. *Fatbergs can cost millions to remove each year. Here's how to stop them.* [Online] Available at: https://www.abc.net.au/news/2019-01-10/fatberg-how-to-remove-and-stop-them-building-up/10701656
[Accessed 17 March 2023].

Sultana, N. et al., 2022. Understanding the properties of fat, oil, and grease and their removal using grease interceptors. *Water Research,* Volume 225, p. 119141.

Surface Measurement Systems Ltd, 2015. *Inverse Gas Chromatography and Its Applications – Surface Measurement Systems' Automated Solution.* [Online] Available at: https://www.azom.com/article.aspx?ArticleID=11831
[Accessed 15 June 2020].

Talebi, A. et al., 2020. Selective adsorption and recovery of volatile fatty acids from fermented landfill leachate by activated carbon process. *Science of The Total Environment,* Volume 707, p. 134533.

Thermo Fisher Scientific Inc. , 2024. *TABLE OF ELEMENTS: OXYGEN.* [Online] Available at: https://www.thermofisher.com/be/en/home/materials-science/learning-center/periodic-table/non-metal/oxygen.html
[Accessed April 2024].

Thermo Fisher Scientific Inc., 2006. *Carbon X-ray photoelectron spectra, carbon electron configuration, and other elemental information..* [Online] Available at: https://www.thermofisher.com/be/en/home/materials-science/learning-center/periodic-table/non-metal/carbon.html

Thermo Fisher Scientific Inc, 2006. *X-Ray Photoelectron Spectroscopy Imaging.* [Online] Available at: https://www.thermofisher.com/be/en/home/materials-science/learning-center/surface-analysis/xps-imaging.html#:~:text=This%20method%20enables%20measurements%20of%20the%20distribution%20of,Nexsa%20Surface%20Analysis%20System%20this%20is%2010%20%CE%BCm.

Thermo Fisher Scientific, 2008. *Energy Resolution in X-ray Photoelectron.* [Online] Available at: https://documents.thermofisher.com/TFS-Assets/CAD/Application-Notes/D16105~.pdf

Thermo Fisher Scientific, 2008. *Energy Resolution in X-ray Photoelectron Spectroscopy (XPS).* [Online] Available at: https://documents.thermofisher.com/TFS-Assets/CAD/Application-Notes/D16105~.pdf

Tiberg, F., 1996. Physical characterization of non-ionic surfactant layers adsorbed at hydrophilic and hydrophobic solid surfaces by time-resolved ellipsometry. *Journal of the Chemical Society, Faraday Transactions,* 92(4), pp. 531-538 .

Toppr, 2020. *Adsorption Isotherm.* [Online] Available at: https://www.toppr.com/guides/chemistry/surface-chemistry/adsorption-isotherm/ [Accessed 10 June 2020].

Traces Centre, 2021. *Understanding Raman Spectroscopy Principles and Theory.* [Online] Available at: https://www.utsc.utoronto.ca/~traceslab/PDFs/raman_understanding.pdf [Accessed 8 January 2024].

Tran, H. N., 2023. Applying Linear Forms of Pseudo-Second-Order Kinetic Model for Feasibly Identifying Errors in the Initial Periods of Time-Dependent Adsorption Datasets. *Water,* 15(6), p. 1231.

Tran, H. N. et al., 2021. Thermodynamic parameters of liquid–phase adsorption process calculated from different equilibrium constants related to adsorption isotherms: A comparison study. *Journal of Environmental Chemical Engineering,* 9(6), p. 106674.

Umpleby II, R. J. et al., 2001. Application of the Freundlich adsorption isotherm in the characterization of molecularly imprinted polymers. *Analytica Chimica Acta,* 435(1), p. 35–42.

Vansant, E. E., Van Der Voort, R. & Vrancken, K. C., 1995. *CHARACTERIZATION AND CHEMICAL MODIFICATION OF THE SILICA SURFACE.* Amsterdam: ELSEVIER.

Voinova, M. V., Rodahl, M., Jonson, M. & Kasemo, B., 1999. Viscoelastic Acoustic Response of Layered Polymer Films at Fluid-Solid Interfaces: Continuum Mechanics Approach. *Physica Scripta,* Volume 59, pp. 391-396.

Wallace, T., Gibbons, D., O'Dwyer, M. & Curran, T., 2017. International evolution of fat, oil and grease (FOG) waste management-A review. *Journal of Environmental Management,* Volume 187, pp. 424-435.

Wang, J. & Guo, X., 2020. Adsorption isotherm models: Classification, physical meaning, application and solving method. *Chemosphere,* November.Volume 258.

Wang, J., Mueller, D. N. & Crumlin, E. J., 2024. Recommended strategies for quantifying oxygen vacancies with X-ray photoelectron spectroscopy. *Journal of the European Ceramic Society,* 44(15), p. 116709.

Wang, J. et al., 2011. Two-Phase Synthesis of Monodisperse Silica Nanospheres with Amines or Ammonia Catalyst and Their Controlled Self-Assembly. *ACS Applied Materials & Interfaces,* Volume 3, p. 1538–1544.

Wang, Z.-M.et al., 2008. Optimization of biodiesel production from trap grease via acid catalysis. *Korean Journal of Chemical Engineering,* 25(4), p. 670–674.

Watts, J. F. & Wolstenholme, J., 2003. *An Intorduction to Surface Analysis by XPS and AES.* 1st ed. Chichester: John Wiley & Sons Ltd.

Weng, K. C., Kanter, J. L., Robinson, W. H. & Frank, C. W., 2006. Fluid supported lipid bilayers containing monosialoganglioside GM1: A QCM-D and FRAP study. *Colloids and Surfaces B: Biointerfaces,* Volume 50, p. 76–84.

Westwood, M., Kirby, A. R., Parker, R. & Morris, V., 2012. Combined QCMD and AFM studies of lysozyme and poly-l-lysine–poly-galacturonic acid multilayers. *Carbohydrate Polymers,* 89(4), pp. 1222-1231.

Williams, J. B. et al., 2012. Fat, oil and grease deposits in sewers: Characterisation of deposits and formation mechanisms. *Water Research,* 46(19), pp. 6319-6328.

Wittcoff, H. A., Reuben, B. G. & Plotkin, J. S., 2012. Fats and Oils. In: I. John Wiley & Sons, ed. *Industrial Organic Chemicals.* s.l.:John Wiley & Sons,Inc, pp. 493-521.

Wittcoff, H. A., Reuben, B. G. & Plotkin, J. S., 2013. Fats and Oils. In: I. John Wiley & Sons, ed. *Industrial Organic Chemicals.* s.l.:John Wiley & Sons, Inc, pp. 493-521.

XAmplified, 2009. *Adsorption Isotherm.* [Online] Available at: https://www.chemistrylearning.com/adsorption-isotherm/ [Accessed 10 June 2020].

Yamauchi, Y. et al., 2022. Room-Temperature Reversible Chemisorption of Carbon Monoxide on Nickel(0) Complexes. *Journal of the American Chemical Society,* 114(19), p. 8818–8826.

Yang, H. et al., 2014. Direct growth of large-area graphene films onto oxygen plasma-etched quartz for nitrogen dioxide gas detection. *Journal of Physics D: Applied Physics,* Volume 47, p. 315101.

Yang, H. et al., 2017. Selective crystallisation of carbamazepine polymorphs on surfaces with differing properties. *CrystEngComm,* 19(44), pp. 6573-6578.

Yang, T. et al., 2024. Interfacial adsorption dynamics of solid lipid particles at oil/water interfaces through QCM-D technique. *Food Hydrocolloids,* Volume 148, p. 109431.

Yang, T. et al., 2024. Interfacial adsorption dynamics of solid lipid particles at oil/water interfaces through QCM-D technique. *Food Hydrocolloids,* Volume 148, p. 109431.

Yao, M. et al., 2021. Kinetics and Thermodynamics of Hemicellulose Adsorption onto Nanofibril Cellulose Surfaces by QCM-D. *ACS Omega,* 6(45), p. 30618–30626.

Zeng, D. et al., 2015. Effect of Ammonia Concentration on Silica Spheres Morphology and Solution Hydroxyl Concentration in Stober Process. *Nanoscience and Nanotechnology,* Volume 15, p. 7407–7411.

Zhang, C., Su, H., Baeyens, J. & Tan, T., 2014. Reviewing the anaerobic digestion of food waste for biogas production. *Renewable and Sustainable Energy Reviews,* Volume 38, pp. 383-392.

Zhang, J., 2019. Physical insights into kinetic models of adsorption. *Separation and Purification Technology,* Volume 229, p. 115832.

Zheng, B., Wu, H., Zhang, M. & Lin, S., 2025. Removal of polystyrene microplastics from wastewater by Ti–Al electrode electrocoagulation under pulse current: Efficiency and mechanism. *Water Environment Research,* 97(3), pp. 1-24.

Zulfiqar, U., Subhani, T. & Husai, S. W., 2016. Synthesis of silica nanoparticles from sodium silicate under alkaline conditions. *Sol-Gel Sci Technol,* Volume 77, p. 753–758.

Zulfiq, U., Subhani, T. & Husai, S. W., 2016. Synthesis of silica nanoparticles from sodium silicate under alkaline conditions. *Sol-Gel Sci Technol,* Volume 77, p. 753–758.

Chapter 8 Appendices

8.1 Appendix for Chapter 3

8.1.1 Oleic Acid

8.1.1.1 Polystyrene

8.1.1.1.1 25mg/ml oleic acid ss on polystyrene

Ref.	Name	Peak BE	Height CPS	Height Ratio	Area CPS.eV	Area Ratio	FWHM fit param (eV)	L/G Mix (%) Product	Tail Mix (%)	Tail Height (%)	Tail Exponent
A	Si2p3 SiC	101.49	2225.75	1.00	3022.13	1.00	1.30	24.67	100.00	0.00	0.0000
							0.5 : 3.5	**0 : 100**	**fixed**	**fixed**	**fixed**
B	Si2p1 Organic Si	102.02	1135.50	0.51	1541.79	0.51	1.30	24.67	100.00	0.00	0.0000
		A+0.63 (±0.1)	**A*0.51**				**A*1**	**A*1**	**A*1**	**A*1**	**A*1**
C	Si2p oxide	102.61	452.16	0.20	613.94	0.20	1.30	24.67	100.00	0.00	0.0000
							A*1	**A*1**	**fixed**	**fixed**	**fixed**

	Name	Start BE	Peak BE	End BE	Height CPS	FWHM eV	Area (P) CPS.eV	Area (N) TPP-2M	Atomic %	Peak Type	Q
	Si2p3 SiC	104.08	101.49	99.48	2225.75	1.26	3022.13	63.71	46.84	Fitted	☑
	Si2p1 Organic Si	104.08	102.02	99.48	1135.50	1.26	1541.79	63.73	46.85	Fitted	☑
	Si2p oxide	104.08	102.61	99.48	452.16	1.26	613.94	8.58	6.31	Fitted	☑

O1s

Ref.	Name	Peak BE	Height CPS	Height Ratio	Area CPS.eV	Area Ratio	FWHM fit param (eV)	L/G Mix (%) Product	Tail Mix (%)	Tail Height (%)	Tail Exponent
A	O1s C-O	531.70	15034.20	1.00	21431.60	1.00	1.35	48.26	100.00	0.00	0.0000
							0.5 : 3.5	**0 : 100**	**fixed**	**fixed**	**fixed**
B	O1s C=O	533.21	1356.55	0.09	1933.79	0.09	1.35	48.26	100.00	0.00	0.0000
							A*1	**A*1**	**fixed**	**fixed**	**fixed**

	Name	Peak BE	FWHM eV	Area (P) CPS.eV	Atomic %	Q
	O1s C-O	531.70	1.29	21431.60	91.71	☑
	O1s C=O	533.21	1.29	1933.79	8.29	☑

C1s

Ref.	Name	Peak BE	Height CPS	Height Ratio	Area CPS.eV	Area Ratio	FWHM fit param (eV)	L/G Mix (%) Product	Tail Mix (%)	Tail Height (%)	Tail Exponent
A	C1s C-C	284.16	34143.66	1.00	36375.24	1.00	1.02	31.45	100.00	0.00	0.0000
							0.5 : 3.5	**0 : 100**	**fixed**	**fixed**	**fixed**
B	C1s C-C	284.65	8843.21	0.26	12729.08	0.35	1.21	83.72	100.00	0.00	0.0000
							0.5 : 3.5	**0 : 100**	**fixed**	**fixed**	**fixed**
C	C1s C-C	283.50	1658.31	0.05	2330.25	0.06	1.33	45.91	100.00	0.00	0.0000
							0.5 : 3.5	**0 : 100**	**fixed**	**fixed**	**fixed**
D	C1s O-C=O	288.94	512.28	0.02	483.87	0.01	0.89	0.02	100.00	0.00	0.0000
							0.5 : 3.5	**0 : 100**	**fixed**	**fixed**	**fixed**

	Name	**Peak BE**	FWHM eV	Area (P) CPS.eV	Atomic %	Q
	C1s C-C	284.16	0.98	36375.24	70.06	☑
	C1s C-C	284.65	1.19	12729.08	24.52	☑
	C1s C-C	283.50	1.27	2330.25	4.49	☑
	C1s O-C=O	288.94	0.89	483.87	0.93	☑

8.1.1.1.2 125mg/ml oleic acid on polystyrene

Ref.	Name	Peak BE	Height CPS	Height Ratio	Area CPS.eV	Area Ratio	FWHM fit param (eV)	L/G Mix (%) Product	Tail Mix (%)	Tail Height (%)	Tail Exponent
A	C1s C-C	284.24	25260.77	1.00	27229.90	1.00	1.03	14.55	100.00	0.00	0.0000
							0.5 : 3.5	**0 : 100**	**fixed**	**fixed**	**fixed**
B	C1s C-C	284.46	12876.26	0.51	19986.19	0.73	1.30	84.55	100.00	0.00	0.0000
							A*1 (±0.7)	**A*1 (±0.7)**	**fixed**	**fixed**	**fixed**
C	C1s O-C=O	289.03	1143.50	0.05	1232.64	0.05	1.03	14.55	100.00	0.00	0.0000
							A*1	**A*1**	**fixed**	**fixed**	**fixed**

Ref.	Name	Peak BE	Height CPS	Height Ratio	Area CPS.eV	Area Ratio	FWHM fit param (eV)	L/G Mix (%) Product	Tail Mix (%)	Tail Height (%)	Tail Exponent
D	O1s C-O	531.72	20257.27	1.00	25698.54	1.00	1.20	45.68	100.00	0.00	0.0000
							0.5 : 3.5	**0 : 100**	**fixed**	**fixed**	**fixed**
E	O1s C=O	533.31	2450.12	0.12	3108.24	0.12	1.20	45.68	100.00	0.00	0.0000
							D*1	**D*1**	**fixed**	**fixed**	**fixed**

Ref.	Name	Peak BE	Height CPS	Height Ratio	Area CPS.eV	Area Ratio	FWHM fit param (eV)	L/G Mix (%) Product	Tail Mix (%)	Tail Height (%)	Tail Exponent
F	Si2p3 Si	101.47	4518.74	1.00	4882.75	1.00	1.00	59.99	100.00	0.00	0.0000
							0.5 : 3.5	0 : 100	fixed	fixed	fixed
G	Si2p1 Si-polysyloxane	102.11	2305.31	0.51	2649.65	0.54	1.05	64.99	100.00	0.00	0.0000
		F+0.63 (±0.1)	F*0.51				F*1 (±0.05)	F*1 (±0.05)	F*1	F*1	F*1

	Name	Peak BE	FWHM eV	Area (P) CPS.eV	Atomic %	Q
	C1s C-C	284.24	1.01	27229.90	36.05	☑
	C1s C-C	284.46	1.27	19986.19	26.46	☑
	C1s O-C=O	289.03	1.01	1232.64	1.64	☑
	O1s C-O	531.72	1.15	25698.54	14.08	☑
	O1s C=O	533.31	1.15	3108.24	1.70	☑
	Si2p3 Si	101.47	0.96	4882.75	9.72	☑
	Si2p1 Si-polysyloxane	102.11	1.01	2649.65	10.35	☑

8.1.1.2 Silicon Dioxide

8.1.1.2.1 25mg/ml SiO2

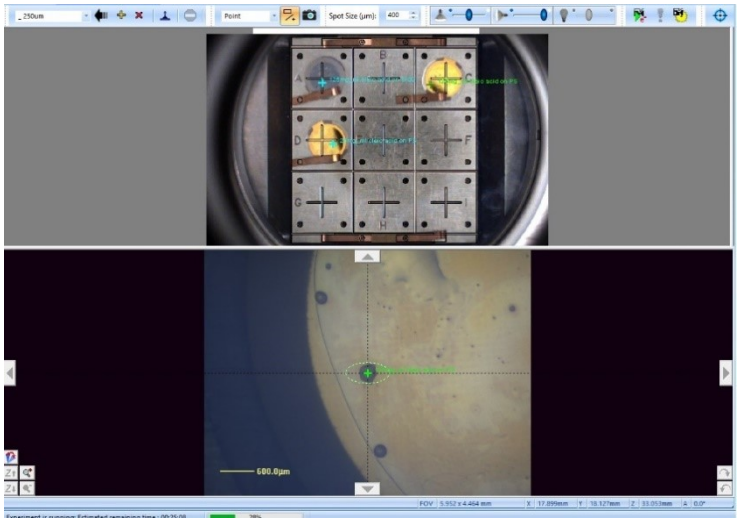
	Name	Peak BE	FWHM eV	Area (P) CPS.eV	Atomic %	Q
	C1s C-C	284.51	1.13	18572.57	24.96	☑
	C1s O-C=O	289.00	0.95	1373.39	1.85	☑
	Si2p3 Si	101.45	1.01	4201.88	8.49	☑
	Si2p1 Si	102.12	1.01	2143.66	8.49	☑
	O1s C-O	531.63	1.01	13075.12	7.27	☑
	O1s SiO2	532.50	2.40	8860.70	4.93	☑
	O1s C-O	531.89	1.47	4679.43	2.60	☑

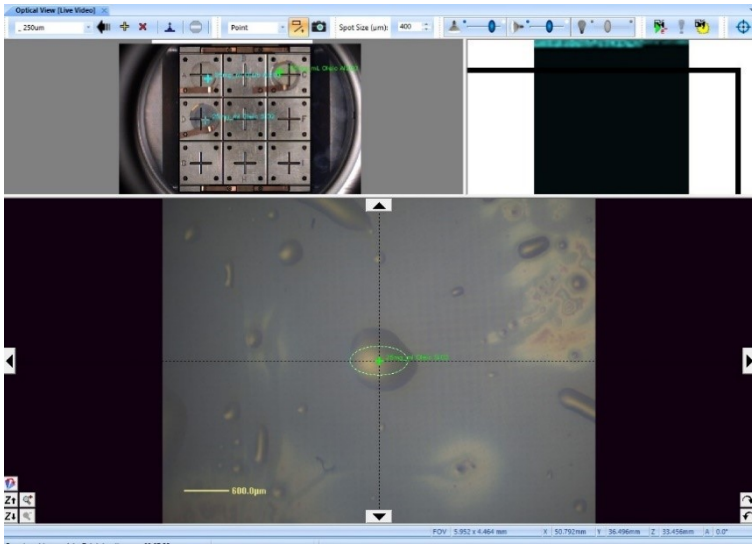
Ref.	Name	Peak BE	Height CPS	Height Ratio	Area CPS.eV	Area Ratio	FWHM fit param (eV)	L/G Mix (%) Product	Tail Mix (%)	Tail Height (%)	Tail Exponent
A	C1s C-C	284.18	29324.25	1.00	30820.75	1.00	0.98	54.34	100.00	0.00	0.0000
							0.5 : 3.5	0 : 100	fixed	fixed	fixed
B	C1s C-C	284.51	13387.90	0.46	18572.57	0.60	1.15	85.83	100.00	0.00	0.0000
							A*1 (±2)	A*1 (±2)	fixed	fixed	fixed
C	C1s O-C=O	289.00	1363.54	0.05	1373.39	0.04	0.95	0.00	100.00	0.00	0.0000
							A*1 (±2)	A*1 (±2)	fixed	fixed	fixed

Ref.	Name	Peak BE	Height CPS	Height Ratio	Area CPS.eV	Area Ratio	FWHM fit param (eV)	L/G Mix (%) Product	Tail Mix (%)	Tail Height (%)	Tail Exponent
G	O1s C-O	531.63	12214.81	1.00	13075.12	1.00	1.01	0.00	100.00	0.00	0.0000
							0.5 : 3.5	0 : 100	fixed	fixed	fixed
H	O1s SiO2	532.50	3468.75	0.28	8860.70	0.68	2.40	0.00	100.00	0.00	0.0000
							0.5 : 3.5	0 : 100	fixed	fixed	fixed
I	O1s C-O	531.89	2778.37	0.23	4679.43	0.36	1.52	67.94	100.00	0.00	0.0000
							0.5 : 3.5	0 : 100	fixed	fixed	fixed

Ref.	Name	Peak BE	Height CPS	Height Ratio	Area CPS.eV	Area Ratio	FWHM fit param (eV)	L/G Mix (%) Product	Tail Mix (%)	Tail Height (%)	Tail Exponent
D	Si2p3 Si	101.45	3647.87	1.00	4201.88	1.00	1.05	63.91	100.00	0.00	0.0000
							0.5 : 3.5	**0 : 100**	**fixed**	**fixed**	**fixed**
E	Si2p1 Si	102.12	1861.02	0.51	2143.66	0.51	1.05	63.91	100.00	0.00	0.0000
		D+0.63 (±0.1)	**D*0.51**				**D*1**	**D*1**	**D*1**	**D*1**	**D*1**

8.1.2 Aluminium Oxide





8.1.2.1 25mg/ml oleic acid ss on aluminium oxide

Ref.	Name	Peak BE	Height CPS	Height Ratio	Area CPS.eV	Area Ratio	FWHM fit param (eV)	L/G Mix (%) Product	Tail Mix (%)	Tail Height (%)	Tail Exponent
A	Si2p3 (C6H5)3SiOSi(C6H5)3	101.35	1837.05	1.00	2094.29	1.00	1.05	59.43	100.00	0.00	0.0000
							0.5 : 3.5	**0 : 100**	**fixed**	**fixed**	**fixed**
B	Si2p1 Si	101.88	937.20	0.51	1068.44	0.51	1.05	59.43	100.00	0.00	0.0000
		A+0.63 (±0.1)	**A*0.51**				**A*1**	**A*1**	**A*1**	**A*1**	**A*1**
C	Si2p SiO2(Al2O3)0.22	102.05	1067.59	0.58	1655.02	0.79	1.47	3.41	100.00	0.00	0.0000
							0.5 : 3.5	**0 : 100**	**fixed**	**fixed**	**fixed**

	Name	Peak BE	FWHM eV	Area (P) CPS.eV	Atomic %	Q
	Si2p3 (C6H5)3SiOSi(C6H5)3	101.35	1.01	2094.29	4.12	☑
	Si2p1 Si	101.88	1.01	1068.44	4.12	☑
	Si2p SiO2(Al2O3)0.22	102.05	1.46	1655.02	2.16	☑
	C1s C-C	284.12	0.94	35674.78	46.63	☑
	C1s C-C	284.46	1.18	18446.03	24.12	☑
	C1s (-CH2C(CH3)(C*(O)OCH2CH2CH2CH3)-)n	288.89	0.94	1405.41	1.84	☑
	O1s C-O	531.57	1.12	23111.05	12.50	☑
	O1s C=O	532.85	1.95	6162.06	3.34	☑
	Al2p3 Al	73.80	1.80	192.02	0.59	☑
	Al2p1 Al	74.14	1.81	96.27	0.59	☑

Ref.	Name	Peak BE	Height CPS	Height Ratio	Area CPS.eV	Area Ratio	FWHM fit param (eV)	L/G Mix (%) Product	Tail Mix (%)	Tail Height (%)	Tail Exponent
D	C1s C-C	284.12	34195.10	1.00	35674.78	1.00	0.98	50.00	100.00	0.00	0.0000
							0.5 : 3.5	**0 : 100**	**fixed**	**fixed**	**fixed**
E	C1s C-C	284.46	12548.12	0.37	18446.03	0.52	1.21	87.73	100.00	0.00	0.0000
							D*1 (±0.5)	**D*1 (±0.5)**	**fixed**	**fixed**	**fixed**
F	C1s (-CH2C(CH3)(C*(O)OCH2CH2CH2CH3)-)n	288.89	1414.23	0.04	1405.41	0.04	0.93	0.00	100.00	0.00	0.0000
							D*1 (±0.5)	**D*1 (±0.5)**	**fixed**	**fixed**	**fixed**

Ref.	Name	Peak BE	Height CPS	Height Ratio	Area CPS.eV	Area Ratio	FWHM fit param (eV)	L/G Mix (%) Product	Tail Mix (%)	Tail Height (%)	Tail Exponent
G	O1s C-O	531.57	18112.38	1.00	23111.05	1.00	1.16	64.96	100.00	0.00	0.0000
							0.5 : 3.5	**0 : 100**	**fixed**	**fixed**	**fixed**
H	O1s C=O	532.85	2965.98	0.16	6162.06	0.27	1.96	1.49	100.00	0.00	0.0000
							0.5 : 3.5	**0 : 100**	**fixed**	**fixed**	**fixed**

Ref.	Name	Peak BE	Height CPS	Height Ratio	Area CPS.eV	Area Ratio	FWHM fit param (eV)	L/G Mix (%) Product	Tail Mix (%)	Tail Height (%)	Tail Exponent
I	Al2p3 Al	73.80	100.71	1.00	192.02	1.00	1.79	0.45	100.00	0.00	0.0000
							0.5 : 3.5	**0 : 100**	**fixed**	**fixed**	**fixed**
J	Al2p1 Al	74.14	50.49	0.50	96.27	0.50	1.79	0.45	100.00	0.00	0.0000
		I+0.44 (±0.1)	**I*0.501**				**I*1**	**I*1**	**I*1**	**I*1**	**I*1**

8.1.2.2 125mg/ml oleic acid ss on aluminium oxide

	Name	Peak BE	FWHM eV	Area (P) CPS.eV	Atomic %	Q
	O1s C-O	531.69	1.12	20088.79	12.66	☑
	O1s C=O	532.88	1.96	5669.57	3.58	☑
	C1s C-C	284.29	1.00	40657.90	61.92	☑
	C1s C-C	284.71	2.09	7546.85	11.50	☑
	C1s O-C=O	288.98	0.90	1010.79	1.54	☑
	Si2p3 Si	101.61	1.30	1707.93	3.91	☑
	Si2p1 Si	102.14	1.30	871.33	3.91	☑
	Al2p3 Aluminosilicate	74.08	1.74	135.96	0.49	☑
	Al2p1 Aluminosilicate	74.42	1.74	68.16	0.49	☑

Ref.	Name	Peak BE	Height CPS	Height Ratio	Area CPS.eV	Area Ratio	FWHM fit param (eV)	L/G Mix (%) Product	Tail Mix (%)	Tail Height (%)	Tail Exponent
A	O1s C-O	531.69	16093.23	1.00	20088.79	1.00	1.16	55.55	100.00	0.00	0.0000
							0.5 : 3.5	**0 : 100**	**fixed**	**fixed**	**fixed**
B	O1s C=O	532.88	2722.67	0.17	5669.57	0.28	1.96	0.89	100.00	0.00	0.0000
							0.5 : 3.5	**0 : 100**	**fixed**	**fixed**	**fixed**

Ref.	Name	Peak BE	Height CPS	Height Ratio	Area CPS.eV	Area Ratio	FWHM fit param (eV)	L/G Mix (%) Product	Tail Mix (%)	Tail Height (%)	Tail Exponent
C	C1s C-C	284.29	36908.36	1.00	40657.90	1.00	1.04	48.04	100.00	0.00	0.0000
							0.5 : 3.5	**0 : 100**	**fixed**	**fixed**	**fixed**
D	C1s C-C	284.71	3305.24	0.09	7546.85	0.19	2.18	37.83	100.00	0.00	0.0000
							0.5 : 3.5	**0 : 100**	**fixed**	**fixed**	**fixed**
E	C1s O-C=O	288.98	1062.33	0.03	1010.79	0.02	0.89	0.00	100.00	0.00	0.0000
							0.5 : 3.5	**0 : 100**	**fixed**	**fixed**	**fixed**

Ref.	Name	Peak BE	Height CPS	Height Ratio	Area CPS.eV	Area Ratio	FWHM fit param (eV)	L/G Mix (%) Product	Tail Mix (%)	Tail Height (%)	Tail Exponent
F	Si2p3 Si	101.61	1167.67	1.00	1707.93	1.00	1.35	59.37	100.00	0.00	0.0000
							0.5 : 3.5	**0 : 100**	**fixed**	**fixed**	**fixed**
G	Si2p1 Si	102.14	595.70	0.51	871.33	0.51	1.35	59.37	100.00	0.00	0.0000
		F+0.63 (±0.1)	**F*0.51**				**F*1**	**F*1**	**F*1**	**F*1**	**F*1**

Ref.	Name	Peak BE	Height CPS	Height Ratio	Area CPS.eV	Area Ratio	FWHM fit param (eV)	L/G Mix (%) Product	Tail Mix (%)	Tail Height (%)	Tail Exponent
H	Al2p3 Aluminosilicate	74.08	73.65	1.00	135.96	1.00	1.74	0.21	100.00	0.00	0.0000
							0.5 : 3.5	**0 : 100**	**fixed**	**fixed**	**fixed**
I	Al2p1 Aluminosilicate	74.42	36.92	0.50	68.16	0.50	1.74	0.21	100.00	0.00	0.0000
		H+0.44 (±0.1)	**H*0.501**				**H*1**	**H*1**	**H*1**	**H*1**	**H*1**

8.1.3 Linoleic Acid

8.1.3.1 Polystyrene

XPS Knowledge View | 75 LIN ON PS

	Name	Peak BE	FWHM eV	Area (P) CPS.eV	Atomic %	Q
	C1s C-C	284.19	1.12	44357.58	61.85	☑
	C1s C-O-C	285.70	1.12	1886.84	2.63	☑
	C1s O-C=O	290.68	1.12	473.35	0.66	☑
	O1s C-O	531.71	1.12	12525.63	7.23	☑
	O1s H-O-C	532.10	1.73	13728.07	7.92	☑
	Si2p3 Si-O	101.70	1.40	4178.87	8.76	☑
	Si2p1 Si-O	102.43	1.73	2660.64	10.94	☑

XPS Knowledge View | 75 LIN ON PS

Ref.	Name	Peak BE	Height CPS	Height Ratio	Area CPS.eV	Area Ratio	FWHM fit param (eV)	L/G Mix (%) Product	Tail Mix (%)	Tail Height (%)	Tail Exponent
A	C1s C-C	284.19	35710.88	1.00	44357.58	1.00	1.17	52.01	100.00	0.00	0.0000
							0.5 : 3.5	0 : 100	fixed	fixed	fixed
B	C1s C-O-C	285.70	1519.04	0.04	1886.84	0.04	1.17	52.01	100.00	0.00	0.0000
							A*1	A*1	fixed	fixed	fixed
C	C1s O-C=O	290.68	381.08	0.01	473.35	0.01	1.17	52.01	100.00	0.00	0.0000
							A*1	A*1	fixed	fixed	fixed

XPS Knowledge View | 75 LIN ON PS

Ref.	Name	Peak BE	Height CPS	Height Ratio	Area CPS.eV	Area Ratio	FWHM fit param (eV)	L/G Mix (%) Product	Tail Mix (%)	Tail Height (%)	Tail Exponent
D	O1s C-O	531.71	10482.29	1.00	12525.63	0.91	1.13	1.76	100.00	0.00	0.0000
							0.5 : 3.5	0 : 100	fixed	fixed	fixed
E	O1s H-O-C	532.10	7103.57	0.68	13728.07	1.00	1.80	57.18	100.00	0.00	0.0000
							0.5 : 3.5	0 : 100	fixed	fixed	fixed

XPS Knowledge View | 75 LIN ON PS

Ref.	Name	Peak BE	Height CPS	Height Ratio	Area CPS.eV	Area Ratio	FWHM fit param (eV)	L/G Mix (%) Product	Tail Mix (%)	Tail Height (%)	Tail Exponent
G	Si2p3 Si-O	101.70	2801.26	1.00	4178.87	1.00	1.43	11.96	100.00	0.00	0.0000
							0.5 : 3.5	0 : 100	fixed	fixed	fixed
H	Si2p1 Si-O	102.43	1429.11	0.51	2660.64	0.64	1.79	20.39	100.00	0.00	0.0000
		G+0.63 (±0.1)	G*0.51				G*1 (±0.9)	G*1 (±0.9)	G*1	G*1	G*1

8.1.4 Silicon Dioxide

75 lin silica

	Name	Peak BE	FWHM eV	Area (P) CPS.eV	Atomic %	Q
	C1s C-C	284.27	1.33	39960.61	42.80	☑
	C1s C-O-C	285.56	2.28	8663.55	9.29	☑
	C1s O-C=O	288.90	1.08	2305.83	2.48	☑
	O1s C-O	531.75	1.15	26821.73	11.89	☑
	O1s H-O-C	532.47	2.02	22996.33	10.20	☑
	Si2p3 SiC	101.63	1.21	6605.98	10.64	☑
	Si2p1 SiC	102.36	1.40	4025.34	12.72	☑

Ref.	Name	Peak BE	Height CPS	Height Ratio	Area CPS.eV	Area Ratio	FWHM fit param (eV)	L/G Mix (%) Product	Tail Mix (%)	Tail Height (%)	Tail Exponent
A	C1s C-C	284.27	28226.44	1.00	39960.61	1.00	1.33	0.32	100.00	0.00	0.0000
							0.5 : 3.5	0 : 100	fixed	fixed	fixed
B	C1s C-O-C	285.56	3295.79	0.12	8663.55	0.22	2.36	69.50	100.00	0.00	0.0000
							0.5 : 3.5	0 : 100	fixed	fixed	fixed
C	C1s O-C=O	288.90	1896.50	0.07	2305.83	0.06	1.13	56.61	100.00	0.00	0.0000
							0.5 : 3.5	0 : 100	fixed	fixed	fixed

Ref.	Name	Peak BE	Height CPS	Height Ratio	Area CPS.eV	Area Ratio	FWHM fit param (eV)	L/G Mix (%) Product	Tail Mix (%)	Tail Height (%)	Tail Exponent
D	O1s C-O	531.75	21979.73	1.00	26821.73	1.00	1.15	0.00	100.00	0.00	0.0000
							0.5 : 3.5	**0 : 100**	**fixed**	**fixed**	**fixed**
E	O1s H-O-C	532.47	10477.71	0.48	22996.33	0.86	2.10	37.70	100.00	0.00	0.0000
							0.5 : 3.5	**0 : 100**	**fixed**	**fixed**	**fixed**

75 lin silica

Ref.	Name	Peak BE	Height CPS	Height Ratio	Area CPS.eV	Area Ratio	FWHM fit param (eV)	L/G Mix (%) Product	Tail Mix (%)	Tail Height (%)	Tail Exponent
F	Si2p3 SiC	101.63	5100.88	1.00	6605.98	1.00	1.24	10.35	100.00	0.00	0.0000
							0.5 : 3.5	**0 : 100**	**fixed**	**fixed**	**fixed**
G	Si2p1 SiC	102.36	2602.29	0.51	4025.34	0.61	1.46	49.60	100.00	0.00	0.0000
		F+0.63 (±0.1)	**F*0.51**				**F*1 (±0.5)**	**F*1 (±0.5)**	**F*1**	**F*1**	**F*1**

75 silica

8.1.5 Aluminium Oxide

75 linoleic acid

XPS Knowledge View | 75 lin alumina 2

Name	Peak BE	FWHM eV	Area (P) CPS.eV	Atomic %	Q
Si2p3 SiO	101.73	1.42	4481.22	9.65	☑
Si2p1 SiO	102.30	1.42	2286.17	9.65	☑
Si2p SiO2	103.14	1.28	585.74	0.84	☑
O1s C=O	532.14	2.02	16339.92	9.68	☑
O1s C-O	531.73	1.12	15438.03	9.14	☑
C1s O-C=O	288.61	1.27	948.21	1.36	☑
C1s C-O-C	286.09	1.27	2869.30	4.11	☑
C1s C-C	284.31	1.27	38839.40	55.58	☑

XPS Knowledge View | 75 lin alumina 2

Ref.	Name	Peak BE	Height CPS	Height Ratio	Area CPS.eV	Area Ratio	FWHM fit param (eV)	L/G Mix (%) Product	Tail Mix (%)	Tail Height (%)	Tail Exponent
A	C1s C-C	284.31	27871.75	1.00	38839.40	1.00	1.33	41.02	100.00	0.00	0.0000
							0.5 : 3.5	**0 : 100**	**fixed**	**fixed**	**fixed**
B	C1s C-O-C	286.09	2059.05	0.07	2869.30	0.07	1.33	41.02	100.00	0.00	0.0000
							A*1	**A*1**	**fixed**	**fixed**	**fixed**
C	C1s O-C=O	288.61	680.45	0.02	948.21	0.02	1.33	41.02	100.00	0.00	0.0000
							A*1	**A*1**	**fixed**	**fixed**	**fixed**

XPS Knowledge View | 75 lin alumina 2

Ref.	Name	Peak BE	Height CPS	Height Ratio	Area CPS.eV	Area Ratio	FWHM fit param (eV)	L/G Mix (%) Product	Tail Mix (%)	Tail Height (%)	Tail Exponent
E	O1s C-O	531.73	12956.00	1.00	15438.03	0.94	1.12	0.04	100.00	0.00	0.0000
							0.5 : 3.5	**0 : 100**	**fixed**	**fixed**	**fixed**
F	O1s C=O	532.14	7323.52	0.57	16339.92	1.00	2.11	47.32	100.00	0.00	0.0000
							0.5 : 3.5	**0 : 100**	**fixed**	**fixed**	**fixed**

si25 | 75 lin silica | XPS Knowledge View | 75 lin alumina | Data Grid 5

Ref.	Name	Peak BE	Height CPS	Height Ratio	Area CPS.eV	Area Ratio	FWHM fit param (eV)	L/G Mix (%) Product	Tail Mix (%)	Tail Height (%)	Tail Exponent
H	Si2p3 SiO	101.73	2968.58	1.00	4481.22	1.00	1.42	0.00	100.00	0.00	0.0000
							0.5 : 3.5	**0 : 100**	**fixed**	**fixed**	**fixed**
I	Si2p1 SiO	102.30	1514.47	0.51	2286.17	0.51	1.42	0.00	100.00	0.00	0.0000
		H+0.63 (±0.1)	**H*0.51**				**H*1**	**H*1**	**H*1**	**H*1**	**H*1**
J	Si2p SiO2	103.14	430.01	0.14	585.74	0.13	1.28	0.00	100.00	0.00	0.0000
							0.5 : 3.5	**0 : 100**	**fixed**	**fixed**	**fixed**

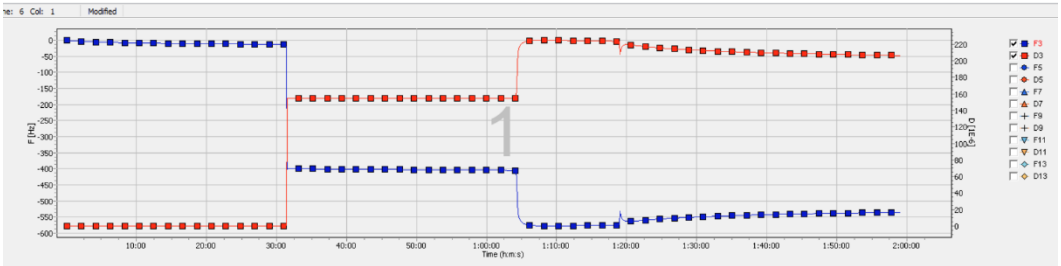
8.2 Appendix for Chapter 4

8.2.1 Raw data for Sequencing Experiments

8.2.1.1 Polystyrene

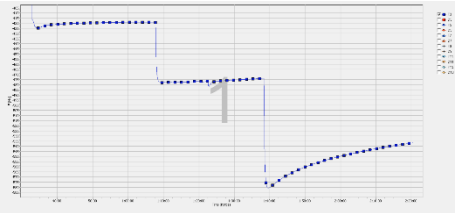
OPL

0:15 PS Hydrophobic sensor
31:21 added 0.25ml of ethanol
1:04:13 added 0.25ml 140mg/ml oleic acid ss
1:18:38 added 0.25ml 140mg/ml palmitic acid ss (slight force when adding ss)
1:34:48 added 0.25ml 140mg/ml linoleic acid ss

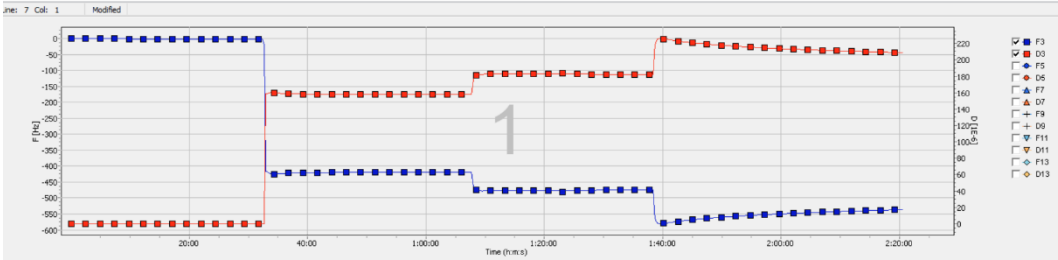


Shows OPL sequence.

LPO



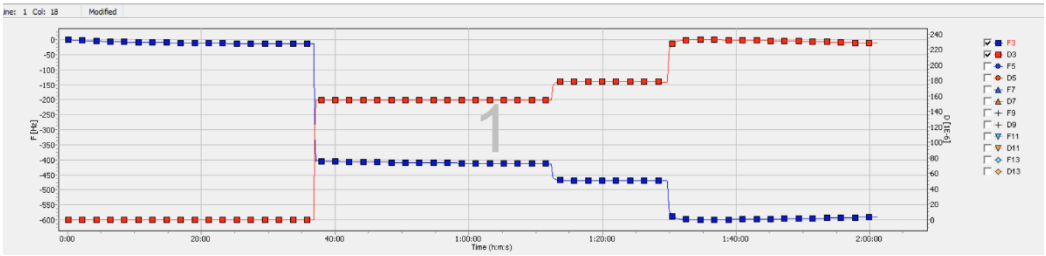
0:15	Hydrophobic Polystyrene sensor
32:21	added 0.25ml ethanol
1:07:25	added 0.25ml of 140mg/ml linoleic acid
1:20:06 -24:20	added 0.25ml of 140mg/ml palmitic acid
1:38:10	added 0.25ml of 140mg/ml oleic acid



Shows LPO sequence.

LOP

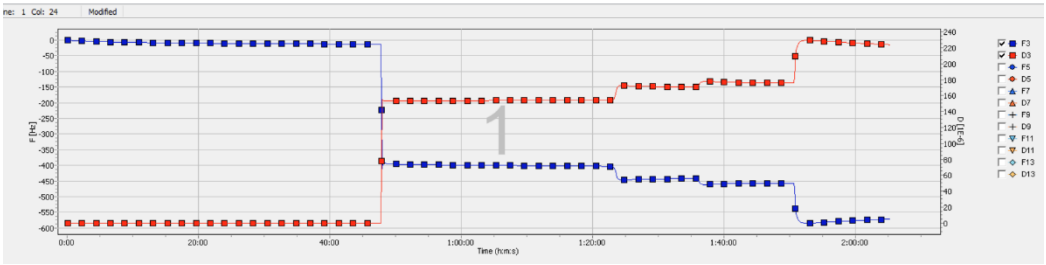
0:07	PS Hydrophobic sensor
36:54	added 0.25ml ethanol
1:12:19	added 0.25ml 140mg/ml linoleic acid ss
1:29:42	added 0.25ml 140mg/ml oleic acid ss
1:49:52	added 0.25ml 140mg/ml palmitic acid ss



Equation shows LOP sequence.

PLO

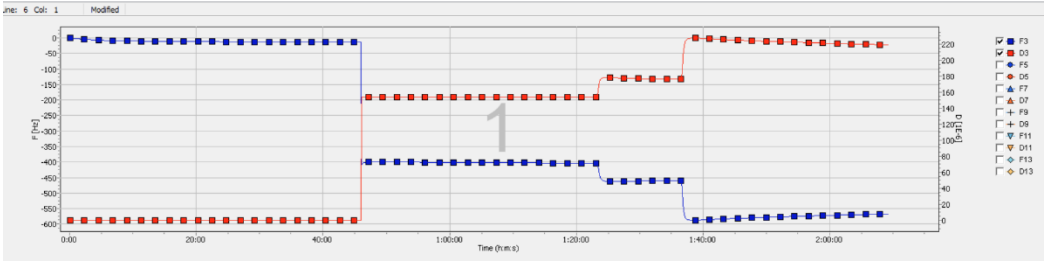
0:04	PS hydrophobic sensor
47:51	added 0.25ml ethanol
1:23:11	added 0.25ml 140mg/ml palmitic acid ss
1:35:45	added 0.25ml 140mg/ml linoleic acid ss
1:50:38	added 0.25ml 140mg/ml oleic acid ss



Shows PLO sequence.

POL

0:05	PS hydrophobic sensor
46:00	added 0.25ml ethanol
1:23:22	added 0.25ml 140mg/ml palmitic acid ss
1:36:36	added 0.25ml 140mg/ml oleic acid ss
1:50:58	added 0.25ml 140mg/ml linoleic acid ss

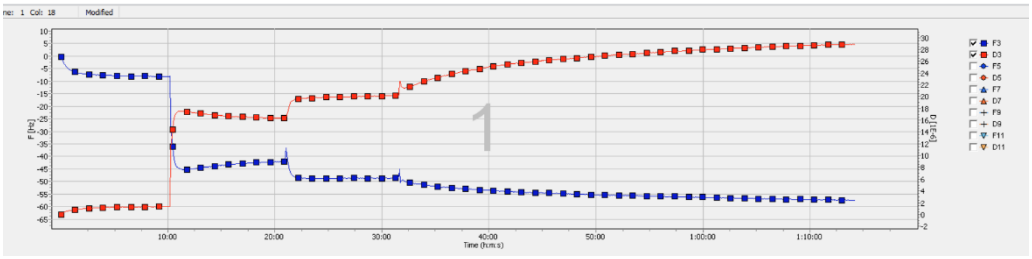


Shows POL sequence.

8.2.1.2 Silicon Dioxide

OLP

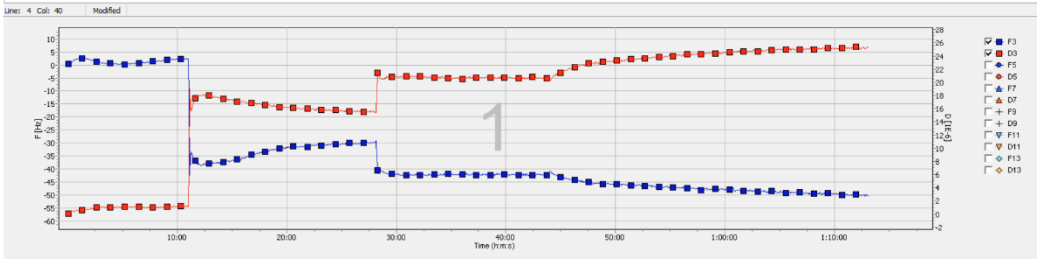
0:05 silica with ethanol OLP (0.2ml)
10:16 100mg/ml oleic acid ss (0.2ml)
20:59 100mg/ml linoleic acid ss (0.2ml)
31:39 100mg/ml palmitic acid ss (0.2ml)



Shows OLP sequence on SiO_2.

OPL

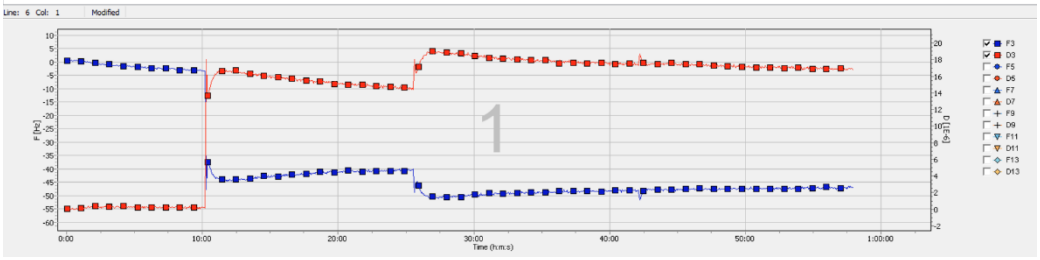
0:01 0.2ml ethanol on silica OPL
11:06 0.2ml 100mg/ml oleic acid ss
28:15 0.2ml 100mg/ml palmitic acid ss
43:43 0.2ml 100mg/ml linoleic acid ss



Shows OPL sequence on SiO_2.

LOP

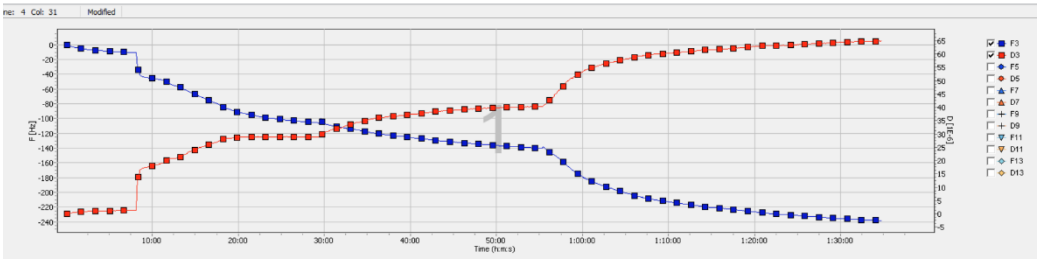
0:01 0.2ml ethanol on silica LOP
10:17 0.2ml 100mg/ml linoleic acid ss
25:37 0.2ml 100mg/ml oleic acid ss
42:13 0.2ml 100mg/ml palmitic acid ss



Shows LOP sequence on SiO_2.

LPO

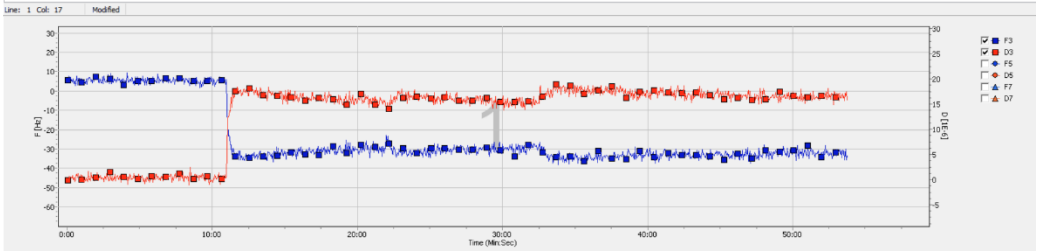
0:01	ethanol buffer silica LPO 0.2ml each
8:06	100mg/ml linoleic acid ss
29:30	100mg/ml palmitic acid ss
55:20	100mg/ml oleic acid ss



Shows LPO sequence on SiO_2.

PLO

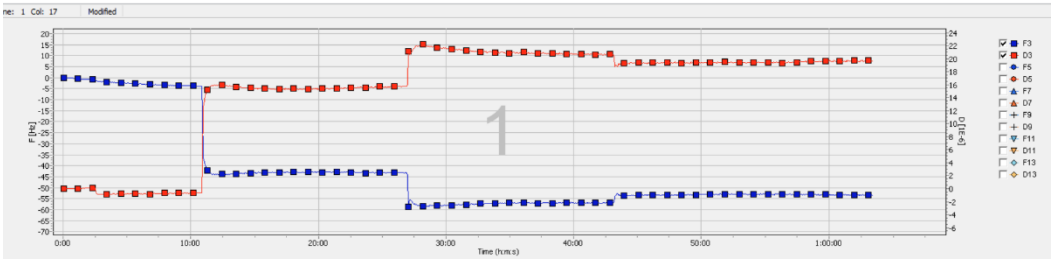
0:04	ethanol on silica 0.2ml PLO
10:58	0.2ml 100mg/ml palmitic acid ss
21:55	0.2ml 100mg/ml linoleic acid ss
32:33	0.2ml 100mg/ml oleic acid ss



Shows PLO sequence on SiO_2.

POL

0:01	0.2ml ethanol on silica POL
10:57	0.2ml 100mg/ml palmitic acid ss
27:06	0.2ml 100mg/ml oleic acid ss
43:11	0.2ml 100mg/ml linoleic acid ss

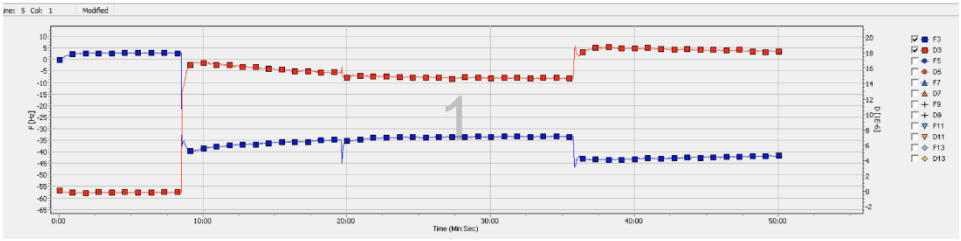


Shows POL sequence on SiO_2.

8.2.1.3 Aluminium Oxide

OLP

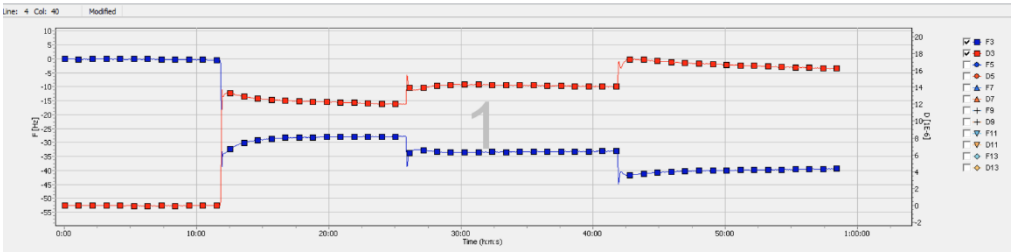
0:01	0.2ml ethanol on alumina
8:33	0.2ml 100mg/ml oleic acid ss
19:42	0.2ml 100mg/ml linoleic acid ss
35:50	0.2ml 100mg/ml palmitic acid ss



Shows OLP sequence on Al_2O_3.

OPL

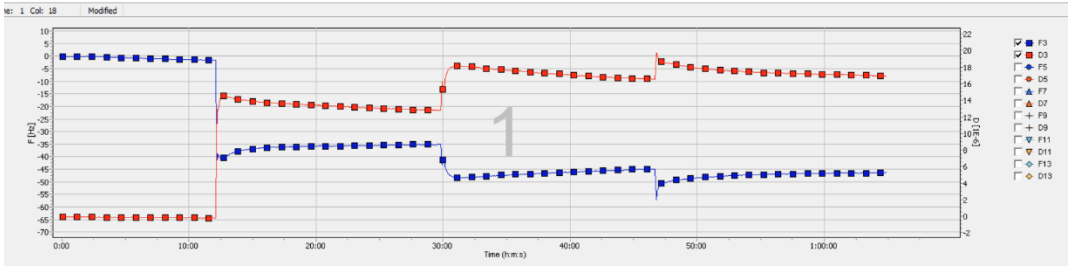
0:01	0.2ml ethanol on Alumina OPL
11:51	0.2ml 100mg/ml oleic acid ss
25:55	0.2ml 100mg/ml palmitic acid ss
41:55	0.2ml 100mg/ml linoleic acid ss



Shows OPL sequence on Al_2O_3.

LOP

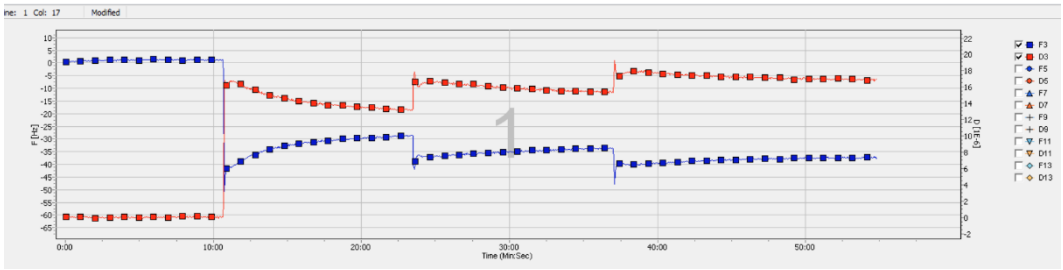
0:01 0.2ml ethanol on alumina LOP
12:10 0.2ml 100mg/ml linoleic acid ss
29:48 0.2ml 100mg/ml oleic acid ss
46:43 0.2ml 100mg/ml palmitic acid ss



Shows LOP sequence on Al_2O_3.

LPO

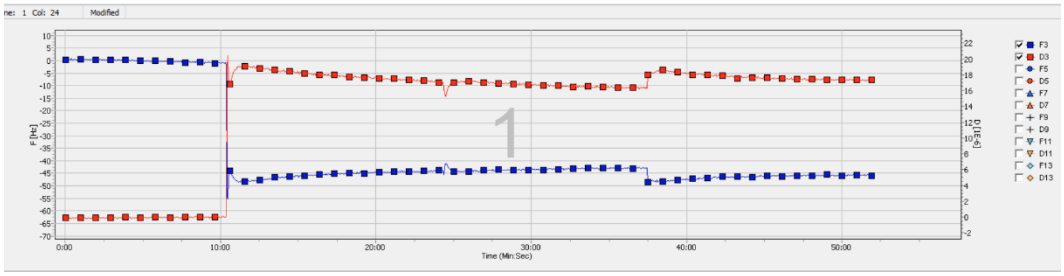
0:01 0.2ml ethanol on alumina LPO
10:42 0.2ml 100mg/ml linoleic acid ss
23:30 0.2ml 100mg/ml palmitic acid ss
37:03 0.2ml 100mg/ml oleic acid ss



Shows LPO sequence on Al_2O_3.

PLO

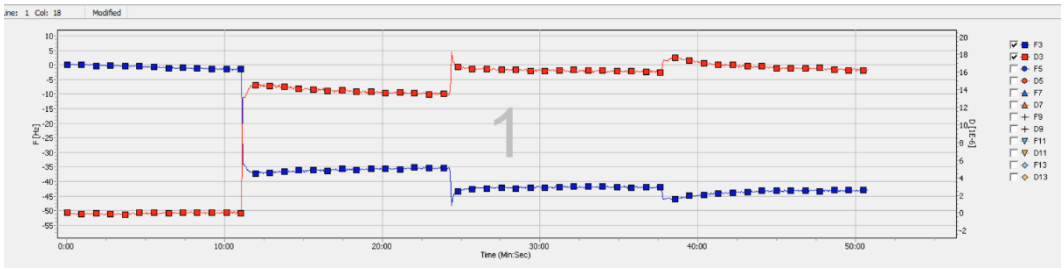
0:01 0.2ml ethanol on alumina PLO
10:28 0.2ml 100mg/ml palmitic acid ss
24:23 0.2ml 100mg/ml linoleic acid ss
37:29 0.2ml 100mg/ml oleic acid ss



Shows PLO sequence on Al_2O_3.

POL

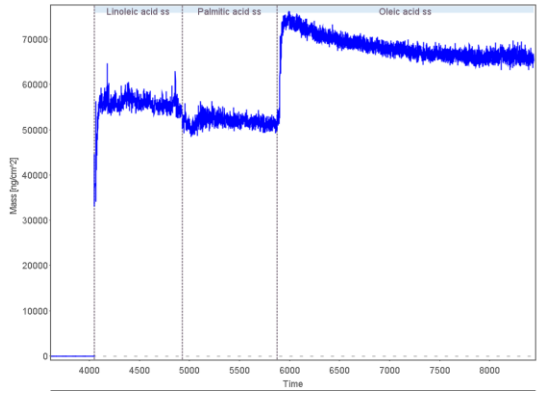
0:01 0.2ml ethanol on alumina POL
11:08 0.2ml 100mg/ml palmitic acid ss
24:22 0.2ml 100mg/ml oleic acid ss
37:47 0.2ml 100mg/ml linoleic acid ss

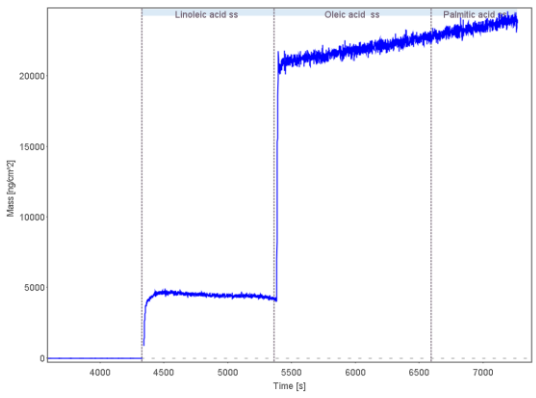


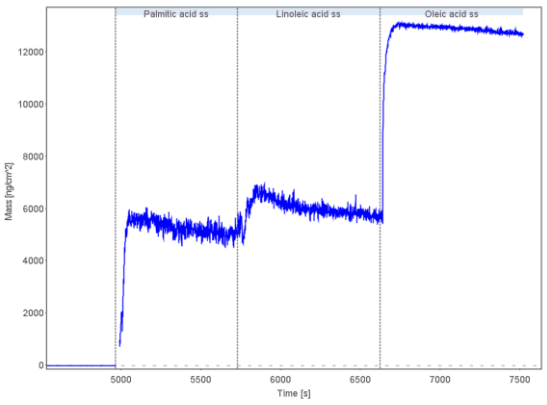
Shows POL sequence on Al_2O_3.

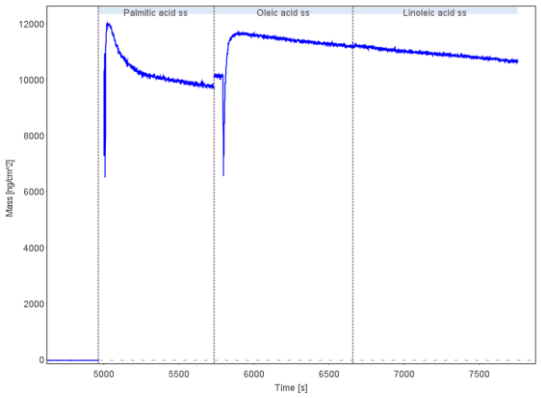
8.2.2 Effect of sequencing : Mass Adsorbed

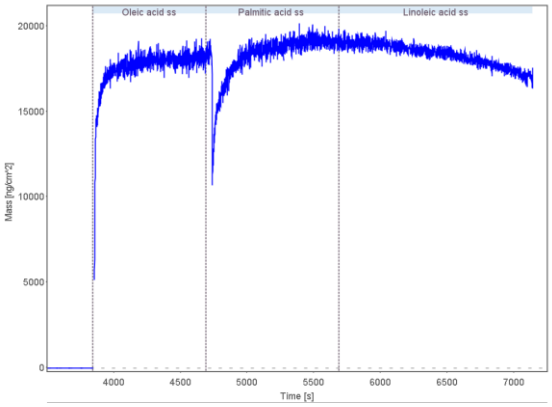
8.2.2.1 Polystyrene

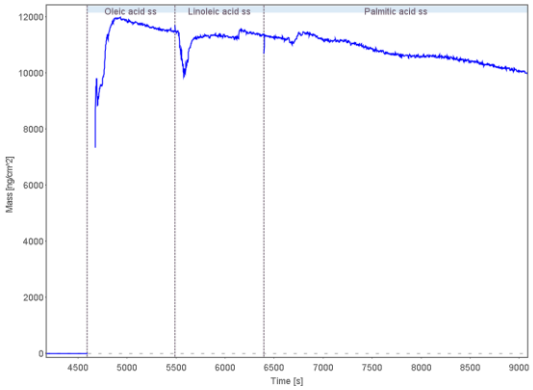





Palmitic acid ss
Linoleic acid ss
Oleic acid ss
Mass [ng/cm^2]
Time [s]

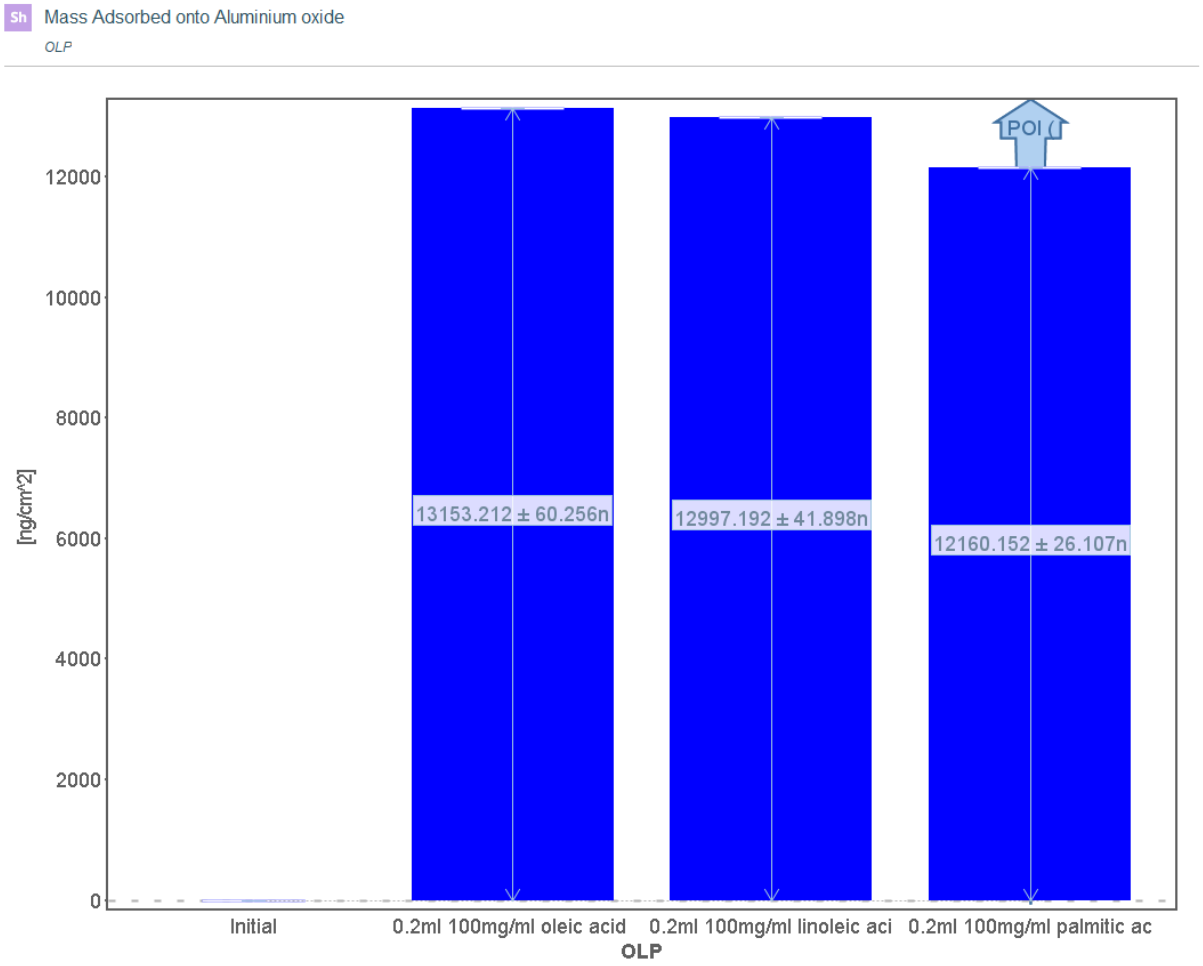

Palmitic acid ss
Oleic acid ss
Linoleic acid ss
Mass [ng/cm^2]
Time [s]


Oleic acid ss
Palmitic acid ss
Linoleic acid ss
Mass [ng/cm^2]
Time [s]


Oleic acid ss
Linoleic acid ss
Palmitic acid ss
Mass [ng/cm^2]
Time [s]

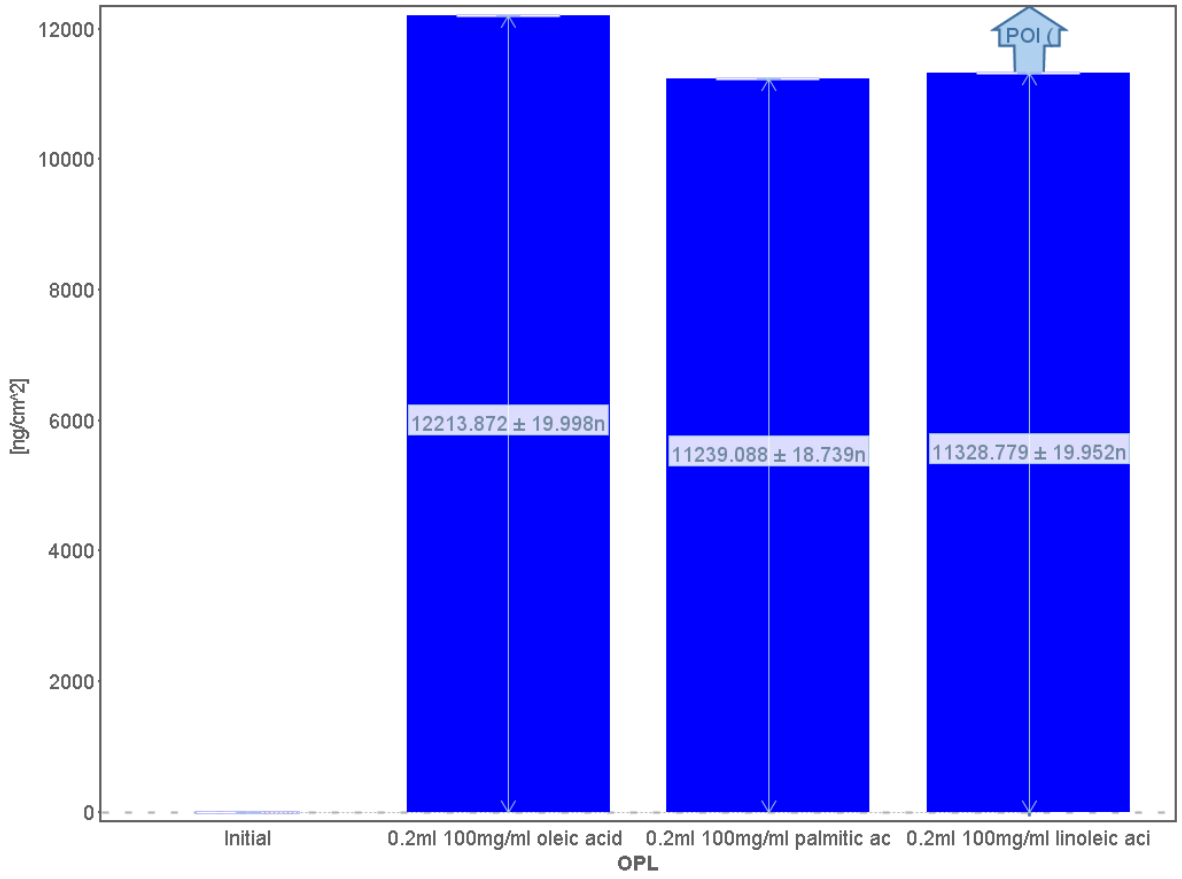
8.2.2.2 Silicon Dioxide

8.2.2.3 Aluminium oxide



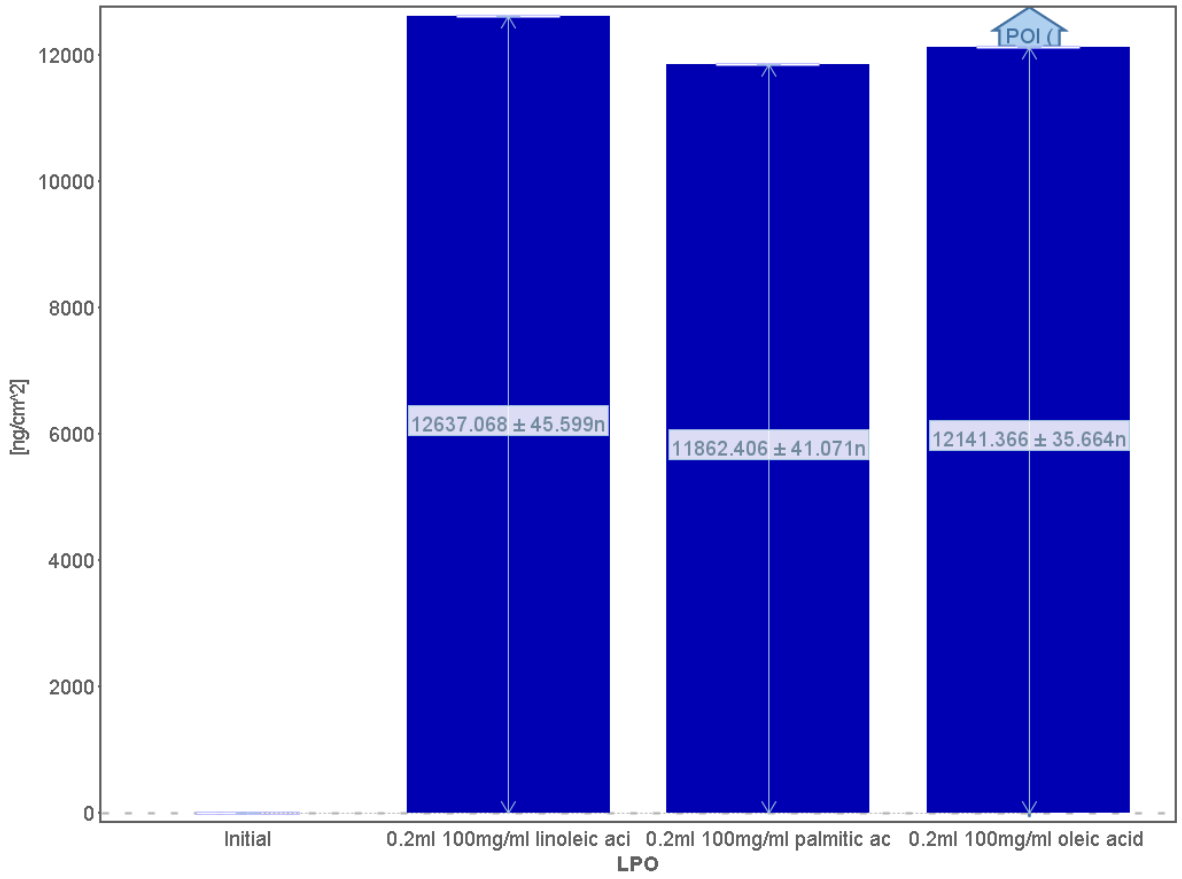
Sh Mass Adsorbed onto Aluminium oxide

OPL



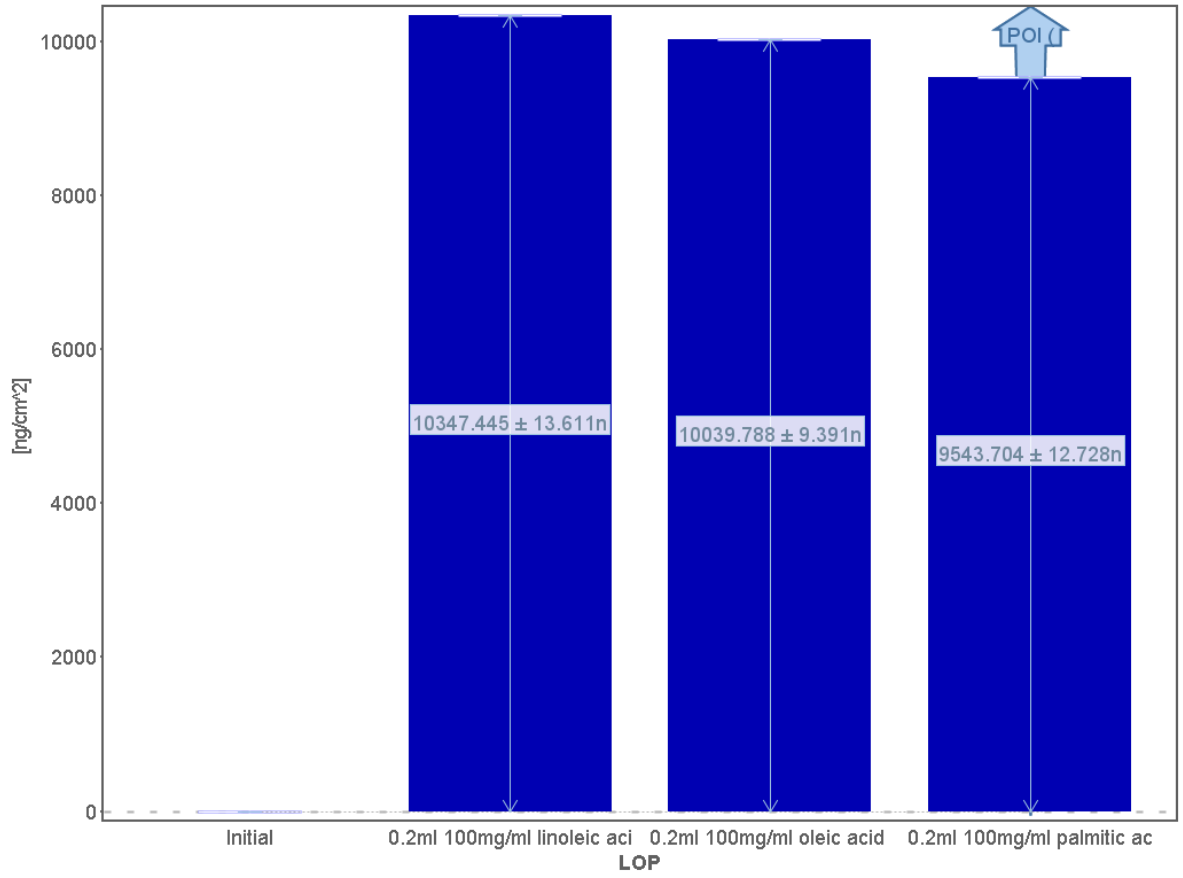
Sh Mass Adsorbed onto Aluminium oxide

LPO



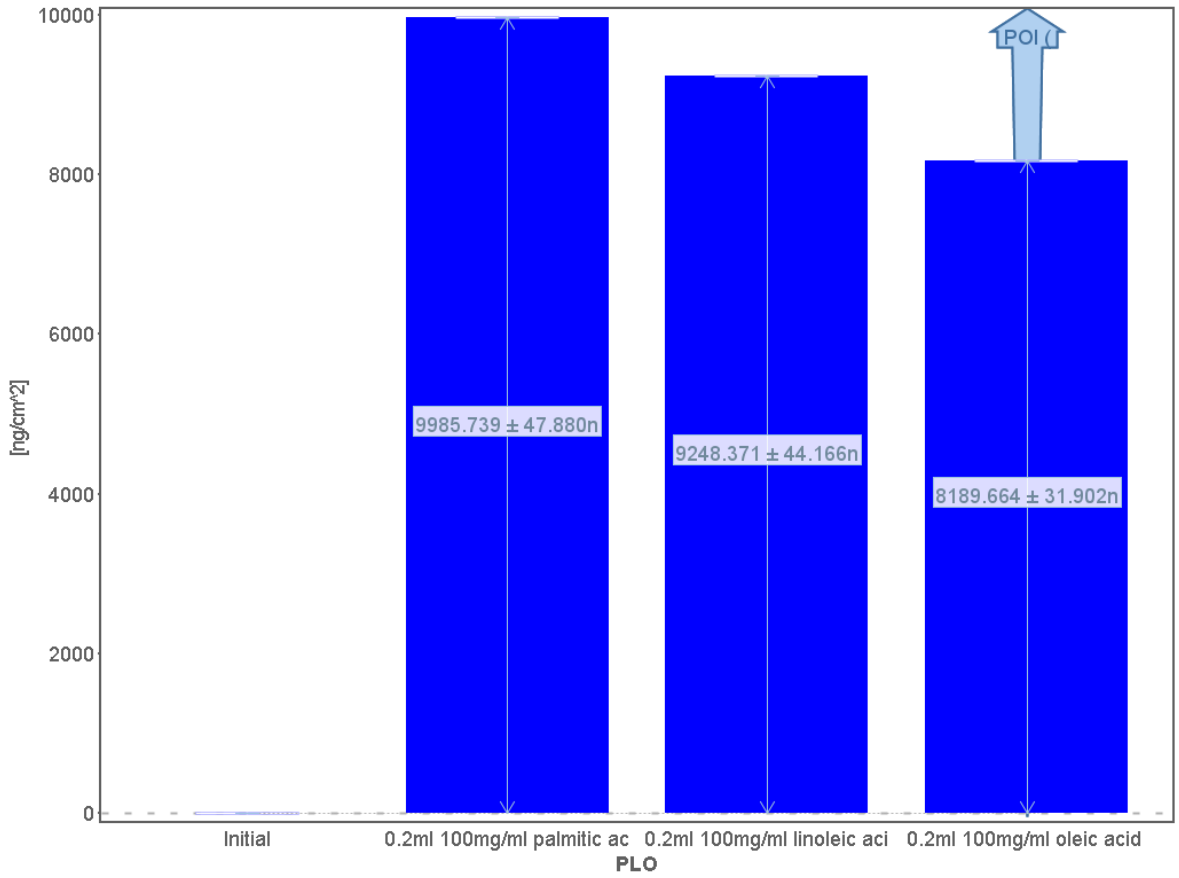
Sh Mass Adsorbed onto Aluminium oxide

LOP



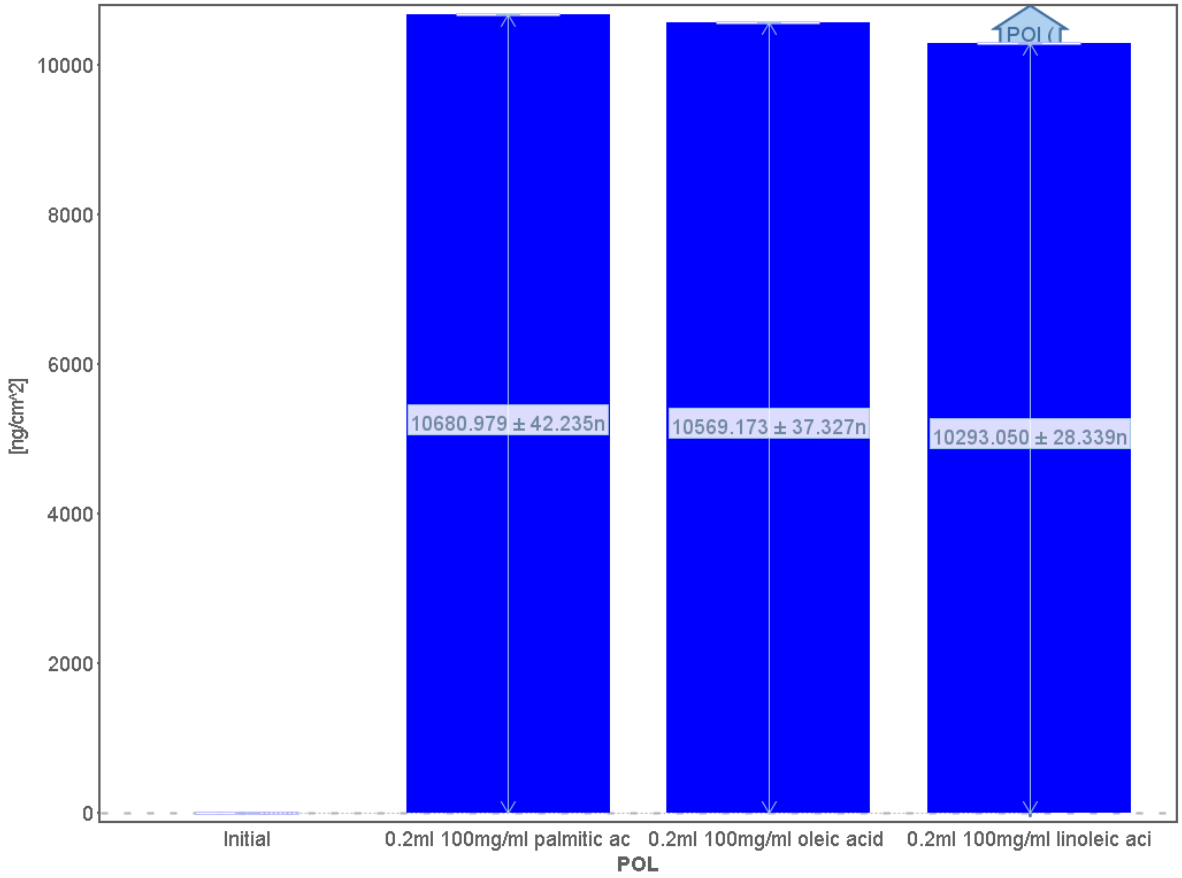
Sh Mass Adsorbed onto Aluminium oxide

PLO



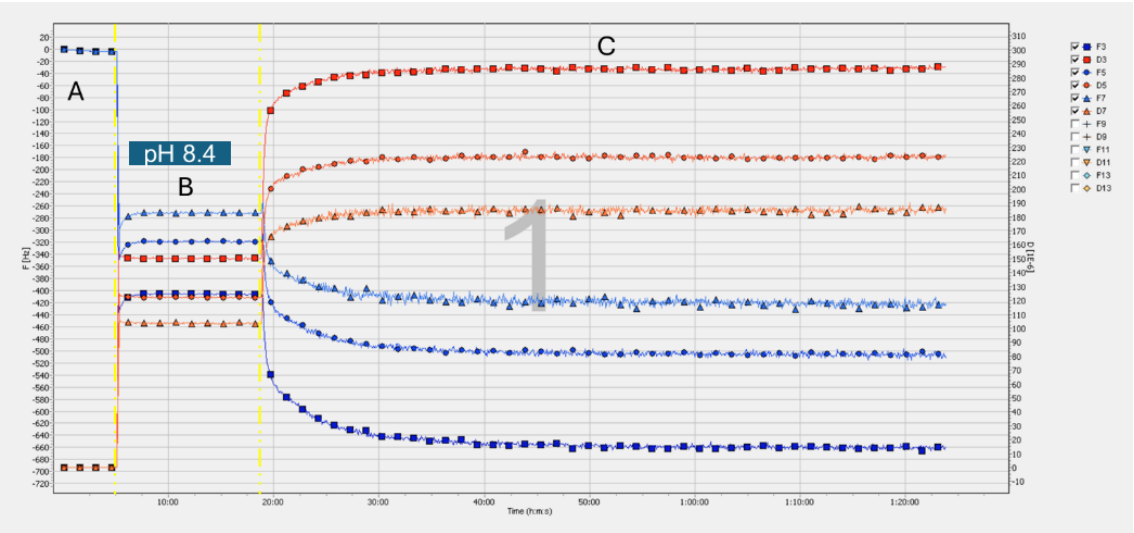
Sh Mass Adsorbed onto Aluminium oxide

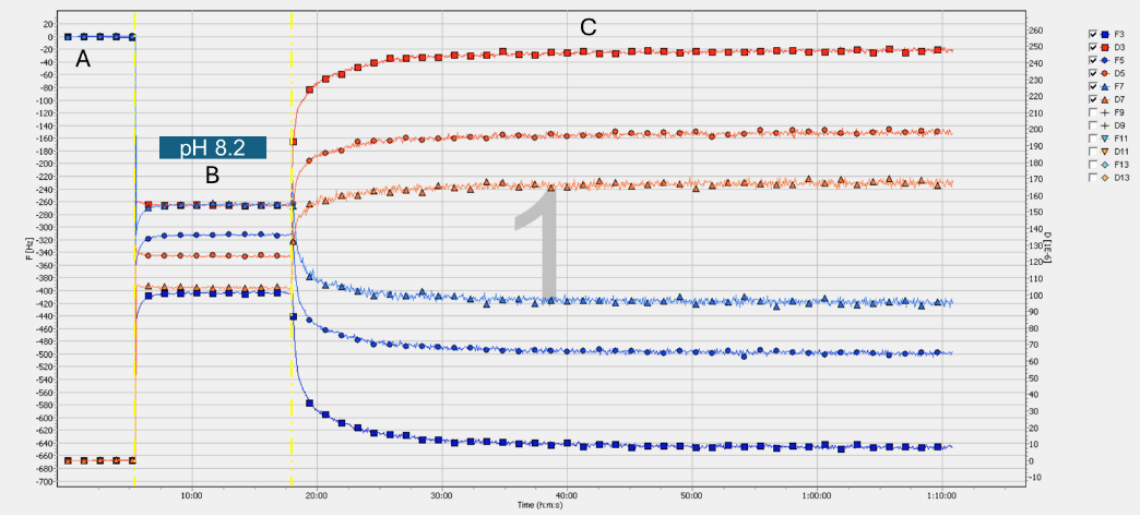
POL

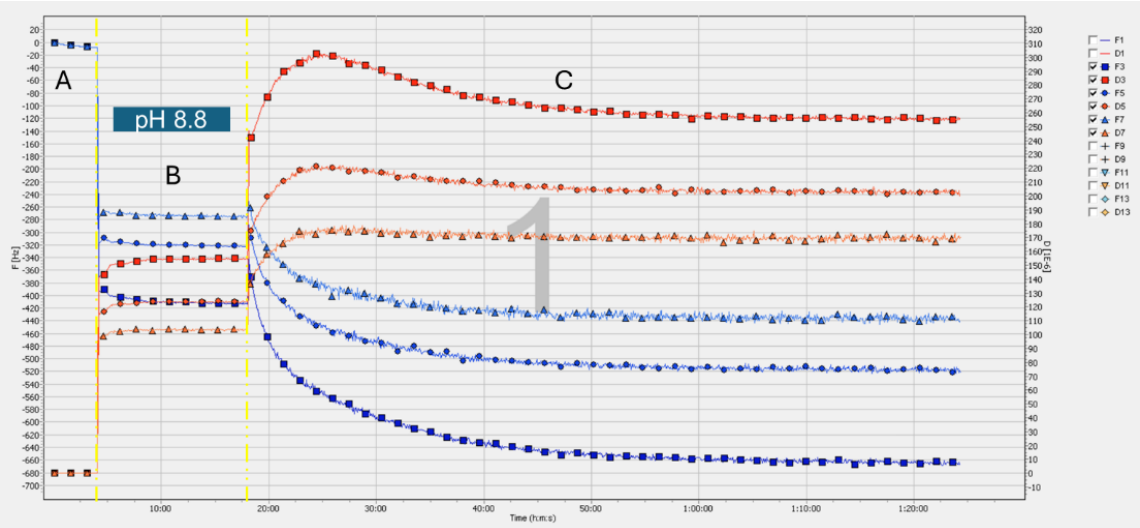


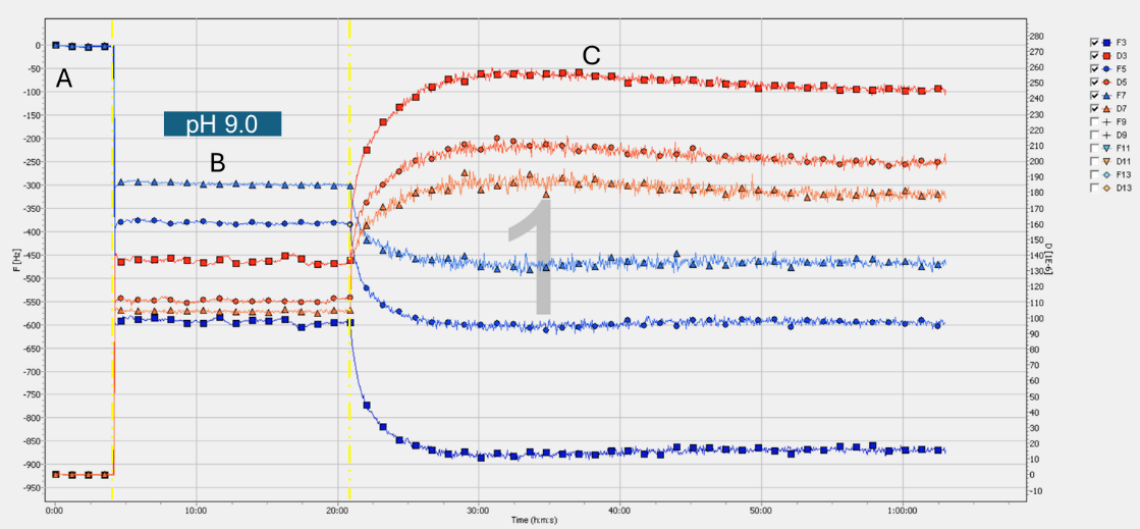
8.3 Appendix for Chapter 5

8.3.1 Palmitic Acid

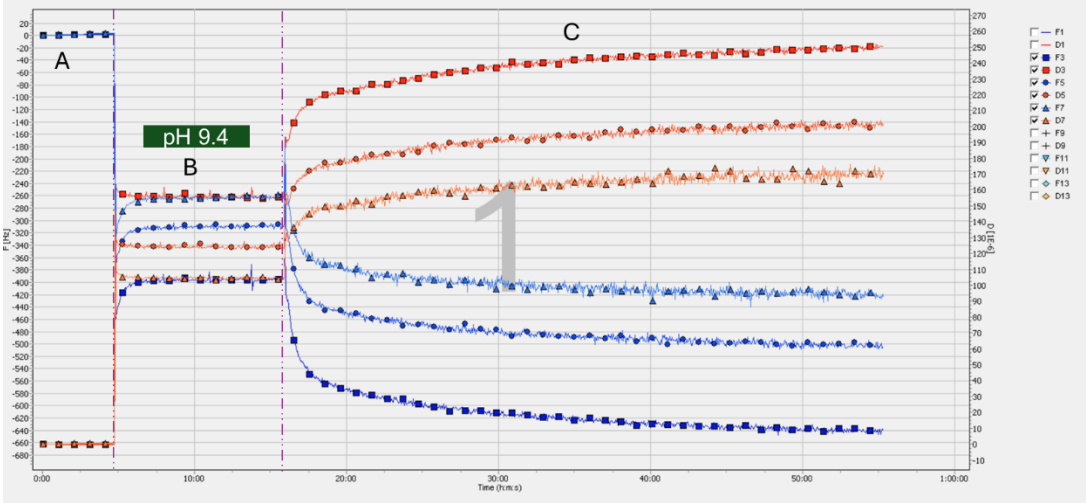


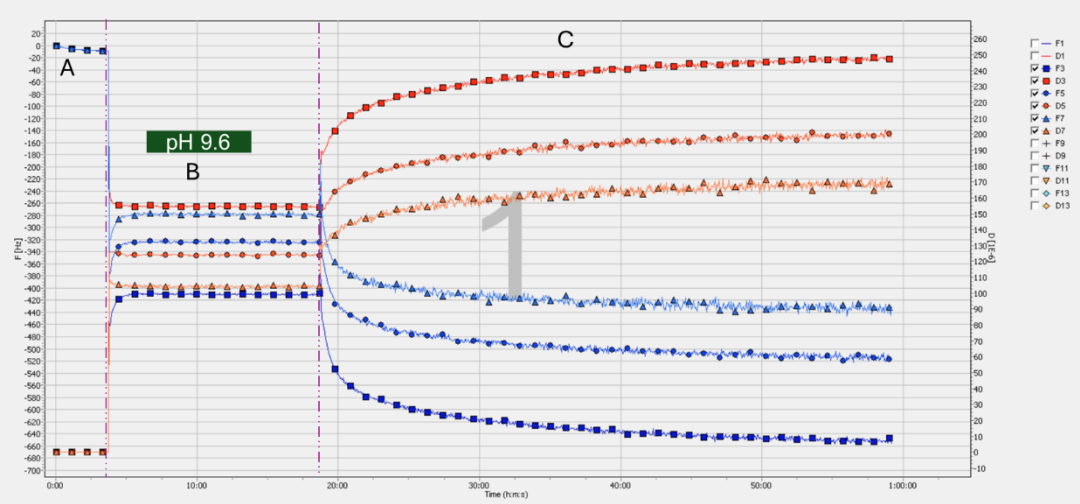


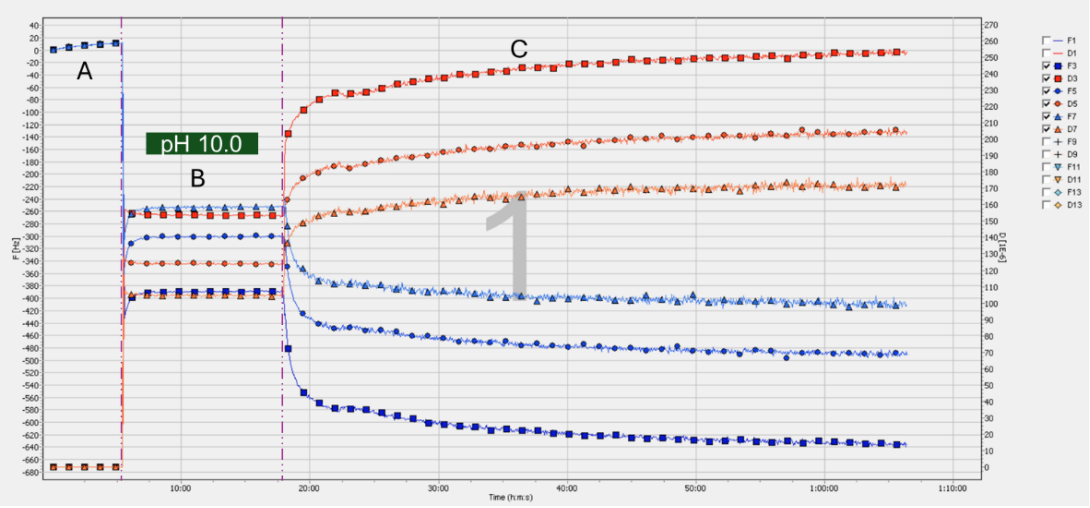


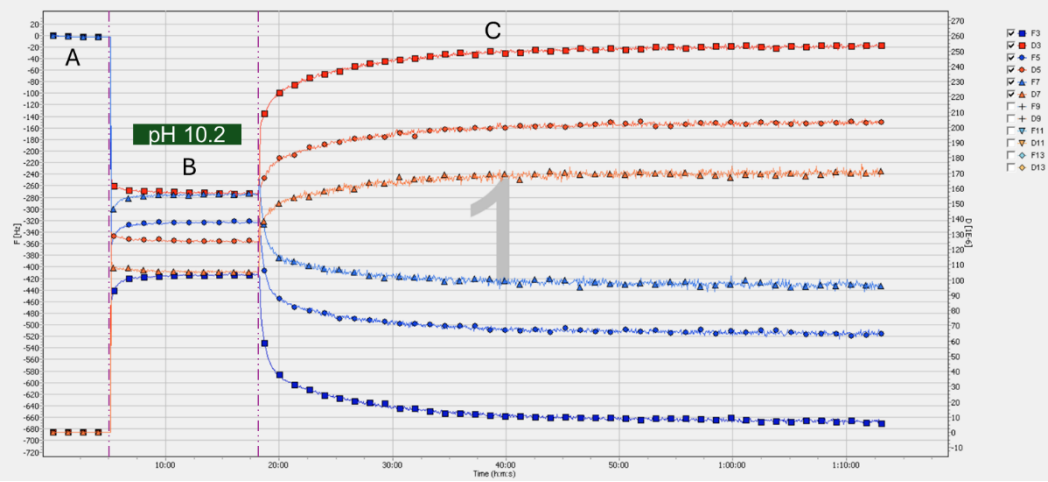


8.3.2 Oleic Acid

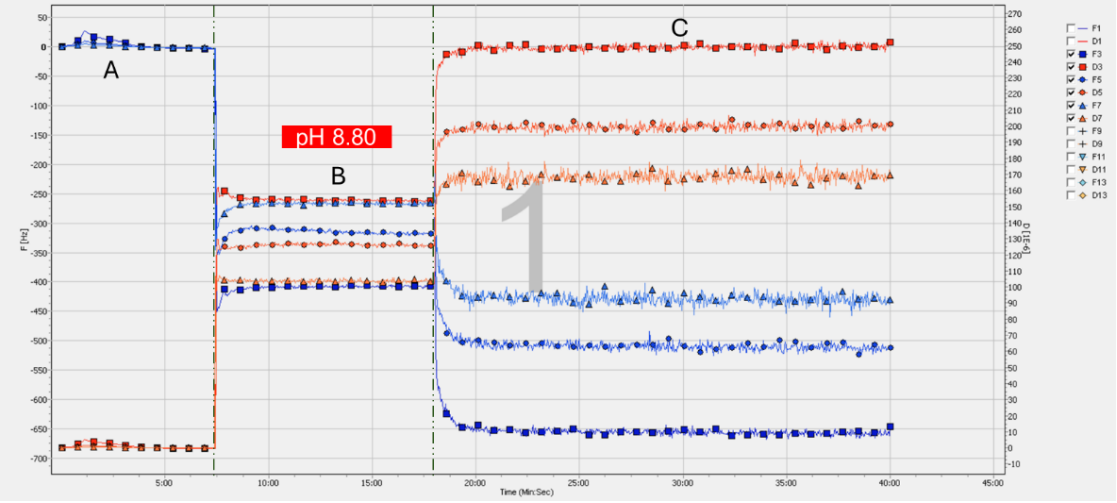


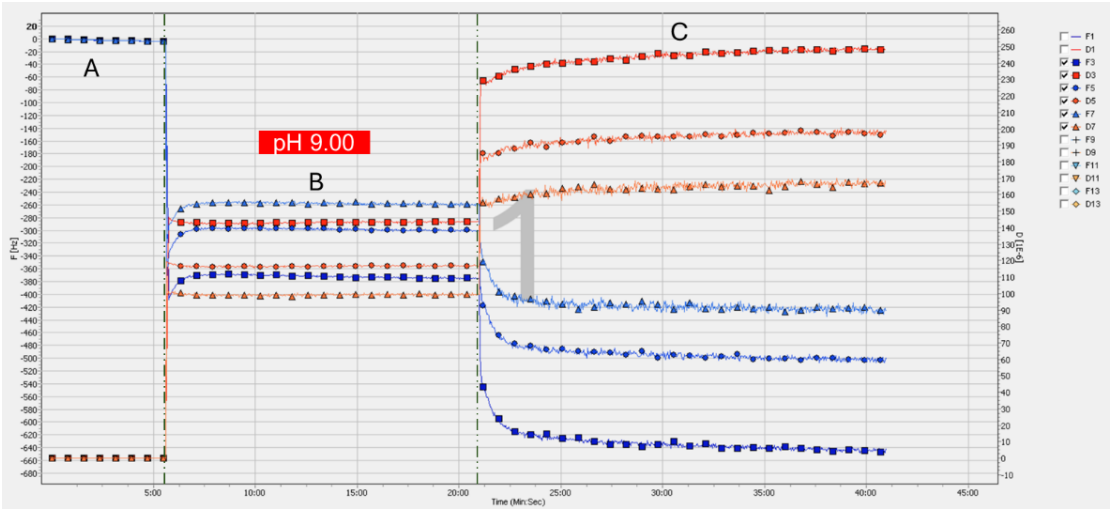


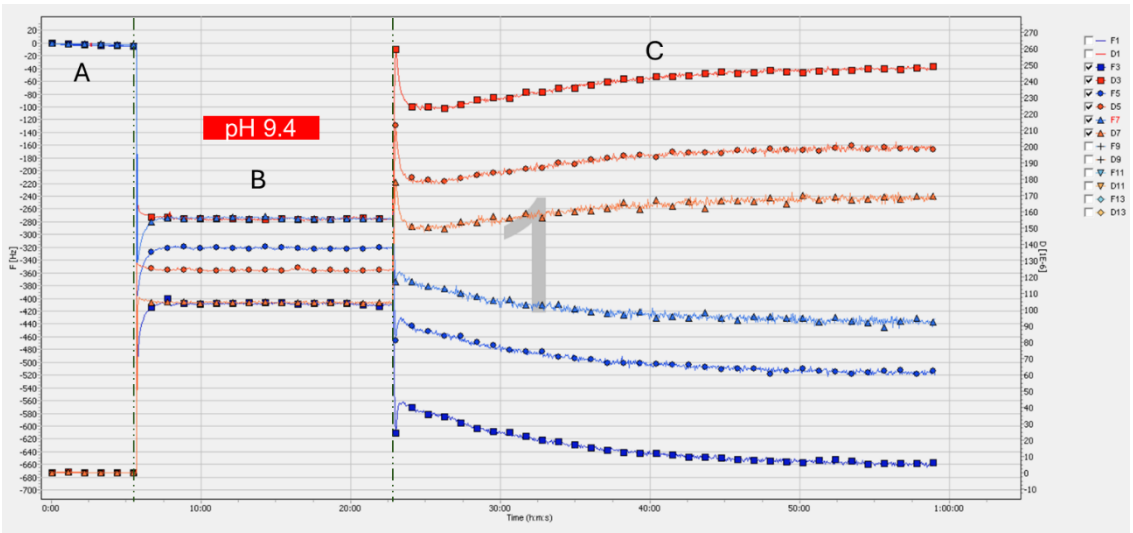


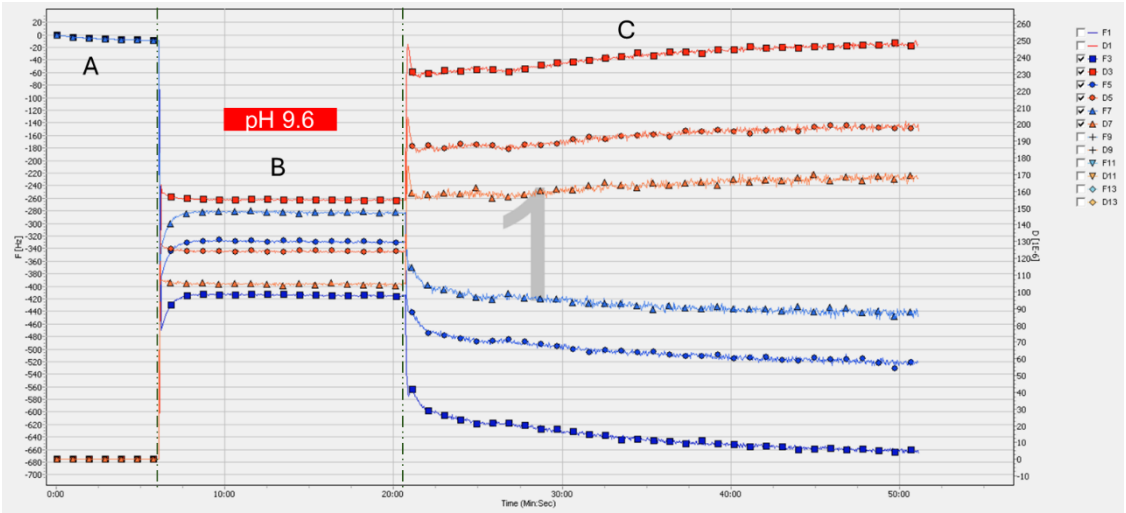


8.3.3 Linoleic Acid




A
pH 9.00
B
C
1
F [Hz]
D [E-9]
Time (Min:Sec)


A
pH 9.4
B
C
1
F [Hz]
D [E-9]
Time (h:m:s)


A
pH 9.6
B
C
1
F [Hz]
D [E-9]
Time (Min:Sec)

Page No.	Type of work:	Name of work	Source of work	Copyright holder and contact	permission requested on	I have permission yes /no	Permission note
5	figure	Fig. 8. Proposed mechanisms of FOG deposit formation in sewer lines.	Mechanisms of Fat, Oil and Grease (FOG) deposit formation in sewer lines, Water Research, Volume 47, Issue 13, 2013, Pages 4451-4459, ISSN 0043-1354, https://doi.org/10.1016/j.watres.2013.05.002.	Copyright © 2013 Elsevier Ltd.	02.05.24	Yes	Granted by *Elsevier*
7 12	figure	Fig. 1. Preparation of silica particles by sequential addition method. Fig. 4. (A) Effect of ammonia on particle size	A novel method for synthesis of silica nanoparticles, Journal of Colloid and Interface Science, Volume 289, Issue 1, 2005, Pages 125-131, ISSN 0021-9797, https://doi.org/10.1016/j.jcis.2005.02.019.	Copyright © 2005 Elsevier Inc.	02.05.24	Yes	Granted by *Elsevier*

			(https://www.sciencedirect.com/science/article/pii/S0021979705001566)				
9	figure	Graphical Abstract	Synthesis of silica nanoparticles from sodium silicate under alkaline conditions Volume 77, pages 753–758, (2016) https://doi.org/10.1007/s10971-015-3950-7	© 2024 Springer Nature	02.05.24	Yes	Granted by *Elsevier*
10 11	figure	Fig. 1. Small-angle X-ray scatting patterns for the synthesized ordered mesoporous silica. Fig. 2. Scanning electron diffraction images measured for the synthesized ordered mesoporous silica.	Effect of synthesis temperature on the ordered pore structure in mesoporous silica studied by positron annihilation spectroscopy, Applied Surface Science, Volume 363, 2016, Pages 445-450, ISSN 0169-4332, https://doi.org/10.1016/j.apsusc.2015.12.055.	Copyright © 2015 Elsevier B.V.	02.05.24	Yes	Granted by *Elsevier*
13	figure	Scheme 1. Common techniques in	Synthesis and surface functionalization of silica	*Copyright © 2014 Elsevier B.V.*	02.05.24	Yes	Granted by *Elsevier*

		silica nanoparticle synthesis.	nanoparticles for nanomedicine, Surface Science Reports, Volume 69, Issues 2–3, 2014, Pages 132-158, ISSN 0167-5729, https://doi.org/10.1016/j.surfrep.2014.07.001.				
15 16	figure	Fig. 3. Photograph of the examined quartz crystals. Fig. 7. Averaged responses of the sequential and triplicate injections at respective antibody concentrations for the rectangular and circular systems.	Quartz crystal microbalance sensor design: I. Experimental study of sensor response and performance, Sensors and Actuators B: Chemical, Volume 123, Issue 1, 2007, Pages 27-34, ISSN 0925-4005, https://doi.org/10.1016/j.snb.2006.07.027.	*Copyright © 2006 Elsevier B.V.*	02.05.24	Yes	Granted by *Elsevier*
22	figure	Figure 9.1:Definitions of adsorbent, adsorpt, and adsorbate.	Butt, H.-J., Graf, K. and Kappl, M. (2003). Adsorption. In Physics and Chemistry of Interfaces	*Copyright © 2003 Wiley-VCH Verlag GmbH & Co. KGaA*	02.05.24	Yes	Granted by *Elsevier*

23 25		Figure 9.2:Schematic plot of eight types of adsorption isotherms commonly observed. Figure 9.5:Schematic drawing of the Langmuir adsorption model.	Pages 177 - 205 https://doi.org/10.1002/352760231 3.ch9				
22	Table	Table 3. Basic types of industrial adsorbents	Adsorption — from theory to practice, Advances in Colloid and Interface Science, Volume 93, Issues 1–3, 2001, Pages 135-224, ISSN 0001-8686, https://doi.org/10.1016/S0001-8686(00)00082-8.	*Copyright © 2001 Elsevier Science B.V.*	02.05.24	Yes	Granted by *Elsevier*
24	figure	Fig. 1. Binding isotherms for polymer 1.	Application of the Freundlich adsorption isotherm in the characterization of molecularly imprinted polymers, Analytica Chimica Acta, Volume 435, Issue 1, 2001,	*Copyright © 2001 Elsevier Science B.V.*	02.05.24	Yes	Granted by *Elsevier*

			Pages 35-42, ISSN 0003-2670, https://doi.org/10.1016/S0003-2670(00)01211-3.				
26	figure	Fig. 1. The adsorption isotherm obtained when 6 mg of capric acid, 8 mg lauric acid, 10 mg myristic acid, 11 mg palmitic acid and 12 mg stearic acid are dissolved in 20 mL benzene and incubated at 25 °C with variable amounts of montmorillonite for 60 min.	Application of Langmuir isotherm to saturated fatty acid adsorption, Microporous and Mesoporous Materials, Volume 87, Issue 3, 2006, Pages 203-206, ISSN 1387-1811, https://doi.org/10.1016/j.micromeso.2005.08.009.	*Copyright © 2005 Elsevier Inc.*	02.05.24	Yes	Granted by *Elsevier*
31 to 33	Table	Table 15.1 Common Fatty Acids	Industrial Organic Chemicals: Chapter 15. Pages 493 – 521. ISBN 9780470537435, https://doi.org/10.1002/9781118229996.ch15	*Copyright © 2013 John Wiley & Sons, Inc.*	02.05.24	Yes	Granted by *Elsevier*

27	figure	Fig. 5. The adsorption mechanisms revealed by the BET model.	Adsorption isotherm models: Classification, physical meaning, application and solving method. Pages :127279 Volume: 258 ISSN 0045-6535 https://doi.org/10.1016/j.chemosphere.2020.127279	© *2020 Elsevier Ltd.*	11.01.26	Yes	Granted by *Elsevier*
14	figure	Figure 2: The bottom diagram illustrates the difference in dissipation signal generated by a rigid (red) and soft (green) molecular layer on the sensor crystal. Figure 2. A schematic depiction of Sauerbrey's findings: (a) the quartz crystal oscillates at a constant frequency when appropriate voltage is applied, (b) the oscillation frequency	[Technology Note] 1 Quartz Crystal Microbalance with Dissipation (QCM-D) (Nanoscience Instruments, 2020)	*Biolin Scientific AB, 2020*	01.10.2024	Yes	Eva Ekerot (Marketing and Communications Director) Qsense Organisation: Biolin Scientific AB

		starts to decrease as molecules begin to deposit on the crystal surface, and (c) frequency further decreases as more molecules deposit. (Illustration copyright belongs to Biolin Scientific/Q-Sense. Reproduced with permission.)					
21	figure	Abstract figure	Unsaturated Fatty Acids in Alkane Solution: Adsorption to Steel Surfaces. Langmuir, Volume 23, Issue 21, 2007 Pages 10598–10602 ISSN 0743-7463 https://doi.org/10.1021/la700909v	*Copyright © 2007, American Chemical Society*	09.09.2024	Yes	American Chemical Society